

The Design of Ultrasensitive Immunosensors Based on a New Multi-Signal Amplification
Gold Nanoparticles-dotted 4-Nitrophenylazo Functionalised Graphene Sensing Platform for
the Determination of Deoxynivalenol



By

Christopher Edozie Sunday

BSc (Hons), PGD (Ibadan) and MSc (Ibadan)

UNIVERSITY of the
WESTERN CAPE

A thesis submitted in fulfilment of the requirement for the Degree of Philosophiae Doctor in
the Department of Chemistry, University of the Western Cape, South Africa.

Supervisor

Professor Emmanuel I. Iwuoha

Co-supervisor

Professor Priscilla G. L. Baker

March 2014

Keywords

The Design of Ultrasensitive Immunosensors Based on a New Multi-Signal Amplification Gold Nanoparticles-dotted 4-Nitrophenylazo Functionalised Graphene Sensing Platform for the Determination of Deoxynivalenol

C. E. Sunday

Deoxynivalenol mycotoxin

Graphene

4-nitrophenyl diazonium cation

Gold nanoparticle

UV-Vis spectroscopy

Raman spectroscopy

Cyclic voltammetry

Electrochemical impedance spectroscopy

Electrochemiluminescence

Chronoamperometry/Chronocoulometry



Abstract

The Design of Ultrasensitive Immunosensors Based on a New Multi-Signal Amplification Gold Nanoparticles-dotted 4-Nitrophenylazo Functionalised Graphene Sensing Platform for the Determination of Deoxynivalenol

C. E. Sunday

PhD Thesis, Department of Chemistry, University of the Western Cape

A highly dispersive gold nanoparticle-dotted 4-nitrophenylazo functionalised graphene nanocomposite (AuNp/G/PhNO₂) was successfully synthesised and applied in enhancing sensing platform signals. Three label-free electrochemical immunosensors for the detection of deoxynivalenol mycotoxin (DON) based on the systematic modification of glassy carbon electrodes (GCE) with AuN_p/G/PhNO₂ was effectively achieved. General electrochemical impedance method was employed for the sensitive and selective detection of DON in standard solutions and reference material samples. A significant increase in charge transfer resistance (R_{ct}) of the sensing interface was observed due to the formation of insulating immune-complexes by the binding of deoxynivalenol antibody (DONab) and deoxynivalenol antigen (DONag). Further attachments of DONab and DONag resulted in increases in the obtained R_{ct} values, and the increases were linearly proportional to the concentration of DONag. The three immunosensors denoted as GCE/PDMA/AuNp/G/PhNH₂/DONab, GCE/Nafion/[Ru(bpy)₃]²⁺/AuNp/G/PhNH₂/DONab and GCE/Nafion/[Ru(bpy)₃]²⁺/G/PhNH₂/DONab have detection range of 6 – 30 ng/mL for DONag in standard samples. Their sensitivity and detection limits were 43.45 ΩL/ng and 1.1

pg/L; 32.14ΩL/ng and 0.3 pg/L; 9.412 ΩL/ng and 1.1 pg/L respectively. This result was better than those reported in the literature and compares reasonably with Enzyme Linked Immunosorbent Assay (ELISA) results. The present sensing methodology represents an attractive alternative to the existing methods for the detection of deoxynivalenol mycotoxin and other big biomolecules of interest due to its simplicity, stability, sensitivity, reproducibility, selectivity, and inexpensive instrumentation. And they could be used to develop high-performance, ultra-sensitive electrochemiluminescence, voltammetric or amperometric sensors as well.

March 2014

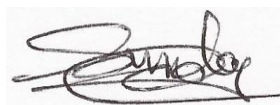


Declaration

I declare that “*The Design of Ultrasensitive Immunosensors Based on a New Multi-Signal Amplification Gold Nanoparticles-dotted 4-Nitrophenylazo Functionalised Graphene Sensing Platform for the Determination of Deoxynivalenol*” is my own work. That it has not been submitted for any degree or examination in any other university, and that all the sources I have used or quoted have been indicated and acknowledged by means of complete references.

Christopher Edozie Sunday

Date: March 2014

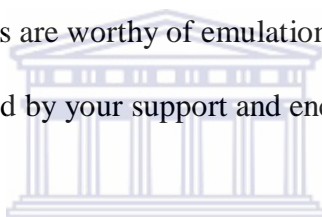


Signed:



Acknowledgements

Foremost, I deeply appreciate almighty God for HIS mercy, favor and faithfulness all through this journey and indeed throughout my life. For the strength and wisdom to finish this research Lord, I ascribe all the glory, honour and adoration to YOU now and forever, amen. I acknowledge University of the Western Cape, South Africa for giving me the opportunity to grow this tall. I place on record my profound gratitude to my supervisor Prof. Emmanuel I. Iwuoha for his patience, support and immense knowledge. I could not have imagined having a better mentor for my PhD study. Your confidence in me inspires me a lot sir. I am grateful to you also my co-supervisor Prof. P. G. L. Baker for all the guidance and invaluable advice, your oratory and supervisory skills are worthy of emulation. My sincere gratitude goes to you Prof Lorna Holtman, I am humbled by your support and encouragement, remain blessed.

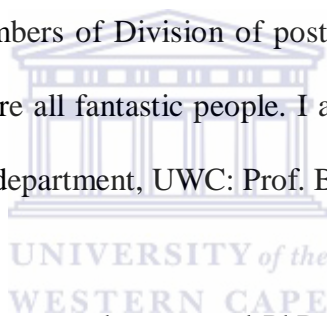


I appreciate my late great father, W.O. Sunday Nnamerenwa, you have passed on but you still live in me. For your true love, moral support, prayers and believing in me when it seemed like it was all over for me, I say a warm and sincere thank you to you my mother, Mrs Lucy Nnamerenwa. Dearest and biggest sister Mrs Ngozi Freda Ajiri, words have failed me in explaining how loving and supportive you have been to me, thank you also. I appreciate all my siblings, Mr Okechukwu Sunday, Mrs. Ucheoma Glory, Mrs Oluchi Nwoha and Mr. Uchechukwu Sunday for your moral support and encouragement.

I sincerely cherish you and your family Mr. Akobundu Godson Festus for all your support, you are a friend indeed and you stick closer than a brother. I call you my brother from another mother Mr Ikenna Festus, thank you also for everything. You are a father to me Mr

Uchechukwu Festus; I express my gratitude to you for lending me your shoulder to cry on sir. Thanks to my supportive friend, Dr Innocent C. Nnorom and family (Ezi enyi Kris ndewo).

I thank you senior post-doctor Tesfaye for all the constructive criticisms. To all my colleagues in sensor laboratory: Dr Masikini, Dr Abebaw, Dr Stephen, Dr Njomo, Dr Fanelwa, Dr Chinwe, Dr Ndangili, Dr Abdul, Noluthando, Bulelwa, Hlamulo, Kerileng, Usispho, Oluwakemi, Lerato, Mawethu, Lindsay, Gertrude, Lutgarde, Nontle, Babes, Sinazo and many others, I express my sincere gratitude for the cordial work relationship. My special thank you goes to Chemistry Department (both academic and technical staffs) for your support in providing all the apparatus and instrumentation required for this research. I can't say enough thank you to all members of Division of postgraduate studies, UWC: Dr Allie, Peter, Adrian and Brenton, you are all fantastic people. I appreciate all members of electron microscope unit (EMU), physics department, UWC: Prof. Basil, Dr. Subelia and Mr. Adrian.



This study was made possible by research grant and PhD bursaries from National Research Foundation (NRF), South Africa. My humble appreciation goes to you also my sponsor. And to all whose names I may not have mentioned, who have contributed directly or indirectly to the success of this research, you are equally appreciated and I say a big.....



Dedication

I dedicate this project to

My mother Mrs. Lucy Sunday Nnamerenwa,

My sister Mrs Ngozi Freda Ajiri

And to the blessed memory of my father

Late W.O.1 Sunday Nnamerenwa



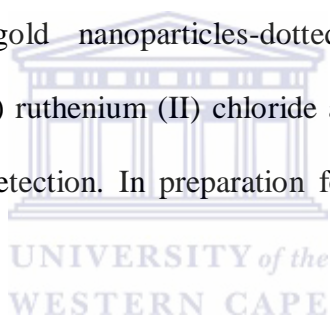
List of publications

- 1. Christopher E. Sunday^a**, Mawethu Bilibana^a, Sinazo Qakala^a, Oluwakemi Tovide^a, Kerileng M. Molapo^a, Gertrude Fomo^a, Chinwe O. Ikpo^a, Tesfaye Waryo^a, Gcineka Mbambisa^a, Bulelwa Mpushe^a, Avril Williams^{a,b}, Priscilla G.L. Bakera, Sibulelo Vilakazi^c, Robert Tshikhudo^c, Emmanuel I. Iwuoha^{a*}, Modulation of the matrix effect of Nafion on tris (bipyridine) ruthenium (II) electrochemical probes by functionalisation with 4-nitrophenylazo graphene-gold nanocomposite. *Electrochimica Acta* 2014.
- 2. Njagi Njomo^a**, Tesfaye Waryo^a, Milua Masikini^a, Chinwe O. Ikpo^a, Stephen Mailu , Oluwakemi Tovide^a, Natasha Ross^a, Avril Williams^b, Nolubabalo Matinise^a, **Christopher E. Sunday^a**, Noluthando Mayedwa^a, Priscilla G.L. Baker^a, Kenneth I. Ozoemena^c, Emmanuel I. Iwuoha^{a*}, Graphenated tantalum (IV) oxide and poly(4-styrene sulphonic acid)-doped polyaniline nanocomposite as cathode material in an electrochemical capacitor, *Electrochimica Acta* 2014.
- 3. Oluwakemi Tovide^a**, Nazeem Jaheed^a, Nurali Mohamed^a, Ezo Nxusani^a, **Christopher E. Sunday^a**, Abebaw Tsegaye^a, Rachel F. Ajayi^a, Njagi Njomo^a, Hlamulo Makelane^a, Mawethu Bilibana^a, Priscilla G. Baker^a, Avril Williams^b, Sibulelo Vilakazi^c, Robert Tshikhudo^c, Emmanuel I. Iwuoha^{a*}, Graphenated polyaniline-doped tungsten oxide nanocomposites sensor for real time determination of phenanthrene, *Electrochimica Acta* 2014.

4. Olowu R., **Christopher E. Sunday**, et al., Assessment of proximate and mineral status of rhinoceros beetle larva, *oryctes rhinoceros* Linnaeus (1758) (Coleoptera: Scarabaeidae) from Itokin, Lagos state, Nigeria. *Research Journal of Environmental Sciences* 2012.

5. **Christopher E. Sunday**^a, Emmanuel I. Iwuoha^a. Enhanced solid-state electrochemiluminescence film based on gold nanoparticles-dotted nitrophenylazo functionalised graphene nanocomposite. Under review in *Journal of Electroanalytical Chemistry* 2014.

6. **Christopher E. Sunday**^a, Emmanuel I. Iwuoha^a, Ultrasensitive electrochemiluminescent immunosensor based on gold nanoparticles-dotted nitrophenylazo functionalised graphene and tris (bipyridine) ruthenium (II) chloride as a cationic reactant mediated in Nafion for deoxynivalenol detection. In preparation for *Biosensors and Bioelectronics* 2014.



Oral presentations

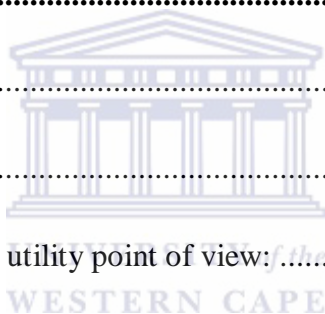
1. **Christopher Edozie Sunday**, Priscilla G. Baker and Emmanuel I. Iwuoha, A Novel Ultrasensitive Electrochemiluminescent Immunosensor Design Based On Enhanced Electro-generated Chemiluminescence From $[\text{Ru}(\text{Bpy})_3]^{2+}$ Ion Exchanged In $\text{PANI-GAu}_x\text{Cu}_y$ Ternary Hybrid Nano-material Film For The Determination Of Deoxynivalenol In Grains And Peanut Products, 2nd International symposium on Electrochemistry, Electrochemistry for energy, African Routes Conference Centre, University of the Western Cape (UWC), South Africa; 19-20th July, 2012.
2. **Christopher Edozie Sunday**, Priscilla G. Baker and Emmanuel I. Iwuoha, A Multi-Signal Biocompatible Platform from $[\text{Ru}(\text{Bpy})_3]^{2+}$ ion Exchanged in AuCuG/Perfluorosulfonate Ionomer Composite Films And Its Potential Applications In Electrochemical Sensors, 13th Topical Meeting of the International Society of Electrochemistry Advances in Electrochemical Materials Science and Manufacturing, Pretoria, South Africa; 7-10th April, 2013.

Table of contents

<i>Title page</i>	<i>i</i>
<i>Keywords</i>	<i>ii</i>
<i>Abstract</i>	<i>iii</i>
<i>Declaration</i>	<i>v</i>
<i>Acknowledgements</i>	<i>vi</i>
<i>Dedication</i>	<i>viii</i>
<i>List of publications</i>	<i>ix</i>
<i>Oral presentations</i>	<i>xi</i>
<i>Table of contents</i>	<i>xii</i>
<i>List of Figures</i>	<i>xxiii</i>
<i>List of Tables</i>	<i>xxxi</i>
<i>List of Schemes</i>	<i>xxxii</i>
<i>List of Abbreviations</i>	<i>xxxiii</i>
<i>List of symbols</i>	<i>xxxv</i>
<i>Chapter One</i>	<i>1</i>
<i>Introduction</i>	<i>1</i>
1.1 Background information	1
1.2 Problem statement	8
1.3 Aim and approach of this research	9
1.4 Research framework	11



1.5 Thesis layout	12
Chapter Two	14
Literature Review	14
2.1 Deoxynivalenol mycotoxin	14
2.2 Metallic nanoparticles.....	17
2.2.1 Liquid phase fabrication	18
2.2.2 Gas (vapour) phase fabrication	19
2.3 Graphene.....	20
2.4 Polymer	21
2.4.1 Natural polymers	22
2.4.2 Synthetic polymer	23
2.4.2.1 Characterization by utility point of view:.....	23
2.4.2.2 Characterization by mode of polymerization reaction.....	24
2.4.2.3 Characterisation by monomer composition.....	28
2.5 Ionomers.....	29
2.6 Nafion	31
2.7 Sensor	34
2.7.1 Physical sensor	35
2.7.2 Chemical sensors.....	36
2.7.2.1 The receptor.....	36
2.7.2.2 The transducer	37



2.7.3 Biosensors	39
2.7.3.1 Immunosensor	40
2.7.3.2 Covalent binding	41
2.7.3.3 Attachment by affinity interactions (encapsulation and confining).....	41
2.7.3.4 Electrochemical immobilization (physical adsorption)	42
2.8 Fundamental principles of ultraviolet-visible spectroscopy	43
2.9 Fundamental principles of Raman spectroscopy	46
2.9.1 Components of a Raman spectrometer	48
2.10 Fundamental principles of atomic force microscopy (AFM).....	49
2.10.1 Operation of AFM	49
2.10.1.1 Piezocrystals	50
2.10.1.2 Probe	51
2.10.2 Modes of operation	51
2.10.2.1 Contact mode	51
2.10.2.2 Non-contact mode	52
2.10.2.3 Tapping mode	52
2.11 Fundamental principles of scanning electron microscopy (SEM).....	53
2.11.1 Components of a scanning electron microscope	54
2.11.2 Basic operation principle of SEM.....	54
2.12 Fundamental principles of transmission electron microscopy (TEM)	56
2.13 Fundamental principles of Energy Dispersive X-ray Spectroscopy (EDX)	59



2.14	Fundamental principles of cyclic voltammetry (CV)	61
2.14.1	Instrumentation for cyclic voltammetry (CV) experiments	61
2.14.2	Definition of electrochemical terminology	63
2.14.3	Principles for the generation of a cyclic voltammetric curve.....	66
2.14.4	Analytical criteria to identify a reversible processes	69
2.14.5	Analytical criteria to identify a irreversible processes.....	72
2.14.6	Analytical criteria to identify a quasi-reversible processes.....	73
2.15	Fundamental principles of square wave voltammetry (SWV)	74
2.16	Fundamental principles of electrochemical impedance spectroscopy	76
2.16.1	Operating principle of electrochemical impedance spectroscopy EIS.	76
2.16.2	Data presentation	79
2.16.2.1	Nyquist plot.....	80
2.16.2.2	Bode plot.....	81
2.16.3	Electric circuit components	82
2.16.4	Resistor.....	83
2.16.5	Inductor	83
2.16.6	Capacitor	83
2.16.7	Serial and parallel combinations of circuit elements	84
2.16.8	Equivalent electrical circuit modelling	85
2.16.8.1	Warburg element (Z_w).....	87
2.16.8.2	Constant phase element (CPE).....	88

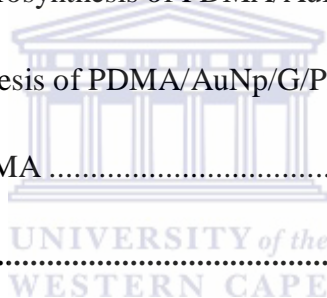
2.16.8.3 Electrochemical double layer capacitance	88
2.16.8.4 Solution resistance.....	89
2.16.8.5 Charge transfer resistance.....	90
2.17 Fundamental principles of chronoamperometry (CA).....	91
2.18 Fundamental principles of chronocoulometry (CC).....	95
2.18.1 Concentration response	96
2.18.2 Current response	97
2.18.3 Charge response.....	97
2.18.4 Adsorption.....	98
2.19 Fundamental principles of electrochemiluminescence (ECL).....	100
2.19.1 Luminescence	100
2.19.2 Electrochemiluminescence.....	102
2.19.3 Components of an electrochemiluminescent system	102
2.19.4 Mechanisms of electrochemiluminescence	103
2.19.4.1 Hot electron-induced electrochemiluminescence (HEI ECL)	104
2.19.4.2 Two-step potential sweep method (Annihilation pathway).....	105
2.19.4.3 One-step potential sweep method (co-reactant pathway).....	106
2.19.5 Optimization of electrochemiluminescence	108
<i>Chapter Three</i>	110
<i>Experimental Procedures and Analytical Methods</i>	110
3.1 Chemical synthesis of graphene oxide.....	110

3.1.1	Chemicals.....	110
3.1.2	Experimental procedure.....	110
3.2	Chemical synthesis of 4-nitrophenyl diazonium tetrafluoroborate (NDT)	112
3.2.1	Chemicals	112
3.2.2	Experimental procedure.....	112
3.3	Chemical synthesis of nitrophenylazo functionalized graphene (G/PhNO₂) ..	113
3.3.1	Chemicals and reagents	113
3.3.2	Experimental procedure.....	113
3.3.2.1	Pre-reduction of GO	114
3.3.2.2	Functionalisation of pre-reduced GO	115
3.3.2.3	Post-reduction with hydrazine	115
3.4	Chemical synthesis of gold nanoparticles-dotted 4-nitrophenylazo functionalized graphene (AuNp/G/PhNO₂)	117
3.4.1	Chemicals and reagents	117
3.4.2	Experimental procedure.....	117
3.5	Preparation of G/PhNO₂ and AuNp/G/PhNO₂ modified GCE	119
3.5.1	Chemicals and reagents	119
3.5.2	Pre-cleaning of working electrode	119
3.5.3	Experimental procedure.....	119
3.6	Preparation of AuNp/G/PhNO₂ and G/PhNO₂ composite with [Ru(bpy)₃]²⁺ mediated in Nafion on GCE	120
3.6.1	Chemicals and reagents	120

3.6.2	Experimental procedure.....	120
3.7	Electrochemical synthesis of PDMA and PDMA/ AuNp/G/PhNO₂ composite	121
3.7.1	Chemicals and reagents	121
3.7.2	Experimental procedure.....	122
3.8	Spectroscopic characterisation	123
3.8.1	Ultraviolet–visible spectroscopy	123
3.8.2	Raman spectrometry.....	123
3.9	Microscopic characterisations	124
3.9.1	High resolution transmission electron microscopy (HRTEM)	124
3.9.2	Scanning electron microscopy (SEM).....	124
3.9.3	Atomic force microscopy (AFM).....	125
3.10	Electrochemical characterisations.....	125
3.10.1	Cyclic voltammetry (CV), Square-wave voltammetry (SWV), chronocoulometry and chronoamperometry.....	125
3.10.2	Electrochemical impedance spectroscopy (EIS)	126
3.11	The application of Nafion/[Ru(bpy)₃]²⁺/AuNp/G/PhNO₂ and Nafion/[Ru(bpy)₃]²⁺/G/PhNO₂ sensor platforms for TPA detection via ECL system	126
3.11.1	Chemicals and reagents.....	126
3.11.2	Experimental procedure	126
3.12	Preparation of immunosensor	128
3.12.1	Chemicals and reagent	128
3.12.2	Preparation of standard solutions.....	128

3.12.3	Sample preparation and extraction	129
3.12.4	DON antibody immobilization	129
3.12.5	Application of the immunosensors as impedimetric DON mycotoxin sensor	132
3.12.6	Real sample studies.....	132
3.12.7	Competitive direct enzyme linked immunosorbent assay (CD-ELISA).....	133
Chapter Four.....		134
Results and discussion- Part one.....		134
4.1	Spectroscopic and microscopic characterisations of AuNp/G/PhNO₂.....	134
4.1.1	Ultraviolet-visible spectroscopy (UV-Vis)	134
4.1.2	Raman spectroscopy	136
4.1.3	Transmission electron microscopy (TEM)	137
4.1.4	Scanning electrochemical microscopy (SEM) and Energy-dispersive X-ray (EDX) spectrum	139
4.1.5	Atomic force microscopy (AFM).....	141
4.2	Electrochemistry of starting materials.....	143
4.2.1	Electrochemical behaviour of [Ru(bpy) ₃]Cl ₂ in solution.....	143
4.2.2	Electrochemistry of AuNp/G/PhNO ₂ and NDT in 0.1 M PBS solution.....	145
4.2.3	Electrochemistry of G/PhNO ₂ and AuNp/G/PhNO ₂	146
4.2.4	Construction of sensor platforms and optimization	149
4.2.5	CV of GCE/Nafion/[Ru(bpy) ₃] ²⁺ , GCE/Nafion/[Ru(bpy) ₃] ²⁺ /G/PhNO ₂ and GCE/Nafion/[Ru(bpy) ₃] ²⁺ /AuNp/G/PhNO ₂ sensor platforms.....	152

4.2.6 Chronoamperometric studies of GCE/Nafion/ $[\text{Ru}(\text{bpy})_3]^{2+}$, GCE/Nafion/ $[\text{Ru}(\text{bpy})_3]^{2+}/\text{G}/\text{PhNO}_2$ and GCE/Nafion/ $[\text{Ru}(\text{bpy})_3]^{2+}/\text{AuNp}/\text{G}/\text{PhNO}_2$ sensor platforms	159
4.2.7 Chronocoulometric studies of GCE/Nafion/ $[\text{Ru}(\text{bpy})_3]^{2+}$, GCE/Nafion/ $[\text{Ru}(\text{bpy})_3]^{2+}/\text{G}/\text{PhNO}_2$ and GCE/Nafion/ $[\text{Ru}(\text{bpy})_3]^{2+}/\text{AuNp}/\text{G}/\text{PhNO}_2$ sensor platforms	162
4.2.8 EIS studies of GCE/Nafion/ $[\text{Ru}(\text{bpy})_3]^{2+}$, GCE/Nafion/ $[\text{Ru}(\text{bpy})_3]^{2+}/\text{G}/\text{PhNO}_2$ and GCE/Nafion/ $[\text{Ru}(\text{bpy})_3]^{2+}/\text{AuNp}/\text{G}/\text{PhNO}_2$ sensor platforms	165
4.3 Detection of tri-n-propylamine via electrochemiluminescent system.....	173
4.4 Electrochemical synthesis and characterisation of PDMA/AuNp/G/PhNO₂..	175
4.4.1 Optimization for electrosynthesis of PDMA/AuNp/G/PhNO ₂ on GCE.....	176
4.4.2 Electrochemical synthesis of PDMA/AuNp/G/PhNO ₂ composite	181
4.4.3 Characterisation of PDMA	183
Chapter Five.....	188
Results and discussion- Part two.....	188
5.1 Fabrication of deoxynivalenol mycotoxin immunosensors.....	188
5.1.1 Electro-reduction of nitrophenyl group to aminophenyl group.	189
5.1.2 CV behaviour of electrochemically reduced modified electrodes	190
5.1.3 EIS study of electrochemically reduced modified electrodes.....	191
5.2 Immobilisation of DON antibody	193
5.3 UV-Vis study of DON antibody-antigen reactivity	194
5.4 GCE/Nafion/$[\text{Ru}(\text{bpy})_3]^{2+}/\text{AuNp}/\text{G}/\text{PhNH}_2/\text{DONab}$ immunosensor	196
5.4.1 CV behaviour of the stepwise modification processes	196



5.4.2	Chronoamperometric behaviour of stepwise modification processes	198
5.4.3	Optimisation of assay condition.....	199
5.4.3.1	Effect of antibody concentration.....	199
5.4.3.2	Effect of pH.....	200
5.4.3.3	Effect of incubation time	201
5.4.4	GCE/Nafion/[Ru(bpy) ₃] ²⁺ /AuNp/G/PhNH ₂ /DONab/BSA performance.....	202
5.5	GCE/Nafion/[Ru(bpy)₃]²⁺/G/PhNH₂/DONab/BSA immunosensor.....	205
5.5.2	Chronoamperometric behaviour of stepwise modification processes	206
5.5.3	GCE/Nafion/[Ru(bpy) ₃] ²⁺ /G/PhNH ₂ /DONab/BSA performance	207
5.6	GCE/PDMA/AuNp/G/Ph-NH₂/DONab/BSA immunosensor	209
5.6.1	Immobilisation of DON antibody	210
5.6.2	GCE/PDMA/AuNp/G/PhNH ₂ /DONab/BSA performance.....	211
5.7	Stability of the immunosensors.....	213
5.8	Reproducibility of the immunosensors.....	214
5.9	Repeatability of the immunosensors.....	214
5.10	Selectivity study of the immunosensors.....	214
5.11	Detection of DONag and certified reference materials by Veratox ELISA test kit	215
Chapter Six.....		218
Conclusions and Recommendations.....		218
6.1	Conclusions	218

6.2 Recommendations..... 220
References..... 221



List of Figures

Figures	Title	Page
Figure 1.1	Relationship between tolerable daily intake and NOAEL.....	3
Figure 2.1	Chemical structure of deoxynivalenol.....	15
Figure 2.3	Mechanism of liquid phase fabrication.....	19
Figure 2.4	Mechanism of gas phase fabrication.....	19
Figure 2.5	Graphene.....	20
Figure 2.6	The chemical formula of Nafion.....	32
Figure 2.7	The Yeager 3 Phase Model of Nafion® Clusters.....	33
Figure 2.8	Functional principles of the receptor.....	37
Figure 2.9	Classification of chemical sensor based on operating principle of the transducer.....	38
Figure 2.10	Methods for immobilising bio-molecules on the transducer.....	42
Figure 2.11	Basic schematic representation of a UV-Vis spectrometer.....	43
Figure 2.12	Illustration of molecular orbital theory.....	44
Figure 2.13	(a) Illustration of incident light scattering and (b) energy level diagram showing the states involved in Raman signal (c) typical Raman spectra.....	47
Figure 2.14	Representation of basic parts Raman of spectrometer.....	49
Figure 2.15	Schematic illustration operational principles of AFM.....	50
Figure 2.16	AFM image of gold nanoparticles-dotted 4-nitrophenylazo functionalized graphene (AuNp/G/PhNO ₂).....	53

Figure 2.17	Schematic representation of a scanning electron microscope.....	56
Figure 2.18	A representation of TEM operating system and a TE microscope.....	57
Figure 2.19	The typical TEM image of (A) silver nanoparticles, (B) gold nanoparticles.....	58
Figure 2.20	Illustration of incident electron beam on a thin sample and X-rays produced.....	59
Figure 2.21	A typical EDX spectrum.....	60
Figure 2.22	A representation of potentiostatic three-electrode system.....	62
Figure 2.23	A pictorial representation of an electrochemical cell.....	63
Figure 2.24 (a)	A typical cyclic voltammetry potential waveform.....	67
Figure 2.24 (b)	Expected response of a redox couple.....	68
Figure 2.25	Qualitative diagrams showing concentration-distance profile.....	71
Figure 2.26	Illustrative cyclic voltammogram for an irreversible electrochemistry process.....	74
Figure 2.27	(a) Excitation signal for square wave voltammetry, (b) Theoretical square-wave voltammogram.....	75
Figure 2.28	Sinusoidal Current Response in a Linear System.....	77
Figure 2.29	Typical impedance diagram.....	80
Figure 2.30	(a) A typical Nyquist plot (b) Nyquist plot showing some kinetic parameters.....	81
Figure 2.31	Typical Bode plot.....	82
Figure 2.32	Impedances in Parallel.....	84

Figure 2.33	Impedances in Series.....	85
Figure 2.34	Randles equivalent circuit in series with the solution resistance.....	85
Figure 2.35	Chronoamperometric experiment.....	92
Figure 2.36	Potential wave form for chronocoulometry.....	95
Figure 2.37	Charge response due to changes of the potential.....	97
Figure 2.38	Illustration of excitation and relaxation pathways of an atom: (1) Vibrational relaxation, (2) Internal conversion, (3) Absorption, (4) Fluorescence, (5) Intersystem crossing, (6) Phosphorescence.....	101
Figure 2.39	Schematic illustration of electrochemiluminescent components.....	103
Figure 2.40	The schematic illustration of annihilation pathway ECL.....	106
Figure 2.41	Illustration of surface plasmon is excited plasma wave of free electrons.....	109
Figure 3.1	The schematic illustration of $[\text{Ru}(\text{bpy})_3]^{2+}/\text{TPA}$ ECL system.....	127
Figure 4.1	UV-visible spectra of AuNp, GO, (G/PhNO ₂), and (AuNp/G/PhNO ₂).....	135
Figure 4.2	Raman spectra of GO and G/PhNO ₂	137
Figure 4.3	HRTEM images of (a) AuNp/G/PhNO ₂ and (b) G/PhNO ₂	138
Figure 4.4	(a) SEM image of AuNp/G/PhNO ₂ and (b) EDX spectrum of AuNp/G/PhNO ₂	140
Figure 4.5	a) SEM image of G/PhNO ₂ and (b) EDX spectrum of G/PhNO ₂	141
Figure 4.6	(a) 2-D and (b) 3-D AFM images of AuNp/G/PhNO ₂	142
Figure 4.6	(c) 2-D and (d) 3-D AFM images of G/PhNO ₂	142

Figure 4.7	(i) CV of bare GCE in 0.1 M PBS (pH 7.2) solution, and (ii) bare GCE in 0.5 mM [Ru(bpy) ₃]Cl ₂ at 50 mV/s.....	144
Figure 4.8	CV at various scan rates of bare GCE in 0.5 mM [Ru(bpy) ₃]Cl ₂	144
Figure 4.9	CV of bare GCE in (A) 0.2% AuNp/G/PhNO ₂ in 0.1 M (B) 0.1 M NDT (C) 0.1 M PBS.....	146
Figure 4.10	CV of GCE/G/PhNO ₂ and GCE/AuNp/G/PhNO ₂ in 0.1 M PBS.....	147
Figure 4.11	CV of bare GCE, GCE/G/PhNO ₂ and GCE/AuNp/G/PhNO ₂ in 5 mM HRC.....	149
Figure 4.12	CV of GCE/Nafion/[Ru(bpy) ₃] ²⁺ and GCE/Nafion in the insert in 0.1 M PBS.....	150
Figure 4.13	CV of Nafion/[Ru(bpy) ₃] ²⁺ /AuNp/G/PhNO ₂ composite films prepared with 1% (v/v) Nafion solution containing 0, 0.2, 0.3, 0.6 and 0.8% AuNp/G/PhNO ₂	151
Figure 4.14	CV of Nafion/[Ru(bpy) ₃] ²⁺ /G/PhNO ₂ composite films prepared with 1% (v/v) Nafion solution containing 0, 0.2, 0.3, 0.6 and 0.8% G/PhNO ₂	152
Figure 4.15	CV of (a) GCE/Nafion/[Ru(bpy) ₃] ²⁺ /AuNp/G/PhNO ₂ (0.2%), (b) GCE/Nafion/[Ru(bpy) ₃] ²⁺ /G/PhNO ₂ (0.2%) and (c) GCE/Nafion/[Ru(bpy) ₃] ²⁺	153
Figure 4.16	SWV of GCE/Nafion/[Ru(bpy) ₃] ²⁺ , GCE/Nafion/[Ru(bpy) ₃] ²⁺ /G/PhNO ₂ (0.2%) and GCE/Nafion/[Ru(bpy) ₃] ²⁺ /AuNp/G/PhNO ₂ (0.2%) in 0.1 M PBS.....	154
Figure 4.17	CV of GCE/Nafion/[Ru(bpy) ₃] ²⁺ /AuNp/G/PhNO ₂ at various scan rates.....	155
Figure 4.18	The plots of peak currents versus square root of scan rate.....	156

Figure 4.19	The plots of the anodic peak current versus scan rate.....	157
Figure 4.20 (a)	The plot of $\log I_p$ vs $\log v$ for data at higher scan rate (100-500 mV/s).....	158
Figure 4.20 (b)	The plot of $\log I_p$ vs $\log v$ for data at lower scan rates (5- 40 mV/s)	158
Figure 4.21 (a)	Chronoamperogram of GCE/Nafion/[Ru(bpy) ₃] ²⁺ /AuNp/G/PhNO ₂ , GCE/Nafion/[Ru(bpy) ₃] ²⁺ /G/PhNO ₂ and GCE/Nafion/([Ru(bpy) ₃] ²⁺ sensor platforms.....	161
Figure 4.21 (b)	Bar chart indicating anodic peak currents of the platforms.....	161
Figure 4.22 (a)	Chronocoulograms of GCE/Nafion/([Ru(bpy) ₃] ²⁺ , GCE/Nafion/[Ru(bpy) ₃] ²⁺ /G/PhNO ₂ and GCE/Nafion/[Ru(bpy) ₃] ²⁺ /AuNp/G/PhNO ₂ sensor platforms.....	164
Figure 4.22 (b)	Anson plot of GCE/Nafion/[Ru(bpy) ₃] ²⁺ /AuNp/G/PhNO ₂ chronocoulogram.....	164
Figure 4.23	Nyquist plot of GCE/Nafion/[Ru(bpy) ₃] ²⁺ /AuNp/G/PhNO ₂ performed at different bias potentials: 0, 100, 200, 400, 600, 800 and 1000 mV respectively.....	166
Figure 4.24	Nyquist plots for GCE, GCE/Nafion/([Ru(bpy) ₃] ²⁺ , GCE/Nafion/[Ru(bpy) ₃] ²⁺ /G/PhNO ₂ and GCE/Nafion/[Ru(bpy) ₃] ²⁺ /AuNp/G/PhNO ₂ , measured in 0.1 M PBS solution at 0 mV.....	167
Figure 4.25	Equivalent circuit used for the analysis of the electrochemical impedance data.....	168
Figure 4.26 (a)	The phase angle versus frequency plot for EIS data.....	171
Figure 4.26 (b)	The impedance versus frequency plot for EIS data.....	171

Figure 4.27 (a)	ECL signals of CSPE/ Nafion/[Ru(bpy) ₃] ²⁺ /AuNp/G/PhNO ₂ sensor with different concentrations of TPA (0, 5, 50, 500, 1000 and 10000 pg/mL).....	174
Figure 4.27 (b)	Relationship between ΔECL and TPA concentration.....	175
Figure 4.28 (a)	CV behaviour of PDMA/AuNp/G/PhNO ₂ films prepared from the growth solutions containing 0, 0.3, 0.6, 0.8 and 1.0% AuNp/PhNO ₂ in 1 M HCl.....	178
Figure 4.28 (b)	CV behaviour of PDMA/AuNp/G/PhNO ₂ films prepared from the growth solutions containing 0, 0.3, 0.6, 0.8 and 1.0% AuNp/G/PhNO ₂ in 0.1 M PBS solution.....	178
Figure 4.29 (a)	CV of GCE/PDMA and GCE/PDMA/AuNp/G/PhNO ₂ (0.3%) in 1 M HCl solution.....	180
Figure 4.29 (b)	CV of GCE/PDMA and GCE/PDMA/AuNp/G/PhNO ₂ (0.3%) in 0.1 M PBS solution.....	180
Figure 4.30 (a)	CV for electrochemical synthesis of PDMA in 1.0 M HCl.....	182
Figure 4.30 (b)	CV for electrochemical synthesis of PDMA/AuNp/G/PhNO ₂ films in 1.0 M HCl.....	182
Figure 4.31 (a)	CV at various scan rates (10-70 mV/s) of GCE/PDMA in 1 M HCl	183
Figure 4.31 (b)	CV at various scan rates (10-70 mV/s) of GCE/PDMA/AuNp/G/PhNO ₂ (0.3%) in 1 M HCl.....	184
Figure 4.32 (a)	The Randles-Sevcik plots of I _{pa} peak (c) vs scan rate.....	185
Figure 4.32 (b)	The Randles-Sevcik plots of I _{pc} peak (c') vs square root of scan rate.....	187
Figure 5.1	Electrochemical reduction of 4-nitrophenyl group to 4-aminophenyl on the electrode surface.....	190

Figure 5.2	CV of (i) bare GCE, (ii) GCE/Nafion/[Ru(bpy) ₃] ²⁺ /G/PhNO ₂ and (iii) GCE/Nafion/[Ru(bpy) ₃] ²⁺ /AuNp/G/PhNH ₂ recorded in 5 mM [Ru(NH ₃) ₆] ^{2+/3+}	191
Figure 5.3	Nyquist plots in 5 mM [Fe(CN) ₆] ^{3-/4-} in frequency range of 100 mHz–10 kHz.....	192
Figure 5.4 (a)	The absorption spectra of DON prepared in MPBS.....	195
Figure 5.4 (b)	The absorption spectra of DON antigen-antibody reactivity.....	196
Figure 5.5	CV response of different immobilisation steps.....	197
Figure 5.6 (a)	Chronoamperometric response of different immobilisation steps.....	198
Figure 5.6 (b)	Bar chart of the chronoamperogram.....	199
Figure 5.7	The plot of R _{ct} values versus deoxynivalenol concentration.....	200
Figure 5.8	The plot of anodic peak currents from CV versus solution pH.....	201
Figure 5.9	The plot of peak currents from chronocoulograms versus incubation time.....	202
Figure 5.10	EIS responses of GCE/Nafion/[Ru(bpy) ₃] ²⁺ /AuNp/G/PhNH ₂ /DONab/BSA immunosensor to standard DONag solutions.....	203
Figure 5.11	The calibration plot of EIS detection data of the immunosensor.....	204
Figure 5.12	CV response of different immobilisation steps.....	205
Figure 5.13 (a)	Chronoamperometric response of different immobilisation steps.....	206
Figure 5.13 (b)	Bar chart of the chronoamperogram.....	207

Figure 5.14	EIS responses of GCE/Nafion/[Ru(bpy) ₃] ²⁺ /G/PhNH ₂ /DONab/BSA immunosensor to standard DONag solutions: a, b, c, d, e and f represents 0, 6, 12, 18, 24 and 30 ng/mL DONag respectively.....	208
Figure 5.15	The calibration plot of EIS detection data of the immunosensor.....	209
Figure 5.16	EIS responses of GCE/PDMA/AuNp/G/PhNH ₂ /DONab/BSA immunosensor to standard DONag solutions in PBS.....	212
Figure 5.17	The calibration plot of EIS detection data of the immunosensor.....	212
Figure 5.18	The selectivity chart of GCE/PDMA/AuNp/G/PhNH ₂ /DONab.....	215
Figure 5.19	The detection plot of DONag standards by ELISA.....	216



List of Tables

Tables	Title	Page
Table 1.1	Exposure to Deoxynivalenol (DON) - PMTDI for Deoxynivalenol = 1µg/kg body weight.....	3
Table 2.1	Physio-chemical properties of deoxynivalenol.....	15
Table 2.2	Some common addition polymers, their formula, monomer and uses.....	25
Table 2.3	Some common condensation polymers, their formula, monomer and uses.....	27
Table 2.4	Evaluation between TEM and SEM.....	58
Table 2.5	Electric circuit components.....	83
Table 2.6	Common equivalent circuit models.....	86
Table 4.1	EIS parameters of GCE, GCE/Nafion/[Ru(bpy) ₃] ²⁺ , GCE/Nafion/[Ru(bpy) ₃] ²⁺ /G/PhNO ₂ and GCE/Nafion/[Ru(bpy) ₃] ²⁺ /AuNp/G/PhNO ₂	169
Table 4.2	Heterogeneous rate transfer constant and standard exchange current values for the three sensor platforms.....	173
Table 5.1	EIS parameters of GCE, GCE/Nafion/[Ru(bpy) ₃] ²⁺ /AuNp/G/PhNH ₂ , GCE/Nafion/[Ru(bpy) ₃] ²⁺ /G/PhNH ₂ and GCE/PDMA/AuNp/G//PhNH ₂ in 5 mM [Fe(CN) ₆] ^{3-/4-} solution.....	193
Table 5.2	Sensitivity and detection limits of the immunosensors.....	213
Table 5.3	DON content of corn, wheat and roasted coffee certified reference materials.....	217

List of Schemes

Scheme	Title	Page
Scheme 1	Research framework.....	11
Scheme 2	The illustration for graphene oxide synthesis.....	111
Scheme 3	The illustration for diazotization of 4-nitroaniline.....	113
Scheme 4	The illustration for pre-reduction of graphene oxide.....	114
Scheme 5	The illustration for simultaneous chemical reduction of diazonium cation to diazonium radical, GO to graphene and in situ PhNO ₂ functionalisation of graphene.....	116
Scheme 6	The illustration for the immobilization of gold nanoparticles onto nitrophenylazo functionalized graphene surface.....	118
Scheme 7	The illustration of the stepwise preparation of Nafion/[Ru(bpy) ₃] ²⁺ /AuNp/G/PhNO ₂ on GCE.....	121
Scheme 8	The protonation of PDMA/AuNp/G/PhNO ₂ emeraldine salt to emeraldine base by conditioning in PBS.....	123
Scheme 9	Electrochemical reduction of 4-nitrophenyl group (-PhNO ₂) to 4-aminophenyl group (-PhNH ₂) on the electrode surface.....	130
Scheme 10	The illustration for stepwise immunosensor fabrication processes.....	131

List of Abbreviations

Ab	Antibody
Ag	Antigen
AuNp	Gold nanoparticles
AFM	Atomic Force Microscopy
BSA	Bovine Serum Albumin
CL	Chemiluminescence
CPE	Constant Phase Element
CV	Cyclic Voltammetry
CP	Conducting Polymer
DMA	2, 5-dimethoxyaniline
DONab	Deoxynivalenol antibody
DONag	U Deoxynivalenol antigen
EIS	WESTERN CAPE Electrochemical Impedance Spectroscopy
EB	Emeraldine Base
EDX	Energy Dispersive X-Ray Spectroscopy
ES	Emeraldine Salt
ECL	Electrochemiluminescence
ELISA	Enzyme Linked Immunosorbent Assay
EU	European Union
EPA	Environmental Protection Agency
FAO	Food and Agricultural Organization
FDA	The U.S. Food and Drug Administration
G	Graphene

GCE	Glassy Carbon Electrode
HOMO	Highest Occupied Molecular Orbital
HRSEM	High Resolution Scanning Electron Microscopy
HRTEM	High Resolution Transmission Electron Microscopy
LE	Leucoemeraldine state
LB	Leucoemeraldine Base
LUMO	Lowest Unoccupied Molecular Orbital
MPBS	Methanolic Phosphate Buffer Saline
NOAEL	No Observed Adverse Effect Level
SWV	Square Wave Voltammetry
PANI	Polyaniline
PBS	Phosphate Buffer Saline
PDMA	Poly (2, 5- dimethoxyaniline)
PMTDI	U Provisional Maximum Tolerated Daily Intake
RE	WESTERN CAPE Reference Electrode
SPR	Surface Plasmon Resonance
SPE	Screen-Printed Electrodes
SEM	Scanning Electron Microscopy
SWV	Square Wave Voltammetry
TEM	Transmission Electron Microscopy
UV-Vis	Ultraviolet visible
USDA	United States Department of Agriculture
WE	Working Electrode
W.H.O	World Health Organization

List of symbols

A	Surface area of the electrode
AC	Alternating Current
$E_{p,a}$	Anodic peak potential
$E_{p,c}$	Cathodic peak potential
$I_{p,a}$	Anodic peak current
$I_{p,c}$	Cathodic peak current
I_p	Peak current
DC	Direct Current
D_o	Diffusion coefficient
E_p	Peak potential
E_i	Initial potential
E_λ	Switch potential of the
E^θ	Standard electrode potential
$E^{\theta'}$	Formal potential
$E_{1/2}$	Half peak potential
ΔE_p	Peak to peak potential separation
F	Faraday constant
R_{ct}	Charge transfer resistance
I	Current
I_c	Capacitive current
$I_{p1/2}$	Half peak current
I_p	Peak current
K	Rate constant

k°	Standard rate constant
K^0	Heterogeneous rate constant
α	Transfer coefficient
n	Number of electrons transferred
R	Gas constant
R_s	Solution resistance
T	Temperature
Γ^*	Surface concentration
C	Concentration of redox active species in bulk solution
C_i	Analyte ion concentration
M	Molar concentration
pH	Acidity or alkalinity of a solution
ppm	Parts per million
ppb	Parts per billion
PhNO ₂	4-nitrophenylazo
PhNH ₂	4-aminophenylazo
C^0	Bulk concentration
Q	Charge
μ	Micro
Ω	Ohm
π	pi
λ	Wavelength
τ	Time constant
ν	Scan rate
γ	Activity coefficient

t

Time

j

Current density



They shall mount up with wings as eagles

HE gives power to the faint; and to them that have no might he increases their strength.

Even the youths shall faint and be weary, and the young men shall utterly fall:

But they that wait upon the Lord shall renew their strength;

they shall mount up with wings as eagles;

they shall run, and not be weary;

and they shall walk,

and not faint.

Isaiah 40: 29-31



Chapter One

Introduction

This chapter gives a brief introduction to this research, background information on the aspects involved, motivation, specific objectives and the outline adopted.

1.1 Background information

Herein we describe the development and characterisation of gold nanoparticles-dotted nitrophenylazo functionalized graphene (AuNp/G/PhNO₂) ternary nanocomposite employed in designing signal enhanced immunosensors for the detection and determination of deoxynivalenol (DON) mycotoxin in food items via impedimetric system.

Mycotoxins are natural poisons or toxic by-products of ubiquitous fungi species (particularly *Penicillium* specie, *Fusarium* specie, and *Aspergillus* specie) which originate in the soil of crop fields [1-2]. Nuts, oil seeds, fruits and cereals are mainly affected because of mold growth before harvest, after harvest or during storage. Health effects of mycotoxins may include immunological effects, organ-specific toxicity and in some cases death [1, 3]. The major exposure routes are the intake of contaminated food, inhalation of spore-borne toxins or dermal contamination by skin contact. Mycotoxin contamination is an unavoidable risk because its formation depends on season. It thrives in wet seasons and under humid conditions. Complete prevention is therefore impossible but it can be controlled by the use of fungicides, proper management of the storage conditions (avoiding storage in humid environments) and testing these agricultural products regularly onsite. The best and major

way to control mycotoxins from human and animal food is to detect the contaminated raw materials, then divert them from feed and finished food. Most significant mycotoxins are Aflatoxin, Deoxynivalenol, Ochratoxin, and Fumonism [1, 4].

For the purpose of this study, attention was paid to the detection and determination of Deoxynivalenol (DON) mycotoxin using my newly developed platform. In both experimental animal and livestock, consumption of feed contaminated with DON has been reported to lead to vomiting, weight loss, diarrhoea, anaemia, haemorrhage and immune-suppression [5]. DON has also been implicated with feed refusal and emesis in pig; hence the alternative name vomitoxin. DON produces chronic and toxic effects in humans by inhibiting DNA, RNA and proteins synthesis [2]. And it can also cause human skin irritation, haematological changes, lymphocyte blastogenesis impairment and radiomimetic effects. It has haemolytic activity which causes apoptosis (cytotoxicity) and immunotoxicity to eukaryotic organisms. DON is a worldwide contaminant of foods and feeds. It is an important disease of cereal foods in several countries therefore it constitutes an increasing problem [1].

As a matter of concern, United States Department of Agriculture (USDA), and US Food and Drug Administration (FDA) have established advisory levels for DON of 1 ppm in wheat products destined for human consumption, 5 ppm in grain products for most animal feeds and 10 ppm in grain products for cattle feed [6-7]. Also the European Union (EU) established ranges from 200 to 1750 $\mu\text{g}/\text{kg}$ depending on the kind of cereal and cereal products. Provisional maximum tolerated daily intake (PMTDI) of DON for $1\mu\text{g}/\text{kg}$ body weight (BW) was established by the World Health Organization Joint Expert Committee on Food Additives (WHOJECFA) on the basis of NOAEL (NOAEL = No observed adverse effect level). See Table 1.1 and Figure 1.1 [6, 8]:

Table 1.1: Exposure to Deoxynivalenol (DON) - PMTDI for Deoxynivalenol = 1µg/kg body weight.

Food Item	Region of World Intake (µg/kg BW)				
	Africa	Europe	Far East	Latin America	Middle East
Barley	0.02	0.24	0.04	0.08	0.01
Maize	0.31	0.03	0.09	0.12	0.14
Rice	0.26	0.03	0.7	0.22	0.12
Wheat	0.18	1.2	0.74	0.76	2.1
Total	0.78	1.4	1.6	1.2	2.4

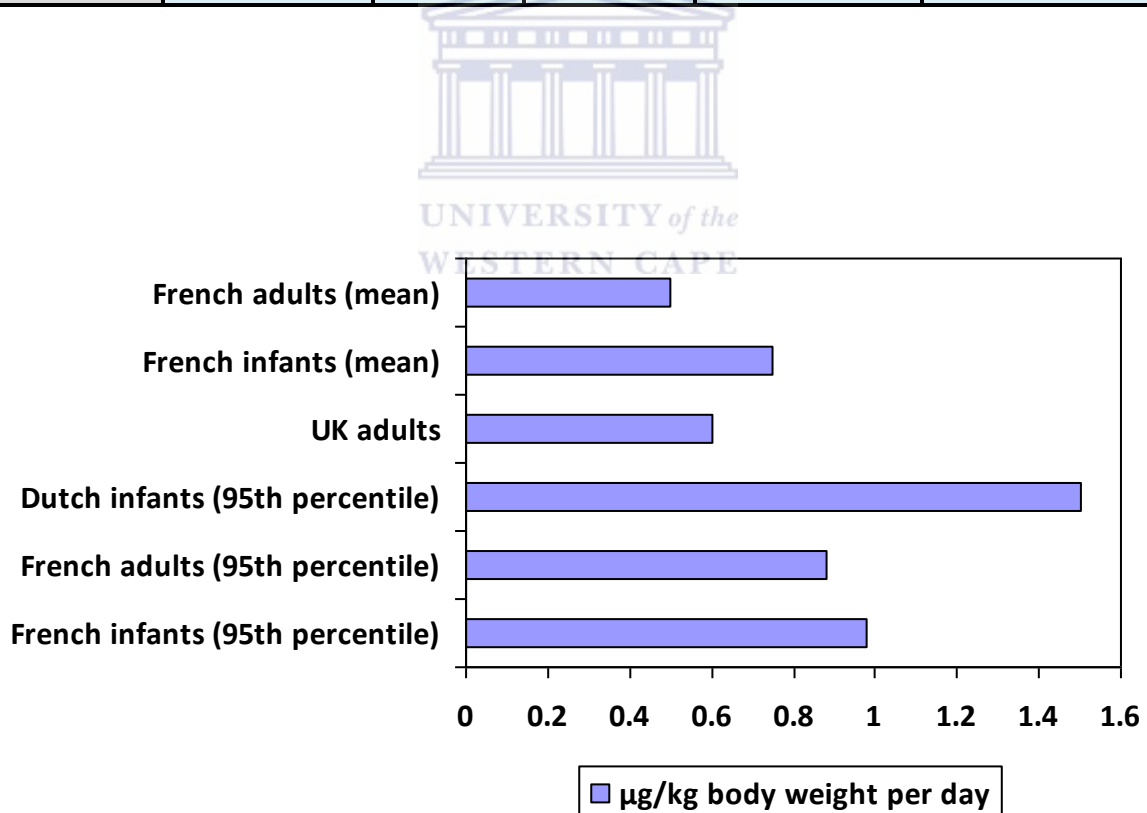
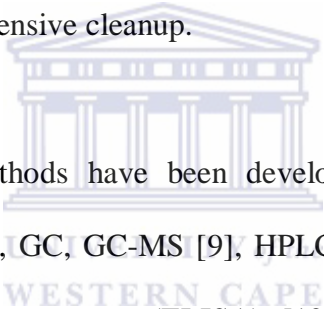


Figure 1.1: Relationship between tolerable daily intake and NOAEL.

Because of the known toxicity of DON, combined with its prevalence and the need to comply with these regulatory policies, the interest in the development of robust, easy-to-use and reliable instrumental analytical methods for in-field application has increased greatly during the last decade. Much effort has therefore been focused on the development of rapid tests with very low detection limits for DON mycotoxin [4]. There are three main approaches for the detection and determination of mycotoxins, namely; biological, chemical and electrochemical methods. Biological and chemical methods may be useful in screening for mycotoxins, especially when the identity of the mycotoxins is not known. However, if it is known which mycotoxin(s) should be looked for, electrochemical assays are preferred because they are more specific, more rapid and more reproducible. They possess lower limits of detection and do not require intensive cleanup.



Presently, several analytical methods have been developed for the detection of DON mycotoxin and they include PCR, GC, GC-MS [9], HPLC, thin-layer chromatography [10-11], Enzyme-linked immunosorbent assay (ELISA) [12] and so on. In applying these methods, it has been reported that most of the occurrence data available for deoxynivalenol was for wheat. There are few data for barley, oats, rice and corn. Among these food items, it has been reported that corn had the highest levels of contamination and contained concentrations above the limits of detection (LOD) for DON which varied in the range 2–2501 g/kg [9]. Some of these methods allow good accuracy of quantification and good detection limits of DON mycotoxin in various food items.

However, they are not cost effective; some suffer from low selectivity and usually require significant amount of time associated with labour-intensive cleanup, sophisticated instrumentation, skilled operators or technical expertise. The ELISA method is sensitive,

relatively simple, requires little sample preparation and it does not have the health hazards associated with radio-immunoassays. However, the entire procedure is complicated, expensive and depends on expertise as well, though its detection range for DON mycotoxin in grains has been reported to be between 0.01 and 100 $\mu\text{g/mL}$ [12-13]. Therefore it is desirable to develop a rapid, sensitive, easy-to-use, cost effective, reproducible immunosensors with lower detection limits which will not require expertise or labour-intensive cleanup for ultrasensitive determination of DON mycotoxin.

In the light of this challenge, I report my investigation into the design of multi-signal amplification platforms which I used to construct label free impedimetric DON mycotoxin immunosensors. It is important to note that immunosensors complement the standard analytical methods. And they are most suitable for the detection and quantification of mycotoxins due to their low cost of analysis, ease of operation, high sensitivity and reduced sample pre-treatment. But the design of an optimum interface between the transducer surface, detector material and bio-components is very challenging and it is a key part of biosensor or electrochemical sensor development. Improving on the electroanalytical efficiency of the interface has been a focus of science research for decades [14-15]. Many signal amplification strategies have been applied in designing sensor platforms with optimized sensitivity, specificity and stability. These strategies include applying new redox-active probes [16], coupling conducting polymers with electrochemical detection probes [17], incorporating nano-structured materials to increase loading of tags etc.

Among these strategies, nano-structured materials such as metallic nanoparticles, quantum dots [18], conducting polymers, carbon nanotubes and graphene have presented very unique optical, magnetic, catalytic and electrochemical properties [19-22]. These unprecedented

properties of nano-structured materials have fostered their use in data storage devices, heterogeneous catalysts, nano-biosensors, chemical sensors, plasmonic devices, optoelectronics, optical markers, drug deliverers, fuel cells, micro/nano-reactors and water-treatment devices among many other applications [23-25]. Consequently various kinds of sensors for clinical and environmental purposes have been developed with the added advantage of analyzing samples without any need for pre-treatment.

Looking at the unique properties of nano-structured materials, I know that gold nanoparticles can improve the quantity of immobilized signal probes due its large specific surface area, high surface adsorption, good stability and biocompatibility. These improved properties are critically sensitive to the nanoparticle particle sizes. [26-29]. Owing to its environmental stability, conductivity, processability and retention of its redox activity at pH above 4, poly(2, 5-dimethoxyaniline) when doped with a suitable electro catalyst can act as a suitable electron transfer mediator for enzyme electrodes [30-34]. Also graphene, a monolayer of sp²-bonded carbon atoms tightly packed into a two-dimensional (2D) lattice, due to its huge surface area (2600 m²/g), high chemical stability and electronic properties serves as scaffold to anchor large amount of nanoparticles. Graphene can also promote the selectivity and efficiency of catalytic processes [35]. The electrical conductivity of graphene can be enhanced by adsorbed nanoparticles acting as donors or acceptors. The enhanced electrical conductivity and mechanical properties make graphene an excellent material for collecting and transporting charge in photo-electrochemical solar cells, photo-catalysis and electrochemical sensors [36-37].

Nafion is an anionic polymer and can bind molecules through coulombic and/or hydrophobic interactions [38-39]. It can facilitate electron transfer from an enzyme active centre to the

electrode surface and acts as a weak mediator for redox-active probes [40]. The rate of charge transfer in pure Nafion film is relatively slow due to its compact nature which is unfavourable for diffusion of analyte. Immobilised cationic reactants such as $[\text{Ru}(\text{bpy})_3]^{2+}$ migrates into electro-inactive hydrophobic region of the ionomer with time, thereby losing electrochemical contact with the electrode. I am therefore interested in improving the behaviour of such cationic reactants in Nafion film; consequently enhance its application in designing reproducible and ultra-sensitive immunosensor.

These unique properties of gold nanoparticles (AuNp), poly (2, 5-dimethoxyaniline) (PDMA), graphene (G) and Nafion were combined in this study to construct ternary nanocomposite systems for ultrasensitive impedimetric determination of DON mycotoxin. Gold nanoparticle-dotted 4-nitrophenylazo functionalised graphene composite ($\text{AuNp}/\text{G}/\text{PhNO}_2$) was used in the preparation of the sensor platforms. Ideally, in the preparation of graphene from graphite oxide, the graphite oxide is rigorously reduced after exfoliation in order to obtain the desirable properties of graphene. However, the reduction of exfoliated graphite oxide leads to graphene nano-sheets with limited water solubility ($< 0.5 \text{ mg/mL}$). To obtain water-soluble graphene sheets, graphene oxide was reduced in three stages following the method of Yongchao Si and Edward T. Samulski [41]. Residual oxygen functionality was removed and para-phenyldiazonium salt was used to introduce negatively charged 4-nitrophenylazo (PhNO_2) units into partially reduced graphene oxide.

The presence of PhNO_2 units on graphitic sheets prevents graphene from aggregating in solution after the final reduction stage of the graphene oxide because of electrostatic repulsion between the graphene sheets, thereby yielding isolated sheets with highly improved water solubility. The highly dispersive 4-nitrophenylazo functionalised graphene (G/PhNO_2)

was further functionalised with gold nanoparticles (AuNp/G/PhNO₂). This was immobilised on glassy carbon electrode surface with perfluorosulfonate ionomer (Nafion 117) and loaded with large amount of tris (bipyridine) ruthenium (II), [Ru(bpy)₃]²⁺ as a cationic signal probe. Another sensor platform that explores the electrocatalytic properties of our new gold nanoparticle-dotted 4-nitrophenylazo functionalised graphene composite (AuNp/G/PhNO₂) was also designed by doping poly (2, 5 dimethoxyaniline) with it. These were employed in the construction of immunosensors for the determination of deoxynivalenol (DON) mycotoxin via impedimetric system. These platforms may as well provide a promising method for clinical immunoassay of other bio-molecules.

1.2 Problem statement

DON is an important toxin of cereal foods and constitutes an increasing problem in several countries because the occurrence of the fungi species that produce it is very high in nature. The formation of these fungi species is season dependant and complete prevention is impossible. Because of concerns with the increasing toxic effects of DON on livestock and humans, the United States Department of Agriculture (USDA), Food & Drug Administration (FDA) and European Community has instituted advisory levels of 1 ppm for wheat products for human consumption, 5 ppm of grain products for most animal feeds and 10 ppm of grain products for cattle feed. There is need to design a sensor to monitor these agricultural products before and after harvest (i.e. during storage) in order to control contamination outbreaks and to ensure regulatory compliance.

Majority of the analytical methods reported for the determination of DON mycotoxin involve PCR, GC, GC-MS, HPLC, thin-layer chromatography and enzyme-linked immunosorbent assay (ELISA) [12-13, 42]. These methods allow good accuracy of quantification and good

detection limits but they are not cost effective; some suffer from low selectivity and usually require significant amount of time associated with labour-intensive cleanup, sophisticated instrumentation, skilled operators or technical expertise. In view of these analytical challenges, it is hoped that the gold nanoparticles-dotted 4-nitrophenylazo functionalised graphene (AuNp/G/PhNO₂) composite developed in this study will provide a promising sensor platform for the construction of easy to use, rapid, cost effective and enhanced signal immunosensors for the detection and determination of DON levels in cereal food items via impedimetric system.

1.3 Aim and approach of this research

The aim of this research is to improve the electrochemical behaviour of cationic reactants in Nafion film, consequently enhance its application in designing reproducible and ultra-sensitive immunosensors. Secondly, to develop a multi-signal amplification sensor platform based on gold nanoparticles-dotted 4-nitrophenylazo functionalised graphene (AuNp/G/PhNO₂) nanocomposite by applying Nafion 117 as a binder and incorporate [Ru(bpy)₃]²⁺ as a cationic reactant and/or luminescent metal centre on glassy carbon electrode (GCE). Thirdly, to design an enhanced signal platform using PDMA doped with AuNp/G/PhNO₂. And fourthly, to introduce for the first time, the use of these developed sensor platforms in the design of cost effective, easy-to-use, rapid and ultrasensitive immunosensors for the detection and determination of DON via impedimetric system.

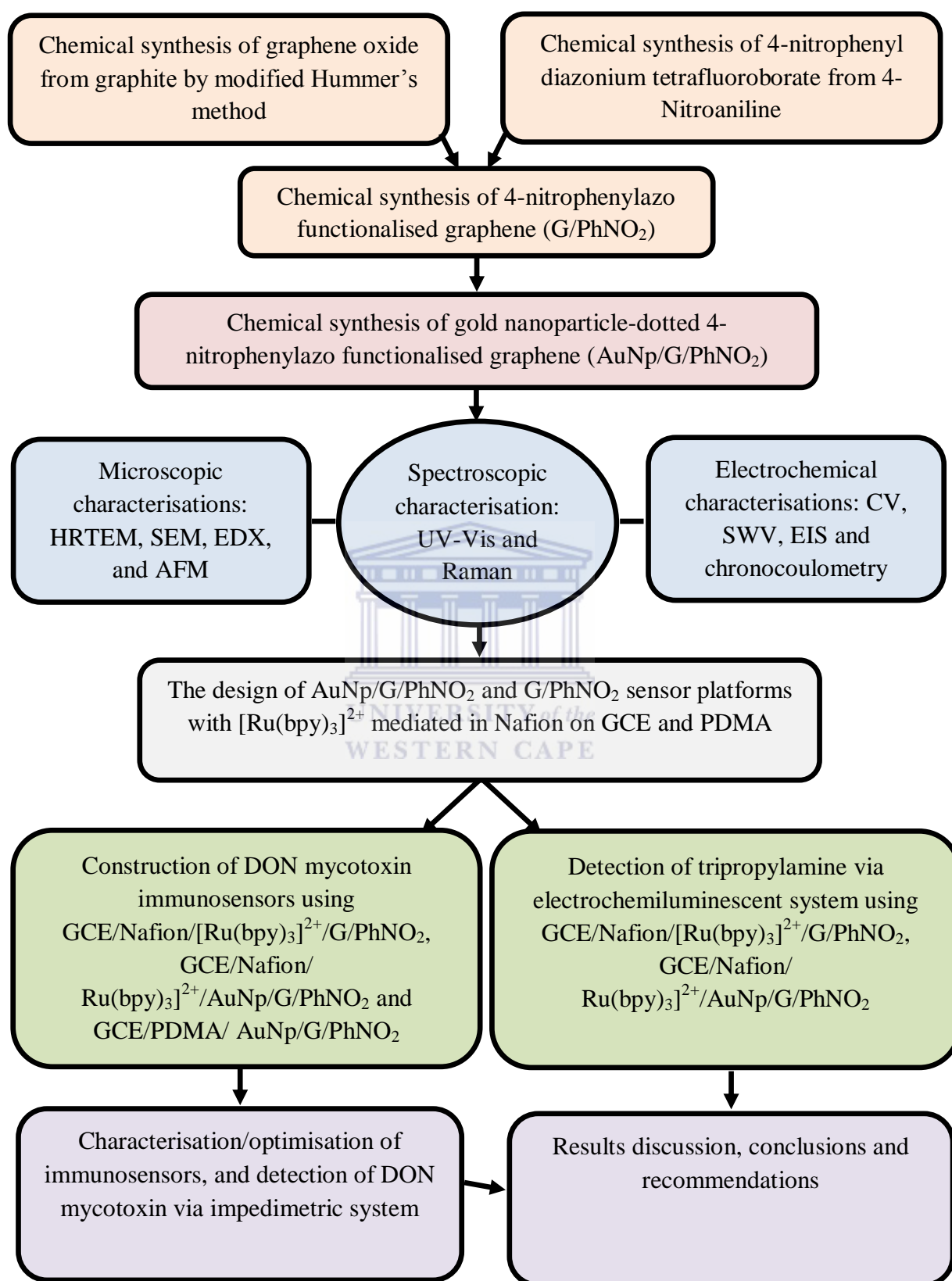
The approach of this research includes:

1. Chemical synthesis of graphene oxide through a modified Hummer's method using natural graphite powder as the starting materials.
2. Chemical synthesis of 4-Nitrophenyl diazonium tetrafluoroborate and highly dispersive 4-nitrophenylazo functionalised graphene (G/PhNO₂).

3. Chemical synthesis of gold nanoparticles dotted 4-nitrophenylazo functionalised graphene (AuNp/G/PhNO₂).
4. Physical and electrochemical characterizations of the synthesised products using UV-Visible spectroscopy, high resolution transmission electron microscopy (HRTEM), scanning electron microscopy (SEM), Raman spectroscopy, atomic force microscopy (AFM), cyclic voltammetry (CV) and electrochemical impedance spectroscopy (EIS) accordingly.
5. Preparation of a nanocomposite thin film of Nafion/[Ru(bpy)₃]²⁺/AuNp/G/PhNO₂ onto GCE in which [Ru(bpy)₃]²⁺ serves as a cationic reactant.
6. Electrochemical synthesis of PDMA doped with AuNp/G/PhNO₂ onto GCE
7. Electrochemical characterization of the thin film sensor platforms in (5) and (6) via CV, OSW, chronocoulometry, chronoamperometry and EIS systems.
8. Develop an inhibition based ultrasensitive immunosensors using my new Nafion/[Ru(bpy)₃]²⁺/G/PhNO₂, Nafion/[Ru(bpy)₃]²⁺/AuNp/G/PhNO₂ and PDMA/AuNp/G/PhNO₂ thin film sensor platforms on GCE for the detection and determination of DON mycotoxin levels in standard solutions via impedimetric system.
9. Apply the newly developed immunosensors by analyzing extracted wheat, corn and roasted coffee.
10. Detect tripropylamine using GCE/Nafion/[Ru(bpy)₃]²⁺/G/PhNO₂ and GCE/Nafion/[Ru(bpy)₃]²⁺/AuNp/G/PhNO₂ sensor platforms via electrochemiluminescent (ECL) system.

The framework of this research is presented in Scheme 1 in accordance to the specific objectives stated in this section.

1.4 Research framework

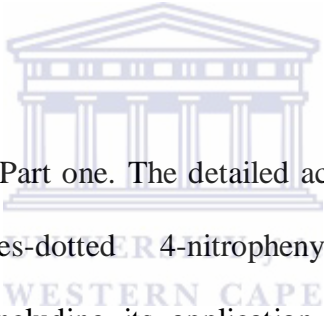


Scheme 1: Research framework.

1.5 Thesis layout

Chapter Two: Literature Review. This chapter discusses in details the properties of the different nanomaterials employed in the design of impedimetric sensing platforms for detection and determination of deoxynivalenol mycotoxin; and the fundamental principles of the different analytical techniques employed.

Chapter Three: Experimental procedures and analytical methods. This chapter gives detailed research methodologies; general experimental procedures; chemicals and sample preparations; chemical synthesis; electrochemical synthesis; characterizations and construction of immunosensor platforms for the determination of deoxynivalenol mycotoxin via impedimetric system.



Chapter Four: Result discussion: Part one. The detailed account of characterizations for the synthesised gold nanoparticles-dotted 4-nitrophenylazo functionalised graphene (AuNp/G/PhNO₂) is presented including its application in constructing thin film sensor platforms with: tris (bipyridine) ruthenium (II) chloride ([Ru(bpy)₃]Cl₂) as a cationic reactant mediated in Nafion and poly (2, 5-dimethoxyaniline).

Chapter Five: Result discussion: Part two. This chapter presents the optimisation and characterisation of DON immunosensors, fabricated with the three sensor platforms that was developed in chapter four. The results obtained from the application of these immunosensors in the determination of DON in standard samples and real samples via impedimetric system are also discussed.

Chapter Six: Conclusions and Recommendations. This chapter discusses and draws conclusions regarding the success of the developed DON immunosensors with recommendations.



Chapter Two

Literature Review

This chapter discusses in details the properties of the different nano-materials employed in the design of impedimetric sensing platforms for detection and determination of deoxynivalenol mycotoxin; and the fundamental principles of the different analytical techniques employed.

2.1 Deoxynivalenol mycotoxin

DON is a type B trichothecene mycotoxin, a group of naturally occurring low molecular weight metabolite and chemical by-product of *Fusarium graminearum* and *Fusarium culmorum* fungal species [2]. Trichothecenes belong to a class of mycotoxins that are commonly found in cereals like barley, wheat, oats, rice and maize. They are classified into group A and group B compounds depending on their structure.

The most important types of group A-trichothecene are T-2 toxin and HT-2 toxin. Deoxynivalenol (DON) and Nivalenol (NIV) fall within group B-trichothecene. Group B trichothecene causes feed refusal, vomiting, anaemia, haemorrhage and immune-suppression in livestock; and humans [5]. DON often co-exists with other mycotoxins such as zearalenone and Nivalenol. DON levels range from $\mu\text{g}/\text{kg}$ to tens of mg/kg and vary year-to-year depending on the climate, season, geographic conditions and agronomic practice. Deoxynivalenol structure is characterized as a tetra-cyclic sesquiterpene with seven stereo centres, six oxygen atoms consisting of an epoxide which would allow for multiple hydrogen bonding, a carbonyl, cyclic ether and three alcoholic OH groups [43-44]. Figure 2.1 and

Table 2.1 shows the chemical structure and physio-chemical properties of DON respectively [2].

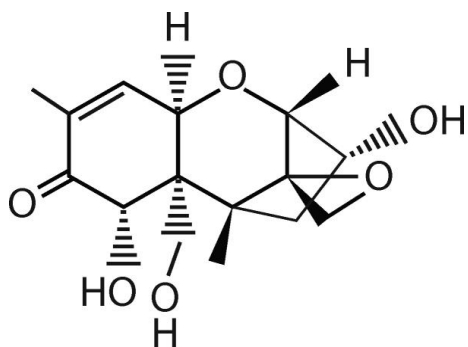


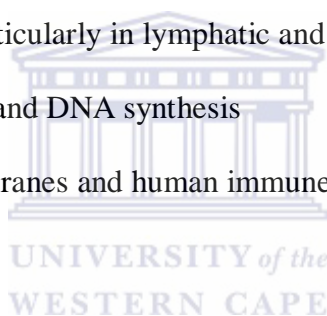
Figure 2.1: Chemical structure of deoxynivalenol.

Table 2.1: Physio-chemical properties of deoxynivalenol

Property	Information
IUPAC Name	12, 13-epoxy-3 α , 7 α , 15-trihydroxytrichothec-9-en-8-one
Molecular formula	C ₁₅ H ₂₀ O ₆
Molecular weight	296.3157 [g/mol]
Melting point	151-153°C
Boiling point	543.9±50 °C
Flash point	206.9±2.5 °C
Vapour Pressure (Torr)	4.26×10 ⁻¹⁴ 25°C
Physical appearance	white crystalline
Purity	At least 98% by TLC
Solubility	Soluble in polar organic solvents as acetonitrile, methanol, ethyl acetate and slightly soluble in water

Deoxynivalenol is very toxic but it has not been reported as having carcinogenic, teratogenic or mutagenic properties [7, 45-46]. The most important structural features causing the biological activities of DON are: the 12, 13-epoxy ring, the presence of hydroxyl/acetyl groups and their position in the chemical structure of DON. Other mycotoxins like T-2 toxin, HT-2 toxin and Nivalenol (NIV) also have the same effect but it appears that they differ in their toxic capacities and it is not clear whether they work via identical mechanisms at cellular level [44]. The main toxic effect of DON at biochemical and cellular level are [2]:

- ❖ strong inhibition of protein synthesis via binding to the ribosome
- ❖ induction of apoptosis particularly in lymphatic and haematopoietic tissue
- ❖ inhibitory effect on RNA and DNA synthesis
- ❖ toxic effects on cell membranes and human immune function



Acute effects of DON mycotoxin in animal and human includes reduced feed uptake, nausea, vomiting, diarrhoea, abdominal pain, headache, dizziness, fever, skin irritation and immune-suppression. No human death has yet been attributed to DON. Humans are directly exposed to these risks through foods of plant origin (cereal grains) or indirectly through foods of animal origin (kidney, liver, milk, eggs) [5, 7]. Provisional maximum tolerated daily intake (PMTDI) of DON is 1 μ g/kg body weight (BW), as mentioned earlier was established by the World Health Organization Joint Expert Committee on Food Additives on the basis of the NOAEL [8].

2.2 Metallic nanoparticles

Nanoparticles are dispersed mono or multi-component nano-materials in nanoscale (1-100 nm diameters) range. They exhibit novel optical and catalytic properties that differ significantly from those of their monometallic counterparts. Size-dependent properties are observed such as surface plasmon resonance in some metal particles and super paramagnetism in magnetic materials [26, 47].

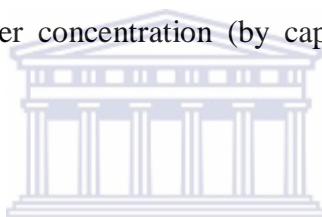
The history of nanoparticle research is long and the use of these particles dates back to the 9th century in Mesopotamia when artisans used them to generate a glittering effect on the surface of pots. Since then it has gained prominence as ideal synthetic building block, nut and bolt for constructing new and useful nanomaterials. Its research is currently the most studied branch of science with applications in various fields. The unprecedented properties of nanoparticles have fostered their use in data storage devices, spintronic devices, heterogeneous catalysts, electrochemical sensors, water-treatment devices, fuel cells, micro/nanoreactors, optoelectronics and plasmonic devices [21-22, 24].

Nanoparticles can be synthesized and modified with various chemical functional groups which allow them to be conjugated with antibodies, ligands, drugs of interest and thus opening a wide range of potential applications in biotechnology, magnetic separation, pre-concentration of target analyte, targeted drug delivery, vehicles for gene and more importantly, diagnostic imaging among many other applications. Nanoparticles improve the immobilized quantity of biological substances due to their large specific surface area, high surface adsorption, good stability and biocompatibility. They also effectively avoid the inactivation resulting from labelling at multiple sites due to their steric hindrance [22, 25-26,

48]. The synthesis of nanoparticles is grouped into two phases: Liquid phase fabrication and gas (vapour) phase fabrication.

2.2.1 Liquid phase fabrication

Liquid phase fabrication, LPF, method includes solvothermal reactions, sol-gel, micellar structured and media reactions. The basic idea is to produce atoms in solution which will be reduced into nanoparticles, and to control their final size and shape by means of a surfactant which will strongly absorb to the nanocrystal surfaces, see Figure 2.3 for illustration [49]. Capping ligands/ surfactant play a vital role as controller of the crystal growth (by slowing it down or stopping it), the crystal shape (by attaching selectively to different crystal surfaces during growth), and the monomer concentration (by capturing atoms and releasing them later).



A strong reducing agent such as NaBH_4 or hydrazine typically generates narrower particles, and is usually coupled with strong surfactants for example PVP or PVA to maintain the particle sizes as well as avoid agglomeration when dispersed. Particle size is controlled by varying surfactant concentration, water-to-surfactant molar ratio (ω), precursor concentration, and molar ratio of reducing agent-to-reagent (R). Particle size increases due to particle agglomeration at higher precursor concentrations. Regardless of the way of producing atoms in solution, similar mechanisms in the nucleation and growing processes controlled by the surfactant are observed.

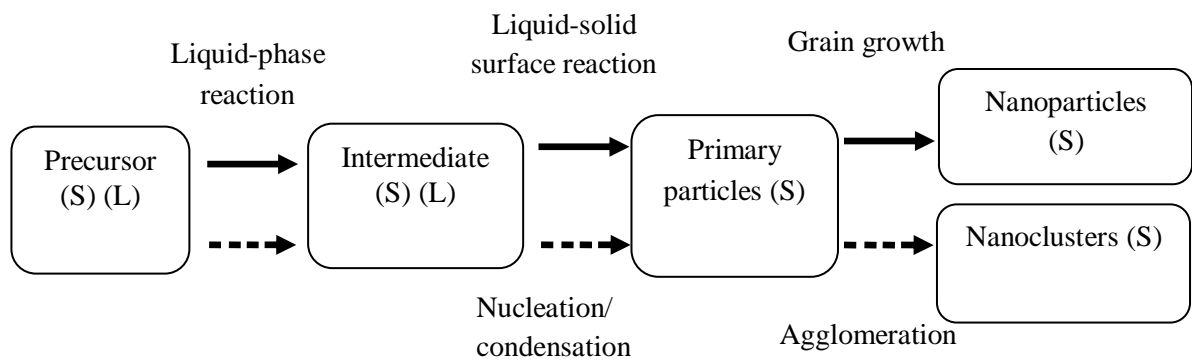


Figure 2.3: Mechanism of liquid phase fabrication.

2.2.2 Gas (vapour) phase fabrication

Gas (vapour) phase fabrication, GPF, includes Pyrolysis (Spray Pyrolysis), Inert Gas Condensation (Chemical Vapour Deposition and Physical Vapour Deposition) etc. This method generally involves precursor vaporization (this typically requires a catalyst), nucleation and growth stage. Irrespective of the various ways of vaporising the precursor, they all observe similar mechanisms in the nucleation and growth stage; see Figure 2.4 [49].

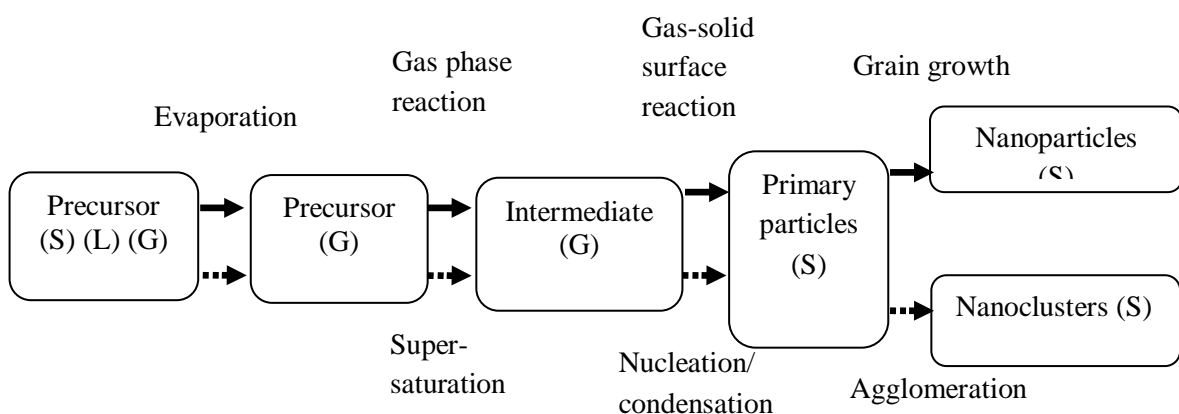


Figure 2.4: Mechanism of gas phase fabrication.

2.3 Graphene

Graphene is an allotrope of carbon, a monolayer of sp^2 -bonded carbon atoms tightly packed into a two-dimensional (2D) lattice (Figure 2.5). It is almost completely transparent, yet so dense that even the smallest atom helium cannot pass through it. Graphene has huge surface area ($2600 \text{ m}^2/\text{g}$), high chemical stability and conducts electricity as efficiently as copper. It outperforms all other materials as a conductor of heat. The electrical conductivity of graphene can be enhanced by absorbed nanoparticles acting as donors or acceptors.

This is possible due to its huge surface area which serves as scaffold to anchor large amount of nanoparticles and also assist in promoting selectivity and efficiency of catalytic processes [35, 50]. The enhanced electrical conductivity and mechanical properties make graphene an excellent material for collecting and transporting charge in photo-electrochemical solar cells, photo-catalysis and electrochemical sensors. Graphene-based nano-sheets give lithium-ion batteries more energy storage; Graphene sensor is 1,000 times more sensitive to light, could enable ultra-low-light photography; transparent graphene-based display could enable contact lens computers etc.

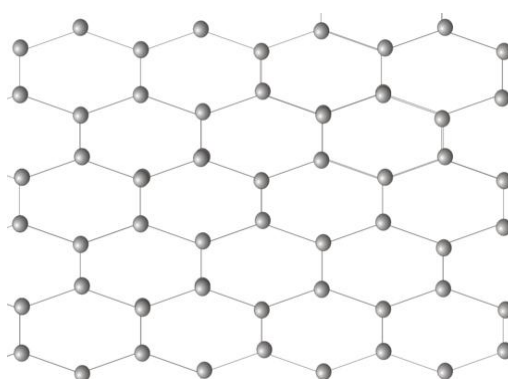


Figure 2.5: Graphene.

Invariably the application of functionalised graphene in the design of electrochemical sensors is based on the change of its electrical conductivity (σ) due to adsorption of molecules on graphene surface [36, 51]. The change in conductivity can be attributed to the change in carrier concentration of graphene due to the absorbed nanoparticles acting as donors or acceptors. Furthermore, some interesting properties of graphene aid to increase its sensitivity up to single atom or molecular level detection:

- ❖ First, graphene is a two-dimensional (2D) material and its whole volume i.e., all carbon atoms are exposed to the analyte of interest [52].
- ❖ Second, graphene is highly conductive with low Johnson noise (electronic noise generated by the thermal agitation of the charge carriers inside an electrical conductor at equilibrium, which happens regardless of any applied voltage), therefore, a little change in carrier concentration can cause a notable variation of electrical conductivity.
- ❖ Third, graphene has very few crystal defects ensuring a low level of noise caused by thermal switching
- ❖ Finally, four-probe measurements can be made on single crystal graphene device with Ohmic electrical contacts having low resistance

2.4 Polymer

A polymer is a chemical compound with high molecular weight consisting of a repeating number of structural units (monomers) which are linked together by covalent bonds. The word "polymer" can be broken down into "poly" (meaning "many" in Greek) and "mer" (meaning "unit"). This indicates how the chemical composition of a polymer is composed of monomer bonded together into larger molecule. The chemical reaction that covalently bonds

monomers together is called polymerization. It can be naturally occurring or synthetic and their general characteristics include:

- ❖ Low density
- ❖ Economical
- ❖ Good mould ability
- ❖ Poor tensile strength
- ❖ Low mechanical properties
- ❖ Poor temperature resistance
- ❖ Good corrosion resistance
- ❖ Low coefficient of friction
- ❖ Excellent surface finish is achievable
- ❖ It can be produced in different colours



Because of these broad ranges of properties, both synthetic and natural polymers play an essential and ubiquitous role in everyday life. [31, 53]. The characterization of a polymer requires several parameters which need to be specified. This is because a polymer consists of a statistical distribution of chains of varying lengths, and each chain consists of monomer residues which affect its properties. However, we will further review polymer in two broad classes based on their mode of occurrence- synthetic polymers and natural polymers.

2.4.1 Natural polymers

These are polymers that results from raw materials that occur in nature and extracted by human for everyday use. Natural polymers include RNA and DNA which are so vital in

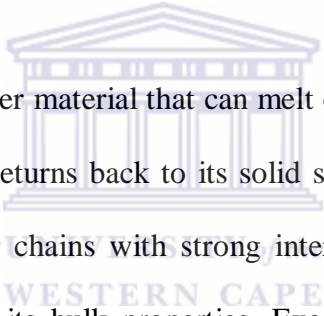
genes and life processes. Other examples of natural polymers are silk, wool, cellulose, rubber, protein etc

2.4.2 Synthetic polymer

These are human made polymers. They can either be characterized from the utility point of view, mode of polymerization reaction or monomer composition.

2.4.2.1 Characterization by utility point of view:

Synthetic polymers are hereby characterised into four main groups as thermosets, thermoplastics, synthetic fibres and elastomers.

- 
- ❖ **Thermoplastic** is a polymer material that can melt or be moulded when heated above specific temperature and returns back to its solid state when cooled. Thermoplastics are composed of polymer chains with strong intermolecular forces which increase upon cooling and restore its bulk properties. Examples of thermoplastics are poly (methyl methacrylate) (PMMA), nylon, polyethylene, polystyrene, polypropylene, polyvinyl chloride and Teflon [54].
 - ❖ **Thermoset** is a polymer material that toughens or hardens by irreversible cross linking of its polymer chains through chemical additives, heat, ultraviolet radiation or electron beam. This process is called vulcanization. Unlike thermoplastics, they do not melt but break down and do not reform upon cooling. Examples are the polyurethanes, vulcanized rubber, bakelite, duroplast, urea-formaldehyde, melamine resin, epoxy resin, polyimides, cyanate esters or polycyanurates [55].

❖ **Synthetic fibres** are man-made polymers made from chemical resources. They are manufactured using plant materials and minerals. Synthetic fibres are continuous filament fibres and do not spun out into yarn. They are resistant to most chemicals; electrostatic; flame resistant; heat sensitive; easy to wash; have low moisture absorbency; resistant to insects, fungi and rot. Synthetic fibres have unique properties which make them popular dress materials such as stain resistance, easy to dry, durable, readily available and easy to maintain. However they are prone to heat damage, they burn more readily than natural, more electrostatic charge is generated by rubbing than with natural fibres. Common examples of synthetic fibres are nylon, polyester, carbon fibre, acrylic, olefin and modacrylic [56].

❖ **Elastomers** is a rubbery material composed of long polymers, that are capable of recovering their original shape after being stretched to great extents, hence the name elastomer, from “elastic polymer”. Common examples of elastomers are polybutadiene, polyisoprene, polyisobutylene and polyurethane [57].

2.4.2.2 Characterization by mode of polymerization reaction

❖ **Addition polymers** are polymers in which the same or different monomer molecules bond to each other without the loss of any other atoms. They are usually linear or branched polymers with little or no cross-linking. Alkene monomers are the biggest groups of polymers in this class. Table 2.2 shows some common addition polymers, their formula, monomer and uses.

Table 2.2: Some common addition polymers, their formula, monomer and uses

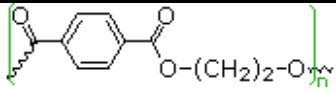
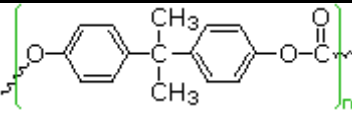
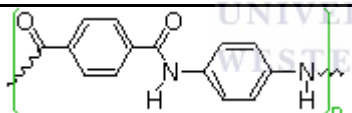
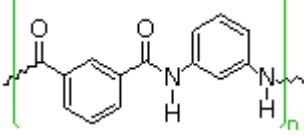
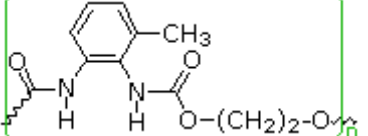
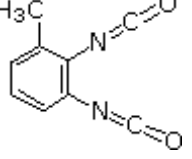
Names	Formular	Monomer	Uses
Polyethylene low density (LDPE)	$-(\text{CH}_2-\text{CH}_2)_n-$	ethylene $\text{CH}_2=\text{CH}_2$	Film wrap, Plastic bags
Polyethylene high density (HDPE)	$-(\text{CH}_2-\text{CH}_2)_n-$	ethylene $\text{CH}_2=\text{CH}_2$	Electrical insulation bottles, Toys
Polypropylene (PP) different grades	$-(\text{CH}_2-\text{CH}(\text{CH}_3))_n-$	propylene $\text{CH}_2=\text{CHCH}_3$	Upholstery
Poly(vinyl chloride) (PVC)	$-(\text{CH}_2-\text{CHCl})_n-$	vinyl chloride $\text{CH}_2=\text{CHCl}$	Pipes, Siding, Flooring
Poly(vinylidene chloride) (Saran A)	$-(\text{CH}_2-\text{CCl}_2)_n-$	vinylidene chloride $\text{CH}_2=\text{CCl}_2$	Seat covers, films
Polystyrene (PS)	$-(\text{CH}_2-\text{CH}(\text{C}_6\text{H}_5))_n-$	styrene $\text{CH}_2=\text{CHC}_6\text{H}_5$	Toys, Cabinets packaging
Polyacrylonitrile (PAN, Orlon, Acrilan)	$-(\text{CH}_2-\text{CHCN})_n-$	acrylonitrile $\text{CH}_2=\text{CHCN}$	Rugs, Blankets
Polytetrafluoroethylene (PTFE, Teflon)	$-(\text{CF}_2-\text{CF}_2)_n-$	tetrafluoroethylene $\text{CF}_2=\text{CF}_2$	Non-stick surfaces electrical insulation
Poly(methyl	$-(\text{CH}_2-$	methyl methacrylate	Lighting

methacrylate) (PMMA, Lucite, Plexiglas)	$C(CH_3)CO_2CH_3]_n-$	$CH_2=C(CH_3)CO_2CH_3$	covers, Signs skylights
Poly(vinyl acetate) (PVAc)	$-(CH_2-$ $CHOCOCH_3)_n-$	vinyl acetate $CH_2=CHOCOCH_3$	Latex paints, Adhesives
cis-Polyisoprene natural rubber	$-[CH_2-$ $CH=C(CH_3)-$ $CH_2]_n-$	isoprene $CH_2=CH-C(CH_3)=CH_2$	Requires vulcanization for practical use
Polychloroprene (cis + trans) (Neoprene)	$-[CH_2-CH=CCl-$ $CH_2]_n-$	chloroprene $CH_2=CH-CCl=CH_2$	Synthetic rubber oil resistant



❖ **Condensation polymers** are polymers in which usually two different monomer units combine with the loss of a small molecule, typically water. Condensation polymers form more slowly than addition polymer, often requiring heat and are generally low in molecular weight. The terminal functional groups on the chain remain active as the groups of shorter chains combine into longer chains in the late stages of polymerization. The polar functional group on the chains often enhances crystallinity, tensile strength and chain-chain attractions, mostly if these involve hydrogen bonding. Table 2.3 shows some common condensation polymers, their formula, monomer and uses.

Table 2.3: Some common condensation polymers, their formula, monomer and uses

Names	Formular	Components	Uses
Polyester Dacron Mylar		para $\text{HO}_2\text{C}-\text{C}_6\text{H}_4-$ CO_2H $\text{HO}-\text{CH}_2\text{CH}_2-\text{OH}$	Clothing, films, tapes
Polycarbonate Lexan		$\text{HO}-\text{C}_6\text{H}_4-\text{C}(\text{CH}_3)_2$ (Bisphenol A) $\text{X}_2\text{C}=\text{O}$ (X = OCH_3 or Cl)	Plastic canopy for aircraft
Polyamide Nylon 66	$-\text{[CO}(\text{CH}_2)_4\text{CO}-$ $\text{NH}(\text{CH}_2)_6\text{NH}]_n-$	$\text{HO}_2\text{C}-(\text{CH}_2)_4-\text{CO}_2\text{H}$ $\text{H}_2\text{N}-(\text{CH}_2)_6-\text{NH}_2$	Women hose, rope, fabric carpeting
Polyamide Kevlar		para $\text{HO}_2\text{C}-\text{C}_6\text{H}_4-$ CO_2H para $\text{H}_2\text{N}-\text{C}_6\text{H}_4-\text{NH}_2$	Bullet proof vests
Polyamide Nomex		meta $\text{HO}_2\text{C}-\text{C}_6\text{H}_4-$ CO_2H meta $\text{H}_2\text{N}-\text{C}_6\text{H}_4-\text{NH}_2$	Electrical laminates
Polyurethane Spandex			Foams

2.4.2.3 Characterisation by monomer composition

- ❖ **Homopolymers** are polymers that consist of chains with identical bonding linkages to the same type of monomer units. This implies that the polymer is made from all identical molecules and bonding linkages. . Common examples are poly (ethylene terephthalate), poly(hexamethylene adipamide) and poly(vinyl alcohol) These may be represented as [58-59]:



- ❖ **Copolymers** are polymers that consist of chains with two or more different type of linkages and usually involving two or more different types of monomer units. This implies that two or more different types of monomer units are joined to in the same polymer chain. Copolymers are classified based on how these monomer units are arranged along the chain [58-60], examples include:

Alternating copolymers are polymers which consist of two monomer units A and B that are arranged in an alternating fashion with nearly equimolar amounts of each in the chain.



Statistical copolymers are polymers in which the sequence of monomer residues follows a statistical rule. The monomeric units are distributed randomly, and sometimes unevenly, in the polymer chain.



Block copolymers are polymers which comprise of two or more homopolymer sub-units linked by covalent bonds. Instead of a mixed distribution of monomeric units, a long sequence or block of one monomer is joined to a block of the second monomer. Block copolymers with two or three distinct blocks are called di-block copolymers and tri-block copolymers (terpolymer), respectively.



Branched copolymers consist of a single main chain with one or more polymeric side chains. Other special types of branched copolymers include star copolymers, brush copolymers, graft copolymers and comb copolymers.

Graft copolymers are a special type of branched copolymer in which the side chains are structurally distinct from the main chain. As the name suggests, side chains of a given monomer are attached to the main chain of the second monomer.



Linear copolymers consist of a single main chain.

2.5 Ionomers

Ionomers are special kind of polyelectrolytes that contains a small amount of ionic repeat groups covalently bonded to the polymer chain with maximum ionic group content of about 15 mol % [61-62]. The percentage is calculated from the number of backbone atoms or repeat units to which ionic groups are attached. The percentage of ionic groups corresponds to the

different structures for the ionomers with long pendant chains (Nafion) and with short pendant chains (Dow membranes), and therefore different properties, even if the backbone is identical. For this reason, the equivalent weight (EW) which is the amount of ionomer (in grams) that contains 1 mol of ionic groups is also an indication of the ionic content [61].

These ionic groups are usually acids or salts with fixed anions on the polymer chain and mobile cations. There is a huge difference in the hydrophobicity between the ionic groups and the rest of the polymer [63]. This causes micro-phase separation of the ionomer into ionic aggregates surrounded by a hydrophobic matrix. The interactions within the ionic aggregates and between the aggregates and the matrix are what control the morphology and properties of the ionomers [64]. Ionomers therefore can also be defined as ion containing polymers in which the bulk properties are governed by ionic interactions in discrete regions of the ionic aggregates [61]. It has been reported that the inclusion of small amounts of ionic groups into organic polymers can modify the physical properties of the materials profoundly while maintaining reasonable processability. Increases in the glass transition by five hundred degrees. And increases in the viscosity by over four orders magnitude have been observed, among many other effects [62, 65].

Due to the fascinating changes in property brought about by the presence of the ionic groups, ionomers have been used in a wide range of applications that utilize different aspects of their unique properties. They have widespread applications in packaging, adhesive and coating technologies due to their excellent toughness, acid functionality and compatibility with various solvents. They have been processed into membranes for a variety of electrochemical devices owing to their high ionic conductivity. Protonated ionomer membranes have been extensively used as the electrolyte in fuel cells. Applications have also been explored in using

ionomers as catalysts because of their high acidity along with their nature as separation media [63, 66].

2.6 Nafion

Ion-containing polymers have been around for some time; however the past fifteen years have witnessed an explosive growth in the literature on ionomers. Most of the research effort on these ionomers have been devoted to the ethylenes, styrenes, rubbers, and those based on poly(tetrafluoroethylene). Nafion® DuPont is one such example of a poly(tetrafluoroethylene) based ionomer [61]. It consists of a polytetrafluoroethylene backbone and regular spaced long perfluorovinyl ether pendant side chains terminated by a sulfonate anionic group [65].

The polymeric chain is chemically and thermally stable, making it very suitable as a backbone for very thin membranes while the acid groups are very appropriate for ion exchange. Nafion® DuPont is the first synthetic ionic polymer and is a brand name for a series of fluorinated sulfonic acid copolymers. The sulfonic acid groups are chemically active, but they are fixed within the Teflon polymer matrix. Thus, Nafion is resistant to chemical breakdown; therefore it is applied as membranes in fuel cells [62]. DuPont de Nemours was the first one in 1962 to develop it [63, 65]. Since then it has etched applications in, fuel cells, liquid and gas separations.

Because of its ion-exchange properties, selectivity, mechanical strength, biocompatibility, insolubility in water, thermal and chemical resistance, its application is only limited by imagination and prudence. It been reported that Nafion can bind molecules through coulombic and/or hydrophobic interactions [38-40, 67]. It can also facilitate electron transfer

from an enzyme active centre to the electrode surface and acts as a weak mediator for redox-active probes [40, 62, 66]. Nafion films therefore have been used extensively for the modification of electrode surfaces and for the construction of biosensors and chemical sensors. Conversely the rate of charge transfer in pure Nafion film is relatively slow due to its compact nature which is unfavourable for diffusion of analyte. The stability of the ECL sensor based on a pure Nafion film-modified electrode is challenging because immobilised luminophore/cationic reactants such as tris (bipyridine) ruthenium(II), $[\text{Ru}(\text{bpy})_3]^{2+}$, migrates into electro-inactive hydrophobic region of the ionomer with time, thereby losing electrochemical contact with the electrode [68-71]. The chemical formula is:

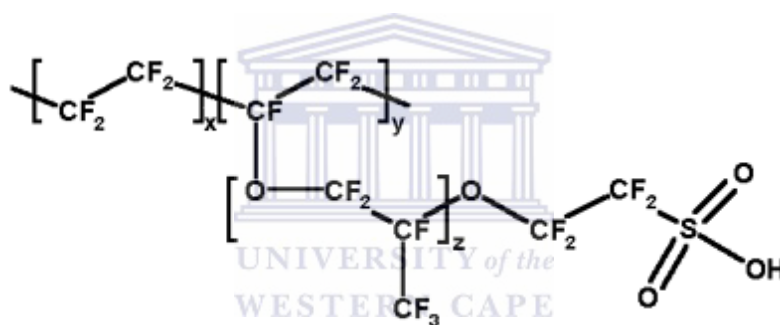


Figure 2.6: The chemical formula of Nafion.

The exact structure of Nafion is not known. Nevertheless several models have been proposed since the early 1970s, to describe the way in which ionic groups aggregate within the polymer. These models include: The Mauritz-Hopfinger Model [64, 72-74], The Yeager Three Phase Model [75], The Eisenberg Model of Hydrocarbon Ionomers [76] and The Gierke Cluster Network Model [72, 77]. A common objective of these models is to predict the fundamental feature of unique equilibrium ionic selectivities and the ionic transport properties of per-fluorinated ionomer membranes.

Due to the electrostatic interactions between the ions and the ion pairs in the parent polymer, ionic groups tend to aggregate to form tightly packed regions referred to as clusters. The hydrophobic region is composed of the polymer fluorocarbon backbone while the hydrophilic region contains the ionic groups and their counter ions [78]. The details on the arrangement of the ionic groups within these clusters have not completely been realized. No one model so far provided a complete explanation of the ionomer properties. Many base these properties on extensive micro-phase split morphology [74, 78].

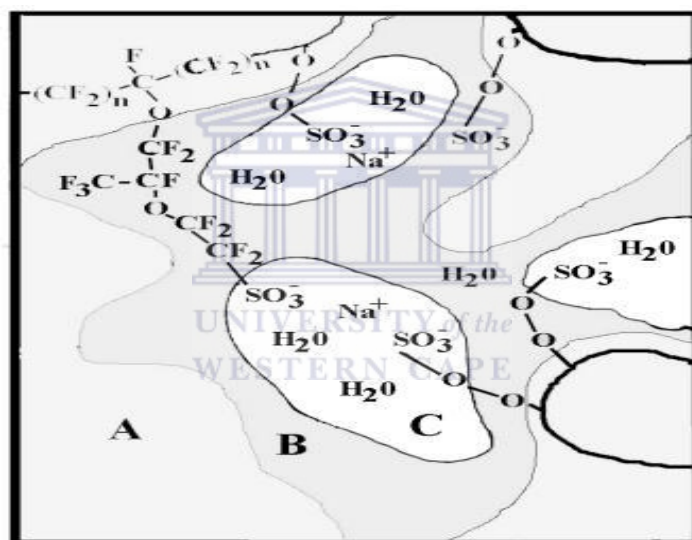


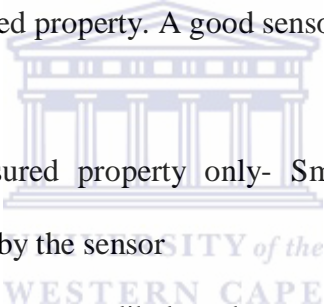
Figure 2.7: The Yeager 3 Phase Model of Nafion® Clusters.

Figure 2.7 shows Yeager Three Phase phenomenological model based on a three-phase clustered system with interconnecting channels within the polymer. The three regions consist of (A) fluorocarbon backbone (B) an interfacial region of relatively large fractional void volume containing some pendant side chains, some water and sulphate or carboxylic groups and counter ions which are not in clusters, and (C) clustered regions where the majority of the

ionic exchange sites and counter ions exist. Nafion exhibited remarked properties due to the extensive micro-phase separation morphology as seen from numerous researchers. We chose to apply Nafion in this study due to its ionic morphology and inherent ionomer properties.

2.7 Sensor

A sensor is a device that can detect and respond to a parameter or an input quantity continuously and convert it into a functionally related output signal which can be read by an instrument [79-80]. There are innumerable applications for sensors which include cars, machines, aerospace, medicine, manufacturing, robotics etc. A sensor's sensitivity indicates how much the sensor's output changes when the measured quantity changes. It is the ratio between output signal and measured property. A good sensor must:

- 
- ❖ be sensitive to the measured property only- Smallest changes in the measured property must be detected by the sensor
 - ❖ be insensitive to any other property likely to be encountered in its application.
 - ❖ reproduce the same results repeatedly - The reading must not vary when repeatedly measured under the same conditions
 - ❖ have a signal output that is proportional or bear a mathematical relationship to the amount of species present in the sample
 - ❖ have good signal-to-noise ratio, which determines the limit of the detection
 - ❖ have a fast response time
 - ❖ not influence the measured property
 - ❖ be accurate
 - ❖ be cost effective
 - ❖ be environmentally friendly

Nevertheless, ideal sensors are far from reality in spite of enormous advances over the past decades. In actuality, a sensor is generally optimized for a particular application. The sensitivity and selectivity aspects of chemical sensing are affected by the phase, dimensional, and temporal aspects of the desired determination. The analyte can be present in a gas, liquid, or solid phase on various dimensional scales ranging from bulk volumes of litres to picolitres. There are three main types of sensors based on the property of the entity sensed- physical sensors, chemical sensors and biosensors [80].

2.7.1 Physical sensor

A physical sensor is a device that provides information about a physical parameter of the system [80-81]. They are different from chemical sensors in that they measure parameters such as temperature, humidity, speed, depth/pressure, turbidity that regulates the transfer or flux of mass or energy. Physical sensors are named according to the type of physical parameter it measures.

Example is turbidimeter used for estimating turbidity of a solution by detecting the attenuation of light as it passes through solution sample using a transmissometer, nephelometer is another turbidity sensor that emit light into the water and then measure how much light is scattered to the side at a 90-degree angle (The amount of scattered light is proportional to the turbidity), fluorometer is used to measure coloured (or chromophoric) dissolved organic matter (CDOM) in a solution, thermocouple measures temperature and convert it to an output voltage which can be read by a voltmeter, the motion detectors are based on the infra red, ultrasonic and microwave and are used in videogames, simulations,

light activation and security detection, the accelerometers are based on the micro electro-mechanical sensor technology and are used for vehicle dynamic systems. And so on.

2.7.2 Chemical sensors

A chemical sensor is a device that transforms chemical information (which may originate from a chemical reaction of the analyte or from a physical property of the system), ranging from the concentration of a specific sample component to total composition analysis, into an analytically useful signal [80, 82]. Chemical sensors contain usually two basic components connected in series: a chemical (molecular) recognition system (receptor) and a physico-chemical transducer [81]. Example is the biosensors- These are based on the electrochemical technology. They are used for food testing, medical care device, water testing, and biological warfare agent detection etc. Chemical sensors contain two basic functional units: a receptor part and a transducer part.



2.7.2.1 The receptor

This transforms the chemical information into a form of energy which can be measured by the transducer [80]. The receptor part of chemical sensors may be based upon various principles as shown in Figure 2.8.

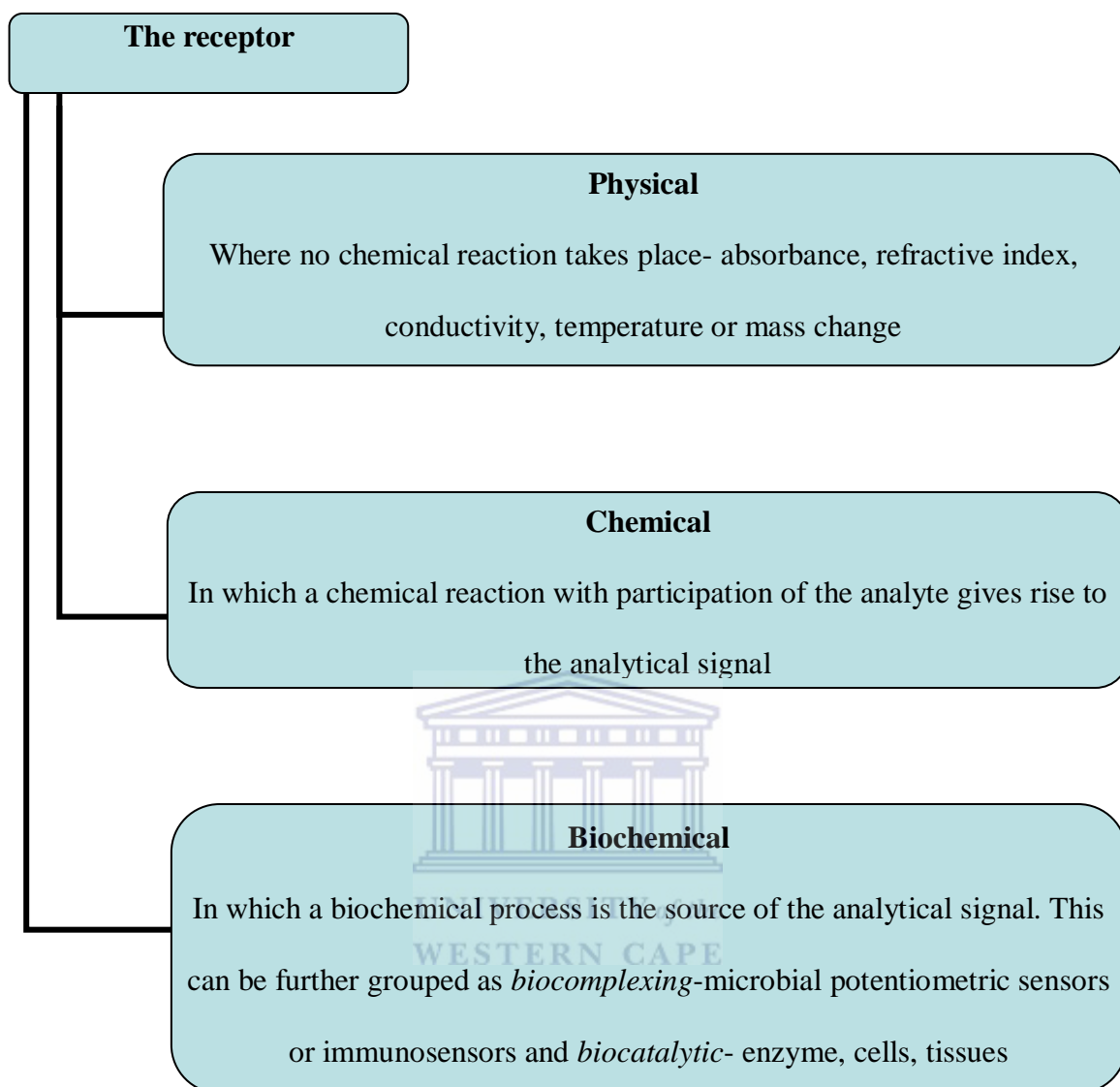


Figure 2.8: Functional principles of the receptor.

2.7.2.2 The transducer

This converts the energy carrying the chemical information about the sample into a useful output signal with a defined sensitivity [80]. Chemical sensors may be classified according to the operating principle of the transducer as shown in Figure 2.9.

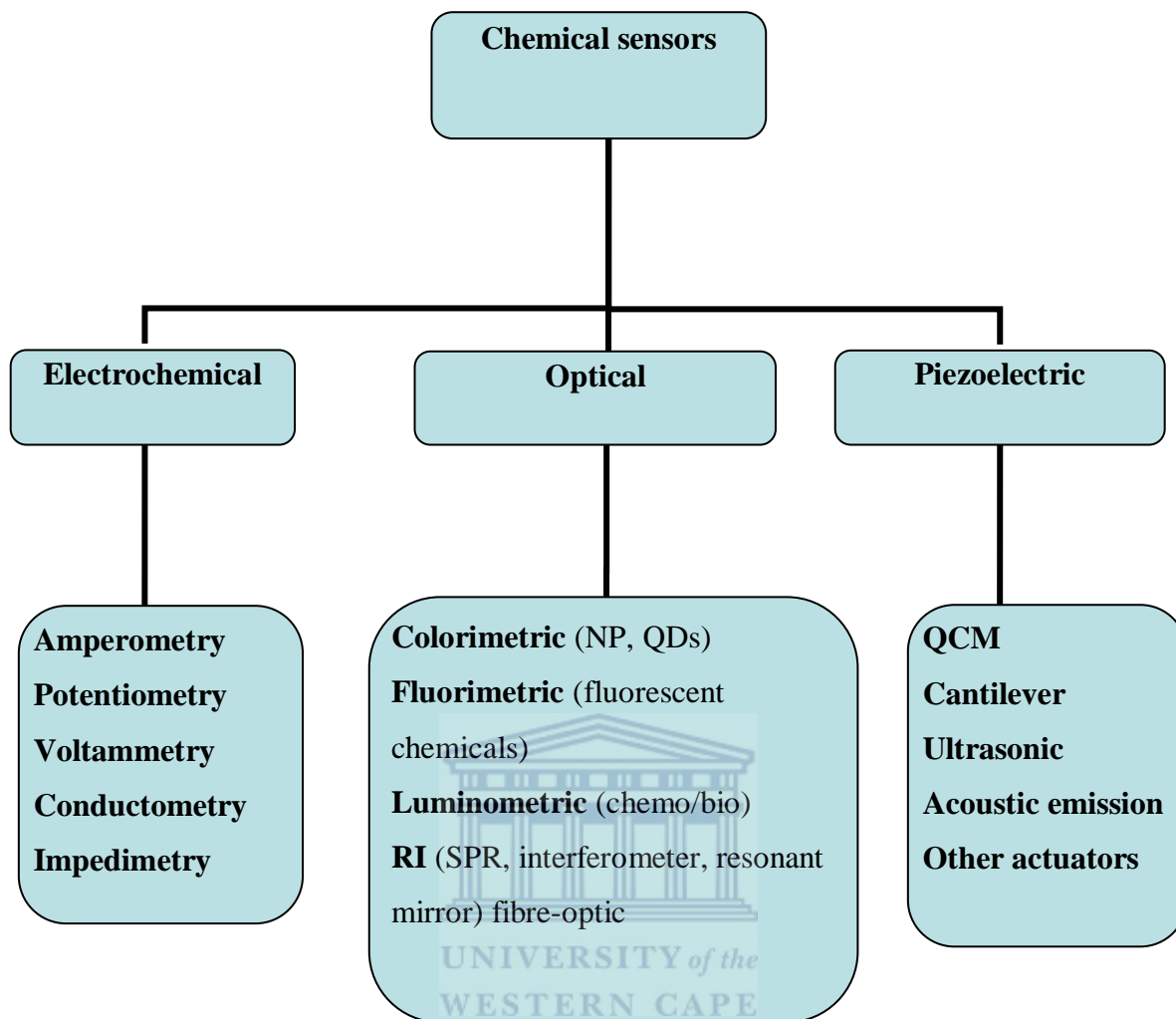


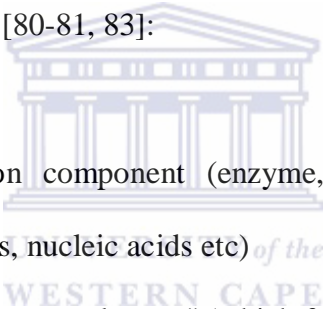
Figure 2.9: Classification of chemical sensor based on operating principle of the transducer.

Another basis for the classification of chemical sensors may be according to the mode of application, for example sensors intended for use in vivo or sensors for process monitoring and so on. Chemical sensors have also been classified according to its application to detect/determine a given analyte. It is possible to use various classifications as long as they are based on clearly defined and logically arranged principles [80]. The capability of chemical sensing technology is substantial and has grown steadily over the past several

decades. However, for the purpose of this research we will be looking at biosensor and immunosensor specifically.

2.7.3 Biosensors

A biosensor is an analytical device designed for the detection of an analyte by combining a biological recognition component (enzyme, antibody, cell receptor, DNA, microorganisms, organelles, nucleic acids etc) with a physicochemical signal transducer. This biomimetic component recognises and binds with the analyte under study. Then the signal transducer (electrode, optical detector, piezo crystal etc.) converts the biochemical response into electric and optic signals which are amplified, measured and decoded by an appropriate electronic unit. Biosensor consists of 3 parts [80-81, 83]:

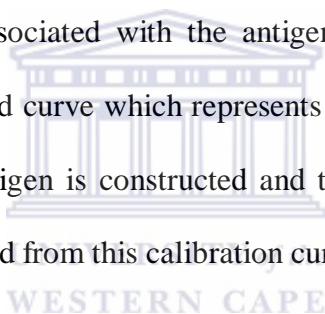
- 
- ❖ The biological recognition component (enzyme, antibody, cell receptor, DNA, microorganisms, organelles, nucleic acids etc)
 - ❖ The "transducer" or the "detector element" (which functions based on electrochemical; optical or piezoelectric principles)
 - ❖ Signal processors that are primarily responsible for the display of the results in a user-friendly way.

Biosensors can be grouped according to their biological element or their transduction principle. The instrument is described as an **affinity sensor** when the detected event is the binding of the sensing element and the analyte. When the interaction between the biological element and the analyte is accompanied by a chemical change in which the concentration of one of the substrates or products is measured the instrument is described as a metabolism sensor. Furthermore, if analytical signal is produced after binding with the analyte without

chemically changing it save for converting an auxiliary substrate, the biosensor is called a **catalytic sensor**. Antibody-based biosensors are called immunosensors [83-84].

2.7.3.1 Immunosensor

Immunosensors are affinity ligand-based analytical devices that use antibody or antigen as the specific sensing element and transduce the antigen-antibody interactions directly into signals that are related to analyte concentration. The basic principle is the specific binding of an antibody to an antigen to form a stable complex [85-86]. Immunosensors have simplified analytical procedures, the possibility of miniaturization, shortened analysis times, lower detection limits, specificity and increased assay sensitivities [87-88]. Immunoanalysis is done by measuring several signals associated with the antigen-antibody interactions of known antigen concentrations. A standard curve which represents the measured signal as a function various concentrations of the antigen is constructed and the value of the unknown antigen (analyte) concentration is extracted from this calibration curve [89-90].

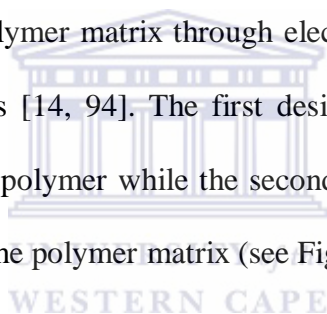


The degree of selectivity or specificity of an immunosensor depends on the bio-recognition element, while the sensitivity of the sensor greatly depends on the transducer. Therefore the design of an optimum interface between bio-components and detector material is a key part of designing an immunosensor [14-15]. This can be achieved by two different procedures namely; biomolecular immobilization and free biomolecular methods. The former is preferred to the later due to its operational advantages which include reusability, enhanced stability, rapid termination of reaction, ease of separating biocatalyst from product and reduced cost of operation [14, 88, 91].

The procedure of biomolecule immobilization on conductive surfaces is a very important step which has direct effect on performance of the resulting immunosensor [92]. For a choice of biomolecule immobilization procedure to be effective, the biomolecule should be compatible and chemically inert towards host structure; should be accessible when immobilized; must retain its biological properties and be stable on the transducer surface [93-94]. There are three ways of attaching a biomolecule to a transducer: (a) covalent binding, (b) attachment by affinity interactions and (c) physical entrapment.

2.7.3.2 Covalent binding

This is a process by which biomaterials are linked with a previously functionalized polymer or by incorporating it into the polymer matrix through electrosynthesis of the polymer using enzyme-functionalized monomers [14, 94]. The first design allows immobilization to take place on the outer surface of the polymer while the second design allows greater amount of biomaterial to be integrated into the polymer matrix (see Figure 2.10) [42, 95].



2.7.3.3 Attachment by affinity interactions (encapsulation and confining)

This method involves the adsorption of biomolecule on the polymer/solution interface due to static interactions between the polycationic matrix of an oxidized polymer and an anionic biomolecule provided the pH is higher than the isoelectric point (IP) of the biomolecule [93]. This process has some limitations like adsorption is restricted to one monolayer on the polymer surface hence amount of enzyme incorporated is very small, binding forces can change with pH, biomaterial is immobilized on the outer layer of conducting polymer and so it is directly exposed to the bulk solution which makes it leach out into sample solution during measurements (see Figure 2.10) [42, 94, 96].

2.7.3.4 Electrochemical immobilization (physical adsorption)

In this method, monomer is electrochemically oxidized in the presence of a bio-molecule to form a polymer which incorporates homogeneously distributed bio-molecules during its growth process (see Figure 2.10). This method is simple, reproducible and has the possibility of immobilizing mediators simultaneously simply by adding them to the polymerization solution. Electro-polymerization is ideally suited for biomolecular immobilization because of its mild encapsulation procedure that enables high retention of the activity of a labile encapsulated species [93-95, 97].

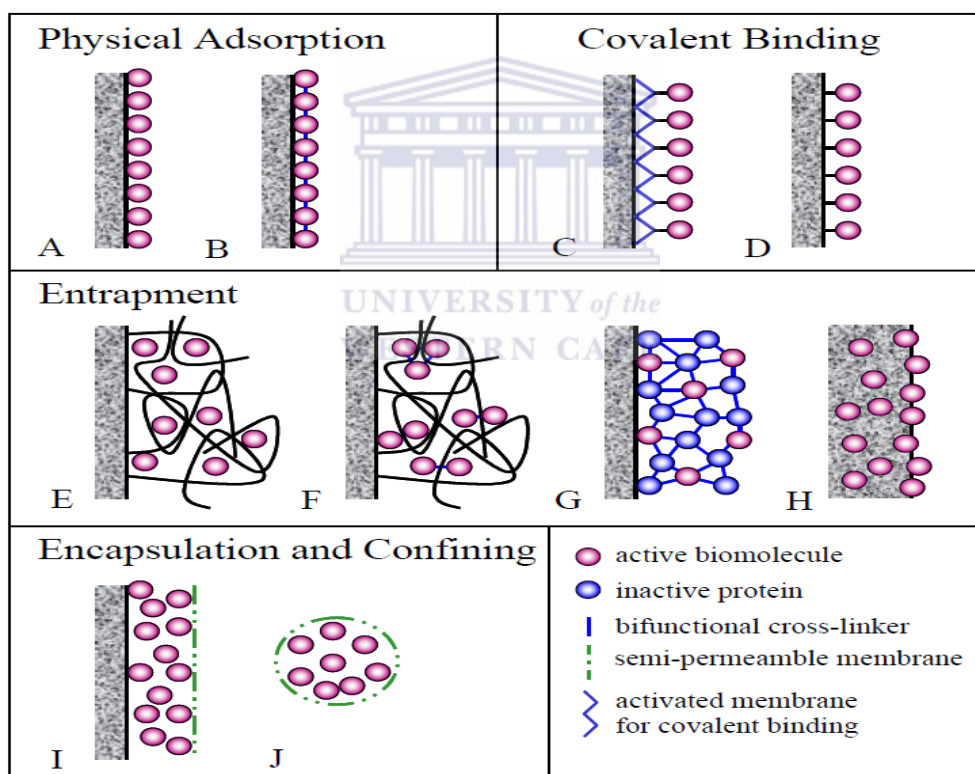


Figure 2.10: Methods for immobilising bio-molecules on the transducer.

2.8 Fundamental principles of ultraviolet-visible spectroscopy

Ultraviolet-visible spectroscopy or ultraviolet-visible spectrophotometry (UV-Vis) is an absorption spectroscopic technique involving the use of light in the ultraviolet- visible spectral region (light in the visible and adjacent i.e. near UV and near infra red ranges) to cause electronic transitions from the ground state to the excited state in the target molecules. The absorption in the visible range directly affects the perceived colour of the chemical involved [98]. A light source of a fixed wavelength is shone through a sample and its absorption (or transmission) intensity measured against a background using a detector [99]. The wavelength is then varied slightly using a diffractometer, and the process repeated until the absorption ratio for a spectrum of wavelengths is obtained [99-100].

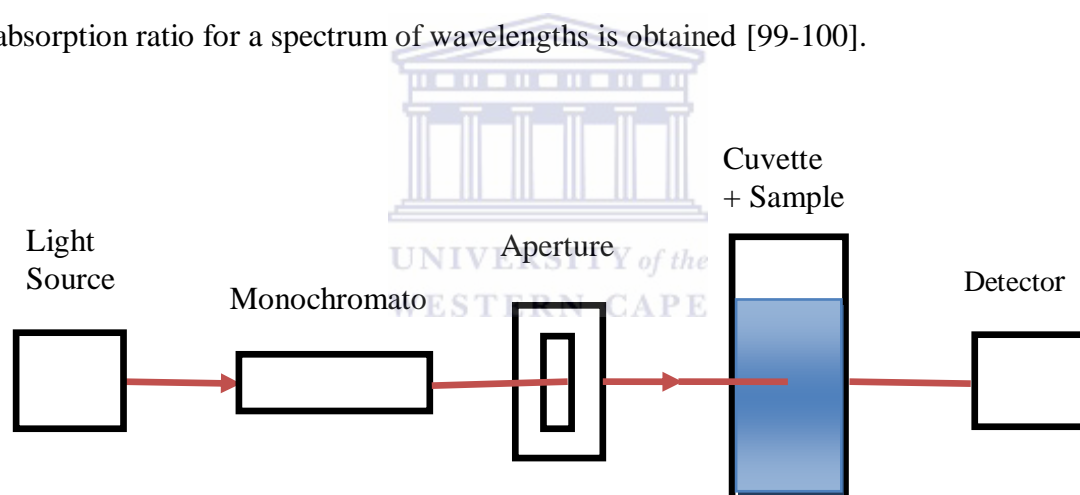


Figure 2.11: Basic schematic representation of a UV-Vis spectrometer.

The absorption of light at a particular wavelength is determined by the ratio of transmitted light to the incident light while Beer-Lamberts law directly relate the absorbance of the molecules at a wavelength to the product of its concentration and the length of the light path [98].

$$A = -\log [I_t/I_i] \quad (1)$$

$$A_\lambda = \epsilon_\lambda C l \quad (2)$$

Where, I_t = transmitted light, I_i = incident light, A_λ = molar extinction coefficient

C = Concentration, l = the length of the light path

UV-Vis spectroscopy operates basically on the principles of molecular orbitals. Briefly, all molecules have molecular orbitals that are formed by adding or subtracting their corresponding atomic orbitals known as bonding and anti-bonding orbitals. The bonding orbital of a molecule is known as the highest occupied molecular orbital (HOMO) and contains the valence electrons. The anti-bonding orbital, on the other hand, is known as the lowest occupied molecular orbital (LUMO) and is normally devoid of electrons [101-102].

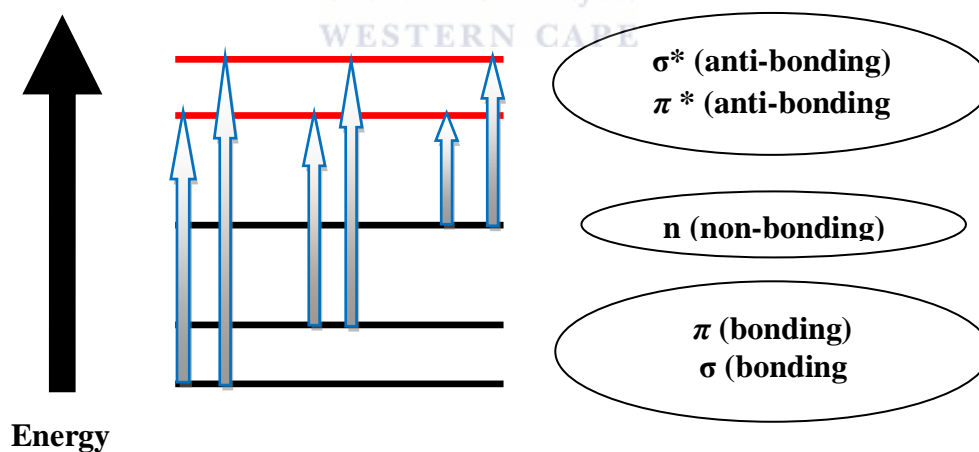


Figure 2.12: Illustration of molecular orbital theory.

This description is applicable for single molecules only. Actually a bulk material is made up of a number of atoms that are bonded together. The HOMOs and LUMOs of each atom add

up to form many closely packed orbitals called bands. Two discrete bands known as the conduction and valence bands are formed. Electrons in the valence band are coupled with their respective nuclei, while electrons in the conduction band are separated from their respective nuclei hence allowing for free motion within the solid [98-99].

The energy distance between the valence and conduction bands is termed band gap. The bigger the band gap, the bigger the energy required to excite electrons from valence band into conduction band [103]. For a smaller sized quantum dot or metal nanoparticles the band gap is larger. This means that more energy will be required to excite an electron from its valence band to conduction band and will in turn emit light of higher energy (i.e. shorter wavelengths) as it relaxes to lower energy state. The reverse is also true.

The difference between the bands in solid and discrete atomic or molecular orbitals is noteworthy. The organization of energy levels is quite different between nano-materials and bulk materials in that the nano-materials have larger band gaps and consist of more discrete energy levels. This could be attributed to the various quantum confinement effects within nanoparticles whose sizes can be as small as only a few dozen atoms wide (couple of nanometers). Quantum confinement is restriction from movement of the particles in one or more dimensions. Conversely bulk solids are composed of several thousands of atoms which contribute to highly overlapping orbitals system, less pronounced energy bands and consequently smaller band gap. Band gap can be calculated from UV-Vis spectra data by applying the following formula:

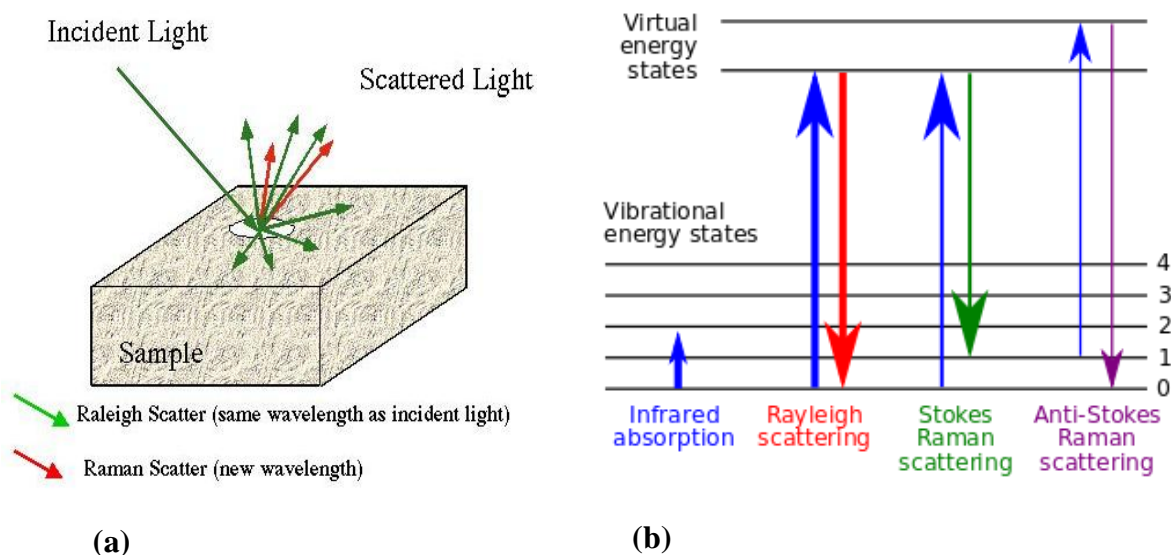
$$E_g^* = hc/\lambda_c \quad (3)$$

Where: λ_c = wavelength absorbed by the sample, c = the speed of light, 299,792,458 m/s, and h = Planck's constant, $6.62606957(29) \times 10^{-34}$ J.S

UV-Vis absorption spectroscopy is an effective technique used to study particle growth of nanocrystal. The radius of the particle is related to the absorption band by effective mass model [104-105]. Therefore UV-Vis characterisation gives an idea about the size of the particles under investigation since the band edge depends on the particle size.

2.9 Fundamental principles of Raman spectroscopy

Raman spectroscopy named after Sir C.V. Raman, is a spectroscopic technique used to observe vibrational, rotational, and other low-frequency modes in a system. Basically a monochromatic light (only one colour and not a mixture), usually from a laser in the visible, near infrared, or near ultraviolet range is focused on a sample, most of which are absorbed, reflected, or transmitted by the sample, see Figure 2.13 for illustration [106].



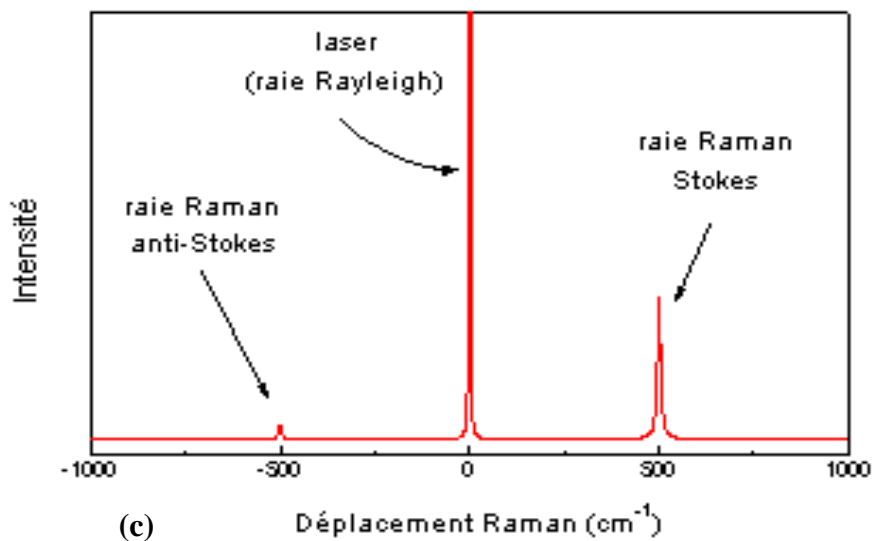


Figure 2.13: (a) Illustration of incident light scattering and (b) energy level diagram showing the states involved in Raman signal (c) typical Raman spectra.

A small fraction of photons interacts with the sample and during this interaction, some energy is transmitted to elementary particles of which materials are constituted (electrons, ions etc.) [107]. This causes their transition from ground energy levels to ‘virtual’ excited states. These excited states are highly unstable and particles decay instantaneously to the ground state by one of the following three different processes (see Figure 2.13) [98]:

- ❖ **Rayleigh scattering:** the emission of a photon of the same energy allows the molecule to relax to its ground vibrational state (elastic scattering). Rayleigh scattering, therefore, bears no information on vibrational energy levels of the sample.
- ❖ **Stokes and anti-Stokes Raman photons (inelastic) scattering:** emission of a photon with energy either below or above that of Rayleigh photons, thereby generating a set of frequency-shifted ‘Raman’ photons. The energy differences of the Stokes and anti-

Stokes Raman photons with respect to the excitation energy give information about molecular vibrational levels

Raman spectroscopy involves molecular and crystal lattice vibrations and is therefore sensitive to the composition, bonding, chemical environment, phase, and crystalline structure of the sample material in any physical form: gases, liquids, solutions, and crystalline or amorphous solids [98].

2.9.1 Components of a Raman spectrometer

A typical Raman spectrometer is made up of five basic parts (see Figure 2.14) [106-107]:

- ❖ Excitation source (generally a laser): A laser is used to produce Raman spectra because it gives a coherent beam of monochromatic light. This gives sufficient intensity to produce a useful amount of Raman scatter [107].
- ❖ Sample illumination and scattered light collection system (probe): The probe is a collection device that collects the scattered photons, filters out the Rayleigh scatter and any background signal from the fibre optic cables, and sends the scattered light to the spectrograph.
- ❖ Sample holder
- ❖ Spectrograph (spectral grid): When Raman-scattered photons enter the spectrograph; they are passed through a transmission grating to separate them by wavelength and are passed to a detector.
- ❖ Detection system (optical multichannel analyser, PMT or a charged coupled device, CCD): this records the intensity of the Raman signal at each wavelength. This data is represented as a Raman spectrum.

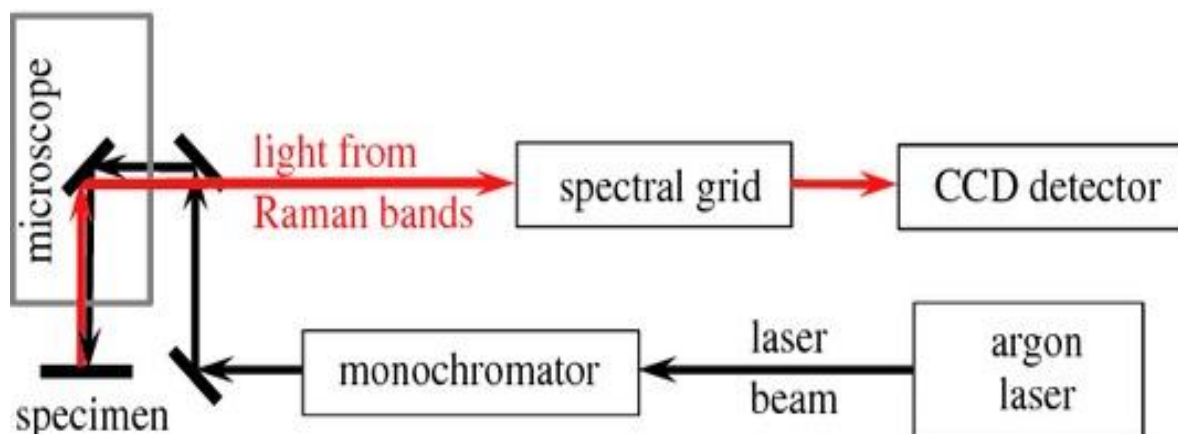


Figure 2.14: Representation of basic parts Raman of spectrometer.

2.10 Fundamental principles of atomic force microscopy (AFM)

Atomic force microscopy (AFM) is an electroanalytical technique that is grouped under the scanning probe microscopy (SPM). It has the ability to view details (morphology) at atomic and molecular level with very high resolution, thus increasing our understanding of how systems work and leading to new discovering in many fields like life science, material science, electrochemistry, polymer science, biophysics, nanotechnology and biotechnology. This technique was discovered by Gerd Binnig and Heinrich Rohrer at IBM Research in Zurich and this earned them the Nobel Prize for Physics in 1986 [108-109].

2.10.1 Operation of AFM

The principle of operation of the AFM is very similar with that of a stylus profilometer where a sharp cantilever tip interacts with the sample surface, sensing the local forces between the molecules of the tip and sample surface. To measure the forces acting between a fine tip and a sample, the tip which is attached to the free end of a cantilever is brought very close to the surface. Attractive or repulsive forces resulting from interactions between the tip and the

surface will cause a positive or negative bending of the cantilever. The bending is detected by means of a laser beam, which is reflected from the back side of the cantilever (see Figure 2.15 for illustration). The microscope consist of two major components- the piezocrystals and the probe as shown in Figure 2.15 [108-109].

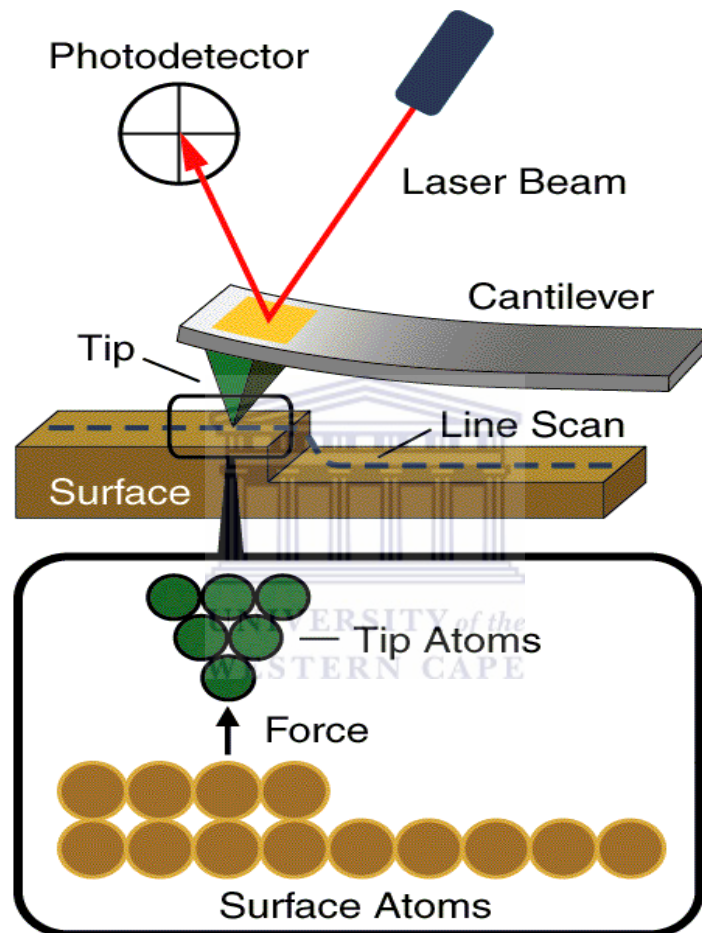


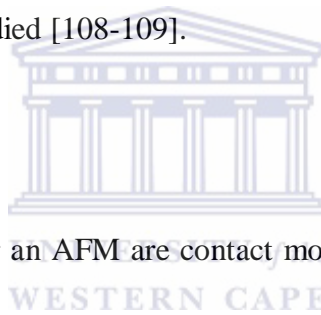
Figure 2.15: Schematic illustration operational principles of AFM.

2.10.1.1 Piezocrystals

Piezocrystals are ceramic materials that expand or contract in the presence of voltage gradient and conversely, they develop an electrical potential in response to mechanical pressure. In this way, movements in x, y and z direction are possible [108-109].

2.10.1.2 Probe

The AFM probe represents a consumable and measuring cantilever with a sharp tip at one end, which is brought into interaction with the sample surface. The dimensions of the cantilever are in the scale of micrometers and different shapes too. V-shaped cantilevers are the most popular (but also there are rectangular), providing low mechanical resistance to vertical deflection, and high resistance to lateral torsion. Cantilevers typically range from 100 to 200 μm in length (l), 10 to 40 μm in width (w), and 0.3 to 2 μm in thickness (t). Integrated cantilevers are usually made from silicon (Si) or silicon nitride (Si_3N_4). They are characterized by their force constant and resonant frequency, which have to be chosen according to the sample to be studied [108-109].



2.10.2 Modes of operation

The main modes of operation for an AFM are contact mode, non contact mode and tapping mode.

2.10.2.1 Contact mode

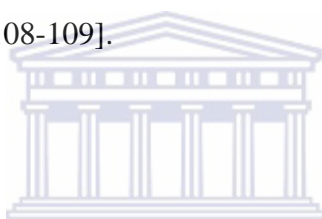
In this mode, the cantilever tip makes a soft physical contact with the surface of the sample then it is dragged across it at a constant small height above the surface or under the conditions of a constant force, and the contours of the surface are measured directly using the deflection of the cantilever. The deflection of the cantilever Δx is proportional to the force acting on the tip, via Hook's law [108-109]:

$$\mathbf{F} = -\mathbf{k} \cdot \Delta \mathbf{x} \quad (4)$$

Where, k is the spring constant of the cantilever.

2.10.2.2 Non-contact mode

Here the probe operates in the attractive force region and the cantilever tip-sample interaction is minimized and the tip of the cantilever does not contact the sample surface. The use of non-contact mode allowed scanning without influencing the shape of the sample by the tip-sample forces. Also non-contact mode AFM does not suffer from tip or sample degradation effects that are sometimes observed after taking numerous scans with contact AFM. This makes non-contact AFM preferable to contact AFM for measuring soft samples. In most cases, the cantilever of choice for this mode is the one having high spring constant of 20-100 N/m so that it does not stick to the sample surface at small amplitudes. The tips mainly used for this mode are silicon probes [108-109].



2.10.2.3 Tapping mode

In tapping mode-AFM, the cantilever oscillates close to its resonance frequency. An electronic feedback loop ensures that the oscillation amplitude remains constant, such that a constant tip-sample interaction is maintained during scanning. Forces that act between the sample and the tip will not only cause a change in the oscillation amplitude, but also change in the resonant frequency and phase of the cantilever. The amplitude is used for the feedback and the vertical adjustments of the piezo-scanner are recorded as a height image. Simultaneously, the phase changes are presented in the phase image (topography). The advantages of the tapping mode are the elimination of a large part of permanent shearing forces and the causing of less damage to the sample surface, even with stiffer probes [108-109]. Example of AFM image obtained by contact mode is shown in Figure 2.16.

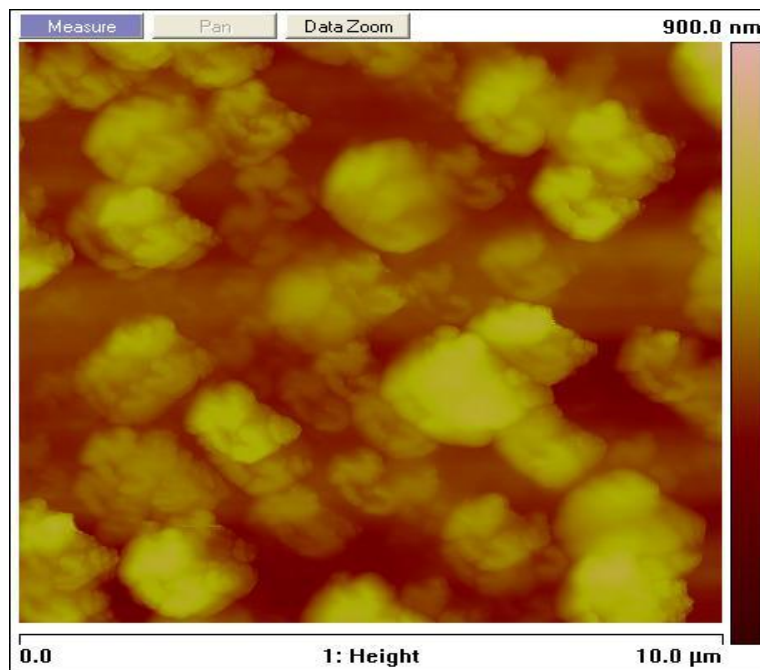
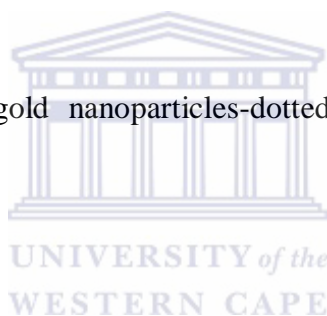


Figure 2.16: AFM image of gold nanoparticles-dotted 4-nitrophenylazo functionalized graphene (AuNp/G/PhNO₂).



2.11 Fundamental principles of scanning electron microscopy (SEM)

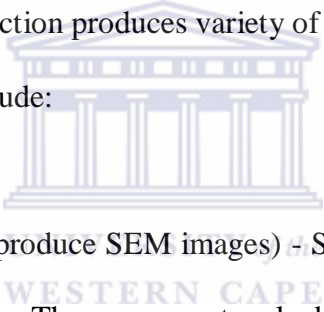
SEM is another powerful technique that is classified under scanning probe microscopy (SPM); it produces images of a sample by scanning it with a focused beam of high-energy electrons. The electrons interact with atoms in the sample surface and produce various signals that can be detected, revealing information about the sample including external morphology (texture), chemical composition, and crystalline structure and orientation of materials making up the sample. In most applications, data are collected over a selected area of the sample surface and a 2-dimensional image is generated that displays spatial variations in these properties [110-111].

2.11.1 Components of a scanning electron microscope

A scanning electron microscope is a machine comprised of an electron generating component called the gun, a column through which the electron beam travels, a series of lenses to shape the electron beam, the sample chamber at the base and a series of pumps to keep the system under vacuum [111-112].

2.11.2 Basic operation principle of SEM

The scanning electron microscope (SEM) enables the investigation of specimens with a resolution down to the nanometre scale. Accelerated electrons from the gun carry significant amounts of kinetic energy and it is focus on a solid sample surface through the column and lenses. The electron-sample interaction produces variety of signal when the incident electrons are decelerated. These signals include:

- 
- ❖ Secondary electrons (that produce SEM images) - Secondary electrons are commonly used for imaging samples: They are most valuable for showing morphology and topography on samples.
 - ❖ Backscattered electrons (BSE) - are also used for imaging samples. They are most valuable for illustrating contrasts in composition in multiphase samples (i.e. for rapid phase discrimination)
 - ❖ Diffracted backscattered electrons - are used to determine crystal structures and orientations of minerals
 - ❖ Photons – these are characteristic X-ray that are used for elemental analysis and continuum X-rays
 - ❖ Visible light – Cathodeluminescenc CL and heat

X-ray is produced by inelastic collisions of the incident electrons with electrons in discrete orbitals (shells) of atoms in the sample. As the excited electrons return to lower energy states, they yield X-rays that are of a fixed wavelength (that is related to the difference in energy levels of electrons in different shells characteristic of a given element). SEM analysis is considered to be "non-destructive"; that is, X-rays generated by electron interactions do not lead to volume loss of the sample, so it is possible to analyze the same materials repeatedly. Figure 2.17 shows a schematic representation of a scanning electron microscope [108, 110-112].



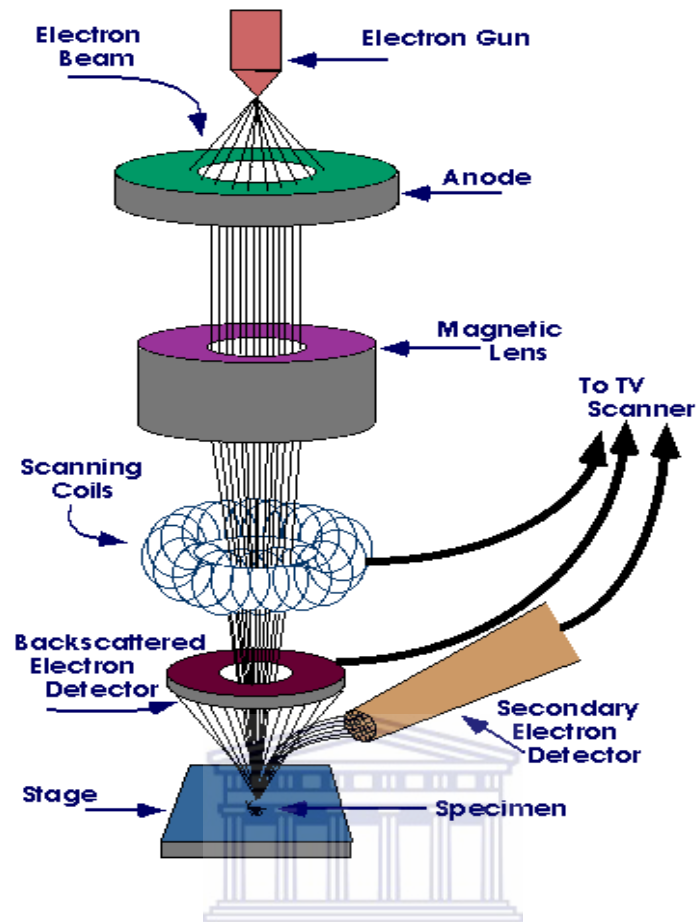


Figure 2.17: Schematic representation of a scanning electron microscope.

WESTERN CAPE

2.12 Fundamental principles of transmission electron microscopy (TEM)

Transmission electron microscopy (TEM) is a scanning probe microscopy (SPM) technique in which a beam of electrons having energy of the order of hundreds of KeV is transmitted through an ultra-thin specimen, interacting with the specimen as it passes through to provide morphologic, topographic, compositional and crystallographic information of the sample. An image is formed from the interaction of the electrons transmitted through the specimen; the image is magnified and focused onto an imaging device or detected by a sensor such as a CCD camera (see Figure 2.18 for illustration) [113].

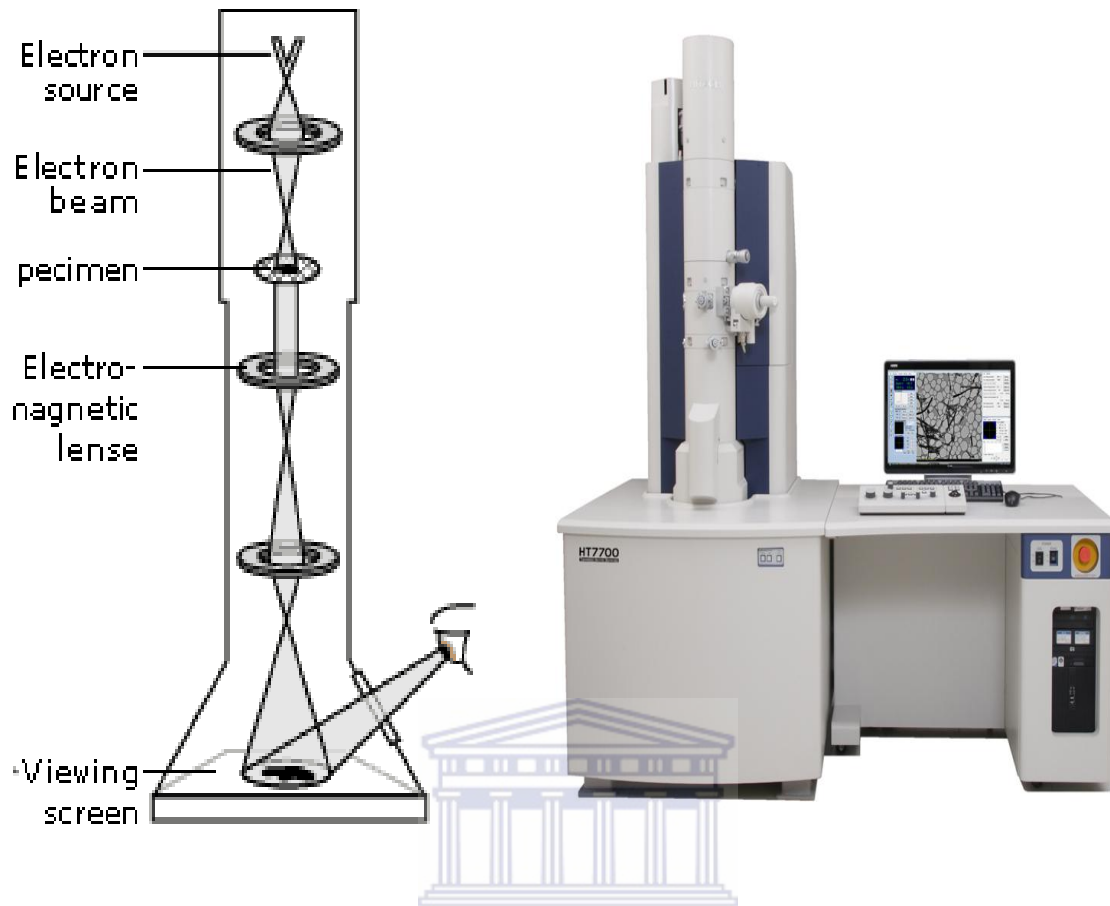


Figure 2.18: A representation of TEM operating system and a TE microscope.

WESTERN CAPE

The images allow researchers to view samples on a molecular level in the order of a few angstroms (10^{-10} m), making it possible to analyze structure and texture at a significantly high resolution (see example in Figure 2.19). High-resolution transmission electron microscopy (HRTEM) is an imaging mode of the transmission electron microscope (TEM) that allows for direct imaging of the atomic structure of the sample rather than just the morphology [98, 114]. The transmission electron microscope (TEM) operates almost on the same basic principles as SEM as both uses electrons. However they vary and their difference are shown in Table 2.4.

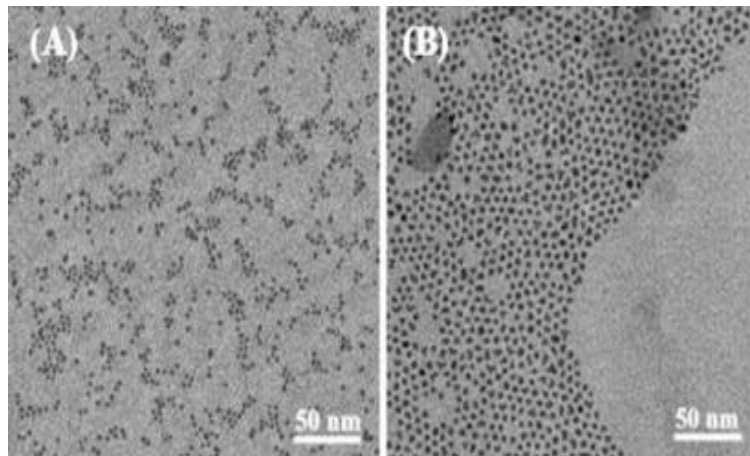


Figure 2.19: The typical TEM image of (A) silver nanoparticles, (B) gold nanoparticles.

Table 2.4: Evaluation between TEM and SEM.

TEM	SEM
Based on transmitted electrons	Based on scattered electrons
Provides the details about internal composition: morphology, crystallization, stress or even magnetic domains	Focuses on the sample's surface reactivity and composition.
Sample in TEM has to be cut thinner	No such need with SEM sample
With TEM only small amount of sample can be analysed at a time	SEM allows for large amount of sample to be analysed at a time
Used for imaging of dislocations, tiny precipitates, grain boundaries and other defect structures in solids	Used for surfaces, powders, polished & etched microstructures, IC chips, chemical segregation
Pictures are shown on fluorescent screens	Picture is shown on monitor.
Provides a 2-dimensional picture	Provides a 3-dimensional image

2.13 Fundamental principles of Energy Dispersive X-ray Spectroscopy (EDX)

Energy Dispersive X-ray Spectroscopy (EDX) is a qualitative and quantitative X-ray micro analytical technique that can provide information on the chemical composition of a sample. An electron beam is focussed on the sample in either a scanning electron microscope (SEM) or a transmission electron microscope (TEM). The electrons from the primary beam penetrate the sample and interact with the compositional atoms. Two types of X-rays result from these interactions: Bremsstrahlung X-rays, which means ‘braking radiation’ also referred to as continuum or background X-rays and characteristic X-rays [115-118] (see Figure 2.20 for illustration).

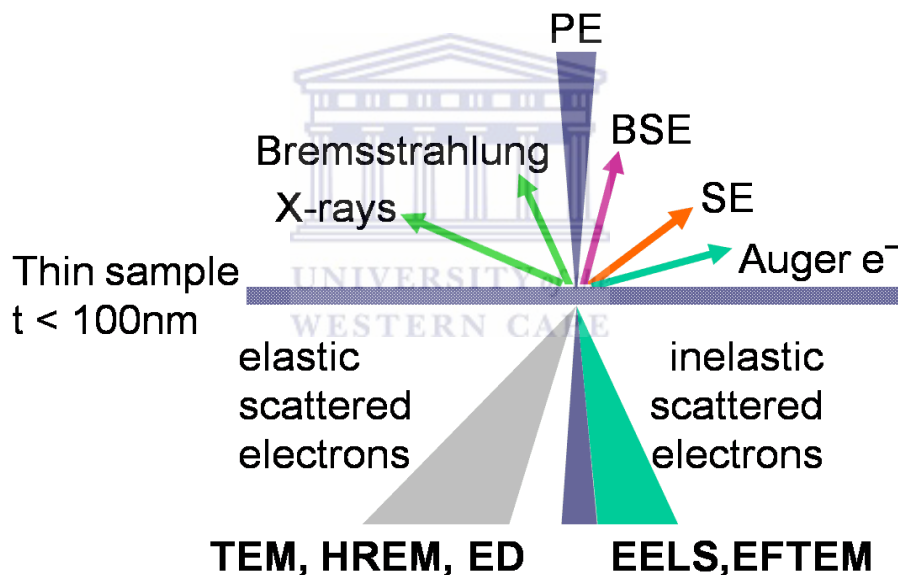


Figure 2.20: Illustration of incident electron beam on a thin sample and X-rays produced.

The X-rays are detected by an Energy Dispersive detector which displays the signal as a spectrum, or histogram, of intensity as shown in Figure 2.21.

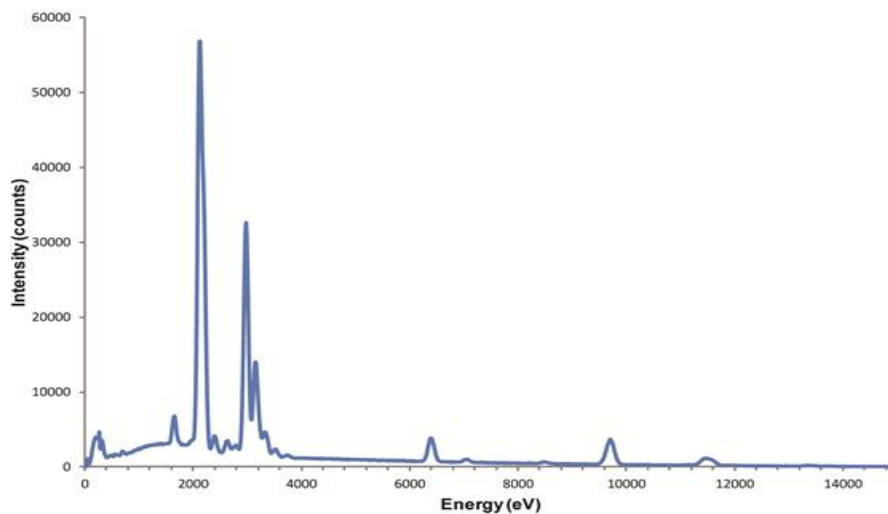


Figure 2.21: A typical EDX spectrum.

Energy dispersive X-ray spectroscopy (EDX) coupled with a transmission electron microscope with high resolution is one of the most revealing analytical methods for analysing the composition of nanomaterials. It uses the X-ray spectrum emitted by a solid sample bombarded with a focused beam of electrons to obtain a localized chemical analysis [117, 119].

- ❖ Qualitative analysis involves the identification of the lines in the spectrum and is fairly straightforward owing to the simplicity of X-ray spectra.
- ❖ Quantitative analysis (determination of the concentrations of the elements present) entails measuring line intensities for each element in the sample and for the same elements in calibration standards of known composition.

The underlying principles for generation of X-rays and detection by EDX are the same for SEM and TEM [115]. However, due to the differences in construction of the two types of

microscope, and the different accelerating voltages used in their operation, there are some differences in how EDX detectors perform on the two platforms [116, 119]. The spatial resolution of EDX analysis in the SEM depends on the size of the interaction volume, which in turn is controlled by the accelerating voltage and the mean atomic number of the sample, Z [118].

For EDX in the SEM, spatial resolution and depth resolution is on the order of a few microns. In the TEM, the sample is a thin foil and there is less spreading of the electron beam at higher accelerating voltages, so the spatial resolution is better at higher kV. The spatial resolution of EDX analysis in the TEM is on the order of nanometres while the depth resolution is governed by the thickness of the sample [117, 119].

2.14 Fundamental principles of cyclic voltammetry (CV)

Cyclic voltammetry is a very versatile electrochemical technique that is classified under sweep techniques and majorly applied in probing the mechanics of redox and transport properties of a system in solution. It is sensitive to the mechanism of deposition and therefore provides information on structural transitions, as well as interactions between the surface and the ad layer. This electroanalytical technique is the most-important and most-widespread applied electrochemical technique and is ideally suited for a quick search of redox couples present in a system; once located, a couple may be characterized by more careful analysis of the cyclic voltammogram

2.14.1 Instrumentation for cyclic voltammetry (CV) experiments

A three-electrode set-up is needed to perform cyclic voltammetry (CV) experiments: a working electrode (WE), a reference electrode (RE), a counter electrode (CE), a potentiostat

and a computer for recording and displaying results. This is accomplished by the continuous potential scan of the WE relative to some reference electrode while the resulting current flowing through a counter (or auxiliary) electrode is monitored in a quiescent solution by the potentiostat. The potentiostat is a controlling electronic, designed such that the potential between the reference and the working electrodes can be adjusted but the big impedance between these two components effectively forces any resulting current to flow through the auxiliary electrode [120-122]. See Figure 2.22 and 2.23 for illustration.

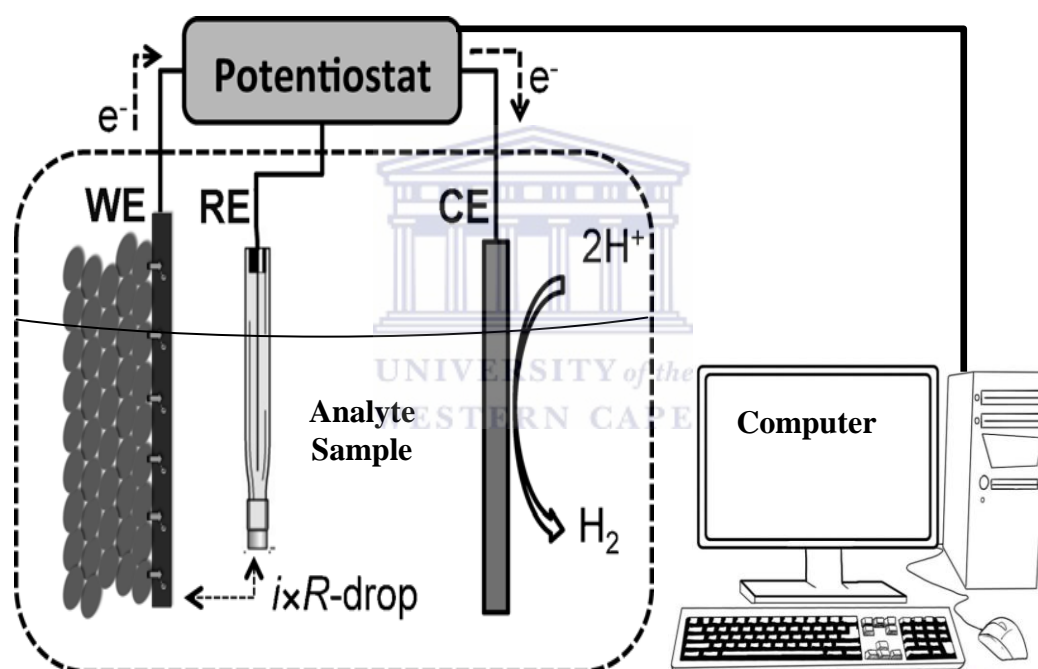


Figure 2.22: A representation of potentiostatic three-electrode system.

Voltage drop exists between the reference electrode and the working electrode and this is determined by iR as illustrated in Figure 2.22, where R is an uncompensated resistance due to the electrolyte between the WE and the RE. This resistance causes a drop in potential in the solution during current flow owing to Ohm's law [100]. This drop increases with solution

resistivity and with the distance between the WE and the reference point [99, 123]. Hence, it is advisable to place the RE outside the path of ion migration between the WE and the CE. When this is not possible because of the setup configuration, one should try to place the RE as close as possible to the WE to avoid large potential drops between the WE and the RE, which are responsible for incorrect potential measurement or control. The effect of uncompensated resistance can be calculated or measured separately for a given setup; thus, corrections can be made to enable data analysis, although at the price of larger experimental errors [108, 124].

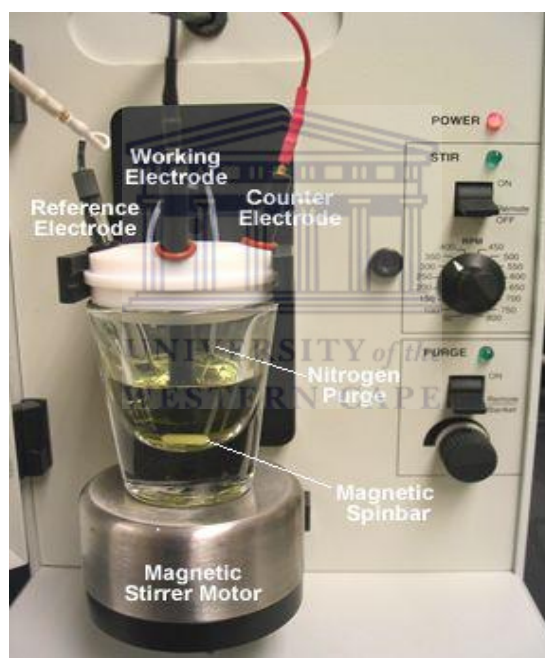


Figure 2.23: A pictorial representation of an electrochemical cell.

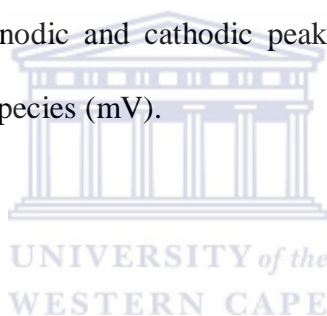
2.14.2 Definition of electrochemical terminology

To understand the working principles of cyclic voltammetry properly, I will first define some commonly used electrochemical terminologies [99-100, 108, 121, 123-124].

- ❖ **Electrode:** An electron conductor usually made of a solid material like graphite or metal.
- ❖ **Anode:** The electrode where an oxidation takes place.
- ❖ **Cathode:** The electrode where a reduction takes place.
- ❖ **Potentiostat:** An electronic amplifier that controls the potential drop between an electrode (the WE) and the electrolyte solution; it usually constitutes a RE as a sensing component and a CE for balancing the current flow. In other words, it is a device used to keep a working electrode (WE) at desired potential with respect to a reference electrode (RE).
- ❖ **Reference Electrode (RE):** A non-polarisable (stable) electrode with a fixed potential that sets or measures the potential of the WE. It establishes the electrical potential against which other potentials may be measured.
- ❖ **Working Electrode (WE):** An electrode at which a given electrochemical reaction of interest is examined; its potential is controlled versus the RE in a three-electrode system.
- ❖ **Counter Electrode (CE):** Also called auxiliary electrode allows the reaction at the WE to take place by accompanying it with a respective reverse reaction. In other words it functions as a cathode whenever the working electrode is operating as an anode and vice versa. The counter electrode often has a surface area much larger than that of the working electrode to ensure that the half-reaction occurring at the counter electrode can occur fast enough so as not to limit the process at the working electrode.
- ❖ **Three-Electrode Arrangement:** An experimental set-up used for electroanalytical measurements consisting of WE, RE, CE and usually using a potentiostat as the measuring and controlling device.

- ❖ **Electrolyte Solution:** An ionic conductor; here, an aqueous solution containing a dissolved inorganic salt.
- ❖ **Electro-catalysis:** An effect that increases the reaction rate of an electrochemical reaction at a given potential by decreasing the over potential needed to drive the reaction to a certain current.
- ❖ **Standard Potential (E^0):** Represents the equilibrium potential of an electrode under standard conditions, i.e., in solutions with the relative activities of all components being unity and under a pressure of 1 atm and pH 7.0 (mV).
- ❖ **Formal Potential (E^0):** Replaces the standard potential when the activities of the species involved and of the side-reactions are unknown or too complex. It is arithmetic mean of the anodic and cathodic peak potentials of an electrochemical reaction involving redox species (mV).

$$E^0 = \frac{E_{pa} + E_{pc}}{2}$$



(5)

- ❖ **Start Potential:** The set potential of the WE at the start of a scan in a voltammetric experiment.
- ❖ **Peak Potential (E_p):** The potential of the working electrode at which the peak current in a voltammetric measurement is obtained (mV).
- ❖ **Scan Rate (v):** The speed of potential change per unit of time in a voltammetric experiment (mV/s).
- ❖ **Current (I):** The flow of electric charge (A).
- ❖ **Current Density (j):** Current divided by the electrode surface area (Am^{-2}).
- ❖ **Capacitive Current (I_c):** The current related to the change in the electrode surface charge, not related to an oxidation/reduction reaction.

- ❖ **Faradaic Current (I_f):** The current generated from the oxidation (positive current) or reduction (negative current) of chemical species.
- ❖ **Peak Current (I_p):** The maximum current at the working electrode in a voltammetric measurement (A).
- ❖ **Charge (q):** Its values can be determined by the integration of current-time curves (C).

2.14.3 Principles for the generation of a cyclic voltammetric curve

Usually the potential is scanned back and forth linearly with time between two extreme values [121, 125]. When the potential of the working electrode is more positive (i.e. if scanned from a negative to a positive potential) than that of a redox couple present in the solution, the corresponding species may be oxidized (i.e. electrons going from the solution to the electrode) and produce an anodic current. The current is first observed to peak at E_{pa} (with value I_{pa}) indicating that an oxidation is taking place and then drops due to depletion of the reducing species from the diffusion layer [100, 126].

During the return scan, the processes are reversed as the working electrode potential becomes more negative (i.e. scanning from a positive to negative potential) than the reduction potential of a redox couple, electrons flows away from the electrode and reduction occurs to cause a cathodic current. By IUPAC convention, anodic currents are positive and cathodic currents negative [108, 121, 123, 125-126]. A linearly dependent potential relative to the RE is imposed on the working electrode beginning at an initial potential (E_i) to final (or reverse) potential (E_f) and then returns to the initial potential. The potential at which the change in direction occurs is also known as the switch potential. The scan rate (v) is the change of potential as function of time and can be deduced from the gradient of the curve [99, 108].

Scan rate is the same for both directions and it is always written with positive numbers. Potential and current are interrelated because they are both functions of time, therefore the current flow can be plotted as a function of the applied electrode voltage. A typical cyclic voltammogram is shown in Figure 2.24

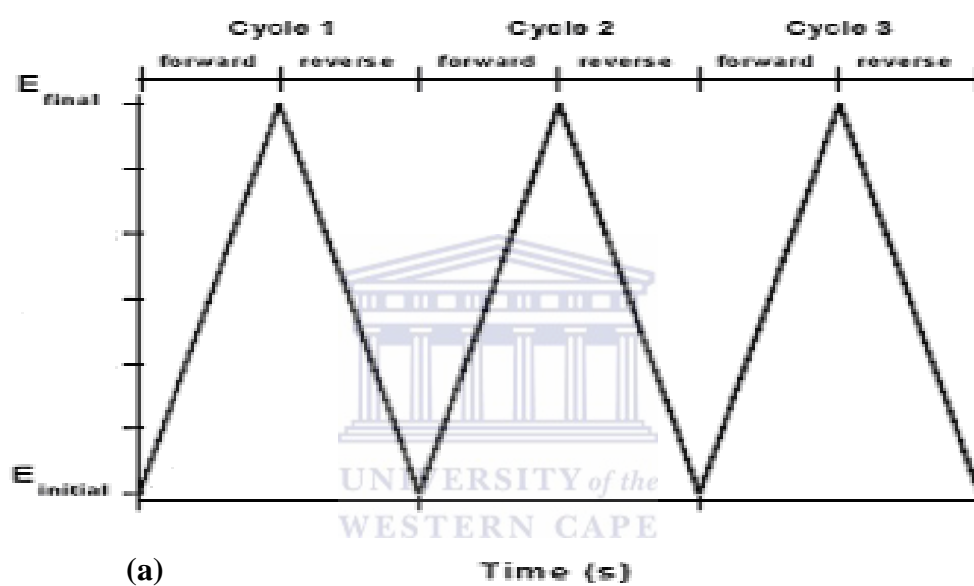


Figure 2.24: (a) A typical cyclic voltammetry potential waveform

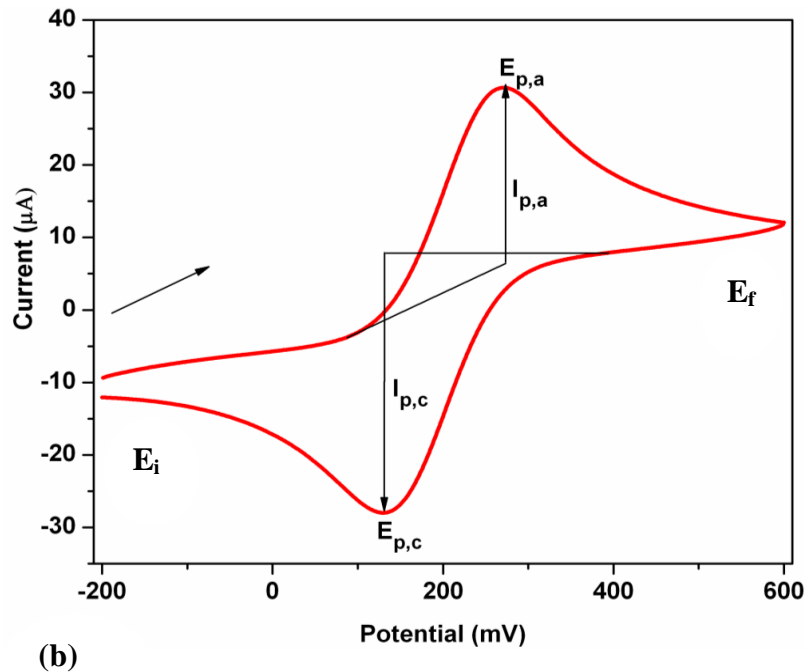
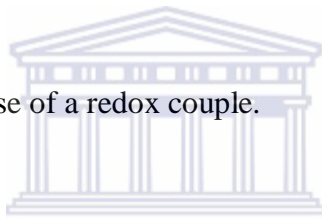


Figure 2.24: (b) Expected response of a redox couple.



The overall electrochemical rate of the many processes occurring at the working electrode surface can be determined by the magnitude of the observed faradaic current. The slowest rate determines the rate as is the case for any multi-step process. For any redox reaction induced at a working electrode, the rate determining step may be any one of the following:

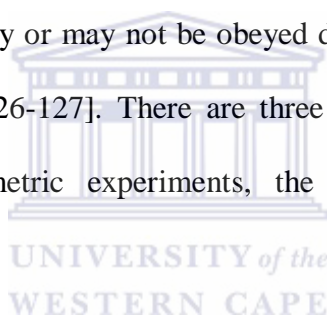
- ❖ rate of mass transport of the electroactive species in solution,
- ❖ rate of adsorption or de-sorption at the electrode surface,
- ❖ rate of the electron transfer between the electroactive species and the electrode, interfacial electron transfer.
- ❖ rate of the individual chemical reactions which are part of the overall reaction scheme.

For the oxidation reaction involving n electrons (4), the Nernst equation gives the relationship between the potential and the concentrations of the oxidized and reduced form of the redox couple at equilibrium (at 298 K) as shown in equation (6)



$$E = E^{0'} + \frac{0.059}{n} \log_{10} \frac{[\text{Ox}]_t}{[\text{Red}]} \quad (7)$$

Where E is the applied potential and $E^{0'}$ the formal potential; $[\text{OX}]$ and $[\text{Red}]$ represent surface concentrations at the electrode/solution interface, not bulk solution concentrations. Note that the Nernst equation may or may not be obeyed depending on the system or on the experimental conditions [108, 126-127]. There are three main types of processes usually encountered in cyclic voltammetric experiments, the reversible, quasi-reversible and irreversible process.



2.14.4 Analytical criteria to identify a reversible processes

For reversible charge-transfer processes (diffusion-controlled) where there is no surface interaction between the electrode and the reagents, and that the redox products are stable, at least in the time frame of the experiment:

- ❖ the ratio of the reverse and the forward current $I_{pr}/I_{pf} = 1.0$
- ❖ the corresponding peak potentials E_{pa} and E_{pc} are independent of scan rate and concentration
- ❖ the formal potential is centered between E_{pa} and E_{pc} : $E^{0'} = (E_{pa} + E_{pc})/2$

- ❖ separation between peaks is given by $\Delta E_p = E_{pa} - E_{pc} = 59/n \text{ mV}$ (for a n electron transfer reaction) at all scan rates (however, the measured value for a reversible process is generally higher due to uncompensated solution resistance and non-linear diffusion. Larger values of ΔE_p , which increase with increasing scan rate, are characteristic of slow electron transfer kinetics).

It is possible to relate the half-peak potential ($E_{p/2}$, where the current is half of the peak current) to the polarographic half-wave potential, $E_{1/2}$: $E_{p/2} = E_{1/2} \pm 29 \text{ mV}/n$ (The sign is positive for a reduction process.) For multi-electron-transfer (reversible) processes, the cyclic voltammogram consists of several distinct peaks, if the E° values for the individual steps are successively higher and are well separated [100, 128-129]. The electrochemical processes are occurring at the interface of two different phases, the electrode and the electroactive species in solution. Therefore the processes under studies are usually heterogeneous in nature. For the electron transfer to occur therefore, the molecules in solution have to approach the electrode.

In a cyclic voltammetry experiment, when the solution is kept unstirred, mass transport can occur only by diffusion due to concentration gradients created around the electrode surface. The magnitude of the observed signal will be very much a function of these diffusional properties of the system. Intuitively, the current intensity (i.e. the flow of electrons) is expected to depend on the surface area of the working electrode and the concentration of the electroactive species. Also, one can expect the voltage scanning rate to affect the concentration profile around the electrode which itself directly affects the rate of charge transport, and for this matter the diffusion coefficient appears explicitly. The expression of

the peak current (A) for the forward sweep in a reversible system at 298 K is given by the Randles–Sevcik equation [98, 100, 130]:

$$i_{pf} = (2.69 \times 10^5) n^{3/2} A D^{1/2} \nu^{1/2} C^* \quad (8)$$

Where n is the number of electron equivalent exchanged during the redox process, A (cm^2) the active area of the working electrode, D (cm^2/s) and C^* (mol/cm^3) the diffusion coefficient and the bulk concentration of the electroactive species; ν is the voltage scan rate (mV/s).

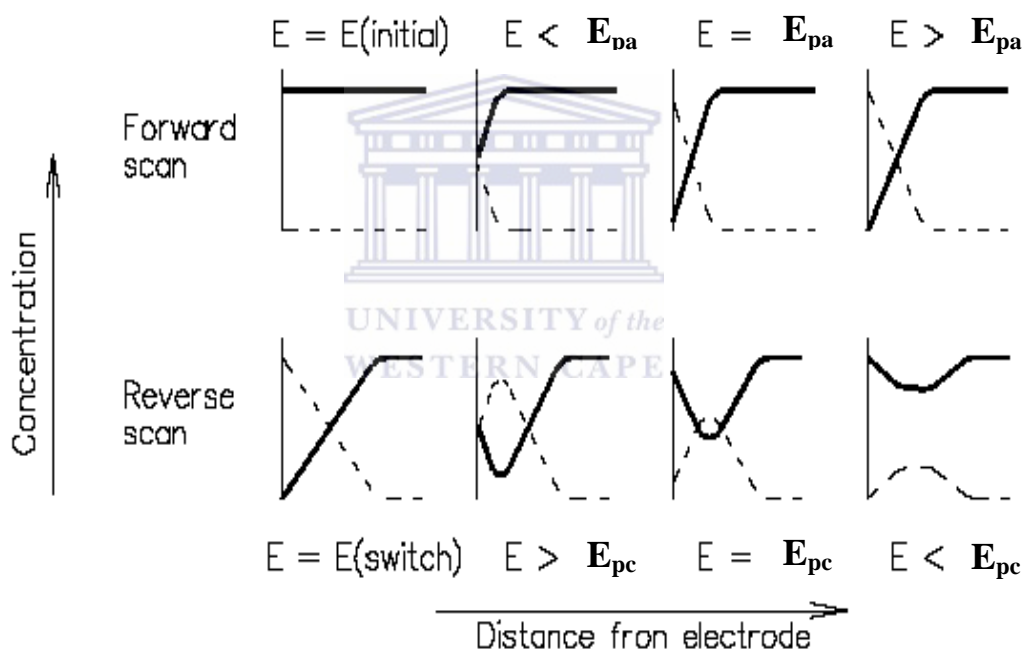


Figure 2.25: Qualitative diagrams showing concentration-distance profile.

Figure 2.25 represents concentration-distance profile at various stage of the cyclic voltammogram; the solid lines correspond to the reducing species and the dotted lines to the oxidizing species.

2.14.5 Analytical criteria to identify a irreversible processes

To distinguish between reversible (diffusion-controlled) and irreversible (charge-transfer controlled) kinetics of electrode processes, potential scan-rate is used as diagnostic tool.

- ❖ The rate of reagent transport is proportional to square root of scan-rate. Thus in one experimental set a shift in reversibility might be executed and analysis of ΔE_p vs. $v^{1/2}$ gives information on reversibility and applicability of further calculations [100].
- ❖ Irreversible processes are those with sluggish electron exchange, therefore the individual peaks are reduced in size and widely separated. Totally irreversible systems are characterized by a shift of the peak potential with the scan rate [99]:

$$E_p = E^\circ - (RT/\alpha nF) [0.78 - \ln(k^\circ/(D)^{1/2}) + \ln(\alpha n_a Fv/RT)^{1/2}] \quad (9)$$

Where α is the transfer coefficient and n is the number of electrons involved in the charge-transfer step. Thus, E_p occurs at potentials higher than E° , with the over potential related to k° (standard rate constant) and α . Independent of the value k° , such peak displacement can be compensated by an appropriate change of the scan rate. The peak potential and the half-peak potential (at 25 °C) will differ by $48/\alpha n$ mV [100]. Hence, the voltammogram becomes more drawn-out as αn decreases. The peak current, given by:

$$i_p = (2.99 \times 10^5) n(\alpha n_a)^{1/2} A C D^{1/2} v^{1/2} \quad (10)$$

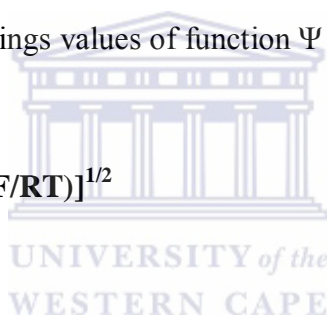
And is still proportional to the bulk concentration, but will be lower in height (depending upon the value of α). Assuming $\alpha = 0.5$, the ratio of the reversible-to-irreversible current

peaks is 1.27 (i.e. the peak current for the irreversible process is about 80% of the peak for a reversible one).

2.14.6 Analytical criteria to identify a quasi-reversible processes

For quasi-reversible systems (with $10^{-1} > k^{\circ} > 10^{-5}$ cm/s) the current is controlled by both the charge transfer and mass transport. The shape of the cyclic voltammogram is a function of the ratio $k^{\circ}/(\pi\nu nFD/RT)^{1/2}$. As the ratio increases, the process approaches the reversible case. For small values of it, the system exhibits an irreversible behavior. Overall, the voltammogram of a quasi-reversible system are more drawn out and exhibit a larger separation in peak potentials compared to a reversible system [99-100]. For quasi-reversible reaction (ΔE_p up to 200 mV) a numerical approach brings values of function Ψ (see Figure 2.26):

$$\Psi = k_s (D_{ox}/D_{red})^{a/2} / [D_{ox}\pi(nF/RT)]^{1/2} \quad (11)$$



Summarily, the following analytical condition distinguishes quasi-reversible processes:

- ❖ $|I_p|$ increases with $v^{1/2}$ but is not proportional to it
- ❖ $I_{pa} = I_{pc}$ or $I_{pa}/I_{pc} = 1$ provided $\alpha c = \alpha a = 0.5$
- ❖ ΔE_p is greater than $59/n$ mV and increases with increasing v
- ❖ E_{pc} shifts negatively with increasing v .

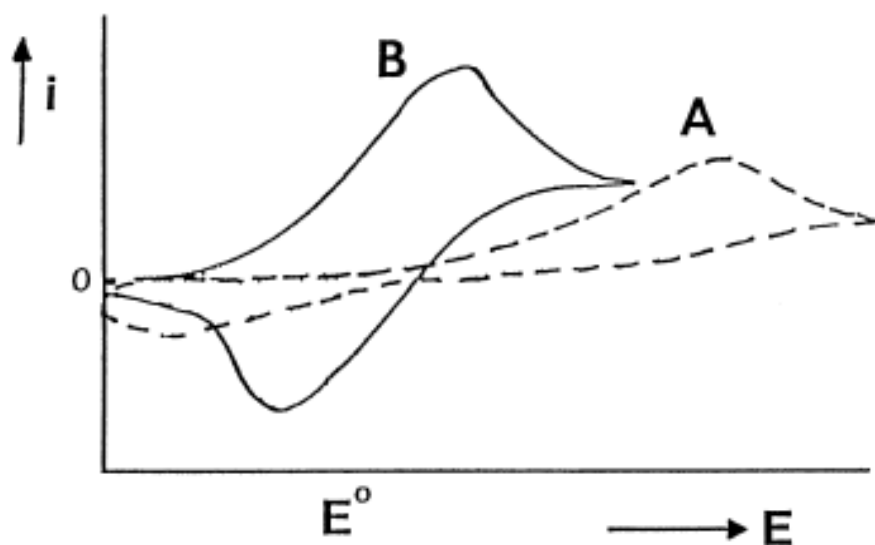


Figure 2.26: Illustrative cyclic voltammogram for an irreversible electrochemistry process (Curve A) and for a quasi-reversible process (Curve B)

2.15 Fundamental principles of square wave voltammetry (SWV)

Square wave voltammetry is an electroanalytical technique that is classified under pulse technique. It is a derivative of linear sweep voltammetry. In linear sweep voltammetry the current at a working electrode is measured while the potential between the working electrode and a reference electrode is swept linearly in time [128, 131]. But in this technique, a potential waveform, consisting of a square wave of constant amplitude is applied to the working electrode, oxidation or reduction of species is registered as a peak in the current signal at the potential at which the species begins to be oxidized or reduced, see Figure 2.27 (a).

The current is measured at the end of each half cycle, right before the next, so that the contribution to the current signal from the capacitive charging current is minimized, and the current measured on the reverse half-cycle (I_r) is subtracted from the current measured on the

forward half-cycle (I_f). This difference current ($I_f - I_r$) is displayed as a function of the applied potential. A square wave voltammogram therefore is just a graph of the difference ($\Delta\Phi$) between these two currents as a function of the applied potential ($E-E_0$), see Figure 2.27 (b). A typical potential wave form for square wave voltammogram is shown in Figure 2.27 (a) [100, 132].

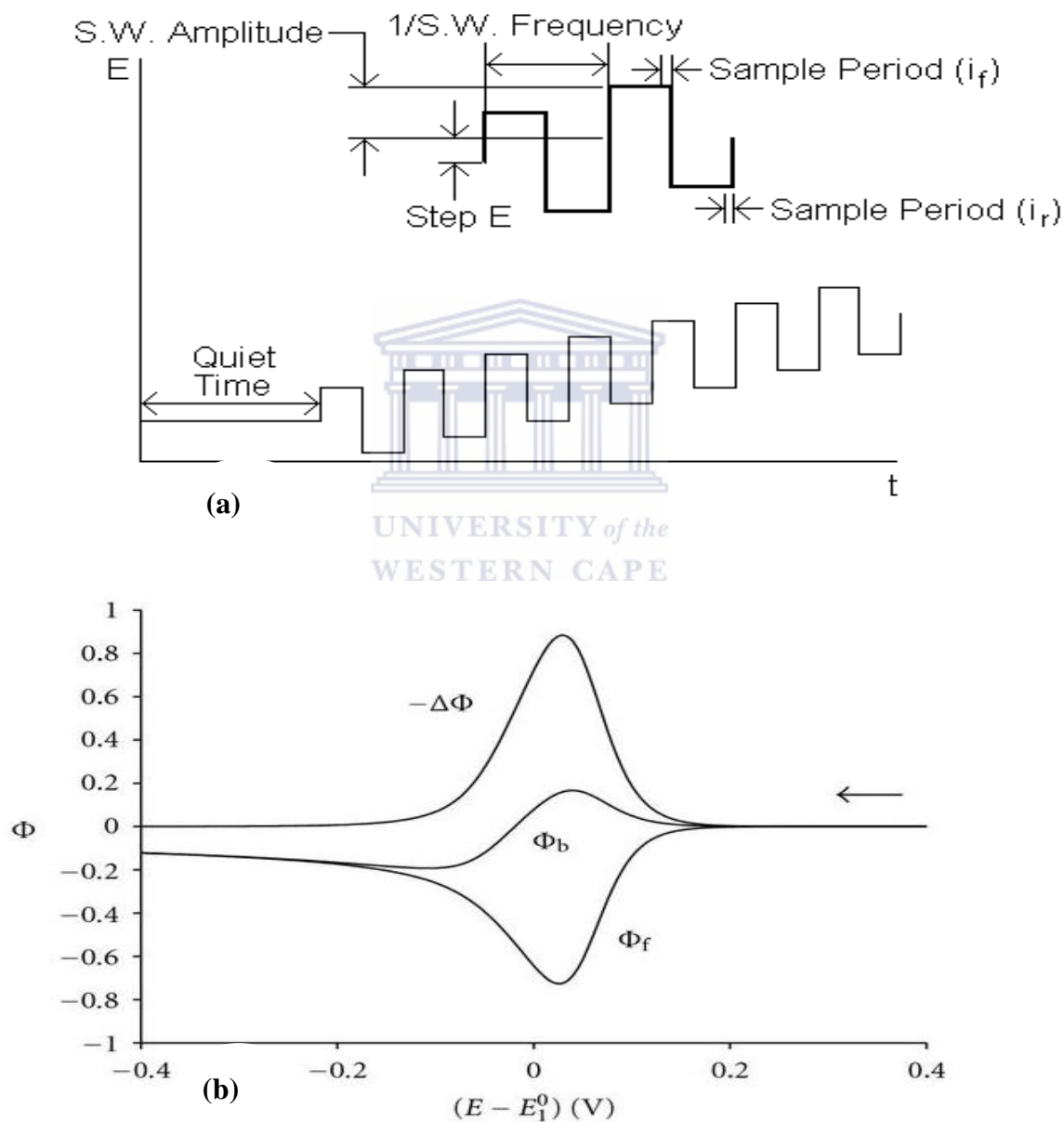


Figure 2.27: (a) Excitation signal for square wave voltammetry, (b) Theoretical square-wave voltammogram.

2.16 Fundamental principles of electrochemical impedance spectroscopy

Electrical impedance is the measure of the opposition to the passage of a current when a voltage is applied in a circuit. It is the frequency domain ratio of the voltage to the current. Quantitatively, it is the complex ratio of the voltage to the current in an alternating circuit (AC). Impedance is measured as a function of the frequency of the ac source [133]. The technique where the cell or electrode impedance is plotted vs. frequency is called electrochemical impedance spectroscopy (EIS). EIS studies the system response to the application of a periodic or perturbative small amplitude ac signal and these measurements are carried out in a range of ac frequencies [126, 134-137].

The response of the system as a function of the perturbation frequency can reveal internal dynamics [137]. EIS is capable of high precision and is frequently used for the evaluation of heterogeneous charge-transfer parameters and for the studies of double-layer structure. Impedance in ac circuits possesses both magnitude and phase unlike resistance which has only magnitude. There is no distinction between impedance and resistance when a circuit is driven by a direct current (DC), it can be thought of as impedance with zero phase angles [133, 138].

2.16.1 Operating principle of electrochemical impedance spectroscopy EIS.

Basically, as mentioned in the last section, EIS is performed by applying a small, sinusoidal voltage or current signal to an electrochemical cell, and measuring the system's response to the applied current or voltage with respect to amplitude and phase repeatedly for a range of different frequencies [100, 137, 139]. This is done so that the cell's response is pseudo-linear.

In a linear (or pseudo-linear) system, the current response to a sinusoidal potential will be a sinusoid at the same frequency but shifted in phase [99] (see Figure 2.28)

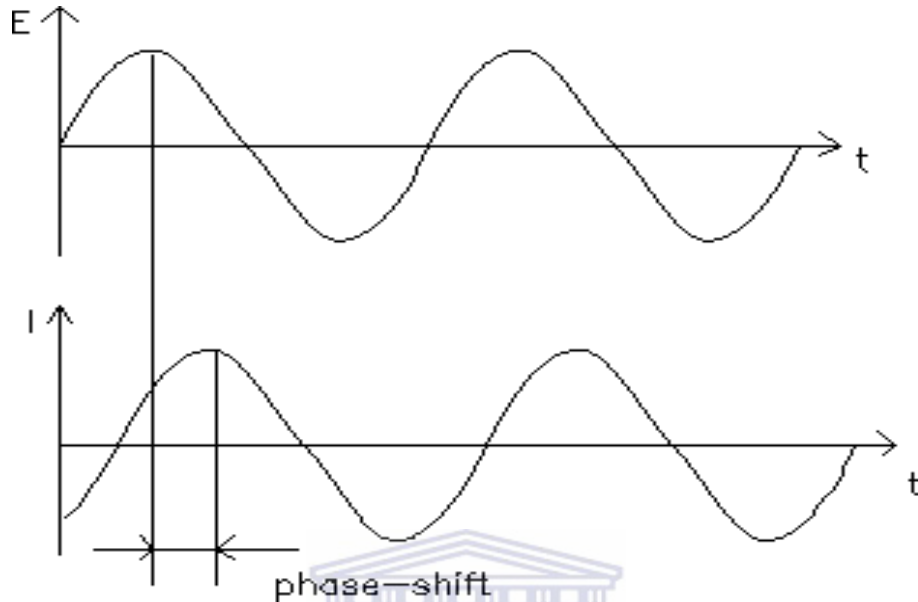


Figure 2.28: Sinusoidal Current Response in a Linear System.

The excitation signal when expressed as a function of time has the form,

$$E_t = E_0 \sin(\omega t) \quad (12)$$

Where, E_t is the potential at time t , E_0 is the amplitude of the signal and ω is the radial frequency. The relationship between radial frequency ω (expressed in radians/second) and frequency f (expressed in hertz) is [135]:

$$\omega = 2\pi f \quad (13)$$

In a linear system, the response signal, I_t , is shifted in phase (Φ) and has different amplitude than I_0 as expressed in equation (13) [134, 140-142]:

$$I_t = I_0 \sin(\omega t + \phi) \quad (14)$$

An expression analogous to Ohm's Law allows us to calculate the total impedance of the system in terms of a magnitude, Z_0 , and a phase shift, Φ as:

$$Z = \frac{E_t}{I_t} = \frac{E_0 \sin(\omega t)}{I_0 \sin(\omega t + \phi)} = Z_0 \frac{\sin(\omega t)}{\sin(\omega t + \phi)} \quad (15)$$

And in terms of frequency with real and imaginary components as:

$$Z(j\omega) = \frac{E(j\omega)}{I(j\omega)} = Z'(\omega) + jZ''(\omega) \quad (16)$$

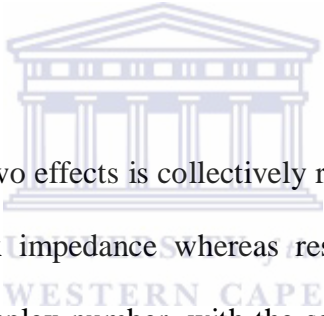
Where $Z'(\omega)$ and $jZ''(\omega)$ are real and imaginary impedance respectively, $j = \sqrt{-1}$ and is an imaginary number.

For a sinusoidal current (AC) or voltage input, the polar form of the complex impedance relates the amplitude and phase of the voltage and current [98, 141]. In particular,

- ❖ The magnitude of the complex impedance is the ratio of the voltage amplitude to the current amplitude.
- ❖ The phase of the complex impedance is the phase shift by which the current is ahead of the voltage.

Frequency-domain analysis requires that the system under investigation is linear or at least can be linearized with respect to signal amplitudes in its working point. The concept of impedance in ac circuits is necessary because there are two additional mechanisms impeding the flow of current besides the normal resistance of DC circuits. The mechanisms include [134, 143]:

- ❖ **Inductance**, which is the generation of voltages in conductors self-induced by the magnetic fields of currents
- ❖ **Capacitance**, which is the electrostatic storage of charge induced by voltages between conductors



The impedance caused by these two effects is collectively referred to as **reactance** and forms the **imaginary part** of complex impedance whereas resistance forms the **real part**. In general, impedance will be a complex number, with the same units as resistance, for which the SI unit is the Ohm (Ω). The reciprocal of impedance is **admittance** which is the current-to-voltage ratio, and it conventionally carries units of Siemens [141, 143].

2.16.2 Data presentation

To simplify the calculations of impedances, the result obtained from the periodic perturbation of an electrical circuit may be represented using complex notation and various forms of graph [100, 139]. The most common is the Nyquist and Bode plots. The expression for total impedance $Z(\omega)$ is composed of a real and an imaginary part (see Figure 2.29).

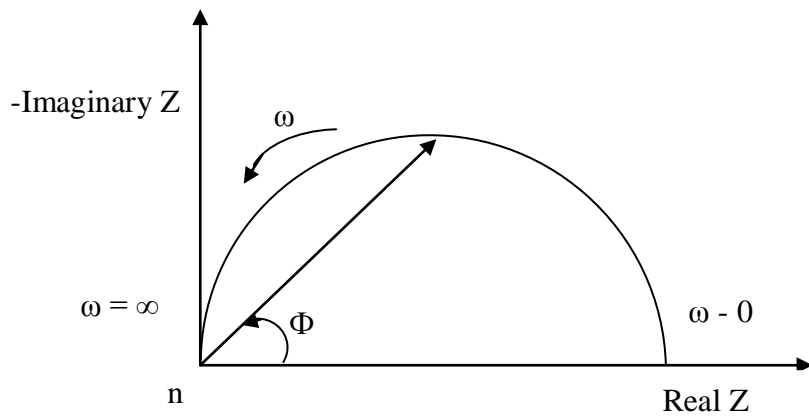
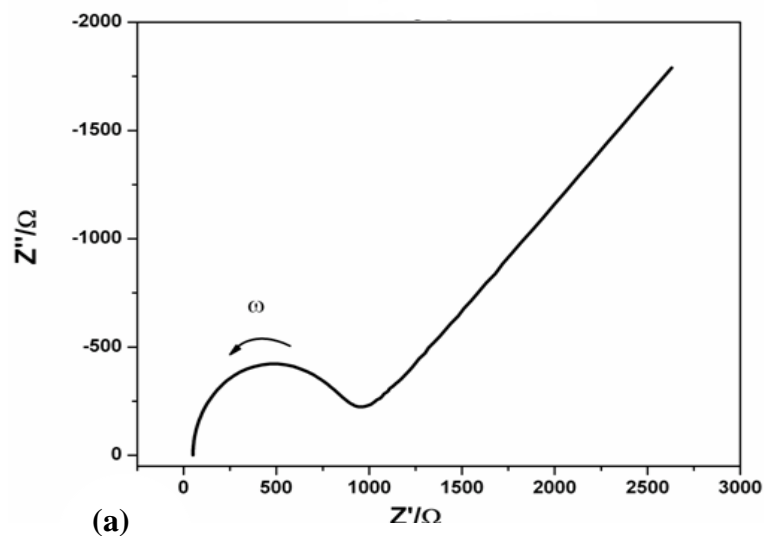


Figure 2.29: Typical impedance diagram.

2.16.2.1 Nyquist plot

If the real part (Z_r) is plotted on the X-axis and the imaginary part (Z_i) is plotted on the Y-axis of a chart) over a wide frequency range normally 100 kHz to 0 Hz, we get a "Nyquist Plot" (see Figure 2.30). Interpretation of the Nyquist plots is most often used in the electrochemical literature because they allow for an easy prediction of the circuit elements. Nyquist plots allow for an easy relation to the electrical model [144-145].



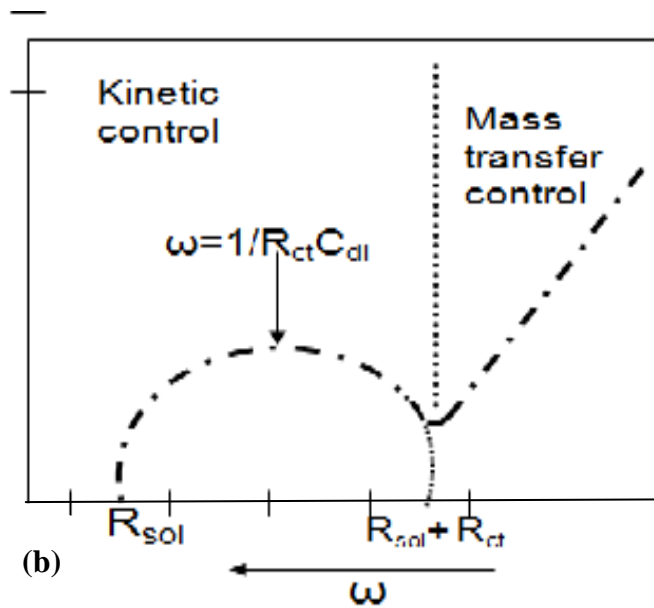


Figure 2.30: (a) a typical Nyquist plot (b) Nyquist plot showing some kinetic parameters.

Notice that in this plot, the Y-axis is negative and that each point on the Nyquist Plot is the impedance at one frequency. Figure 2.30 (a) has been annotated to show that low frequency data are on the right side of the plot and higher frequencies are on the left. A major shortcoming of Nyquist plot is the when you look at any data point on the plot; you cannot tell what frequency was used to record that point [145-146].

2.16.2.2 Bode plot

In the Bode plot, the impedance is plotted with log frequency on the X-axis and both the absolute values of the impedance ($|Z| = Z_0$) and the phase-shift on the Y-axis. Bode plots contain all the necessary information. That is why Bode plots are mainly used in the circuit analysis. The Bode magnitude plots may be easily predicted from the circuit impedance. Unlike the Nyquist Plot, the Bode Plot does show frequency information (see Figure 2.31) [99, 138].

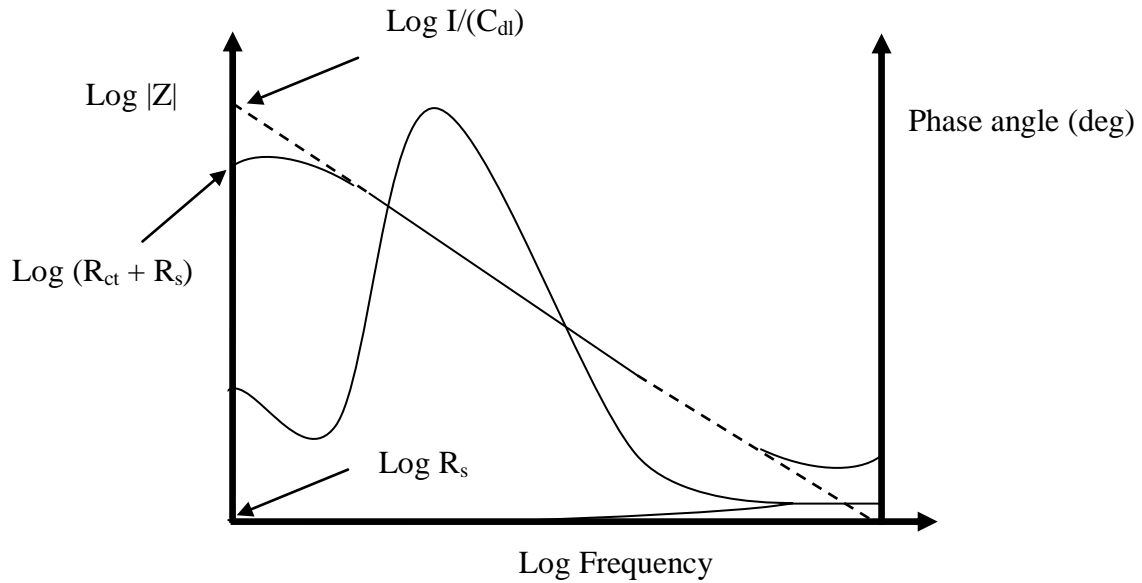


Figure 2.31: Typical Bode plot.

2.16.3 Electric circuit components

An electric circuit is formed by individual electronic components through which electric current (I) can flow continuously [135, 139, 147]. The electronic components include ideal resistors (R), capacitors (C), and inductors (L). Voltage (v) is the measure of potential energy present in a circuit capable to move electrons from one point to another one (see Table 2.4). The opposition to a motion of free electrons in a circuit is called resistance (R) and similar to voltage, it is relative to two points. Capacitors and inductors are associated with space-charge polarization regions, such as the electrochemical double layer, and adsorption/desorption processes at an electrode, respectively. By Ohm's law voltage is the product of resistance and current [141];

$$\text{Voltage (V)} = \text{current (I)} \times \text{resistance (R)} \quad (17)$$

Table 2.5: Electric circuit components

Component	Current Vs.Voltage	Impedance
Resistor (R)	$E = IR$	$Z = R$
Capacitor (C)	$I = C \, dE/dt$	$Z = 1/j\omega C$
Inductor (L)	$E = L \, dI/dt$	$Z = j\omega L$

2.16.4 Resistor

The resistor is independent of frequency and has no imaginary component. With only a real impedance component, the current through a resistor stays in phase with the voltage across the resistor [99].



2.16.5 Inductor

The impedance of an inductor increases as frequency increases. Inductors have only an imaginary impedance component. As a result, the current through an inductor is phase-shifted -90 degrees with respect to the voltage [99].

2.16.6 Capacitor

A capacitor's impedance decreases as the frequency is raised. Capacitors also have only an imaginary impedance component. The current through a capacitor is phase shifted 90 degrees with respect to the voltage. The impedance versus frequency behaviour of a capacitor is opposite to that of an inductor [99].

2.16.7 Serial and parallel combinations of circuit elements

Only a few electrochemical cells can be modelled using a single equivalent circuit element. EIS models usually consist of a number of elements in a network in which the circuit elements can be arranged in series and parallel connections [135]. Fortunately, there are simple formulas that describe the impedance of circuit elements in both parallel and series combination.

For linear impedance elements in parallel as shown below (Figure 2.32), you calculate the equivalent impedance from [143]:

$$\frac{1}{Z_{eq}} = \frac{1}{Z_1} + \frac{1}{Z_2} + \frac{1}{Z_3} \quad (18)$$

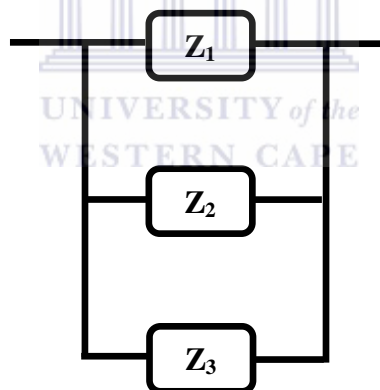


Figure 2.32: Impedances in Parallel.

For linear impedance elements in series as shown below Figure 2.33, you calculate the equivalent impedance from:

$$Z_{eq} = Z_1 + Z_2 + Z_3 \quad (19)$$

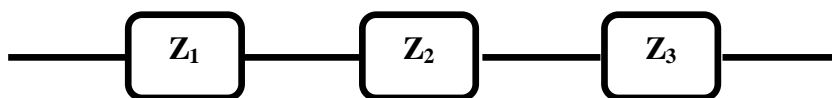


Figure 2.33: Impedances in Series.

A common circuit used for impedance data modelling is Randle equivalent circuit as shown in Figure 2.34.

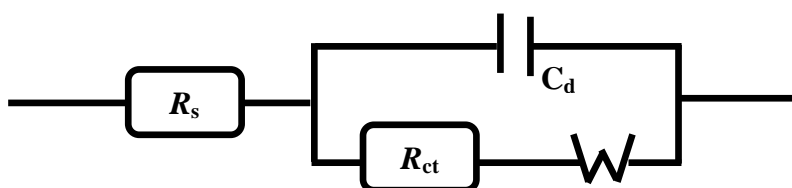


Figure 2.34: Randles equivalent circuit in series with the solution resistance.

2.16.8 Equivalent electrical circuit modelling

In a typical equivalent circuit, resistors represent conductive pathways for ion and electron transfer. They therefore represent the bulk resistance of a material to charge transport such as the resistance of the electrolyte to ion transport or the resistance of a conductor to electron transport. Resistors are also used to represent the resistance to the charge-transfer process at the electrode surface. Other sources that contribute to the resistance of a cell are solution resistance (R_s) and charge transfer resistance (R_{ct}) [99, 136, 145].

EIS data are commonly analyzed by fitting to an equivalent electrical circuit model. An equivalent circuit consists of a number of circuit elements in a network in which the elements can be arranged in series and parallel connections, and at any frequency, the circuit is able to

give the same electrical response as to an electrical ac-stimulus as the electrochemical system under examination [99, 136, 145].

Equivalent circuit modelling of EIS data is used to extract physically meaningful properties of the electrochemical system by modelling the impedance data in terms of an electrical circuit composed of ideal resistors (R), capacitors (C), and inductors (L). Examples of common equivalent circuit models are shown in Table 2.6. Because we are dealing with real systems that do not behave ideally with processes that occur in distributed time and space, we often use specialized circuit elements. These include the generalized constant phase element (CPE) and Warburg element (Z_w).

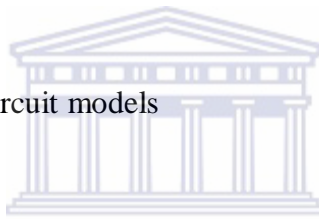


Table 2.6: Common equivalent circuit models

Equivalent Element	Admittance	Impedance
R	$1/R$	R
C	$J\omega C$	$1/J\omega C$
L	$1/J\omega L$	$J\omega L$
W (infinite Warburg)	$Y_0\sqrt{(j\omega)}$	$1/Y_0\sqrt{(j\omega)}$
O (finite Warburg)	$Y_0\sqrt{(j\omega)}\text{Coth}(B\sqrt{(j\omega)})$	$\text{Tanh}(B\sqrt{(j\omega)})/Y_0\sqrt{(j\omega)}$
Q (CPE)	$Y_0(j\omega)^\alpha$	$1/Y_0(j\omega)^\alpha$

2.16.8.1 Warburg element (Z_w)

The Warburg element is used to represent the diffusion or mass transport impedances of the cell. It is the resistance associated with the diffusion of ions across the electrode/electrolyte interface [134-135, 148]. Warburg depends on the frequency of the potential perturbation. At high frequencies, the Warburg impedance is small since diffusing reactants don't have to move very far. At low frequencies, the reactants have to diffuse farther, increasing the Warburg-impedance. On a Nyquist Plot the Warburg impedance appears as a diagonal line with a slope of 45° . On a Bode Plot, the Warburg impedance exhibits a phase shift of 45° . Infinite Warburg impedance is represented by the equation [134, 143]:

$$Z_w = \sigma(\omega)^{-1/2} (1 - j) \quad (20)$$

With σ , the Warburg coefficient mathematically defined as,

$$\sigma = \frac{RT}{n^2 F^2 A \sqrt{2}} \left(\frac{1}{C_o^* \sqrt{D_o}} + \frac{1}{C_r^* \sqrt{D_r}} \right) \quad (21)$$

Where, ω = radial frequency, D_o = diffusion coefficient of the oxidant, D_r = diffusion coefficient of the reductant, A = surface area of the electrode and n = number of electrons involved.

This form of the Warburg impedance is only valid if the diffusion layer has an infinite thickness. If the diffusion layer is bounded (as in thin-layer cell or coated samples), the impedance at lower frequencies no longer obeys equation (21) [134, 143]. Instead, we get the form:

$$Z_o = \sigma \omega^{-1/2} (1 - j) \tanh\left(\delta \left(\frac{j\omega}{D}\right)^{1/2}\right) \quad (22)$$

Where, δ = Nernst diffusion layer thickness, D = some average value of the diffusion coefficient of the diffusing species

This equation is called the finite Warburg. For high frequencies where $\omega \rightarrow \infty$, or for an infinite thickness of the diffusion layer where $\delta \rightarrow \infty$, $\tanh(\delta(j\omega/D)^{1/2})$.

2.16.8.2 Constant phase element (CPE)

The constant phase element is an equivalent circuit component that models the behaviour of a double layer which is an imperfect capacitor. Capacitors in EIS experiments often do not behave ideally. Instead, they act like a constant phase element as defined in equation (23) [134, 142].

$$Z_{CPE} = \frac{1}{(j\omega)^\alpha Y_0} \quad (23)$$

Where $Y_o = C$ = the capacitance, α = exponent equalling 1 for a capacitor. For a constant phase element, the exponent α is less than one. The "double layer capacitor" on real cells often behaves like a CPE, not a capacitor.

2.16.8.3 Electrochemical double layer capacitance

An electrical double layer exists on the interface between an electrode and its surrounding electrolyte. This double layer is formed as ions from the solution adsorb onto the electrode surface [148-149]. The charged electrode is separated from the charged ions by an insulating space, often on the order of angstroms. Charges separated by an insulator form a capacitor so

a bare metal immersed in an electrolyte will behave like a capacitor. The value of the double layer capacitance depends on many variables - Electrode potential, temperature, ionic concentrations, types of ions, oxide layers, electrode roughness, impurity adsorption, etc [148-149].

2.16.8.4 Solution resistance

This simply means resistance to the flow of ions in between the working electrode and the reference electrode in ionic solution. Solution resistance is often a significant factor in the impedance of an electrochemical cell [134, 142]. A modern three electrode potentiostat compensates for the solution resistance between the counter and reference electrodes. However, any solution resistance between the reference electrode and the working electrode must be considered when you model your cell. The resistance of an ionic solution depends on the ionic concentration, type of ions, temperature, and the geometry of the area in which current is carried. In a bounded area with area, A , and length, l , carrying a uniform current, the resistance is defined as [135, 149]:

$$R = \rho \frac{l}{A} \quad (24)$$

Where, ρ is the solution resistivity. The reciprocal of ρ is called the conductivity (κ) of the solution and its relationship with solution resistance is:

$$R = \frac{1}{\kappa} \cdot \frac{l}{A} \Rightarrow \kappa = \frac{l}{RA} \quad (25)$$

Standard chemical handbooks will often list κ values for specific solutions. For other solutions, you can calculate κ from specific ion conductances. The units of κ are Siemens per

meter (S/m) [98, 100, 141]. The Siemen is the reciprocal of the ohm, so $1 \text{ S} = 1/\text{ohm}$. Unfortunately, most electrochemical cells do not have uniform current distribution through a definite electrolyte area. The major problem in calculating solution resistance therefore concerns determination of the current flow path and the geometry of the electrolyte that carries the current. Fortunately, we usually do not calculate solution resistance from ionic conductances. Instead, we calculate it when we fit experimental EIS data to a model [98, 141].

2.16.8.5 Charge transfer resistance

Characteristic quantity for a single, kinetically-controlled electrochemical reaction, indicative of its inherent speed: a large charge-transfer resistance indicates a slow reaction. This charge transfer reaction has a certain speed. The speed depends on the kind of reaction, the temperature, the concentration of the reaction products and the potential [140, 150]. The general relation between the potential and the current (which is directly related with the amount of electrons and so the charge transfer via Faradays law) is:

$$i = i_0 \left(\frac{C_o}{C_o^*} \exp\left(\frac{\alpha n F \eta}{RT}\right) - \left(\frac{C_R}{C_R^*} \exp\left(\frac{-(1-\alpha)n F \eta}{RT}\right) \right) \right) \quad (26)$$

Where, i_0 = exchange current density, C_o = concentration of oxidant at the electrode surface, C_o^* = concentration of oxidant in the bulk, C_R = concentration of reductant at the electrode surface, C_R^* = concentration of the reductant in the bulk, η = over potential ($E_{app} - E_{oc}$), F = Faradays constant, T = temperature, R = gas constant, a = reaction order and n = number of electrons involved.

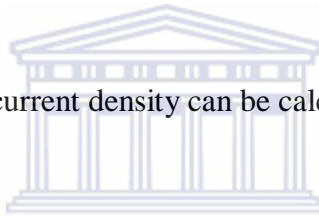
When the concentration in the bulk is the same as at the electrode surface, $C_o = C_o^*$ and $C_R = C_R^*$, this equation simplifies into:

$$i = i_0 \left(\exp\left(\alpha \frac{nF}{RT} \eta\right) - \exp\left(-\frac{nF}{RT} (1-\alpha) \eta\right) \right) \quad (27)$$

This is called Butler-Volmer equation. It is applicable when the polarization depends only on the charge-transfer kinetics. Stirring the solution to minimize the diffusion layer thickness can help minimize concentration polarization. When the over potential, η , is very small and the electrochemical system is at equilibrium, the expression for the charge-transfer resistance changes to [99-100, 126]:

$$R_{ct} = \frac{RT}{nFi_0} \quad (28)$$

From this equation the exchange current density can be calculated when R_{ct} is known.



2.17 Fundamental principles of chronoamperometry (CA)

Chronoamperometry is a very powerful square wave pulsed voltammetric technique where the potential of the working electrode is stepped and the corresponding current due to faradaic processes is measured as a function of time. The recorded current can be analysed and its nature can be identified from the variations with time. As with all pulsed techniques, chronoamperometry generates high charging currents, which decay exponentially with time as any RC circuit [141]. The Faradaic current which is due to electron transfer events and is most often the current component of interest decays as described in the Cottrell equation below. For example: at short times the capacitive current is dominant ($I \propto e^{-t/RC}$; with R = solution resistance and C = capacitance) while at longer time scales, the diffusion limited faradaic current might prevail ($I \propto t^{-1/2}$) [128].

Faradaic currents result from electrochemical reactions at the electrode surface. From the position of the current peak (peak potential), the nature of the species can be deduced. Usually under potentiostatic conditions, faradaic currents are slower to diminish than capacitive currents [141]. The chosen scan rate should therefore be slow enough to reduce the charging current, without letting the magnitude of the faradaic current decline below noise level. In case of fast scan rates, there might be an overlap with the capacitive current. Usually in these cases, one will employ a range of scan rate allowing for detailed analysis of the electrochemical components [128].

At the beginning of the transient experiment the potential of the working electrode is held at E_1 , see Figure 2.35 (a) . At $t=0$ the potential is instantaneously changed to a new value E_f , and corresponding current time response is recorded as shown in Figure 2.35 (b) [99, 151]

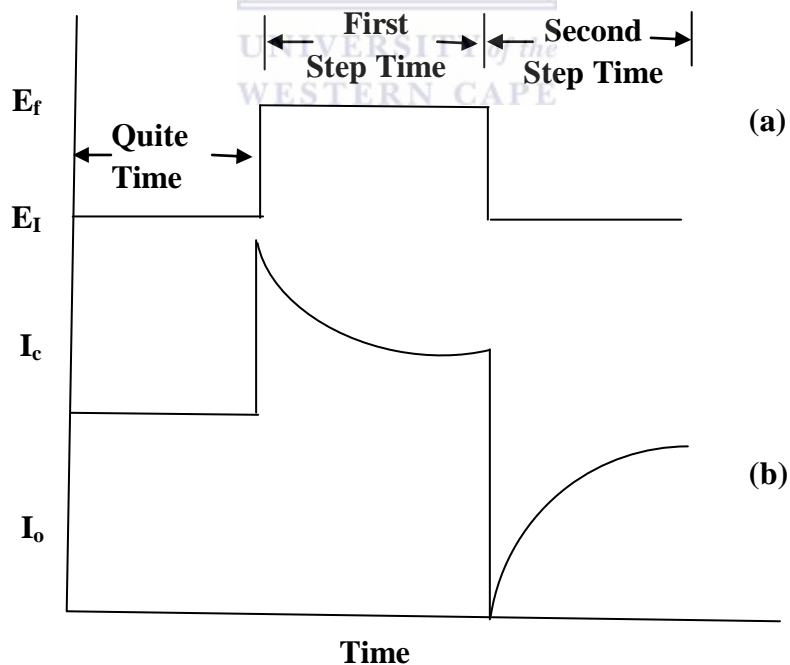


Figure 2.35: Chronoamperometric experiment.

Figure 2.35, (a) is the potential-time profile applied during experiment, E_i is initial value is the potential where no reduction of Ox occurs and E_f is the second step potential or other potential of interest where reduction/oxidation of electroactive specie occurs (b) the corresponding response of the current due to changes of the potential.

In order to determine the exact form of current-time dependence for a planar electrode or the current density, Cottrell equation is used [128, 141]:

$$|I| = \frac{nF\sqrt{D_o}\cdot C_o}{\sqrt{\pi t}} \quad (29)$$

This is also simplified as [152],

$$i = \frac{nFAC_o\sqrt{D_o}}{1/2} (t^{-1/2}) \quad (30)$$

Where, n = number of electrons transferred per ion or molecule (eq/mol), F = Faraday's constant (96,485 C/eq), A = electrode surface area (cm^2), C_o = concentration of Ox (mol/cm), D_o = diffusion coefficient of Ox (cm /s), t = time (s).

For diffusion controlled process, it can be noticed that the current decreases as a function of $t^{-1/2}$. This feature is frequently used as a test for this type of process and from the slope of I vs. $t^{-1/2}$ the diffusion coefficient D_o can be calculated [141].

It is important, that such an analysis has to be applied over a broad time interval in order to ensure the reliability of results. At short times the current consists of a large non faradaic component due to charging of the double-layer capacitance. The non-faradaic current decays

exponentially with time constant $R_u C_d$, where, R_u is an uncompensated resistance and C_d is the double layer capacitance [99]:

$$|I| = \frac{E}{R_u} e^{-t/R_u C_d} \quad (31)$$

Thus, the time constant $R_u C_d$ will determine the shortest time required to conduct the chronoamperometric experiment. Therefore, measurements should be performed for times which are much greater than $R_u C_d$. After passing the time equal to $R_u C_d$, the double layer capacitance is charged by 63 % and after $3R_u C_d$ by 95 %. See equation (30). Thus, knowing the time constant one can easily estimate the time needed for double layer charging [99-100].

At long time, however, the natural convection (may be caused by temperature and concentration gradients) comes into effect and diffusion in that case is not the only mode of the mass transport. Hence, the typical time range of chronoamperometric measurements lies normally in the range from 0.001 to 10 s. However, there are a number of additional instrumental and experimental limitations. For example, current and voltage characteristics of a potentiostat can limit the current maximum and time resolution [128, 141].

Even though the chronoamperometry is relatively simple technique, there are a number of difficulties, which are related to the interpretation of the current-transient curve. Hence, it is very important to find the possibility of comparative analysis of the chronoamperometric results with the results of cyclic voltammetry and other techniques. This type of comparison will also help to understand the studied system more completely and with better precision [99, 128].

2.18 Fundamental principles of chronocoulometry (CC)

Chronocoulometry is a controlled potential electroanalytical technique involving measurement of the charge vs. time response to an applied potential step waveform. The shape of the resulting chronocoulogram can be understood by considering the concentration gradients in the solution adjacent to the electrode surface.

Chronocoulometry (CC) and chronoamperometry (CA) have the same potential wave form which is one of the simplest potential wave forms as shown in Figure 2.36. Chronocoulometry is useful for measuring electrode surface areas, diffusion coefficients, the time window of an electrochemical cell, adsorption of electroactive species, and the mechanisms and rate constants for chemical reactions coupled to electron transfer reactions [108, 128, 131-132, 152-153].

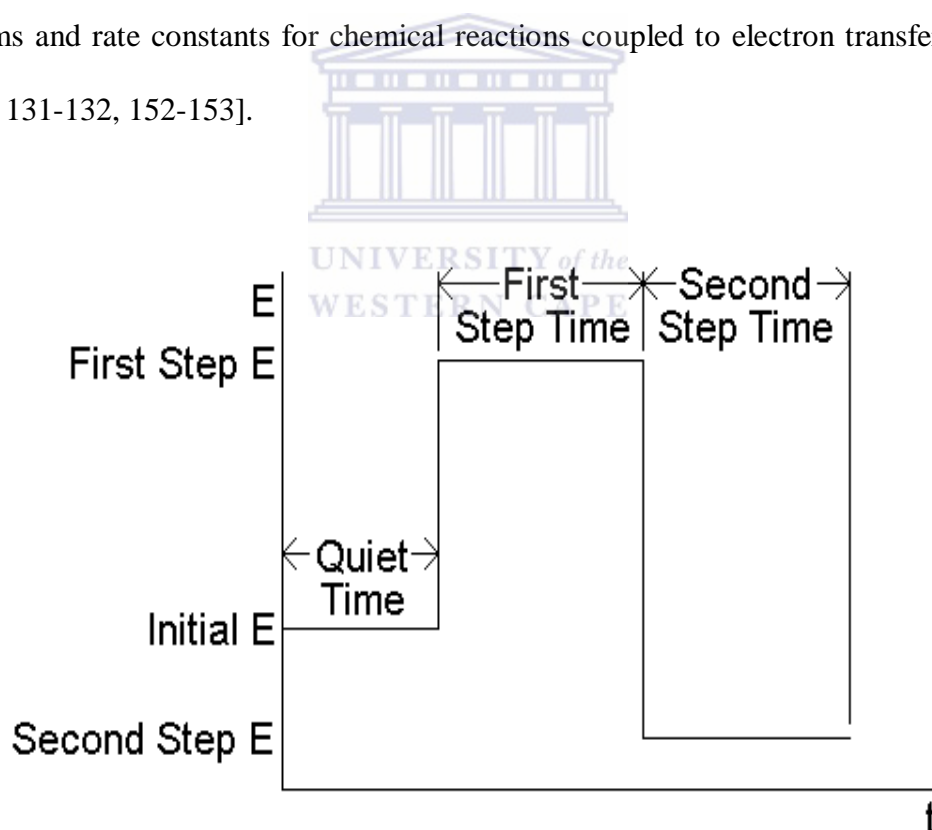


Figure 2.36: Potential wave form for chronocoulometry.

Typically the experiment starts at a potential (Initial E) at which there is no electrolysis. The potential is then changed instantaneously (stepped) to a value that leads to oxidation or reduction of some species in solution (First step E) and is held at that potential for a user-defined time period (First step time). In a single potential step experiment, the experiment is complete at the end of this first step time. In a double potential step experiment, the potential is stepped to a third potential (Second step E) at which the species formed on the first step is re-electrolyzed (in many instances, the Second step E is identical to the Initial E).

The first and second potential steps are also often referred to as the forward and reverse potential steps respectively. The effects of the changes in potential used in the CC experiment can be understood by considering the Nernst equation, which relates the applied potential E (in V), the formal redox potential E° , and the surface concentrations (C^s) of the relevant electroactive species. For the redox couple $Ox + ne = Red$, the Nernst equation is shown in equation (32) [99, 141, 152-153]:

$$E = E^{\circ} + \frac{0.059}{n} \log \frac{C_{Ox}^s}{C_{Red}^s} \quad (32)$$

Where, n = number of electrons transferred.

2.18.1 Concentration response

The changes in the surface concentration that accompany a potential step establish concentration gradients in the solution adjacent to the electrode surface. These gradients can be illustrated graphically using concentration-distance profiles. It is important to note that diffusion is the only mode of mass transport used in the CC experiment; that is, the solution must be in a quiescent state [128, 131].

2.18.2 Current response

The response to a potential step is current due to the electrolysis of Ox or Red. Current vs. time experiment (chronoamperometry) has been explained in section 2.17. Upon application of each potential step, there is a current “spike” followed by a gradual decay in the current, see Figure 2.35 (b). This response can be rationalized by noting that current is a measure of the rate of electrolysis. The current “spike” that follows the application of the potential step is due to electrolysis of the molecules adjacent to the electrode surface [152]. And the current is described by Cottrell equation (29) [131].

2.18.3 Charge response

Charge is the integral of current with respect to time; therefore response for the CC experiment can be obtained by integrating the current response for the CA experiment, and is shown in the Figure 2.37 [128, 132].

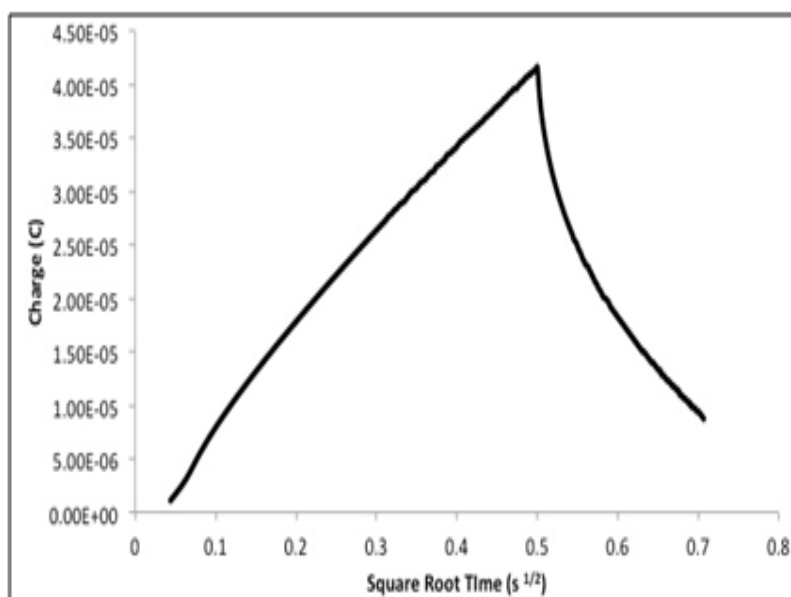


Figure 2.37: Charge response due to changes of the potential.

Similarly, the equation for the Q vs. t curve (the Anson equation) is obtained by integrating the Cottrell equation.

$$Q = \frac{2nFAC_o\sqrt{D_o}}{1/2} (t^{1/2}) \quad (33)$$

From Ansons equation, Q is a function of $t^{1/2}$. Since the value of Q at any time is a measure of the amount of Ox that has been reduced up to that point, the charge will decrease following the reverse step due to the re-oxidation of R generated by the first potential step. And from the slope of Q Vs $t^{1/2}$, we can calculate the electrode surface areas, diffusion coefficients, and concentration of adsorbed electroactive species [132, 152].

2.18.4 Adsorption

Chronocoulometry is particularly useful for studying electroactive material that is adsorbed on an electrode surface [153]. The key feature is that the charge due to electrolysis of the adsorbed species can be distinguished from the charge that is due to electrolysis of solution species. This distinction is based on the fact that the adsorbed material is on the electrode surface and hence is electrolyzed immediately upon application of the potential step, whereas solution species must diffuse to the electrode surface in order to react. The total charge (Q) measured in response to the potential step comes from three sources [128, 131]:

- ❖ charging of the double layer (Q_{dl})
- ❖ electrolysis of adsorbed species(Q_{ad})
- ❖ electrolysis of solution (diffusing) species (Q_{diff})

That is:

$$Q = Q_{\text{diff}} + Q_{\text{ads}} + Q_{\text{dl}} \quad (34)$$

$$Q = 2nFACD^{1/2} \Pi^{1/2} t^{1/2} + nFA\Gamma_0 + Q_{\text{dl}} \quad (35)$$

Where, Q_{diff} = charge due to electrolysis of solution species

Q_{ads} = charge due to electrolysis of adsorbed species

Q_{dl} = double-layer charge

Γ^* = surface concentration of adsorbed species (mol cm^{-2})

D = diffusion coefficient of solution species ($\text{cm}^2 \text{s}^{-1}$)

A = Surface area of the glassy carbon electrode, 0.071 cm^2

F = Faraday's constant, $95484.56 \text{ C mol}^{-1}$

C = Concentration of the electrolyte, 0.1 M

t = Time of potential step (s)

T = time following potential step (s)

The intercept of Q versus $t^{1/2}$ plot is the sum of Q_{dl} and Q_{ads} . The Q_{dl} can be eliminated from the equation by running identical experiment on the electrolyte alone [152-153].

2.19 Fundamental principles of electrochemiluminescence (ECL)

2.19.1 Luminescence

Luminescence is the emission of light which occurs when electrons within an excited molecule relaxes radiatively (moves from its higher energetic state) to less energetic state or to its ground state [89]. There are many types of luminescence and they are classified according to their different sources of excitation energy:

Bioluminescence (BL) is produced by living organisms e.g. glow worms, fireflies etc; radio-luminescence (RL) is a result of bombardment by ionizing radiation; electroluminescence (EL) results from an electric current passed through a substance; piezo-luminescence (PL) is produced by the action of pressure on certain solids; photoluminescence (which includes fluorescence and phosphorescence) is produced by absorption of radiant energy, for phosphorescence the luminescence continues after the radiation causing it has stopped, while for fluorescence the luminescence ceases very shortly after the radiation causing it ceases (see Figure 2.38); thermo-luminescence (TL) is the re-emission of absorbed light when the substance is heated; Chemiluminescence (CL) is produced by chemical reactions and electrochemiluminescence (ECL) is produced by electrochemical reactions.

Chemiluminescence and electrochemiluminescence do not require irradiation of the sample. This is a unique advantage over other luminescence methods because the problem of light scattering, source instability and high background signals due to unselective photo excitation as frequently encountered in photoluminescence is avoided completely [154].

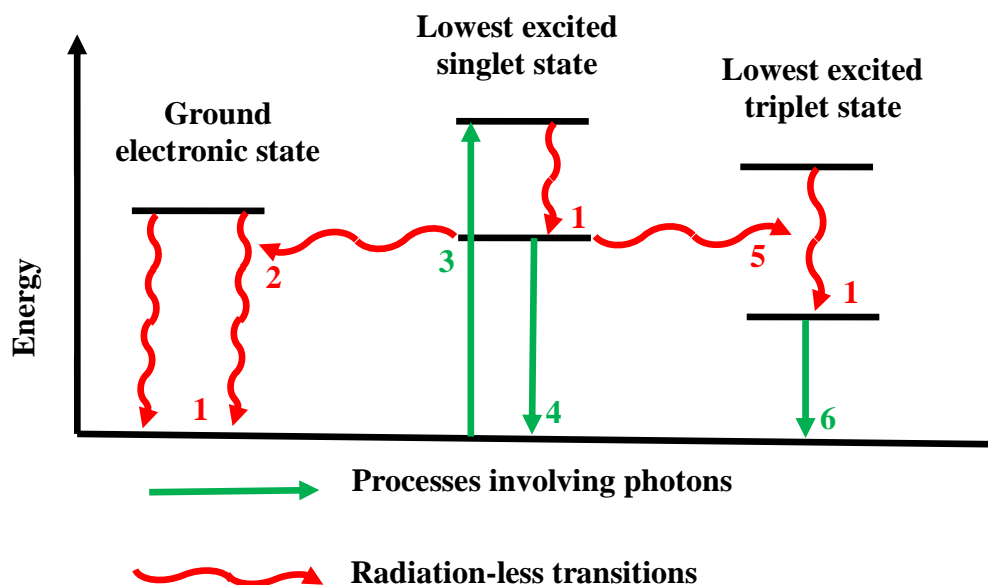
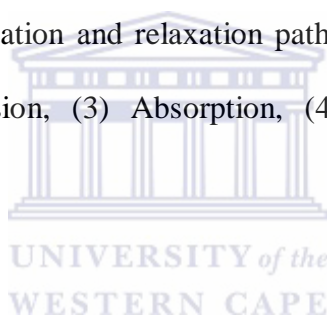


Figure 2.38: Illustration of excitation and relaxation pathways of an atom: (1) Vibrational relaxation, (2) Internal conversion, (3) Absorption, (4) Fluorescence, (5) Intersystem crossing, (6) Phosphorescence



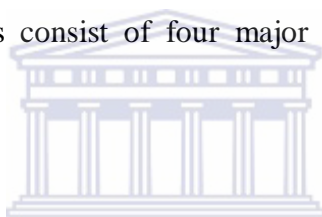
Luminescence measurements and visualization techniques have gained more attention due to the dangers inherent in radioactivity-based methods and its dramatic increase in sensitivity. The analytical sensitivity of CL- and ECL- based immunoassays is better than that obtained with radioactive labels. Detection limits are at sub-picomolar level and detection can be made in a wide linear dynamic range. CL and ECL labels are typically extremely stable, with shelf-lives in excess of one year at room temperature. For these reasons and more, their applications have grown from clinical assays to DNA sequencing, antioxidant detection and high-throughput screening.

2.19.2 Electrochemiluminescence

Electrochemiluminescence (ECL) by simple definition is the emission of light observed when the excited product of an electrochemical reaction relaxes radiatively to its ground state. The reactants that produce this luminescence are formed in situ in the vicinity of an electrode surface to which appropriate potential is applied [155]. By comparison with conventional analytical methods and simple chemiluminescence, highly reactive reagents are produced at a known time, position and concentration from stable precursors and the procedures of storage, handling and mixing of reactive reagents are circumvented.

2.19.3 Components of an electrochemiluminescent system

Electrochemiluminescent systems consist of four major components (see Figure 2.39 for schematic illustration):



- ❖ **Electrochemical instrument/ potentiostat**; which consists of an electrochemical cell, which has the following three electrodes; working, reference and counter. To monitor the electrochemical reaction.
- ❖ **Photomultiplier tube (PMT)**; used as a light detector. The tube multiplies the effect of light that strikes it & converts photons of light into electrical signals so that the light can be precisely measured.
- ❖ **Photodiode**; It's a type of a photo detector capable of converting light into either current voltage.
- ❖ **Charge coupled device (CCD)**; is positioned to collect light from the working electrode, and hence detect ECL.

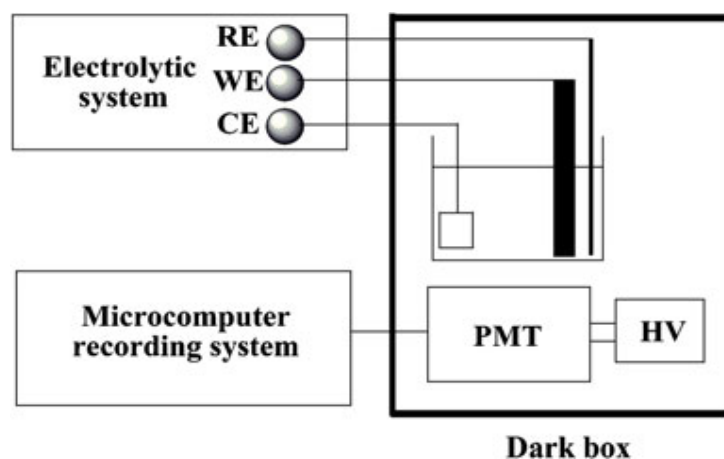


Figure 2.39: Schematic illustration of electrochemiluminescent components.

2.19.4 Mechanisms of electrochemiluminescence

Electrochemiluminescence involves the electro-generation of highly reducing and oxidizing species in the vicinity of the electrode surface, which then annihilate with each other to form excited state compounds if the excitation energy of the compounds produced are smaller than the potential difference of the reduced and oxidized radical. The species that can emit light when electrochemically excited are called ECL luminophores.

An ECL luminophore may be an atom or group of atoms which when present in an organic compound increases the ability of the compound to luminescence e.g. $[\text{Ru}(\text{bpy})_3]^{2+}$, $[\text{Os}(\text{bpy})_3]^{2+}$, $[\text{Cr}(\text{bpy})_3]^{2+}$ complexes and/or clusters containing Ag, Al, Au, Cd, Cr, Cu, Eu, Hg, Ir, Mo, W, Os, Pd, Pt, Re, Ru, Si and Tb.

Electrogeneration of highly reducing and oxidizing species can be carried out in three main ways namely: (a) Hot electron-induced ECL, (b) Two-step potential sweep method (annihilation pathway) and (c) One-step potential sweep method (co-reactant pathway):

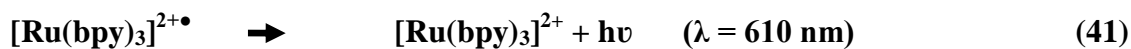
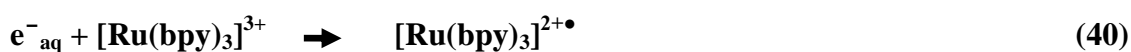
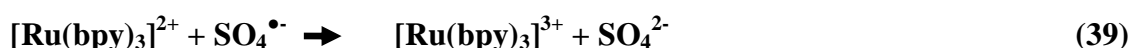
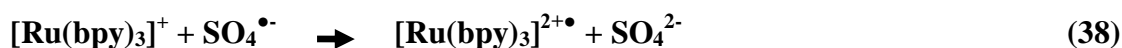
2.19.4.1 Hot electron-induced electrochemiluminescence (HEI ECL)

This is an ECL system in which metal electrodes are covered with oxides of Aluminum, Magnesium, Silicon, Gallium and Tantalum. The oxide-covered electrodes act as cold cathodes during cathodic pulse polarization and tunnel emit hot electrons into an aqueous electrolyte [156]. The injected hot electrons induce electron generated chemiluminescence (ECL) of various luminophore in fully aqueous solutions. It is more of direct formation of the excited states at the electrode surface than electron transfer chemiluminescent reactions of electrochemically generated reactants.

The simultaneous presence of highly reducing and oxidizing species in the vicinity of the electrode surface makes it possible to generate ECL from luminophores that cannot be excited at conventional metal cathodes in fully aqueous solutions [156-157]. This type of ECL provides a means to simultaneously excite several luminophores emitting at different spectral region with different luminescence lifetimes. The difference in emission wavelengths and/or luminescence lifetimes are exploited in the analysis of the electrochemiluminescence signals emerging from these different luminophores [158-159].

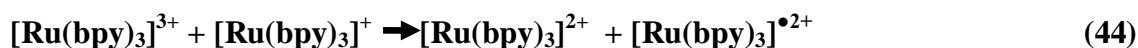
The use of oxide-covered cathode widens the potential range of the electrode. And the wider the potential range, the more energetic the light emissions can be. The injected “hot electron” denotes an electron possessing higher energy in aqueous solution than electron heterogeneously transferred to an electrolyte solution from an active metal electrode in conventional ECL [160]. The mechanism of HEI ECL is illustrated below [157]:





2.19.4.2 Two-step potential sweep method (Annihilation pathway)

Cyclic voltammetric technique is commonly utilized in this method. The forward electrode potential is swept to the value at which an oxidized radical form (A^+) of a luminophore is produced (42), while the reverse potential sweep process produces the reduced radical form (A) of same luminophore (43). As a result of this two-step potential sweep, both oxidized and reduced radical forms of the luminophore exist in the diffusion layer near the electrode surface and can annihilate (44) with each other to form excited state compounds if the excitation energy of the compounds produced are smaller than the potential difference of the reduced and oxidized radical forms of the luminophore. The excited state product relaxes (45) radiatively to its ground state by emitting light [159, 161]. The mechanism of this two-step potential sweep is illustrated below:



Invariably, annihilation pathway involves electron transfer reactions between an oxidized and a reduced species, through alternate pulsing of the electrode potential. Both the oxidized and reduced forms of the luminophore are generated at the electrode

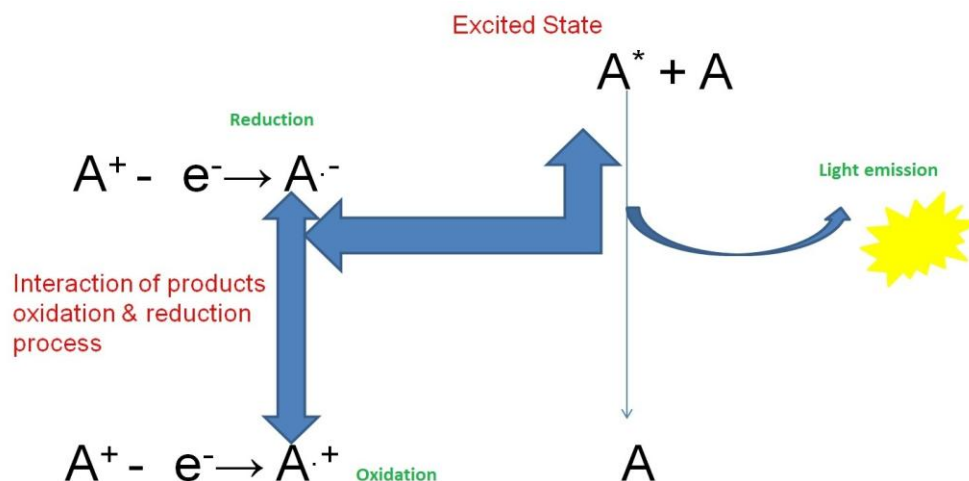


Figure 2.40: The schematic illustration of annihilation pathway ECL.

An advantage of the annihilation pathway is that it requires only the electrochemiluminescent luminophore species, solvent, and supporting electrolyte to generate light. However, the potential window of water is often not sufficiently wide enough to allow the luminophore to be oxidized and reduced, making it necessary to use organic solvents such as acetonitrile and N,N-dimethylformamide. Another problem is that one electron oxidized or reduced radical luminophore is very unstable in aqueous solutions [154-155].

2.19.4.3 One-step potential sweep method (co-reactant pathway)

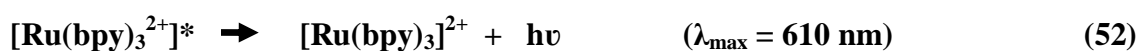
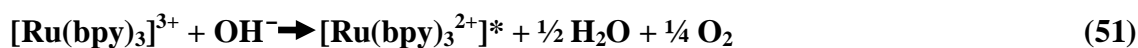
In coreactant pathway, ECL is generated in the presence of a coreactant and an ECL luminophore with a single potential sweep. A coreactant is a species which when electrochemically oxidized produces a radical intermediate that can annihilate with an oxidized luminophore to produce excited state compound e.g. hydrogen peroxide, peroxydisulfate, oxalate ion ($C_2O_4^{2-}$), tri-n-propylamine (TPA) etc. These compounds produce a strong reductant upon oxidation in aqueous solution [155, 162].

An ECL luminophore is an atom or group of atoms which when present in an organic compound increases the ability of the compound to luminescence e.g. $[\text{Ru}(\text{bpy})_3]^{2+}$. At same single potential sweep an ECL luminophore is oxidized to produce a radical oxidant e.g. $[\text{Ru}(\text{bpy})_3]^{\bullet 3+}$, which now annihilate with a reductant e.g. $\text{CO}_2^{\bullet -}$, OH^- , $\text{TPA}^{\bullet -}$ etc forming an excited state product which emit light radiatively on relaxation to its ground state [92, 159]. The mechanism of one-step sweep is illustrated below:

For oxalate ion ($\text{C}_2\text{O}_4^{2-}$),



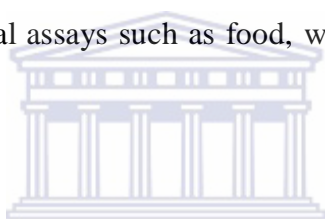
For hydrogen peroxide,



TPA is especially important because it allows efficient ECL not only in aqueous media but also at physiological pH 7.2. The use of this format widens the usable potential window of a conventional metal electrode which especially in aqueous medium, is restricted by cathodic hydrogen evolution, anodic oxygen evolution and their over voltages (this is known as quenching of ECL reaction) [92]. Therefore for a conventional metal electrode system, co-reactant ECL of organic luminophore generally takes place only in organic solvents [161].

Water and dissolved oxygen must be rigorously excluded to avoid quenching of the ECL reaction. ECL emission intensity is usually proportional to the concentration of the emitter or co-reactant, hence, either of them can be used as a probe [26, 159, 163].

Using $[\text{Ru}(\text{bpy})_3]^{2+}/\text{TPrA}$ reaction sequence has a major advantage because $[\text{Ru}(\text{bpy})_3]^{2+}$ is regenerated in its ground state near the electrode surface after the luminescent excited state $[\text{Ru}(\text{bpy})_3]^{\bullet 2+}$ has emitted a photon. Hence, one $[\text{Ru}(\text{bpy})_3]^{2+}$ molecule participates in multiple ECL reaction cycles to produce multiple photons. This mechanism known as “non-destructive mechanism of $[\text{Ru}(\text{bpy})_3]^{2+}$. It lowers detection limit and increases sensitivity [92, 159]. Co-reactant ECL is being used in a wide range of analytical applications including clinical diagnostics, environmental assays such as food, water testing and bio-warfare agent detection [92].



2.19.5 Optimization of electrochemiluminescence

Metallic nanoparticles are known to significantly influence the emission of vicinal luminophores. Their presence close to luminophores enhances the rate of excitation of the luminophore molecules and increases their radiative decay rate by coupling the emission of luminophores with surface plasmon resonance or scattering of nanoparticles [164-166]. Surface plasmon is excited plasma wave of free electrons that vertically oscillate against the ion-bodies of the nanoparticles and horizontally to the metal surface. See Figure 2.41 for illustration [26, 47].

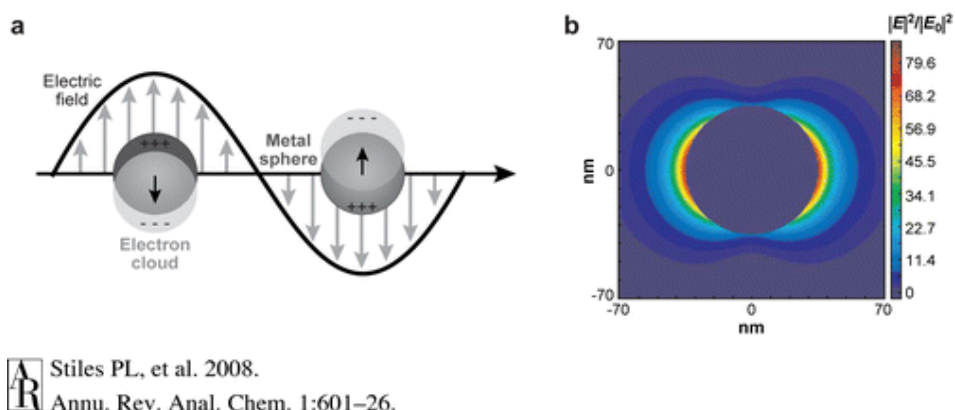
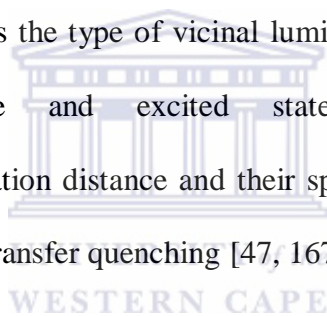


Figure 2.41: Illustration of surface plasmon is excited plasma wave of free electrons.

The degree of the effects of plasmon depends strongly on the chemical structure, composition and nanoparticles sizes as well as the type of vicinal luminophore. To achieve an enhanced emission, the ground state and excited state redox properties of the luminophore/nanoparticles separation distance and their spectral overlap is optimized while minimizing electron and energy transfer quenching [47, 167].

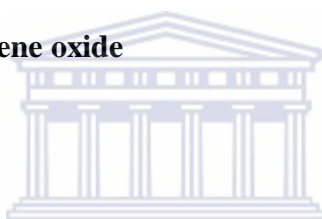


Chapter Three

Experimental Procedures and Analytical Methods

This chapter gives detailed research methodologies; general experimental procedures; chemicals and sample preparations; chemical synthesis; electrochemical synthesis; characterizations and construction of immunosensor platforms for the determination of deoxynivalenol mycotoxin via impedimetric system.

3.1 Chemical synthesis of graphene oxide



3.1.1 Chemicals

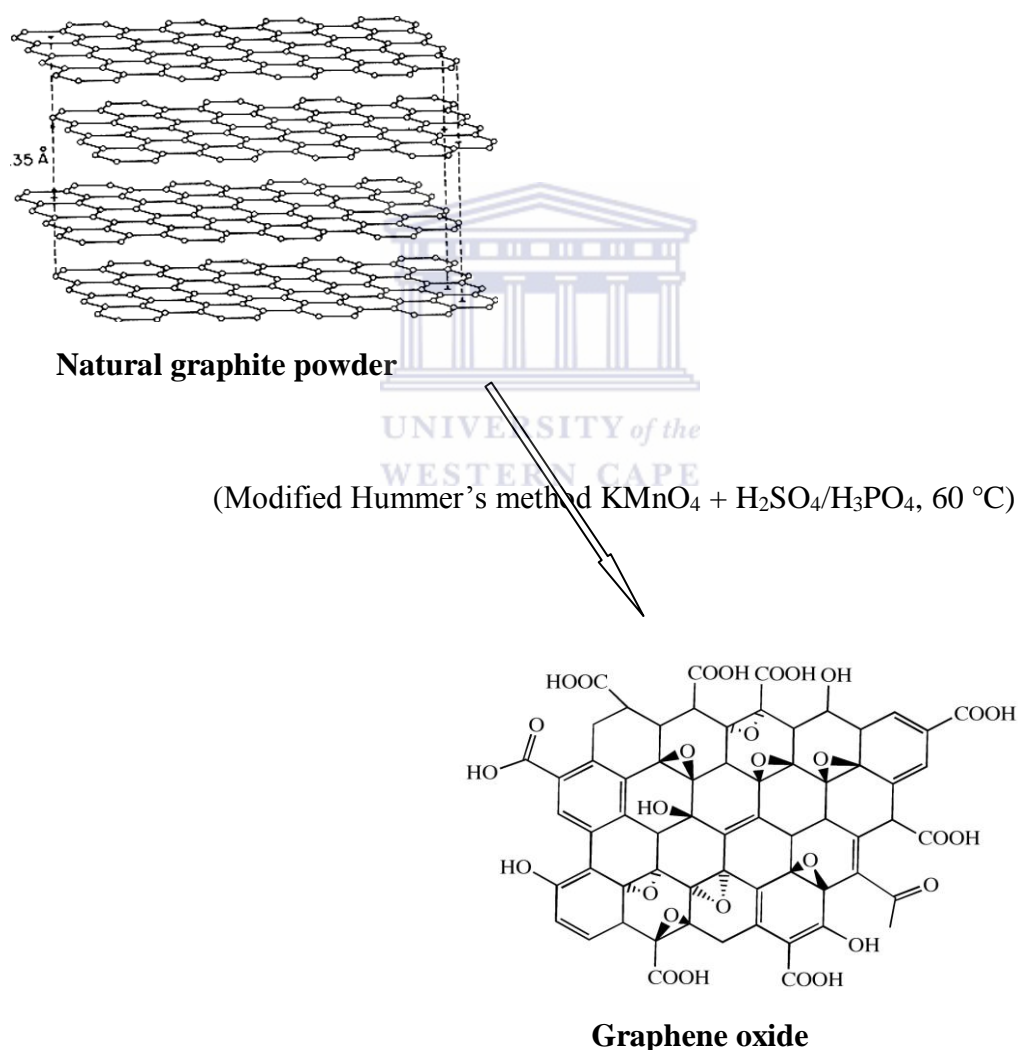
Natural graphite powder (99.9995% purity grade) was purchased from Alfa Aesar, phosphoric acid (H_3PO_4), potassium permanganate (KMnO_4), hydrogen tetraoxosulphate (VI) acid (H_2SO_4), Hydrogen peroxide (H_2O_2), hydrochloric acid (HCl , 37% purity, density 1.19 kg/L) and ethanol ($\text{C}_2\text{H}_6\text{O}$) were all supplied by Sigma Aldrich. The water used throughout all experiments was purified through a Millipore system having a resistivity of 18.2 M Ω .

3.1.2 Experimental procedure

Graphene oxide (GO) was prepared through a modified Hummers and Offeman method using natural graphite powder as the starting materials [35, 37, 168-172]. Briefly, 9:1 mixture of concentrated $\text{H}_2\text{SO}_4/\text{H}_3\text{PO}_4$ (180:20 mL) was added to a mixture of graphite powder (1.5 g) and KMnO_4 (11.5 g) in a 250 mL capped round bottom flask. The reaction was then heated to

60 °C and stirred for 12 h. The reaction mixture was cooled to room temperature and poured onto ice that is mixed with 30% H₂O₂ in the ratio (400 mL: 3 mL).

The mixture was filtered and washed in succession with 300 mL of 37% HCl solution in order to remove metal ions, 300 mL of ethanol, 300 mL of water until the rinse water pH became neutral [168]. The solid obtained was vacuum-dried overnight at ambient temperature and kept in a capped glass bottle for further use.



Scheme 2: The illustration for graphene oxide synthesis

3.2 Chemical synthesis of 4-nitrophenyl diazonium tetrafluoroborate (NDT)

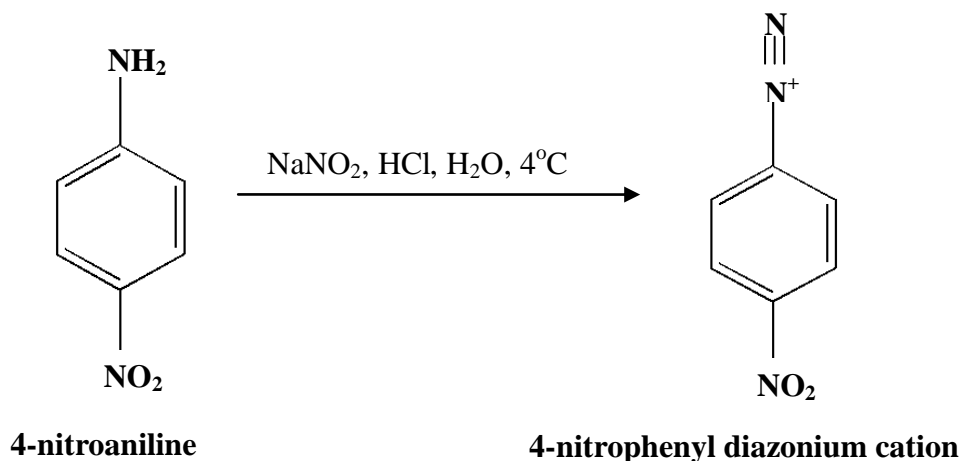
3.2.1 Chemicals

Tetrabutylammonium tetrafluoroborate (NBu_4BF_4), sodium tetrafluoroborate (NaBF_4), 1, 4-nitroaniline ($\text{C}_6\text{H}_6\text{N}_2\text{O}_2$), sodium nitrite (NaNO_2), potassium chloride (KCl), acetonitrile (CH_3CN) and hydrochloric acid (HCl , 37% purity, density 1.19 kg/L), diethyl ether were all purchased from Sigma-Aldrich (South Africa). All reagents were used as received and aqueous solutions were prepared with Millipore system having a resistivity of over 18.2 M Ω .

3.2.2 Experimental procedure

1, 4-Nitrophenyl diazonium tetrafluoroborate was prepared using the method of Saby et al [173]. 4-Nitroaniline (3.5 g) was dissolved in 15 mL of 60% w/w aqueous hydrochloric acid solution and heated on a steam bath for 15 minutes with occasional stirring to achieve complete dissolution. The mixture was cooled in an ice-salt bath and stirred rapidly in order to precipitate the hydrochloride as fine crystals. Cracked ice (10 g) was added and a saturated 10 mL solution of 1.8 g of sodium nitrite was added in drops with rapid mechanical stirring while the temperature of the reaction mixture is maintained between $-4\text{ }^\circ\text{C}$ and $+5\text{ }^\circ\text{C}$ by cooling with the ice-salt bath.

The solution was filtered and sodium tetrafluoroborate (2.7 g) was added into the filtrate. The filtrate was then cooled to $-4\text{ }^\circ\text{C}$ causing crystallization of the product. The crude product (1, 4-nitrophenyl diazonium tetrafluoroborate, NDT) was purified by dissolution in a minimal amount of acetonitrile and re-crystallized using diethyl ether. NDT was recovered by filtration, dried in vacuum for 24 h and kept in an amber bottle for further use.



Scheme 3: The illustration for diazotization of 4-nitroaniline.

3.3 Chemical synthesis of nitrophenylazo functionalized graphene (G/PhNO₂)

3.3.1 Chemicals and reagents

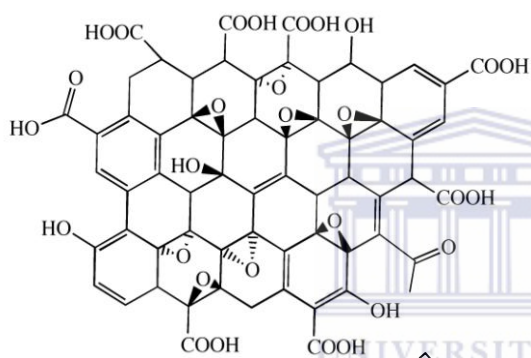
As-synthesised graphene oxide (GO) and 4-nitrophenyl diazonium tetrafluoroborate (NDT). Sodium borohydride (NaBH₄), sodium carbonate (Na₂CO₃), acetonitrile (CH₃CN) and hydrazine monohydrate (N₂H₄·H₂O) were all purchased from Sigma-Aldrich (South Africa). Milli-Q de-ionized water (resistance over 18.2 MΩcm) purified by a Milli-QTM system was used throughout.

3.3.2 Experimental procedure

G/PhNO₂ was synthesised using the as-synthesized GO in three steps by modified Yongchao Si and Edward T. Samulski method [41]:

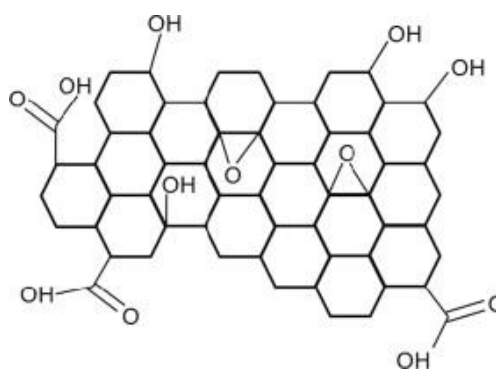
3.3.2.1 Pre-reduction of GO

10 mg of GO was dispersed into separate sheets in 40 mL of distilled water contained in a 100 mL capped flask by simple sonication. Then the pH was adjusted to 9-10 using 10% w/v sodium carbonate solution. Then 1 mL of 1 M NaBH₄ solution was added slowly with constant stirring. The mixture was allowed to stir at 80 °C for 1 h. This pre-reduction step is necessary to achieve complete reduction in the final step (step 3) and to enable the functionalisation reaction in step 2 by increasing the size of sp²-carbon domains for reaction with the aryl diazonium salt.



Graphene oxide

(Pre-reduction of graphene oxide: NaBH₄, pH 10, 80 °C)



Pre-reduced graphene oxide

Scheme 4: The illustration for pre-reduction of graphene oxide

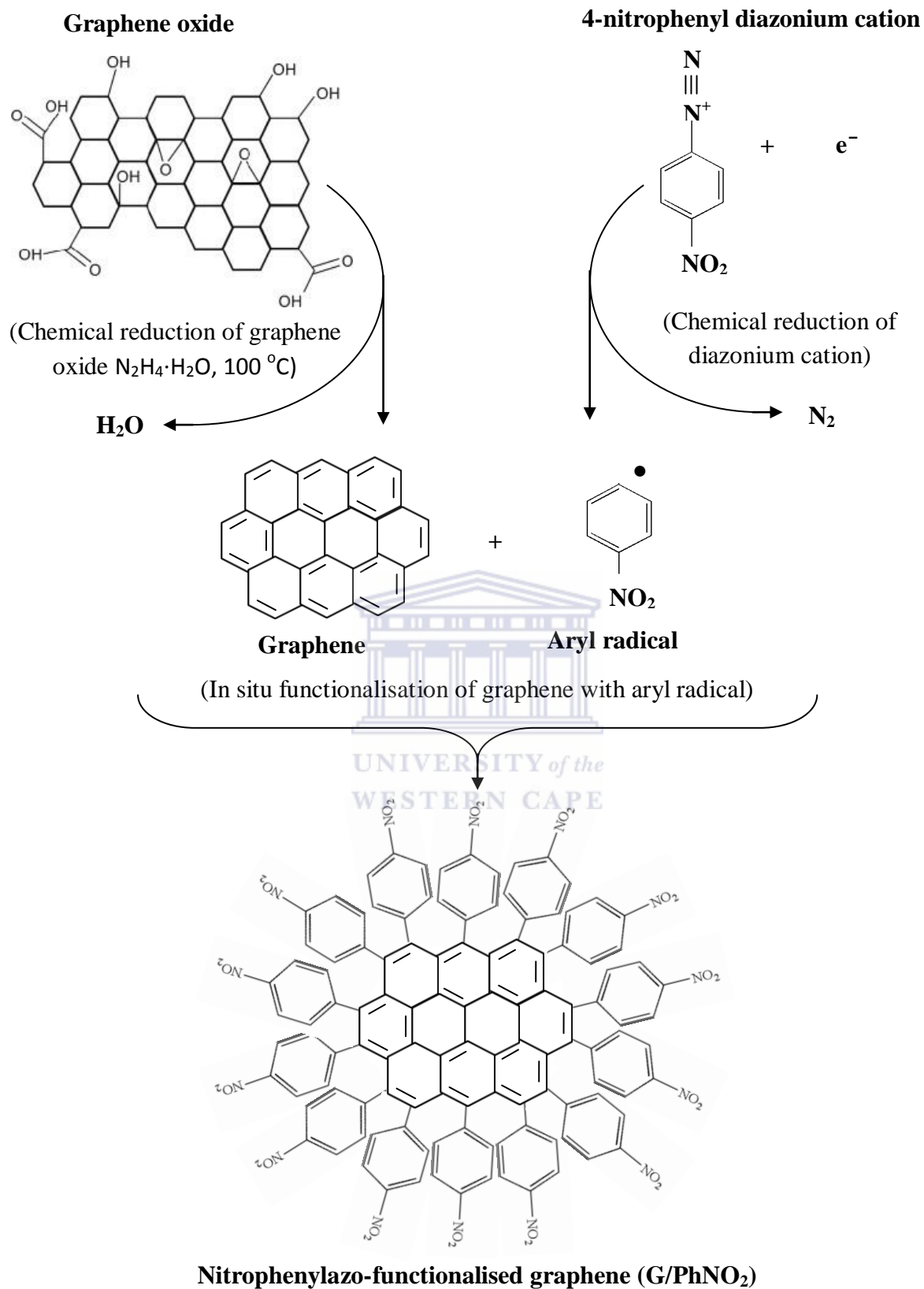
3.3.2.2 Functionalisation of pre-reduced GO

Functionalisation of the pre-reduced GO with 4-nitrophenyl diazonium tetrafluoroborate was done using the method of Saby et al [173]. After centrifuging and rinsing several times with distilled water, partially reduced GO was re-dispersed in 40 mL of distilled water via mild sonication. 0.5 mg of the as synthesised 4-nitrophenyl diazonium salt was dissolved in 5 mL of 1:1 acetonitrile to water mixture and then added to the GO dispersion with constant stirring in ice bath for 3 h.

3.3.2.3 Post-reduction with hydrazine

After centrifuging and rinsing with distilled water severally, 4-nitrophenylazo functionalised GO was re-dispersed in 40 mL of distilled water. Then 3 mL of 1 M hydrazine ($\text{N}_2\text{H}_4 \cdot \text{H}_2\text{O}$) was added into the dispersion and the mixture was kept at 100 °C for 16 h. Highly dispersive 4-nitrophenylazo (PhNO_2) functionalised graphene (henceforth referred to as G/ PhNO_2) was recovered by washing and centrifuging severally with distilled water. It was dried in the vacuum oven at 70 °C for 3 h and kept in an amber bottle for further use.

The chemical reduction of the diazonium cation as illustrated in scheme 5 , leads to the elimination of a nitrogen molecule and the production of highly reactive aryl radical. This radical attacked the pre-reduced GO surface and to form a covalent bond between the aryl group and the GO. Simultaneously the functionalised GO was reduced to 4-nitrophenylazo functionalised graphene with the elimination of H_2O [174-176].



Scheme 5: The illustration for simultaneous chemical reduction of diazonium cation to diazonium radical, GO to graphene and in situ PhNO₂ functionalisation of graphene.

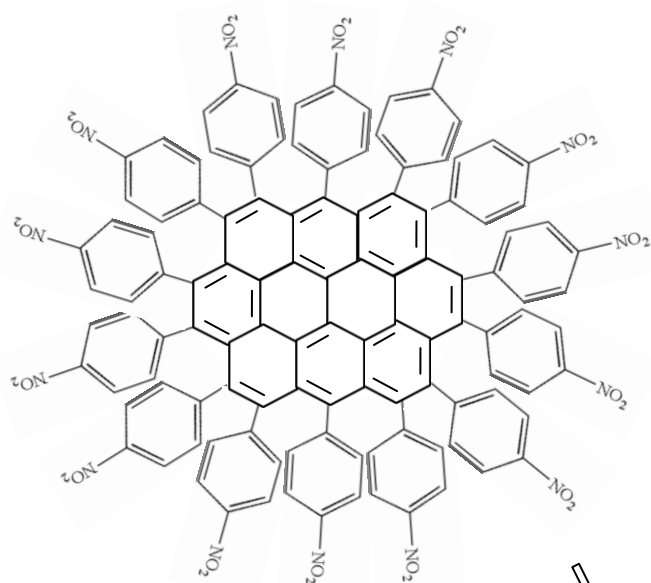
3.4 Chemical synthesis of gold nanoparticles-dotted 4-nitrophenylazo functionalized graphene (AuNp/G/PhNO₂)

3.4.1 Chemicals and reagents

Asynthesised G/PhNO₂. Hydrogen tetrachloroaurate(III) trihydrate (HAuCl₄.3H₂O) and trisodium 2-hydroxypropane-1,2,3-tricarboxylate (trisodium citrate, Na₃C₆H₅O₇) were purchased from Sigma-Aldrich (South Africa). Milli-Q de-ionized water (resistance over 18.2 MΩcm) purified by a Milli-QTM system was used throughout.

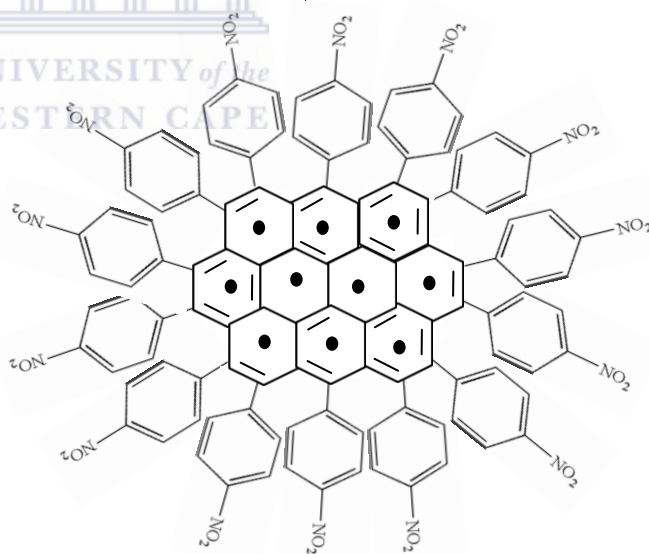
3.4.2 Experimental procedure

The G/PhNO₂ was dispersed in 2 mL of 5 mM HAuCl₄ solution by sonication for 5 min. This was then diluted to 20 mL with doubly distilled water and heated to boiling while stirring. Afterwards, 10 mL of 0.2 M Sodium citrate was slowly added to the boiling solution and allowed to heat with constant magnetic stirring until there was no colour change. The sample was then cooled to room temperature, separated by centrifuge and washed five times with doubly distilled water. The resulting products were dried in a vacuum oven at 70 °C for 3 h [51].



4-nitrophenylazo-functionalised graphene

Synthesis of gold nanoparticles-dotted 4-nitrophenylazo functionalised graphene



**Gold nanoparticles-dotted 4-nitrophenylazo functionalised graphene
(AuNp/G/PhNO₂)**

Scheme 6: The illustration for the immobilization of gold nanoparticles onto nitrophenylazo functionalized graphene surface.

3.5 Preparation of G/PhNO₂ and AuNp/G/PhNO₂ modified GCE

3.5.1 Chemicals and reagents

Newly synthesised AuNp/G/PhNO₂. Methanol (CH₄O), hexaamineruthenium chloride (Ru(NH₃)₆Cl₃) were purchased from Sigma-Aldrich (South Africa). Milli-Q de-ionized water (resistance over 18.2 MΩ cm) purified by a Milli-QTM system was used throughout.

3.5.2 Pre-cleaning of working electrode

Prior to electrochemical synthesis and modifications, glassy carbon electrode (GCE) was polished consecutively with aqueous slurries of 1.0, 0.3 and 0.05 micro alumina powder, for 1 minute on a micro-cloth pad (Buehler) and rinsed thoroughly with doubly distilled water between each polishing step. Residual polishing material was removed by washing successively with 1: 1 water to nitric acid solution, ethanol and doubly distilled water in an ultrasonic bath, air dried and used immediately.

3.5.3 Experimental procedure

The obtained AuNp/G/PhNO₂ was dispersed in 1:1 water to methanol solution to yield 1 mg/mL dispersion by ultra-sonication for 1 h. Then, 2 μL of it was drop-casted on the pre-treated glassy carbon electrode and dried in a desiccator for 24 h at room temperature forming a thin film modified glassy carbon electrode depicted as GCE/AuNp/G/PhNO₂. 0.1 M PBS (pH 7.2) solution was used to prepare 5 mM hexaamineruthenium chloride (HRC) solution. Relative electroactivity (I_{rel}) of the modified electrode was quantified by cyclic voltammetry in the presence of the prepared 5 mM HRC electrolyte as redox probe.

3.6 Preparation of AuNp/G/PhNO₂ and G/PhNO₂ composite with [Ru(bpy)₃]²⁺ mediated in Nafion on GCE

3.6.1 Chemicals and reagents

AuNp/G/PhNO₂ and G/PhNO₂ were prepared as described in section 3.3 and 3.4. tris ruthenium 2, 2-bipyridine chloride (Ru(bpy)₃Cl₂) and methanol (CH₄O) were purchased from Sigma Aldrich, Nafion 117 solution purchased from Fluka, Milli-Q de-ionized water (resistance over 18.2 MΩ cm) purified by a Milli-QTM system was used for aqueous solution preparations throughout.

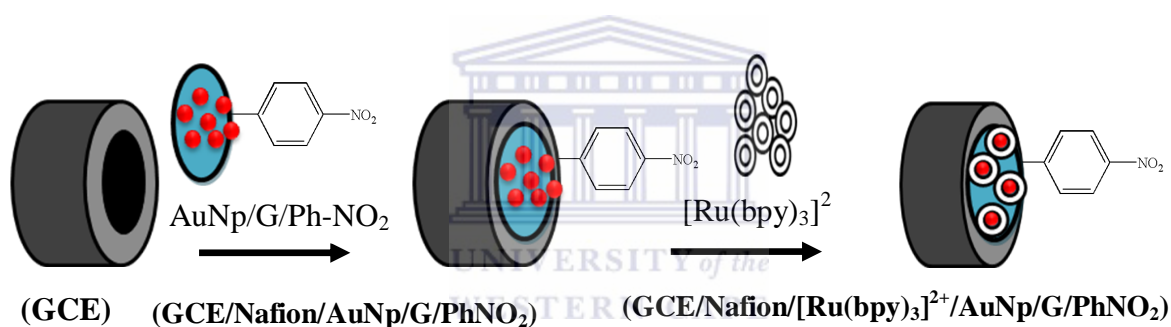
3.6.2 Experimental procedure

Nafion stock solution was diluted with 1:1 water to methanol mixture to yield 1% (v/v) solution. AuNp/G/PhNO₂ was dispersed in the 1% (v/v) Nafion solution by ultra-sonication for 30 min to form 1 mg mL⁻¹ uniform nanocomposite. 4 μL of it was drop-casted on the surface of a pre-cleaned GCE and then excess solvent was allowed to evaporate to dryness in the open at room temperature to form a thin film (Note that the GC electrode was first cleaned following the steps described in section 3.5.2).

The Nafion/AuNp/G/PhNO₂ modified GC electrode was placed in 1 mM Ru(bpy)₃Cl₂ aqueous solution for 2 h to incorporate [Ru(bpy)₃]²⁺ via electrostatic and ion-exchange interactions, forming a thin film modified glassy carbon electrode depicted as GCE/Nafion/[Ru(bpy)₃]²⁺/AuNp/G/PhNO₂. Large amount of the cationic signal probe [Ru(bpy)₃]²⁺ were entrapped on the modified electrode due to the enlarged electroactive surface area of AuNp/G/PhNO₂ immobilized in the anionic matrix of the perfluorosulfonate

ionomer. Also the slight negative charge conferred on the nanocomposite by PhNO₂ units enhanced the quantity and stability of the cation electrostatically.

Two other pre-cleaned GC electrodes were also modified, one with G/PhNO₂ and the other without any catalyst following the same protocol. They were depicted as GCE/Nafion/[Ru(bpy)₃]²⁺/G/PhNO₂ and GCE/Nafion/[Ru(bpy)₃]²⁺ respectively and were all characterized comparatively. Previous research has shown that Nafion as a perfluorosulfonate polymer with a micellar pore structure can incorporate other molecules into its bulk membrane through coulombic and/or hydrophobic interactions [38-39, 67].



Scheme 7: The illustration of the stepwise preparation of Nafion/[Ru(bpy)₃]²⁺/AuNp/G/PhNO₂ on GCE.

3.7 Electrochemical synthesis of PDMA and PDMA/ AuNp/G/PhNO₂ composite

3.7.1 Chemicals and reagents

AuNp/G/PhNO₂. 2, 5 dimethoxyaniline (DMA), hydrochloric acid (HCl, 37% purity, density 1.19 kg/L), ethanol (C₂H₆O), sodium phosphate dibasic (Na₂HPO₄), sodium phosphate monobasic (NaH₂PO₄), potassium Chloride (KCl) were purchased from Sigma-Aldrich

(South Africa). Milli-Q de-ionized water (resistance over 18.2 M Ω cm) purified by a Milli-QTM system was used throughout.

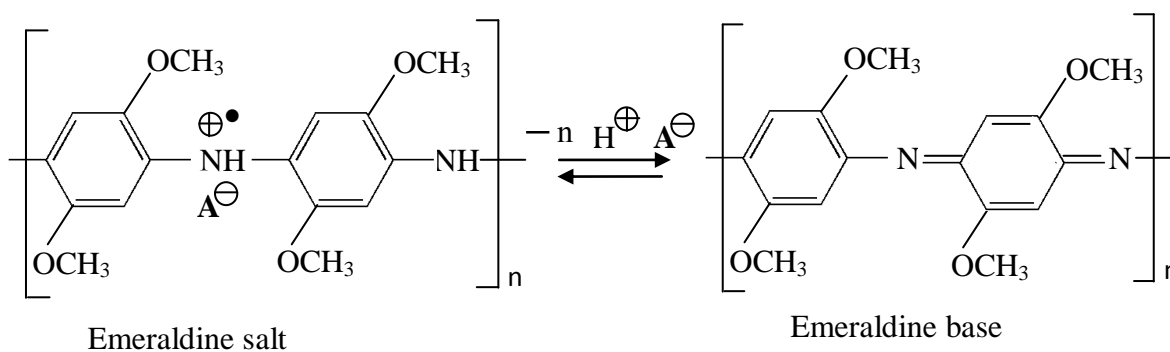
3.7.2 Experimental procedure

Prior to modification, glassy carbon electrode was cleaned as described in section 3.5.2. The electro-polymerization solution was prepared by accurately weighing 0.1915 g of 2, 5 dimethoxyaniline into 25 mL round bottom flask and made up to mark with 1 M HCl solution to give 0.05 M DMA solution. The solution was made to dissolve completely by sonicating for few minutes. 10 mL of the DMA solution was measured out with a 10 mL measuring cylinder and transferred into 20 mL electrochemical cell. The system was set up as described in chapter 2, section 2.14 without the working electrode initially.

The growth solution was de-aerated using dry argon gas for 10 min to remove dissolved oxygen and then the pre-cleaned GCE was connected. Argon atmospheric head space was maintained throughout the duration of the experiment. PDMA was electrodeposited on the GCE by scanning its potential repeatedly between -200 and +900 mV for 10 cycles at a scan rate 50 mV/s. After electro-polymerization the electrode was washed with de-ionized water on the sides to remove the excess monomer from the electrode surface (see scheme 8 for proposed mechanism of protonation).

The same electro-synthetic protocol was followed to synthesise various compositions of PDMA/AuNp/G/PhNO₂ on GCE with the monomer solution containing 0.2, 0.3, 0.6 and 0.8% AuNp/G/PhNO₂ correspondingly. The electrochemical behaviour of GCE/PDMA and GCE/PDMA/AuNp/G/PhNO₂ was investigated in 1.0 M HCl solution by cyclic voltammetry in the potential range between -200 to 900 mV and at varying scan rates (10-100 mV/s) as

well as in 0.1 M phosphate buffer (pH 7.2) in the potential range -1200 to 1200 mV. The 0.1 M phosphate buffered saline (PBS) solution was prepared using 0.1 M Na₂HPO₄; 0.1 M NaH₂PO₄; 0.1 M KCl and kept at 4 °C before use.



Scheme 8: The protonation of PDMA/AuNp/G/PhNO₂ emeraldine salt to emeraldine base by conditioning in PBS



3.8 Spectroscopic characterisation

3.8.1 Ultraviolet–visible spectroscopy

The UV-Vis spectra were recorded on a Nicolet Evolution 100 Spectrometer (Thermo Electron Corporation, UK) at a wavelength of 190 nm to 800 nm. Dilute solutions of the samples (4 mL) were in 5 mL fused quartz cuvette before measurements. The cuvette was thoroughly washed with ethanol and distilled water between every measurement.

3.8.2 Raman spectrometry

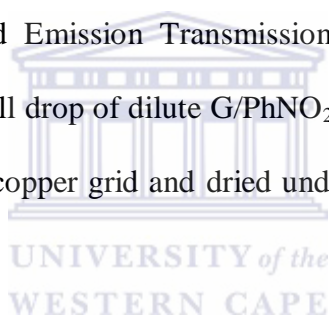
Raman measurements were carried out with Raman spectrometer (LabRam HR by Jobin-Yvon Horiba scientific Explora, France with a 1200 lines mm⁻¹ grating) coupled to a

microscope (Model BX41, Olympus). The excitation of Raman scattering was operated with a laser at a wavelength of 532 nm. The laser beam was focused on the sample by means of an x 100 microscope objective. The samples were prepared by drop coating 10 μ L of G/PhNO₂ and GO suspensions on glass slides followed by drying in air at room temperature to form a homogenous coverage before measurements.

3.9 Microscopic characterisations

3.9.1 High resolution transmission electron microscopy (HRTEM)

HRTEM analysis of the mounted G/PhNO₂ and AuNp/G/PhNO₂ were done using Tecnai G2 F20X-Twin MAT 200 kV Field Emission Transmission Electron Microscope from FEI (Eindhoven, Netherlands). A small drop of dilute G/PhNO₂ and AuNp/G/PhNO₂ suspensions were placed on a carbon coated copper grid and dried under electric bulb for 30 min before measurements.



3.9.2 Scanning electron microscopy (SEM)

Scanning electron microscopy images of G/PhNO₂ and AuNp/G/PhNO₂ were recorded with a Zeiss Auriga HRSEM analyzer using the secondary electron (SE) mode by interchangeable accelerating voltages of 25 kV and a maximum resolution of 20 μ m. The chemical composition of the sample was obtained by energy dispersive x-ray spectroscopy (EDX) which was coupled to the SEM machine. The SEM/EDX samples for G/PhNO₂ and AuNp/G/PhNO₂ were prepared by placing solid nano-material onto a carbon adhesive mounted on aluminium stubs.

3.9.3 Atomic force microscopy (AFM).

Atomic force microscopy (AFM) was used to study the surface morphology of G/PhNO₂ and AuNp/G/PhNO₂ in ambient conditions using Veeco NanoMan V model (Cambridge, USA). The samples were scanned with a silicon tip at a spring constant of 1-5 N/m and resonance frequency of 60-100 kHz in a non contact mode. Samples were prepared by drop coating 10 μL of G/PhNO₂ and AuNp/G/PhNO₂ suspensions on glass slides followed by drying in air at room temperature to form a homogenous coverage before measurements.

3.10 Electrochemical characterisations

3.10.1 Cyclic voltammetry (CV), Square-wave voltammetry (SWV), chronocoulometry and chronoamperometry

All cyclic voltammetry, square wave voltammetry, chronocoulometry and chronoamperometry experiments were recorded with BASi 100B electrochemical work station (LG Fayette) using the conventional three-electrode system described in chapter two, section 2.9. The working electrode used was glassy carbon electrode (surface area = 0.071 cm²), the counter electrode was platinum wire (diameter 1.0 mm) while a platinum mesh or wire and all potentials mentioned in all the experimental results were referred to standard silver/silver chloride (saturated KCl solution) electrode (Bioanalytical Systems Ltd., UK).

10 mL of all the electrolytes used were measured into 20 mL electrochemical cell and de-aerated with argon gas for at least 10 min before measurements. Argon atmospheric head space was maintained throughout the duration of all the experiments, analytical grade argon from Afrox, South Africa was used in degassing the system, alumina micro-polish (1.0, 0.3

and 0.05 mm alumina slurries) and polishing pads (Buehler, IL, USA) were used for polishing the electrode.

3.10.2 Electrochemical impedance spectroscopy (EIS)

All electrochemical impedance spectroscopy studies were measured using Voltalab PGL 402 from Radiometer Analytical (Lyon, France) and the data plotted in the form of complex plane diagrams (Nyquist plots) at perturbation amplitude of 10 mV. 10 mL of all the electrolytes used were measured into 20 mL electrochemical cell and de-aerated with argon gas for at least 10 min before measurements. Argon atmospheric head space was maintained throughout the duration of all the experiments, analytical grade argon from Afrox, South Africa was used in degassing the system, alumina micro-polish (1.0, 0.3 and 0.05 mm alumina slurries) and polishing pads (Buehler, IL, USA) were used for polishing the electrode.

3.11 The application of Nafion/[Ru(bpy)₃]²⁺/AuNp/G/PhNO₂ and Nafion/[Ru(bpy)₃]²⁺/G/PhNO₂ sensor platforms for TPA detection via ECL system

3.11.1 Chemicals and reagents

Tri-n-propylamine (TPA) (C₉H₂₁N), sodium phosphate dibasic (Na₂HPO₄), sodium phosphate monobasic (NaH₂PO₄), potassium Chloride (KCl) was purchased from Sigma Aldrich. Milli-Q de-ionized water (resistance over 18.2 MΩ cm) purified by a Milli-QTM system was used for preparation of 0.1 M PBS (pH 7.2).

3.11.2 Experimental procedure

Two differently modified carbon screen printed electrodes (CSPE), CSPE/Nafion/[Ru(bpy)₃]²⁺/G/PhNO₂ and CSPE/Nafion/[Ru(bpy)₃]²⁺/AuNp/G/PhNO₂ where

prepared following the same protocol described in sections 3.6. They were applied for the ECL detection of TPA adopting the coreactant method as illustrated in Figure 3.1 . Cyclic voltammetric technique and the conventional three electrode set-up as illustrated in Chapter two, section 2.14, Figure 2.22 was adopted. The modified electrodes were tested in a series of TPA solutions with different concentrations prepared with 0.1 M PBS solution. And the ECL responses under continuous scanning to obtain a relative steady ECL intensity was recorded in a special 10 mL fused quartz cuvette

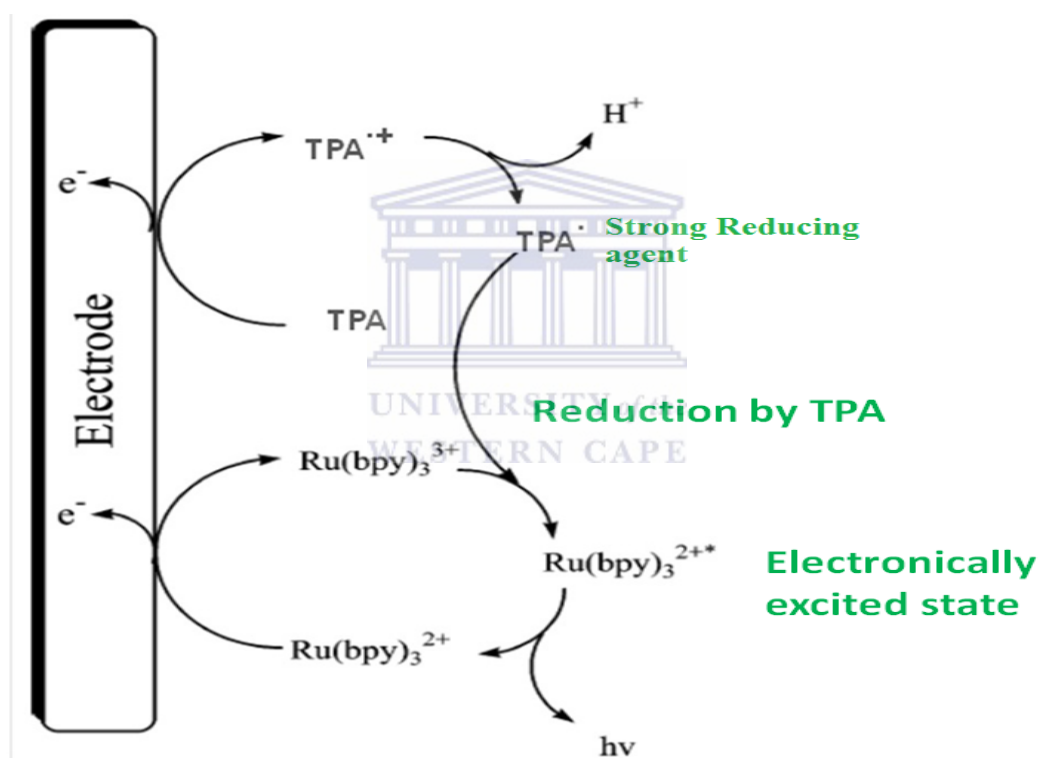


Figure 3.1: The schematic illustration of [Ru(bpy)₃]²⁺/TPA ECL system.

3.12 Preparation of immunosensor

3.12.1 Chemicals and reagent

Deoxynivalenol (formula weight, 296.32 g/mol) was purchased from Sigma-aldrich, USA (product code 01567-5MG), monoclonal antibody of deoxynivalenol (DON, 1 mg) was purchased from Antibodies-online, Germany (order number ABIN1022125), ELISA kit (Veratox 5/5 for deoxynivalenol: 0.1 ppm) was purchased from Neogen Corporation, certified barley and coffee reference materials were purchased from RIDASCREEN®.

Methanol (CH₄O, HPLC grade), ethanol (C₂H₆O, analytical grade), Bovine serum albumin (BSA), 1-ethyl-3-(3-dimethylaminopropyl) carbodiimide hydrochloride (EDC), N-hydroxysuccinimide (NHS), basic salts including sodium phosphate dibasic (Na₂HPO₄), sodium phosphate monobasic (NaH₂PO₄), potassium Chloride (KCl) used in the preparation of 0.1 M phosphate-buffered saline (pH 7.2) were all purchased from Sigma-Aldrich (SA).

All other chemicals were of analytical grade, Milli-Q de-ionized water (resistance over 18.2 MΩ cm) purified by a Milli-QTM system was used for aqueous solution preparations throughout. And analytical grade argon from Afrox, South Africa was used to degas the system.

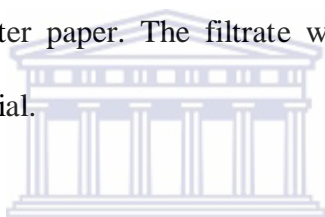
3.12.2 Preparation of standard solutions

Deoxynivalenol (5 mg, formula weight 296.32 g/mol) from Sigma-aldrich was dissolved in 1 mL of analytical grade methanol to give 5 mg/mL (0.0169 M) stock solution and stored as 250 μL aliquots each in tightly sealed vials at -20 °C. Before every experiment, 1x10⁻³ M and 1x10⁻⁶ M of deoxynivalenol standard (DONag) solutions were prepared in a (3:1) mixture of

methanol/PBS solution (hereafter referred to as methanolic phosphate buffer saline (MPBS) solution) and used for further dilutions. The monoclonal antibody of deoxynivalenol (1 mg) was reconstituted by adding 1 mL deionised water to give 1 mg/mL stock solution and stored as 250 μ L aliquots each in tightly sealed vials at -20 $^{\circ}$ C.

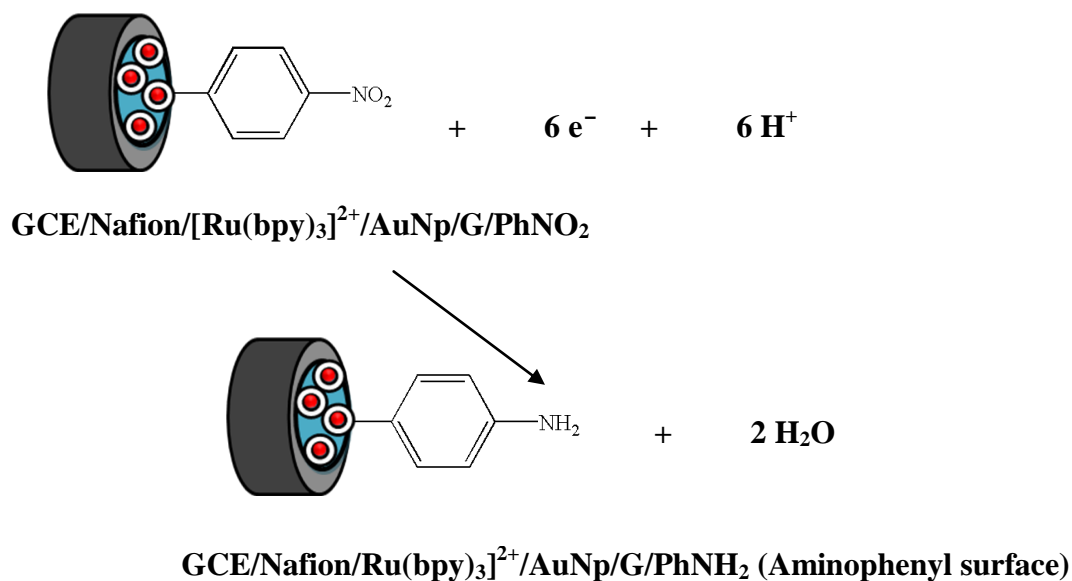
3.12.3 Sample preparation and extraction

Following the extraction procedure described by Veratox Elisa Kit manual, 10 g of ground certified corn, wheat and roasted coffee reference materials were each weighed out into separate 250 mL capped pre-cleaned flask, mixed with 100 mL of deionised water and shaken vigorously using hand for 3 min. The mixture was allowed to settle for 2 min and then filtered using a Whatman #1 filter paper. The filtrate was collected for analysis without further preparation for each material.



3.12.4 DON antibody immobilization

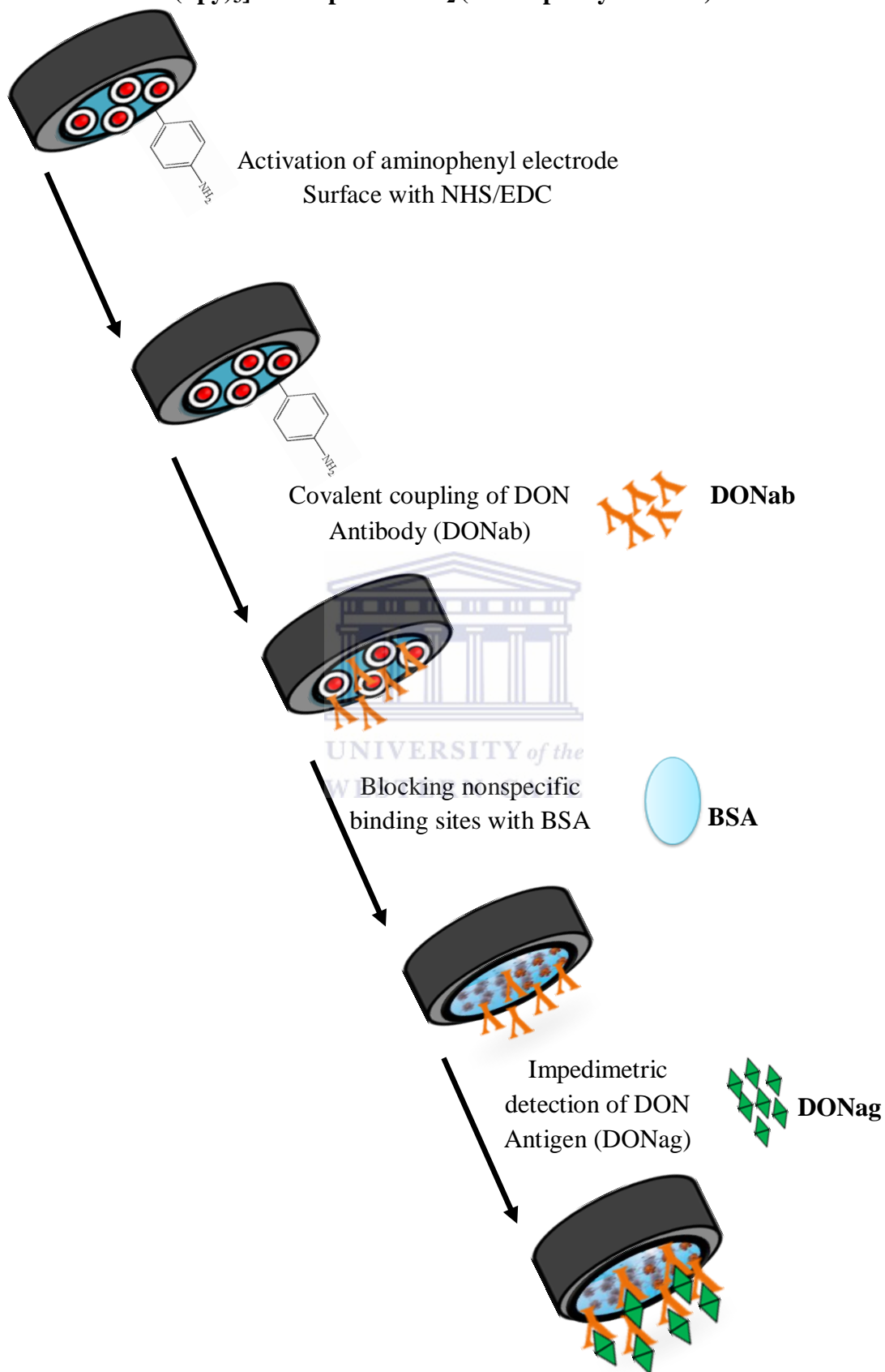
Label free electrochemical inhibition based immunosensors for sensitive detection of DON mycotoxin were developed with three differently modified electrodes, GCE/Nafion/[Ru(bpy)₃]²⁺/G/PhNO₂, GCE/Nafion/[Ru(bpy)₃]²⁺/AuNp/G/PhNO₂ and GCE/PDMA/AuNp/G/PhNO₂, prepared as described in sections 3.6 and 3.5 correspondingly. Before immobilization of antibody, each modified electrode was first reduced electrochemically to generate an aminophenyl surface in 0.1 KCl solutions by two cyclic voltammetric scans over potential range 0 to -1200 mV at 50 mV/s [175-177]. See illustration in Scheme 9. All the electrodes were reduced alike.



Scheme 9: Electrochemical reduction of 4-nitrophenyl group (-PhNO₂) to 4-aminophenyl group (-PhNH₂) on the electrode surface.

The electrode was rinsed out from the sides after reduction using deionised water. The amine on the electrode surface was activated by incubation for 60 min with 1:1 mixture of 0.5 mM EDC and 8 mM NHS. After rinsing the electrode from the side with 0.1 M PBS (pH 7.2) solution, 30 μL of 0.2 $\mu\text{g}/\mu\text{L}$ (in 0.1 M PBS, pH 7.2) monoclonal deoxynivalenol antibody (DONab) was spread on the electrode surface and incubated for 30 min at room temperature. The electrode was again rinsed from the side using 0.1 M PBS (pH 7.2) solution to remove any physically bound antibody and then 10 μL of BSA was spread on the electrode surface to block nonspecific binding sites for 30 min at room temperature and rinsed with PBS (pH 7.2) before making impedimetric measurements [177-179]. The immobilized electrodes were denoted as GCE/Nafion/[Ru(bpy)₃]²⁺/G/PhNH₂/DONab, GCE/Nafion/[Ru(bpy)₃]²⁺/AuNp/G/PhNH₂/DONab and GCE/PDMA/AuNp/G/PhNH₂/DONab. All experiments were carried out at room temperature.

GCE/Nafion/Ru(bpy)₃]²⁺/AuNp/G/PhNH₂ (Aminophenyl surface)



Scheme 10: The illustration for stepwise immunosensor fabrication processes.

3.12.5 Application of the immunosensors as impedimetric DON mycotoxin sensor

The three immunosensors GCE/Nafion/Ru(bpy)₃]²⁺/G/PhNH₂/DONab, GCE/Nafion/Ru(bpy)₃]²⁺/AuNp/G/PhNH₂/DONab, and GCE/PDMA/AuNp/G/PhNH₂/DONab were tested for impedimetric sensing of deoxynivalenol mycotoxin in various concentrations (0 ng/mL, 6 ng/mL, 12 ng/mL, 18 ng/mL, 24 ng/mL, 30 ng/mL and 36 ng/mL) of the deoxynivalenol standard (DONag) solutions prepared in section 3.12.2. In order to compare the different electrode measurements under equivalent conditions and to obtain the normalised values that were plotted, the charge transfer resistance (R_{ct}) value for the blank (0 ng/mL DONag) was subtracted from the R_{ct} values of DONag concentrations. The values of the ΔR_{ct} observed were plotted against the concentrations to construct a standard curve for each of the sensors.

3.12.6 Real sample studies

The applicability of these immunosensors in determining DON mycotoxin in natural samples was demonstrated by testing corn, wheat and roasted coffee purchased from RIDASCREEN®. They were extracted according to section 3.12.3. The pH of the extracted samples was 6.5 on the average and was adjusted to pH 7.2 by adding few drops of 0.1 M NaOH. The samples were then analysed without any further pre-treatment. Following the same protocol in section 3.12.5, 10 μ L of the filtrate was spiked successively in 5 mL MPBS solution contained in an electrochemical cell for impedimetric measurements of DONag.

3.12.7 Competitive direct enzyme linked immunosorbent assay (CD-ELISA)

Veratox 5/5 ELISA kit was used to perform a CD-ELISA of various DONag standard concentrations (0 ng/mL, 25 ng/mL, 50 ng/mL, 100 ng/mL and 200 ng/mL) as described in section 3.12.5. And also of the corn, wheat and roasted coffee reference materials.



Chapter Four

Results and discussion- Part one

The detailed account of characterizations for the synthesised gold nanoparticles-dotted 4-nitrophenylazo functionalised graphene (AuNp/G/PhNO₂) is presented including its application in constructing thin film sensor platforms with: tris (bipyridine) ruthenium (II) chloride ([Ru(bpy)₃]Cl₂) as a cationic reactant mediated in Nafion and poly (2, 5-dimethoxyaniline).

4.1 Spectroscopic and microscopic characterisations of AuNp/G/PhNO₂

4.1.1 Ultraviolet-visible spectroscopy (UV-Vis)

UV-visible spectroscopy has been widely adopted in studying the electronic structure of graphene. The UV-Vis spectrum of GO in Figure 4.1 shows an absorption peak at 230 nm, which is consistent with those in the literature [180-182]. This peak corresponds to π - π^* transitions of aromatic C=C bond. After formation of graphene through the post-reduction of the 4-nitrophenylazo functionalised GO, the peak was observed at 260 nm. The red shift from 230 nm to 260 nm suggests that the electronic conjugation within graphene sheets was restored. Characteristic absorption peak for gold nanoparticle was observed at 530 nm corresponding to the surface plasmon absorption of Au nanoparticles [183-184].

Noticeably, after the chemical reduction of gold ions in the functionalised graphene, the UV-Vis absorption spectroscopy neither showed any absorption peak at 530 nm nor at 260 nm.

This quenching of the surface plasmon absorption peak is most probably attributable to the decrease in electron density due to the charge transfer from Au nanoparticles to G/PhNO₂ [185]. Indicating that above 90% of the synthesized gold nanoparticles were strongly coated on the functionalised graphene (AuNp/G/PhNO₂) surface [51, 186]

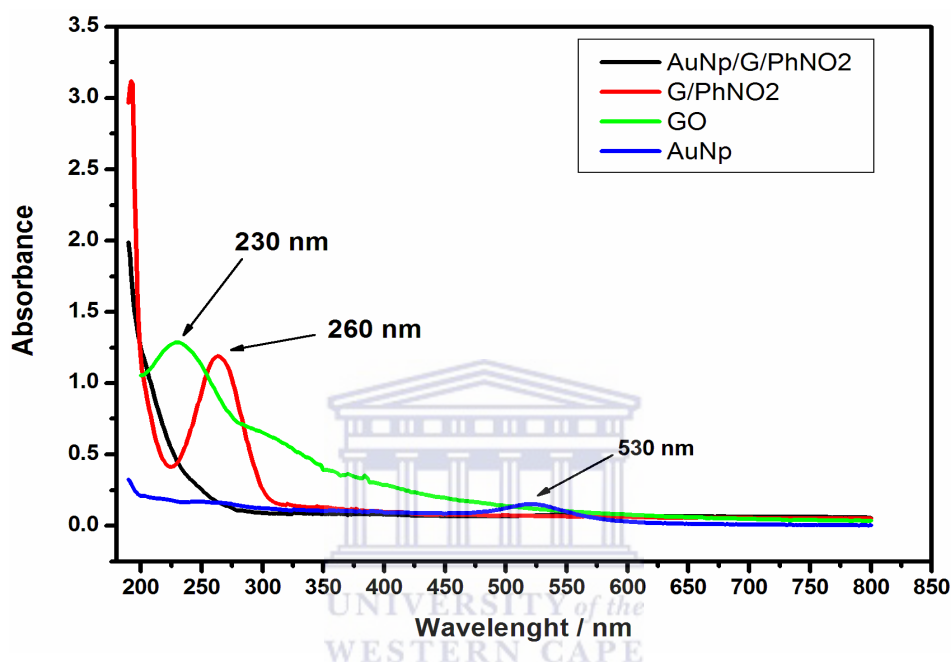


Figure 4.1: UV-visible spectra of AuNp, GO, (G/PhNO₂), and (AuNp/G/PhNO₂).

Based on the spectrum data, the band gaps E_g^* for GO and G/PhNO₂ were determined by applying equation (3), in section 2.8, chapter two. The cut-off wavelength was estimated from the intersection of the tangent line of the peak with the wavelength axis. The band gaps of G/PhNO₂ and GO were calculated as 7.6402×10^{-28} eV and 8.6367×10^{-28} eV respectively. The results of this investigation showed that the incorporation of nitrophenylazo units into graphene structure acted as dopant and lead to a shift in absorbance of the composite towards longer wavelengths.

This is due to the introduction of more molecular orbital states to the total possible states by the PhNO₂ units and so a lower gap in energy exists between the HOMO and LUMO of the composite, causing lower energy transitions as expected by the theory of molecular orbitals [103]. From a qualitative perspective therefore, it is reasonable for a shift to the right to occur, validating the observed spectrum in this investigation.

4.1.2 Raman spectroscopy

Raman spectra of the nanocomposite were examined to further prove the reduction of the functionalised graphene oxide to graphene in the post- reaction step. D band and G band in Raman spectra are usually utilized to characterize the reduction of graphene oxide. The shift of G band to lower wave number and the increase of I_D/I_G ratio (peak intensity of D band: peak intensity of G band) are two major indicators for graphene oxide reduction. As exhibited in Figure 4.2, G band of graphene oxide shifts from 1599 cm⁻¹ to 1587 cm⁻¹ and I_D/I_G ratio increases from 1.00 to 1.36. This agrees well with most reports on graphene oxide reduction [50, 180, 187-188].

The cooperation between D and G peaks gives rise to a D+G combination band induced by disorder at about 2930 cm⁻¹; however the observed low strength of the D+G peak in the spectra indicates a very small disorder in the sample. The 2D band shape and the high energy second-order 2D band at 2675 cm⁻¹ indicate single layer structure and an increase in thickness of G/PhNO₂, which is attributed to the attachment of 4-nitrophenylazo units. The results of UV-Vis and Raman spectra confirm the reduction of GO to graphene in the post-reduction step.

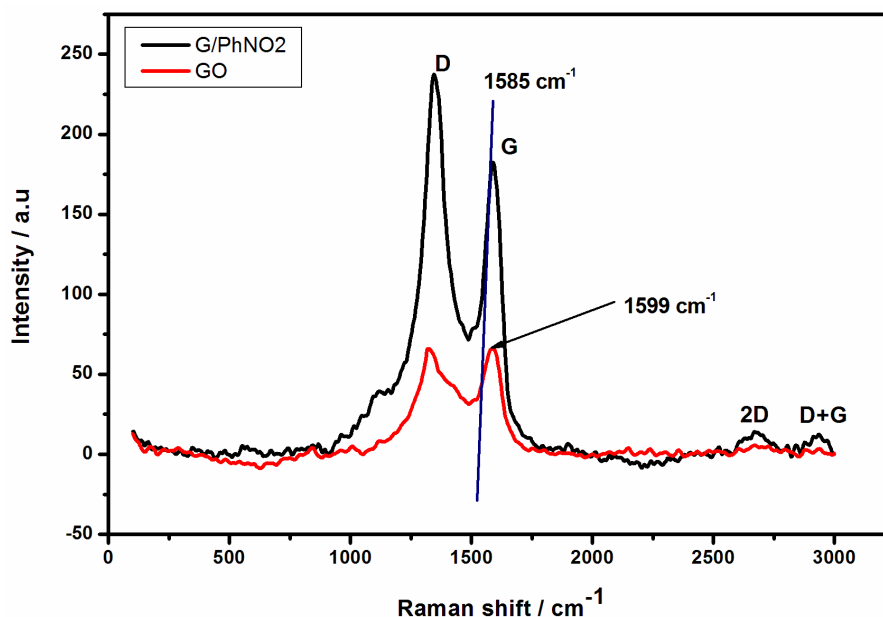


Figure 4.2: Raman spectra of GO and G/PhNO₂.

4.1.3 Transmission electron microscopy (TEM)

The morphology and surface reactivity of the gold nanoparticles-dotted 4-nitrophenylazo functionalised graphene (AuNp/G/PhNO₂) was studied by examining its high resolution transmission electron microscopy (HRTEM), scanning electron microscopy (SEM) and atomic force microscopy (AFM) images comparatively with that of 4-nitrophenylazo functionalised graphene (G/PhNO₂). The HRTEM image in Figure 4.3 (a) clearly shows dark spots as opposed to what is observed for G/PhNO₂ in Figure 4.3 (b).

The presence of such spots can be attributed to the attachment of gold nanoparticles on to G/PhNO₂ surface. Similar dark spots have been observed by other authors with both pristine graphene and functionalised graphene as described elsewhere [50, 187-189]. It could be observed in Figure 4.3 (a) that gold nanoparticles appeared as dark dots on a light shaded graphene substrate with average particle size of 30 nm. The G/PhNO₂ surface was uniformly

decorated by the Au nanoparticles with very few aggregations, indicating a strong interaction between the G/PhNO₂ and Au nanoparticles.

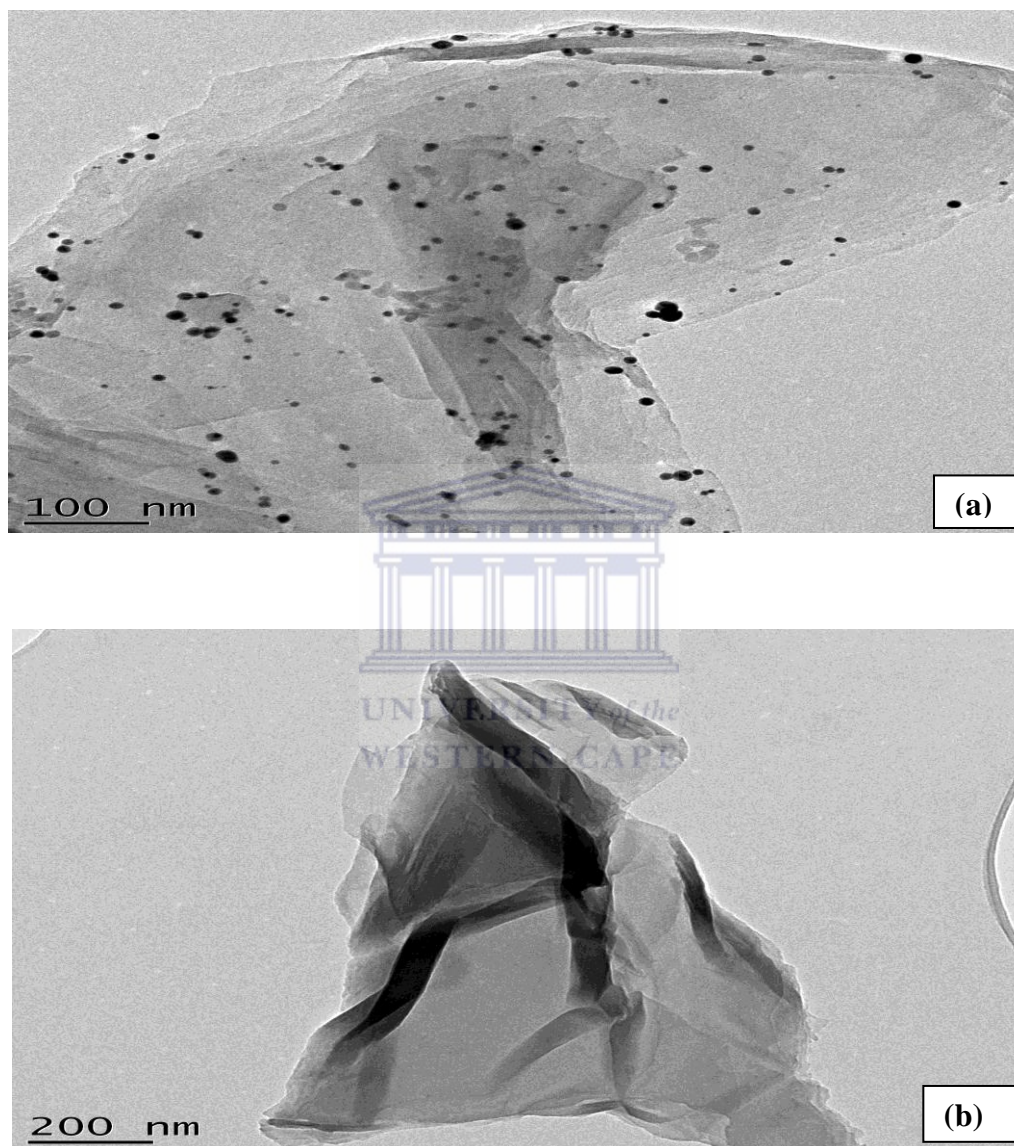
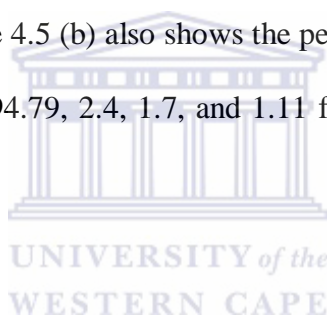


Figure 4.3: HRTEM images of (a) AuNp/G/PhNO₂ and (b) G/PhNO₂.

A monolayer graphene sheet could be observed clearly in Figure 4.3 (b), indicating a smooth surface of the chemically reduced G/PhNO₂ single layer. This corroborates the fact that there was no aggregation of graphitic sheets after post-reduction step. Indicating the presence of negatively charged PhNO₂ units, which in turn imparted sufficient electrostatic repulsion to keep graphene sheets separated in solution [41].

4.1.4 Scanning electrochemical microscopy (SEM) and Energy-dispersive X-ray (EDX) spectrum

Figure 4.4 (b) shows the elemental composition of AuNp/G/PhNO₂ with percentage atomic compositions of 90.34, 2.22, 5.13, 1.27 and 1.04 for Carbon, Nitrogen, Gold, Oxygen and Chlorine respectively. And Figure 4.5 (b) also shows the percentage composition of G/PhNO₂ with percentage composition of 94.79, 2.4, 1.7, and 1.11 for Carbon, Oxygen, Nitrogen and Chlorine respectively.



The EDX results confirmed the functionalisation of graphene with 4-nitrophenylazo and gold nanoparticle during the chemical preparation. The surface morphology of AuNp/G/PhNO₂ is shown in Figure 4.4 (a). It could be further observed that gold nanoparticles were homogeneously embedded into the graphene lattice compared to the surface morphology image of G/PhNO₂ in Figure 4.5 (a).

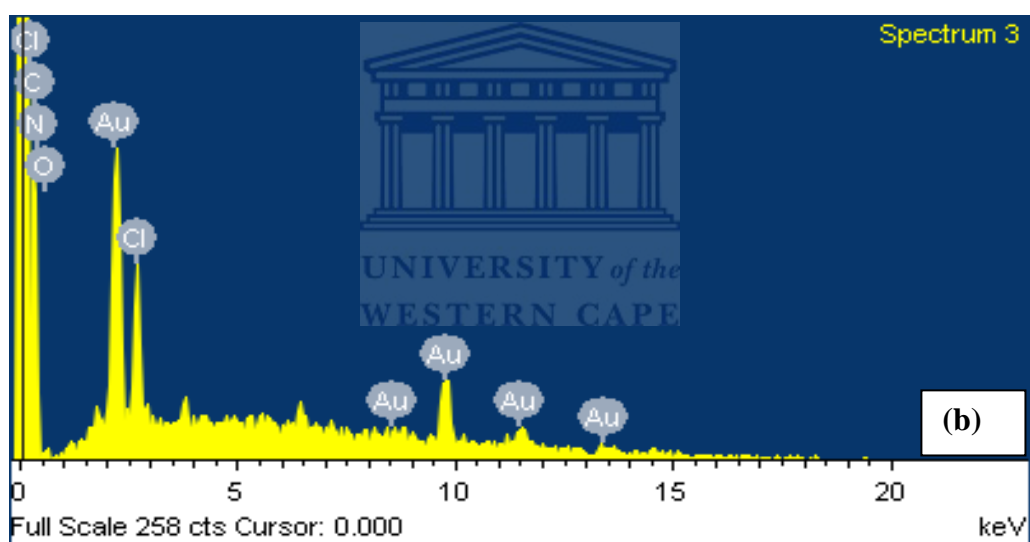
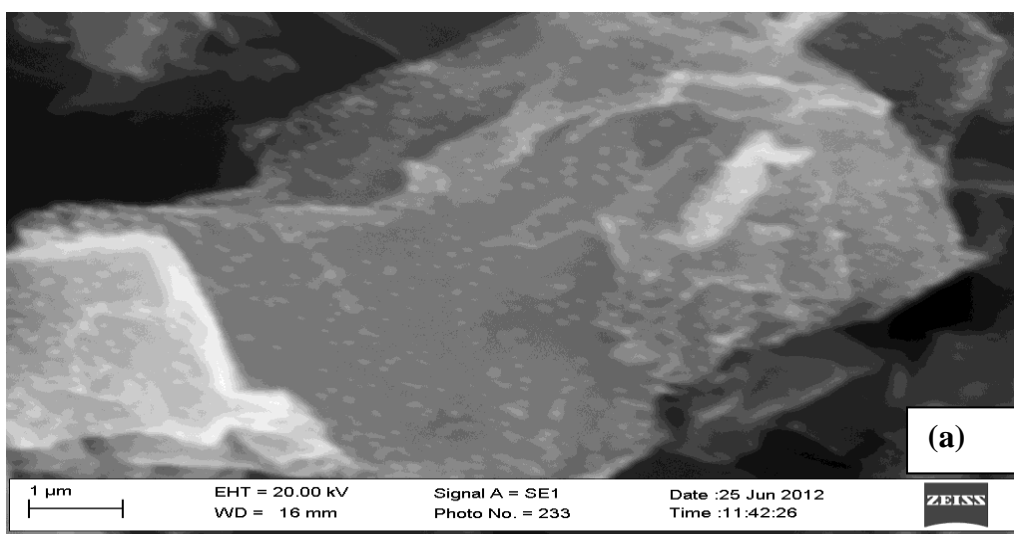


Figure 4.4: (a) SEM image of AuNp/G/PhNO₂ and (b) EDX spectrum of AuNp/G/PhNO₂.

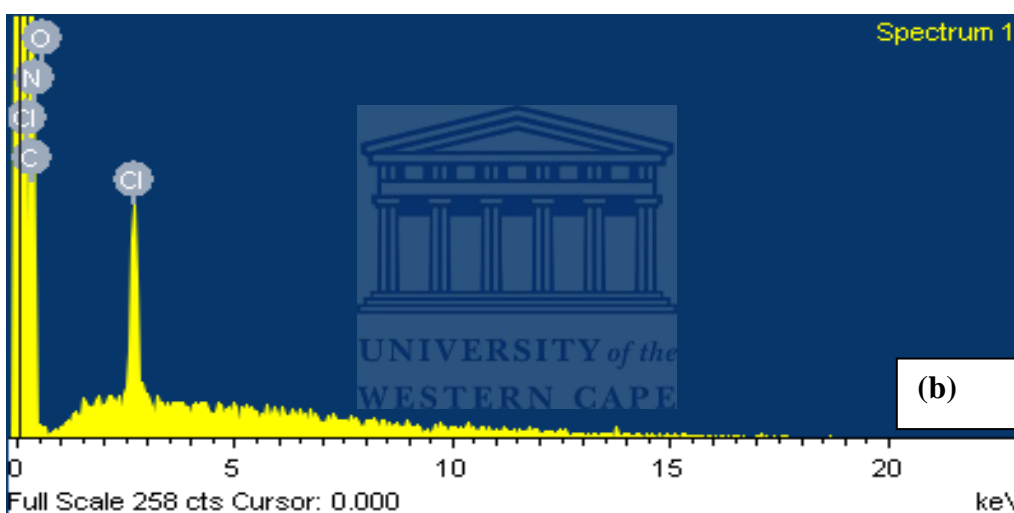
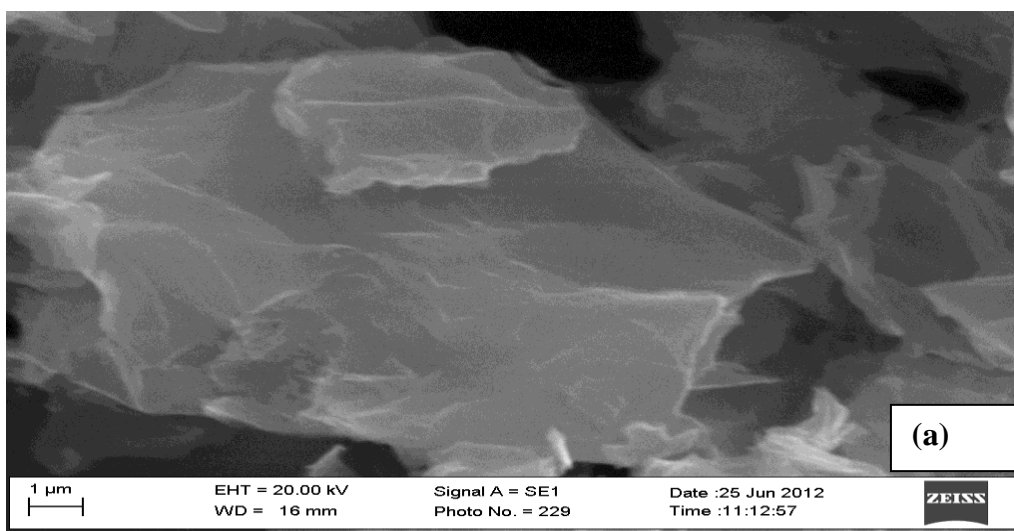


Figure 4.5: (a) SEM image of G/PhNO₂ and (b) EDX spectrum of G/PhNO₂.

4.1.5 Atomic force microscopy (AFM)

The 2-D and 3-D AFM images of the AuNp/G/PhNO₂ nano-sheets are shown in Figure 4.6 (a)-(b). A lot of small dots on the graphene nano-sheet that appears to be in the order of few nanometres could be observed suggesting the successful incorporation of gold nanoparticles with the graphene and an enlarged surface reactivity area compared to that of G/PhNO₂ in Figure 4.6 (c) – (d). This correlates with the HRTEM results.

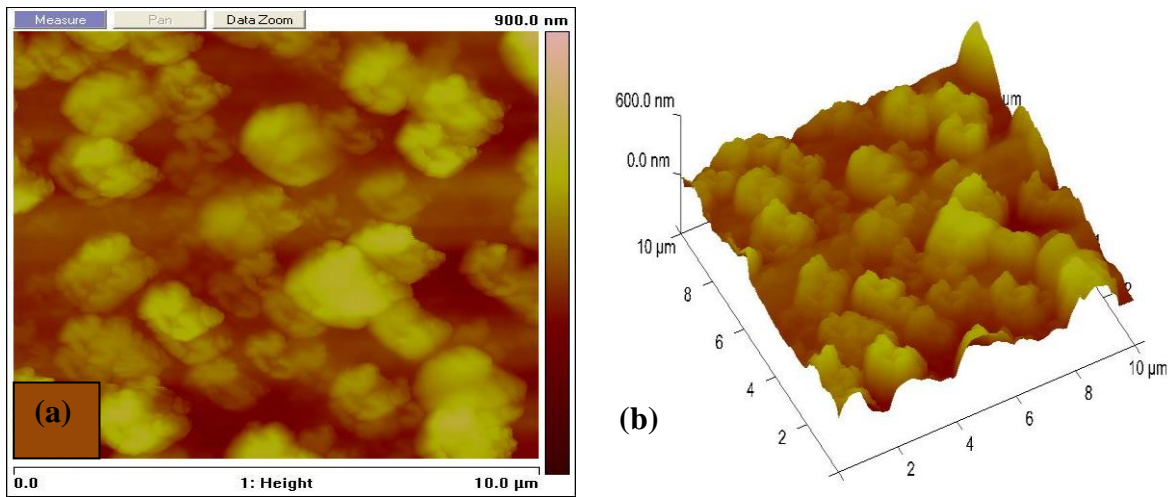


Figure 4.6: (a) 2-D and (b) 3-D AFM images of AuNp/G/PhNO₂.

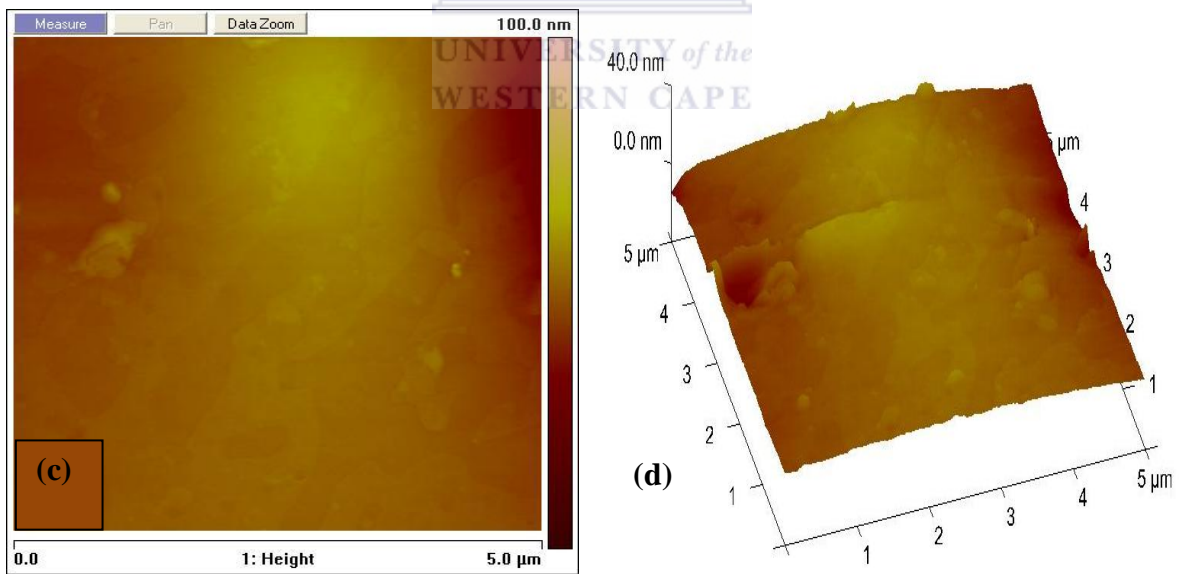


Figure 4.6: (c) 2-D and (d) 3-D AFM images of G/PhNO₂.

4.2 Electrochemistry of starting materials

4.2.1 Electrochemical behaviour of [Ru(bpy)₃]Cl₂ in solution

Figure 4.7 (ii) shows the cyclic voltammogram of bare GCE in 0.5 mM [Ru(bpy)₃]Cl₂ and 0.1 M PBS (pH 7.2) solution and (i) is the cyclic voltammogram of bare GCE in 0.1 M PBS (pH 7.2) solution. The CVs were recorded over a potential range of 650 mV to 1350 mV at a scan rate 50 mV/s. One oxidation peak was observed on the anodic scan; peak a, ($E_{p,a} = 1190$ mV, $I_{p,a} = 4.882$ μ A) and one reduction peak was observed as well on the cathodic scan, peak b, ($E_{p,c} = 1073$ mV, $I_{p,c} = -2.844$ μ A).

Peaks a and b were attributed to the oxidation of tris (bipyridine) ruthenium (II) chloride to [Ru(bpy)₃]³⁺ and its reduction back to [Ru(bpy)₃]²⁺ respectively as illustrated in the equation below.



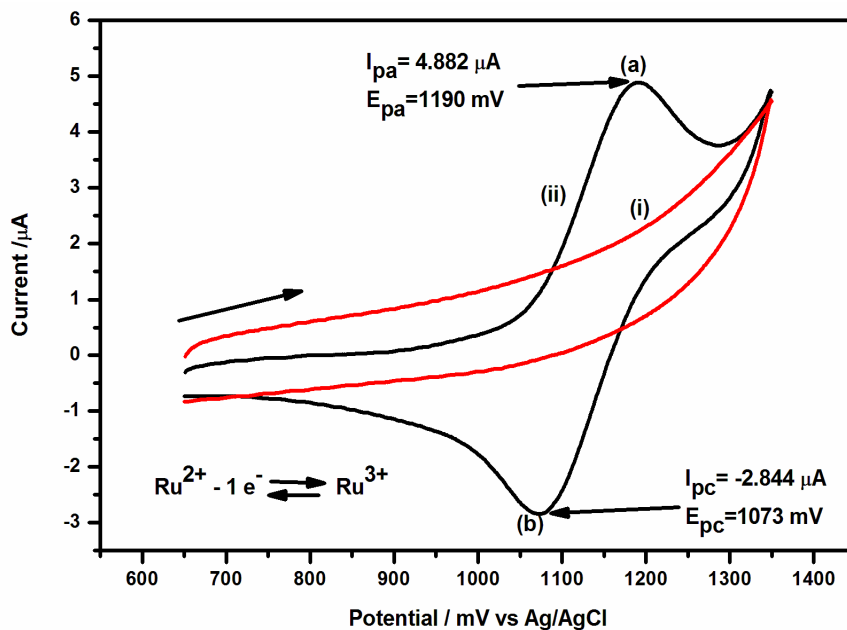


Figure 4.7: (i) CV of bare GCE in 0.1 M PBS (pH 7.2) solution, and (ii) bare GCE in 0.5 mM $[\text{Ru}(\text{bpy})_3]\text{Cl}_2$ at 50 mV/s.

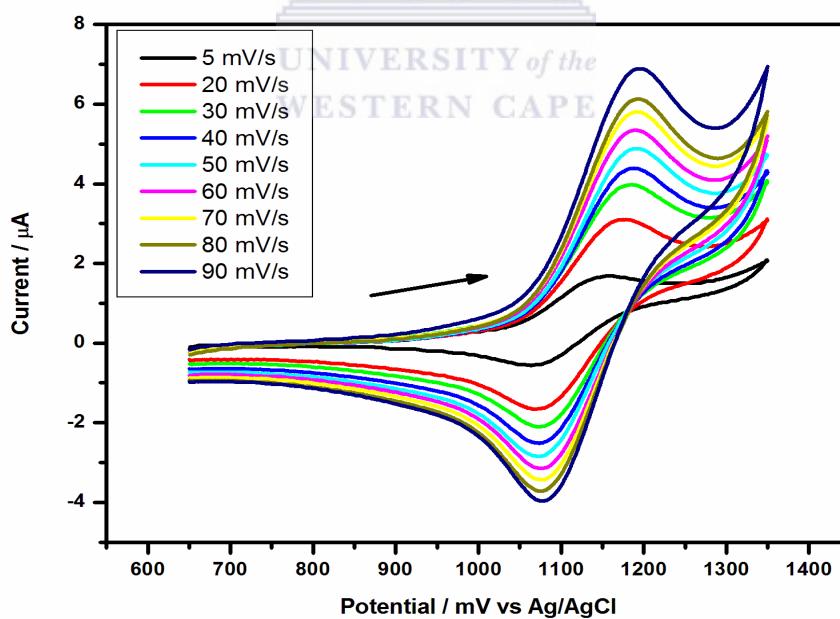


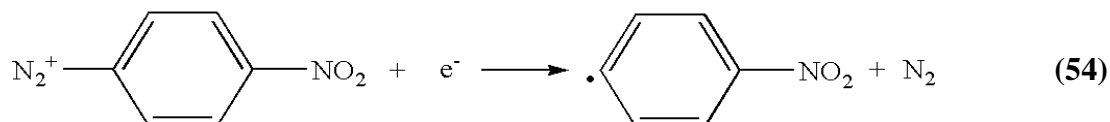
Figure 4.8: CV at various scan rates of bare GCE in 0.5 mM $[\text{Ru}(\text{bpy})_3]\text{Cl}_2$.

The peak current increased with increase in scan rate as shown in Figure 4.8.

4.2.2 Electrochemistry of AuNp/G/PhNO₂ and NDT in 0.1 M PBS solution

The electrochemical behaviour of 4-nitrophenyl diazonium tetrafluoroborate (NDT) and AuNp/G/PhNO₂ is shown in Figure 4.9. The CV of bare GCE in 0.1 M NDT (prepared with 0.1 M PBS) Ar-saturated solution was recorded over a potential range of -1500 mV to 100 mV at a scan rate 100 mV/s. And the CV of 0.2% AuNp/G/PhNO₂ in 0.1 M PBS (pH 7.2) argon saturated solution was also recorded over the same potential range at scan rate 100 mV/s.

One reduction peak was observed on the cathodic scan, peak b, ($E_{p,c} = -1030$ mV, $I_{p,c} = -15.2$ μ A) NDT solution. This is attributed to the formation of 4-nitrophenyl radical from the NDT [190-191]. The electrochemical behaviour of aryl diazonium cations has been studied in great detail by Elofson and co-workers, who have observed aryl radical formation and release of nitrogen upon reduction [175, 192-193]:



The CV of 0.2% AuNp/G/PhNO₂ in 0.1 M PBS (pH 7.2) Ar-saturated solution were recorded over the same potential range and scan rate using bare glassy carbon electrode. An irreversible wave was observed having a reduction peak on the cathodic scan, peak a, ($E_{p,c} = -854$ mV, $I_{p,c} = -2.4$ μ A). This is ascribed to O₂N-C₆H₄[•] radical formation as illustrated in equation (54), indicating that the synthesised graphene was actually engrafted with 4-nitrophenyl diazonium.

The shift in reduction potential and the reduced current in peak a comparing with peak b in Figure 4.9 further confirm that 4-nitrophenyl diazonium was successfully functionalised on the graphene with its valence electrons delocalised within the engrafted graphene conjugated system which caused the relative shift and drop in peak current [175]. The CV of bare GC electrode in 0.1 M PBS (pH 7.2) Argon-saturated solution over the same potential range and scan rate did not show any electro activity.

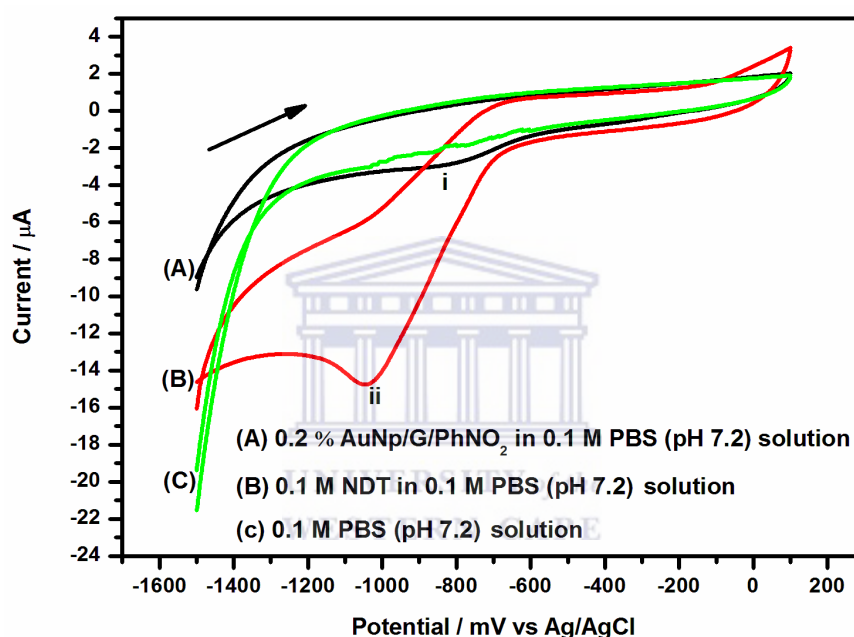


Figure 4.9: CV of bare GCE in (A) 0.2% AuNp/G/PhNO₂ in 0.1 M (B) 0.1 M NDT (C) 0.1 M PBS.

4.2.3 Electrochemistry of G/PhNO₂ and AuNp/G/PhNO₂

Figure 4.10 shows the cyclic voltammogram of G/PhNO₂ and AuNp/G/PhNO₂ modified GC electrodes at scan rate 100 mV/s in 0.1 M PBS (pH 7.2) solution. There was no observed electro activity for both modified GC electrodes over the potential range of 650 mV to 1350 mV.

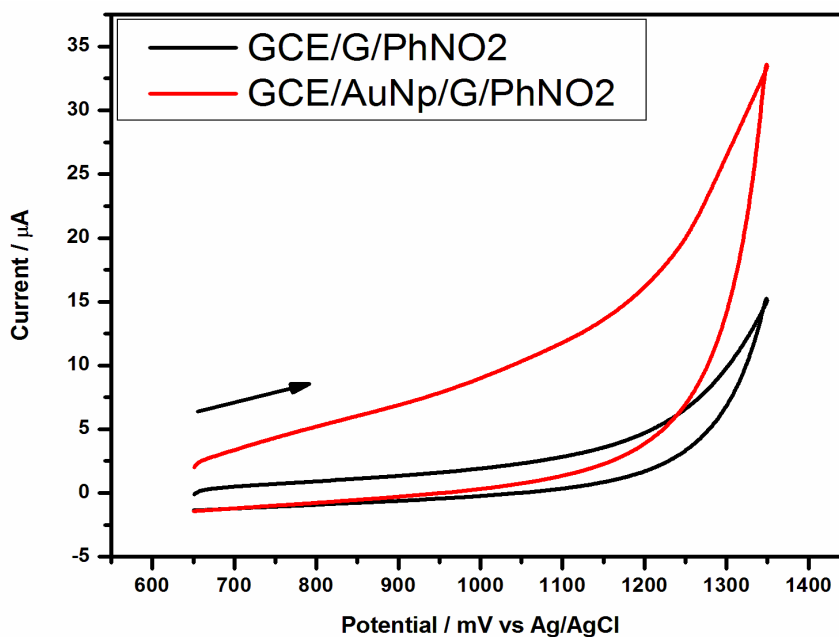


Figure 4.10: CV of GCE/G/PhNO₂ and GCE/AuNp/G/PhNO₂ in 0.1 M PBS.

To further interrogate the electro activity of the synthesised gold nanoparticles-dotted 4-nitrophenylazo functionalised graphene (AuNp/G/PhNO₂) and 4-nitrophenylazo functionalised graphene (G/PhNO₂) on glassy carbon electrode surface, we have used hexaamineruthenium (III) chloride [Ru(NH₃)₆]^{2+/3+} complex as cationic redox probe (because its electrochemistry is well known with one electron couple). Figure 4.11 shows cyclic voltammograms of bare GC electrode, G/PhNO₂ and AuNp/G/PhNO₂ modified GC electrodes, recorded in aqueous 5 mM [Ru(NH₃)₆]^{2+/3+} which was prepared with 0.1 M PBS of pH 7.2, at a scan rate of 50 mV/s.

The voltammogram of the [Ru(NH₃)₆]^{2+/3+} cationic redox system is reversible with bare GC electrode having anodic and cathodic peaks ($E_{p,a} = 160$ mV, $I_{p,a} = 56$ µA) and ($E_{p,c} = -247$ mV, $I_{p,c} = -73.1$ µA) respectively. Relatively, drastic drop in peak currents were observed in the

CV of GCE/G/PhNO₂ ($E_{p,a} = -157$ mV, $I_{p,a} = 37.53$ μ A and $E_{p,c} = -275$ mV, $I_{p,c} = -59$ μ A), evidencing surface saturation and suggesting that a monolayer of fixed 4-nitrophenylazo molecules was achieved or successfully grafted on the graphene surface (see chapter two section 3.3) which led to the inhibition of electron flow and lower conductivity [175].

On the contrary, the AuNp/G/PhNO₂ modified electrode (GCE/AuNp/G/PhNO₂) presented a quasi-reversible electrochemistry with almost equivalent cathodic peak current and peak potential with the CV of bare GCE, indicating almost 100% relative electro activity when substituted into equation (55).

$$I_{rel} (\%) = I_{pc} \text{ GCE-film} / (I_{pc} \text{ Bare GCE})^{-1} \times 100 \quad (55)$$

Where, I_{pc} is cathodic peak current.

The increase in current for GCE/AuNp/G/PhNO₂ was observed due to the fact that gold nanoparticles increases the effective surface area of the gold nanoparticles-dotted 4-nitrophenylazo functionalised graphene (AuNp/G/PhNO₂) and enhances greatly its rate of electron transfer. This is due to the change in carrier concentration of the PhNO₂ functionalised graphene, the adsorbed gold nanoparticles on AuNp/G/PhNO₂ surface acting as donors and acceptors. The slight reduction in anodic peak current is due to inhibition of electron flow through GCE/AuNp/G/PhNO₂ caused by the slight negative charge conferred on the AuNp/G/PhNO₂ composite by PhNO₂ units. This repels some of the reduced electroactive species in solution. Consequently all the reduced species in the vicinity of the electrode were not oxidised completely and this reflected as a slight drop in anodic current [173, 175-176].

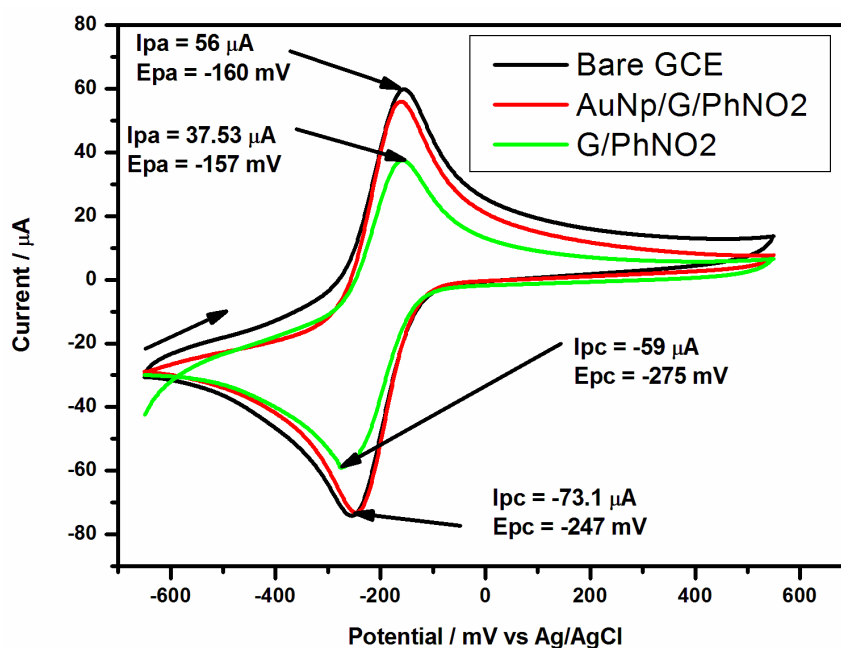
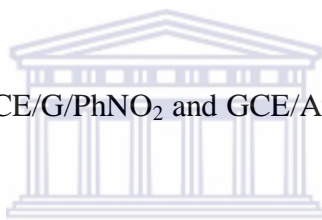


Figure 4.11: CV of bare GCE, GCE/G/PhNO₂ and GCE/AuNp/G/PhNO₂ in 5 mM HRC.



4.2.4 Construction of sensor platforms and optimization

The synthesised gold nanoparticles-dotted 4-nitrophenylazo functionalised graphene (AuNp/G/PhNO₂) and the 4-nitrophenylazo functionalised graphene (G/PhNO₂) were used to design electrochemical sensor platforms by coupling tris (bipyridine) ruthenium (II) chloride ([Ru(bpy)₃]Cl₂) as a cationic reactant mediated in Nafion. Before that, the electrochemical behaviour of [Ru(bpy)₃]Cl₂ and Nafion were studied. The insert in Figure 4.12 (b) shows the cyclic voltammogram of the GCE/Nafion electrode in argon-degassed 0.1 M PBS (pH 7.2) solution at a scan rate 50 mV/s. It did not exhibit any electrochemistry as expected since Nafion is not electroactive but can incorporate other molecules into its bulk membrane through coulombic and/or hydrophobic interaction [38, 40, 67]

This property was explored as described in chapter 3 section 3.6, to incorporate $[\text{Ru}(\text{bpy})_3]^{2+}$ molecules and obtained a modified GC electrode depicted as GCE/Nafion/ $[\text{Ru}(\text{bpy})_3]^{2+}$. A well defined redox couple could be observed at 1124 mV and 1026 mV for its CV in argon degassed 0.1 M PBS (pH 7.2) solution at 50 mV/s. The redox couple consist of cathodic peak ($E_{\text{p,c}}=1026$ mV, $I_{\text{p,c}}=-5.9037$ μA) and an anodic peak ($E_{\text{p,a}}=1124$ mV, $I_{\text{p,a}}=7.1879$ μA) with a midpoint potential E^0 , of 1075 mV. These peaks are due to oxidation of Ru^{2+} and reduction of Ru^{3+} respectively and these corresponds to equation (52).

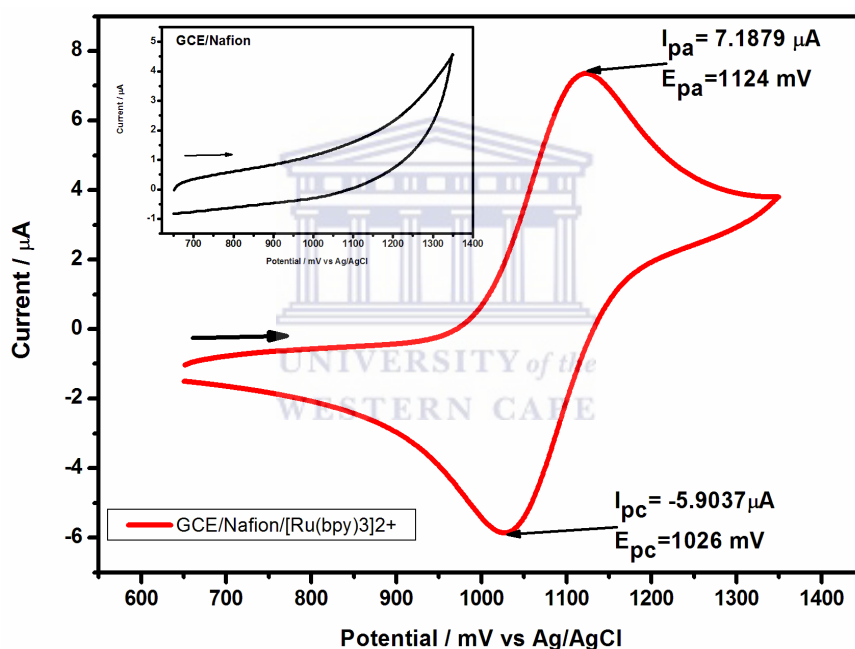


Figure 4.12: CV of GCE/Nafion/ $[\text{Ru}(\text{bpy})_3]^{2+}$ and GCE/Nafion in the insert in 0.1 M PBS.

The synthesised AuNp/G/PhNO₂ and G/PhNO₂ were used to design electrochemical sensor platform following the protocol described in Chapter three Section 3.6. To explicate the effect of AuNp/G/PhNO₂ on the properties of Nafion/ $[\text{Ru}(\text{bpy})_3]^{2+}$ films on glassy carbon electrode, cyclic voltammetric measurement of Nafion/ $[\text{Ru}(\text{bpy})_3]^{2+}$ /AuNp/G/PhNO₂

composite films prepared with 1% (v/v) Nafion solution containing 0, 0.2, 0.3, 0.6 and 0.8% AuNp/G/PhNO₂ in 0.1 M PBS (pH 7.2) solution was performed. Figure 4.13 shows the cyclic voltammograms at the specified percentage compositions.

It could be observed that 0.2% composition exhibited the best electro catalytic properties. Similar result was obtained for the films prepared with 1% (v/v) Nafion solution containing 0, 0.2, 0.3, 0.6 and 0.8% G/PhNO₂ in 0.1 M PBS (pH 7.2) solution at scan rate of 20 mV/s, see Figure 4.14. This result is ascribed to the enlarged electroactive surface area of AuNp/G/PhNO₂ which increased the loaded quantity of the signal probe under the electrochemical condition, consequently benefits its contact with the transducer.

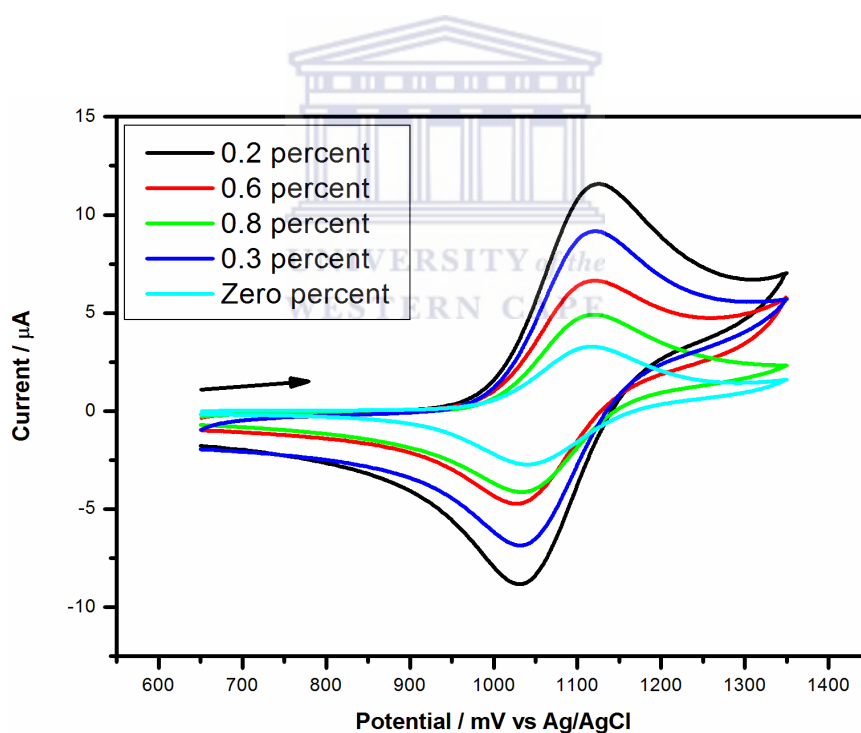


Figure 4.13: CV of Nafion/[Ru(bpy)₃]²⁺/AuNp/G/PhNO₂ composite films prepared with 1% (v/v) Nafion solution containing 0, 0.2, 0.3, 0.6 and 0.8% AuNp/G/PhNO₂.

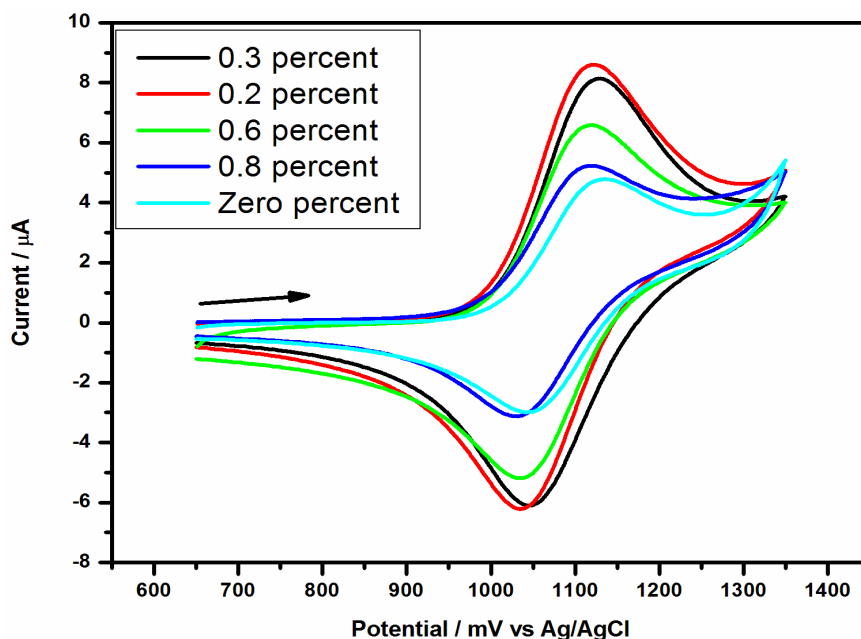
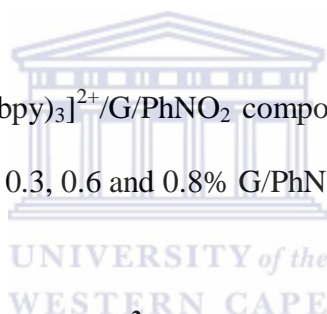


Figure 4.14: CV of Nafion/[Ru(bpy)₃]²⁺/G/PhNO₂ composite films prepared with 1% (v/v) Nafion solution containing 0, 0.2, 0.3, 0.6 and 0.8% G/PhNO₂.



4.2.5 CV of GCE/Nafion/[Ru(bpy)₃]²⁺, GCE/Nafion/[Ru(bpy)₃]²⁺/G/PhNO₂ and GCE/Nafion/[Ru(bpy)₃]²⁺/AuNp/G/PhNO₂ sensor platforms.

Figure 4.15 exhibits the variance in the cyclic voltammetric behaviour of GCE/Nafion/[Ru(bpy)₃]²⁺, GCE/Nafion/[Ru(bpy)₃]²⁺/G/PhNO₂ and GCE/Nafion/[Ru(bpy)₃]²⁺/AuNp/G/PhNO₂ sensor platforms prepared according to the protocol described in Chapter three Section 3.6.

The oxidation peaks a, b, c for the three electrodes and their respective reduction peaks a', b', c' vary significantly. Peak a, ($E_{p,a} = 1132$ mV, $I_{p,a} = 11.01$ μ A) and peak a', ($E_{p,c} = 1040$ mV, $I_{p,c} = -9.103$ μ A); peak b, ($E_{p,a} = 1122$ mV, $I_{p,a} = 9.172$ μ A) and peak b', ($E_{p,c} = 1032$ mV, $I_{p,c}$

= -6.863 μA); peak c, ($E_{p,a} = 1121 \text{ mV}$, $I_{p,a} = 4.921 \mu\text{A}$) and peak c' ($E_{p,c} = 1033 \text{ mV}$, $I_{p,c} = -4.134 \mu\text{A}$).

About 16.7% and 24.6% increase in the magnitude of the $I_{p,a}$ and $I_{p,c}$ respectively could be observed in the CV of GCE/Nafion/[Ru(bpy) $_3$] $^{2+}$ /AuNp/G/PhNO $_2$ and GCE/Nafion/[Ru(bpy) $_3$] $^{2+}$ /G/PhNO $_2$. While average of 55.3% increase in the peak currents was achieved comparing GCE/Nafion/[Ru(bpy) $_3$] $^{2+}$ /AuNp/G/PhNO $_2$ and GCE/Nafion/[Ru(bpy) $_3$] $^{2+}$. The significant increase is most likely attributed to the enhanced electrical conductivity of graphene due to the adsorbed gold nanoparticles which act as donors or acceptors. In addition, the enlarged electroactive surface area of AuNp/G/PhNO $_2$ increased the loaded quantity of the signal probe, consequently benefits its contact with the transducer. The square-wave voltammogram in Figure 4.16 corroborate these findings.

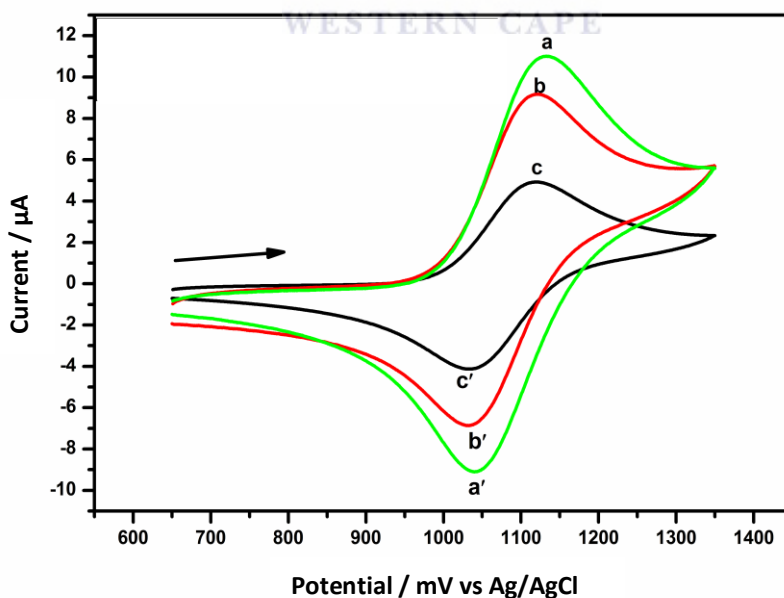


Figure 4.15: CV of (a) GCE/Nafion/[Ru(bpy) $_3$] $^{2+}$ /AuNp/G/PhNO $_2$ (0.2%), (b) GCE/Nafion/[Ru(bpy) $_3$] $^{2+}$ /G/PhNO $_2$ (0.2%) and (c) GCE/Nafion/[Ru(bpy) $_3$] $^{2+}$.

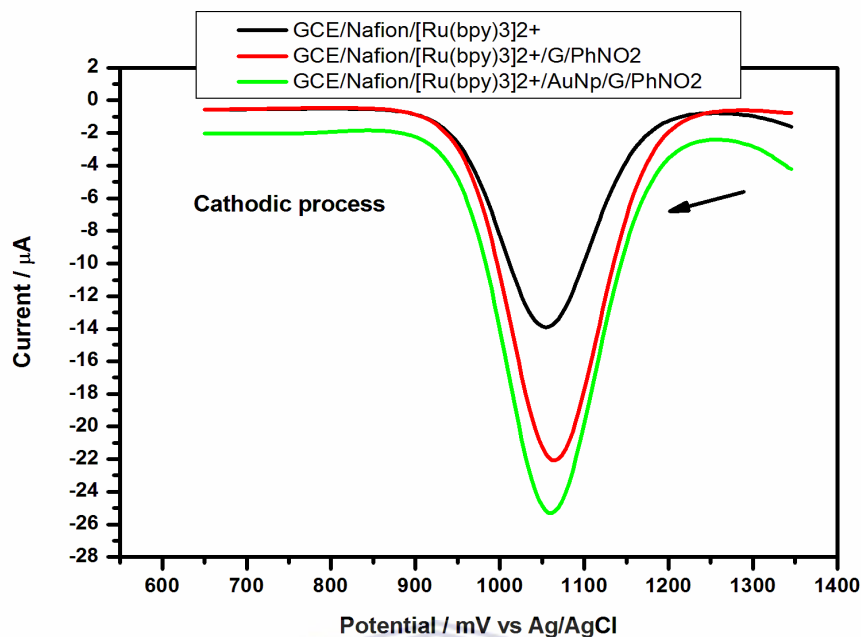
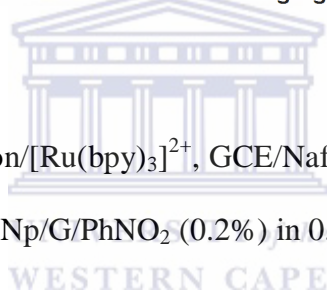


Figure 4.16: SWV of GCE/Nafion/[Ru(bpy)₃]²⁺, GCE/Nafion/[Ru(bpy)₃]²⁺/G/PhNO₂ (0.2%) and GCE/Nafion/[Ru(bpy)₃]²⁺/AuNp/G/PhNO₂ (0.2%) in 0.1 M PBS.



For a better understanding of electro activity of the three sensor platforms, they were subjected to characterization by CV in 0.1 M PBS (pH 7.2) at various scan rates. The scan rate dependence voltammograms (5-500 mV/s) for GCE/Nafion/[Ru(bpy)₃]²⁺/AuNp/G/PhNO₂ is shown in Figure 4.17. It was observed that the anodic peak potentials and corresponding currents vary with increasing scan rate while the cathodic peak potentials are relatively independent of varying scan rate, indicating that surface bound electro active species ([Ru(bpy)₃]²⁺/AuNp/G/PhNO₂ film) was successfully and firmly immobilised onto glassy carbon electrode surface.

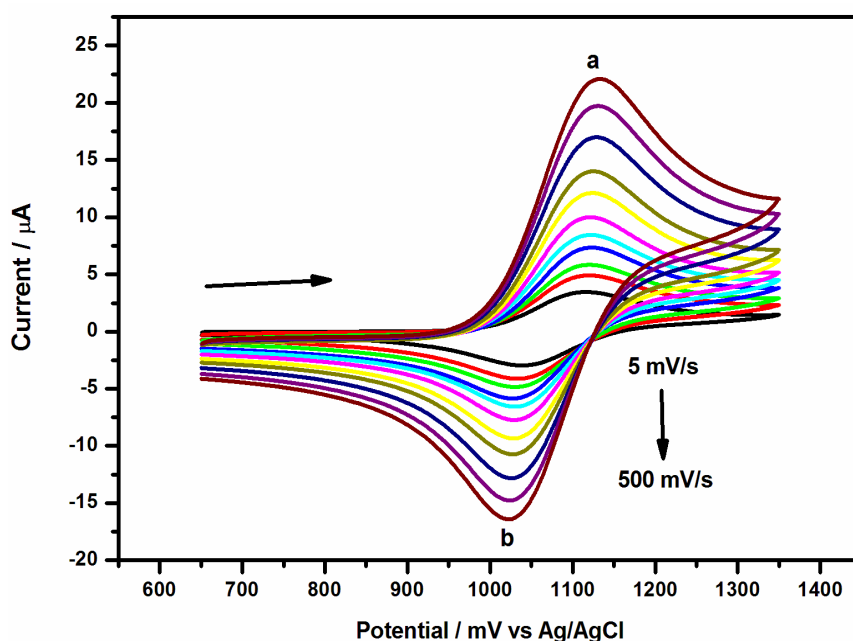


Figure 4.17: CV of GCE/Nafion/[Ru(bpy)₃]²⁺/AuNp/G/PhNO₂ at various scan rates.

The number of electrons transferred was estimated to be one (1) electron using double potential chronocoulometry [99, 152-153]. This is in agreement with those reported in the literature for [Ru(bpy)₃]²⁺ [194-196]. Notably, the ratio of the anodic to cathodic peak currents (I_a/I_c) for all scan rates was not unity (unsymmetrical) meaning that the redox kinetics for the two processes were not similar and suggesting that the electron transfer reaction may be quasi-reversible.

To confirm this, further kinetic studies was performed by plotting peak currents versus square root of scan rate (see Figure 4.18). It could be observed that peak currents increased with square root of scan rate but it was not proportional to it. It was also observed that the ΔE_p was greater than $59/n$ mV and increases with increasing scan rate. This implies that the thin film

was conducting and exhibited quasi-reversible behaviour in PBS (pH 7.2) solution involving one electron process.

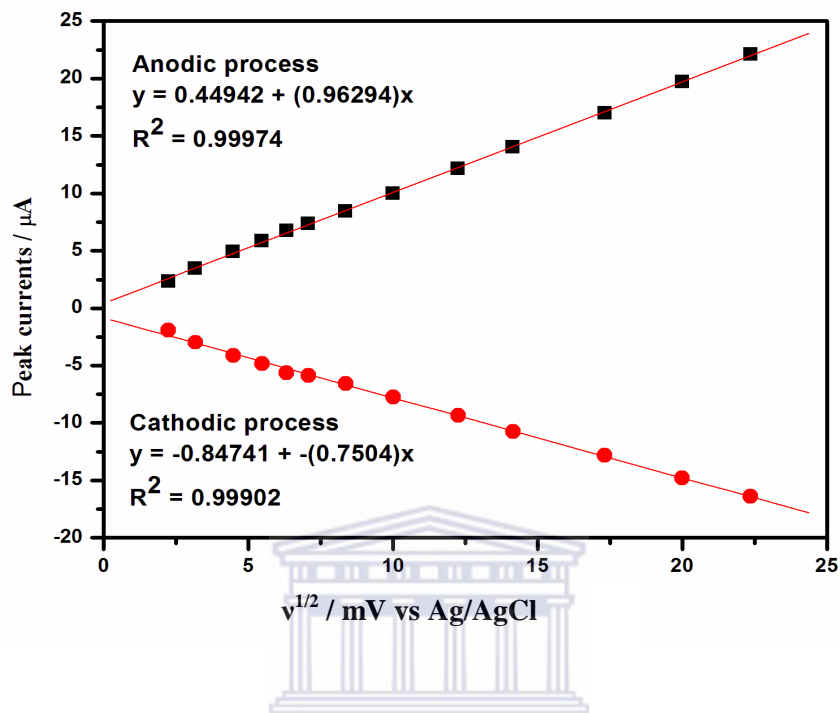


Figure 4.18: The plots of peak currents versus square root of scan rate.

The anodic peak current (I_p) increased linearly with scan rate (v) at very low scan rates and deviated significantly at higher scan rates as shown in Figure 4.19. This implies that the charge transfer at the electrode-film interface, in the absence of oxygen is rapid, adsorption controlled at low scan rates; and both adsorption and diffusion controlled at higher scan rates [99].

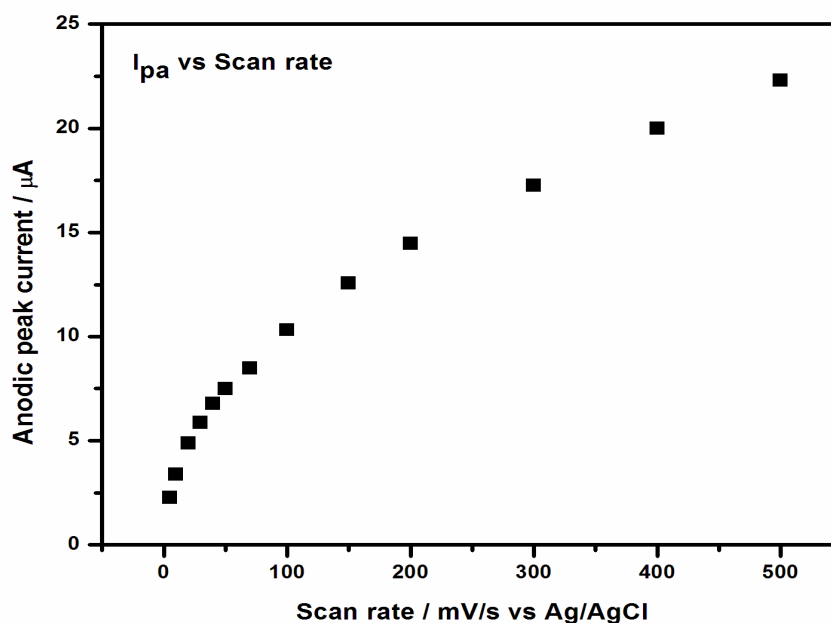


Figure 4.19: The plots of the anodic peak current versus scan rate.

For a more detailed studies of the kinetic behaviour of Nafion/[Ru(bpy)₃]²⁺/AuNp/G/PhNO₂ thin film on GC electrode at higher scan rates (100 - 500 mV/s), a plot of log peak current versus log of scan rate of data from Figure 4.17 show that the peak currents (peak a and peak b) increased linearly with log of scan rate and had non-zero intercept because of non-faradaic current, see Figure 4.20 (a).

This corroborates the result in Figure 4.19, indicating that the redox process of the thin film was limited by both diffusion and adsorption for the peak a (slope = 0.7926) and peak b (slope = 0.6872) [197].

At lower scan rates (5 - 40 mV/s), the plots of peak current versus log scan rate, see Figure 4.20 (b), was linear and had non-zero intercept also, but the redox process involving the film

was limited by adsorption for peak a (slope = 0.9853 \approx 1), and both diffusion and adsorption for peak b (slope = 0.7754) as also observed in Figure 4.19 [197].

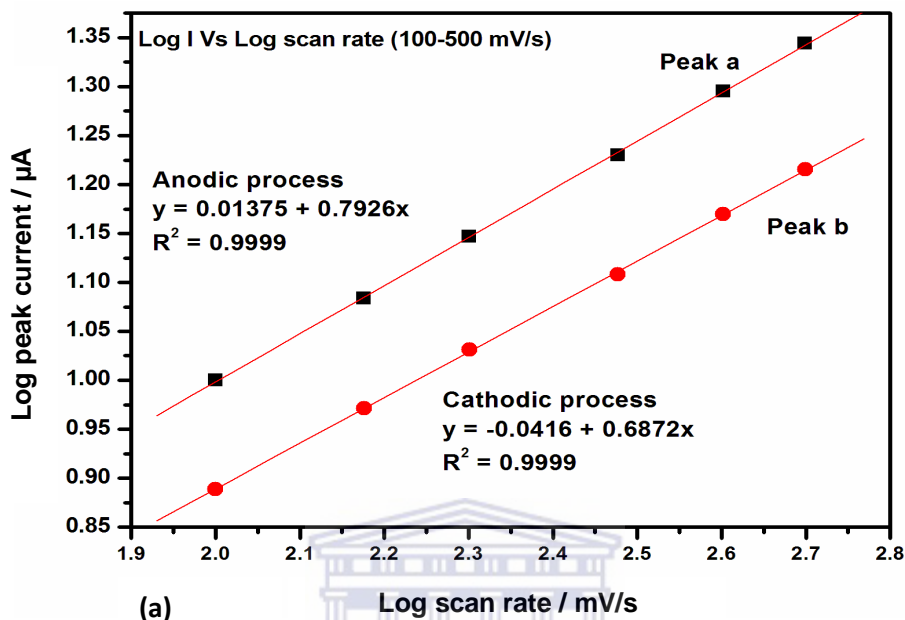


Figure 4.20 (a): The plot of $\log I_p$ vs $\log v$ for data at higher scan rate (100-500 mV/s)

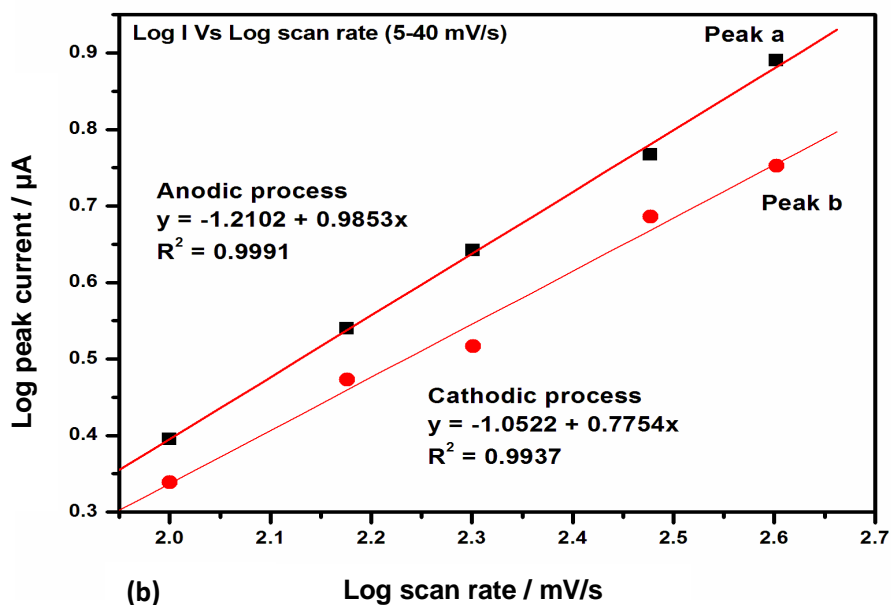


Figure 4.20 (b): The plot of $\log I_p$ vs $\log v$ for data at lower scan rates (5- 40 mV/s)

Similar electro-kinetic studies was carried out for GCE/Nafion/[Ru(bpy)₃]²⁺ and GCE/Nafion/[Ru(bpy)₃]²⁺/G/PhNO₂. It was observed that their anodic peak potentials and corresponding currents vary with increasing scan rate as well while the cathodic peak potentials are relatively independent of varying scan rate. The observed electron transfer reactions for both electrodes were quasi-reversible as well exhibiting the same electrochemical behaviour but at a lower degree.

It could be observed that the relative increases in peak currents at specific scan rates for both electrodes are not the same. The peak currents in GCE/Nafion/[Ru(bpy)₃]²⁺/G/PhNO₂ are greater due to the incorporation of G/PhNO₂ electro-catalyst into sensing platform. This enhanced electrochemical response of GCE/Nafion/[Ru(bpy)₃]²⁺/AuNp/G/PhNO₂ is attributed to the high conductivity and large specific surface area of gold nanoparticle dotted 4 nitrophenylazo functionalised graphene (AuNp/G/PhNO₂) which increased the loaded amount of [Ru(bpy)₃]²⁺. In addition, the slight negative charge conferred on the nanocomposite by PhNO₂ units further enhanced the quantity and stability of the cation electrostatically.

4.2.6 Chronoamperometric studies of GCE/Nafion/([Ru(bpy)₃]²⁺, GCE/Nafion/[Ru(bpy)₃]²⁺/G/PhNO₂ and GCE/Nafion/[Ru(bpy)₃]²⁺/AuNp/G/PhNO₂ sensor platforms

Chronoamperometric technique was also employed to further interrogate the electro catalytic activity of the modified electrodes in 0.1 M PBS (pH 7.2). As mentioned earlier in chapter 2 section 2.17, this is a square wave pulsed voltammetric technique where the potential of the working electrode is stepped from a potential of zero electrolysis to a potential where the

adsorbed electroactive specie(s) on the transducer surface is reduced or oxidised, and the corresponding current due to faradaic processes is measured as a function of time. The current component of interest decays as described by Cottrell equation 29 and 30.

The experiments were done in a 2 step potential mode, 2 sec quiet time, pulse width of 500 msec and quiescent condition. The choice of potential steps for each sensor platform was made from the cyclic voltammogram at 50 mV/s of each modified electrode in 0.1 M PBS (pH 7.2). It ranges from the onset-potential of each platform, to their corresponding peak potentials. It could be observed [Figure 4.21 (a) and (b)] that the electrode containing AuNp/G/PhNO₂ nanocatalyst showed a huge difference in the measured peak currents.

The anodic peak currents were 9.633E-5, 6.341E-5 and 4.15E-5, as presented in the bar chart for platforms (a), (b) and (c) respectively. Since the output current directly depends on the quantity of electroactive species coupled on the surface of the working electrode, which undergoes the faradaic processes when the potential is stepped [99-100, 128, 152], the result therefore implies that more [Ru(bpy)₃]²⁺ were loaded on the sensor platform compared to others. This corroborates the results observed with the CV experiment above and could also be attributed to the high conductivity and large specific surface area of gold nanoparticle dotted 4 nitrophenylazo functionalised graphene (AuNp/G/PhNO₂) which increased the loaded amount of [Ru(bpy)₃]³⁺.

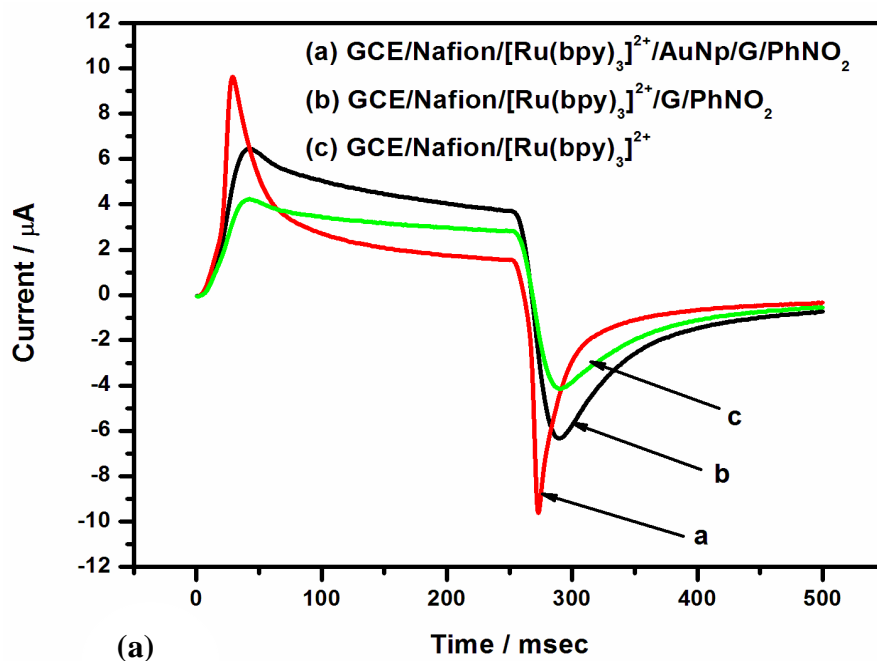


Figure 4.21(a): Chronoamperogram of GCE/Nafion/[Ru(bpy)₃]²⁺/AuNp/G/PhNO₂, GCE/Nafion/[Ru(bpy)₃]²⁺/G/PhNO₂ and GCE/Nafion/[Ru(bpy)₃]²⁺ sensor platforms

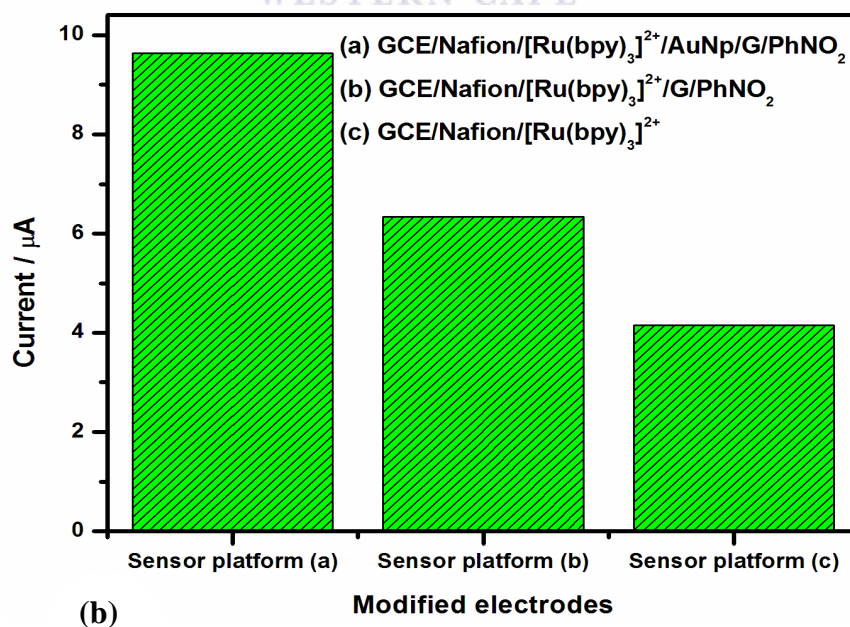


Figure 4.21(b): Bar chart indicating anodic peak currents of the platforms

4.2.7 Chronocoulometric studies of GCE/Nafion/([Ru(bpy)₃]²⁺, GCE/Nafion/[Ru(bpy)₃]²⁺/G/PhNO₂ and GCE/Nafion/[Ru(bpy)₃]²⁺/AuNp/G/PhNO₂ sensor platforms

The diffusion coefficient of solution species and surface concentration of the adsorbed [Ru(bpy)₃]²⁺ for GCE/Nafion/[Ru(bpy)₃]²⁺/AuNp/G/PhNO₂ was determined by chronocoulometry [153]. According to Anson's equation, if the electrolysis of solution species is diffusion-controlled, **Q** depends on **t**^{1/2}. In contrast, the electrolysis of adsorbed species is essentially instantaneously, as well as the double layer charging as already explained in chapter two, section 2.18.4. The equations (33 and 34) for the total charge **Q** were given:

$$Q = Q_{\text{diff}} + Q_{\text{ads}} + Q_{\text{dl}} \quad \text{or} \quad (56)$$

$$Q = 2nFACD^{1/2} \Pi^{-1/2} t^{1/2} + nFA\Gamma^* + Q_{\text{dl}} \quad (57)$$



Where: Q_{diff} = charge due to electrolysis of solution species

Q_{ads} = charge due to electrolysis of adsorbed species

Q_{dl} = double-layer charge

Γ^* = surface concentration of adsorbed species (mol/cm²)

D = diffusion coefficient of solution species (cm²/s¹)

A = Surface area of the glassy carbon electrode, 0.071 cm²

F = Faraday's constant, 95484.56 C mol⁻¹

C = Concentration of the electrolyte, 0.1 M

t = Time of potential step (s)

T = time following potential step (s)

The intercept of Q versus $t^{1/2}$ plot is the sum of Q_{dl} and Q_{ads} . The Q_{dl} was eliminated from the equation by running identical experiment on the electrolyte alone. Noticeably, the adsorption of $[Ru(bpy)_3]^{2+}$ specie produced significant changes in the interfacial capacitance, therefore values of Q_{dl} evaluated in the absence of the reactant did not apply when the reactant is present. From Figure 4.22 (b), the intercept value is 1.27178E-7.

Applying this value in $nF\Delta\Gamma^*$, the surface concentration (Γ^*) of adsorbed $[Ru(bpy)_3]^{2+}$ on GCE/Nafion/ $[Ru(bpy)_3]^{2+}$ /AuNp/G/PhNO₂ was calculated to be $1.87 \times 10^{-11} \text{ mol cm}^{-2}$. Its diffusion coefficient, estimated from the slope ($2nFACD^{1/2} \Pi^{-1/2}$) of Q versus $t^{1/2}$ of Anson's plot (Figure 4.21 a), was calculated as $1.12 \times 10^{-17} \text{ cm}^2/\text{s}$.



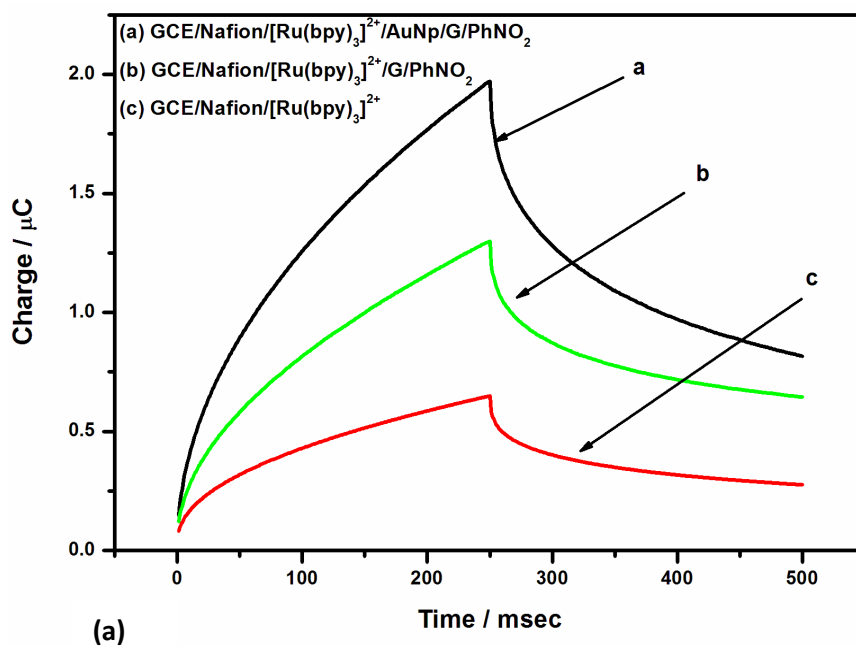


Figure 4.22(a): Chronocoulograms of GCE/Nafion/[Ru(bpy)₃]²⁺, GCE/Nafion/[Ru(bpy)₃]²⁺/G/PhNO₂ and GCE/Nafion/[Ru(bpy)₃]²⁺/AuNp/G/PhNO₂ sensor platforms.

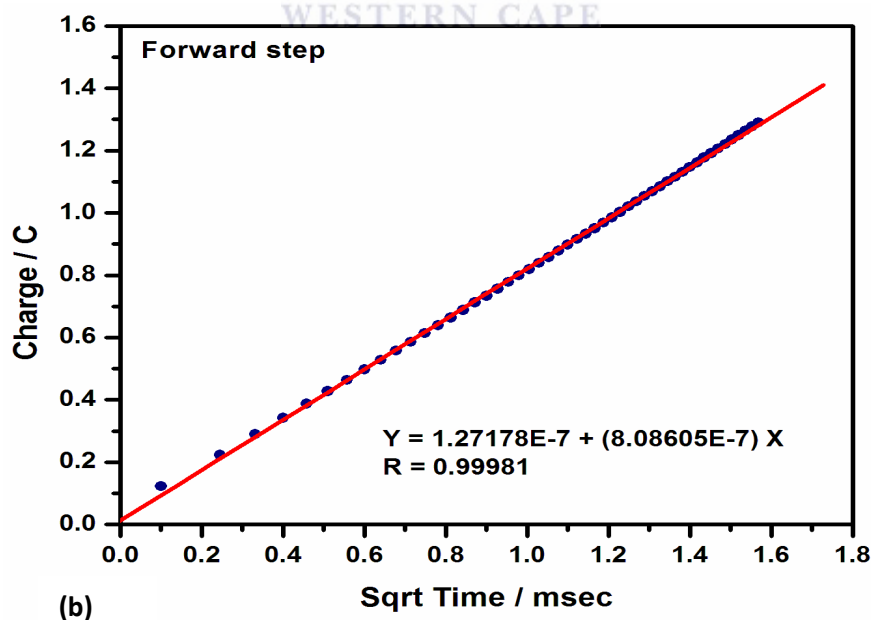


Figure 4.22(b): Anson plot of GCE/Nafion/[Ru(bpy)₃]²⁺/AuNp/G/PhNO₂ chronocoulogram.

From the slope and intercept of Anson's plot for the forward step of GCE/Nafion/[Ru(bpy)₃]²⁺/G/PhNO₂ and GCE/Nafion/([Ru(bpy)₃]²⁺ chronocoulograms (Figure 4.22 b and c), the surface concentration (Γ^*) of adsorbed [Ru(bpy)₃]²⁺ and the diffusion coefficient of solution species observed for both electrodes were derived. The values of surface concentration (Γ^*) of adsorbed [Ru(bpy)₃]²⁺ for GCE/Nafion/[Ru(bpy)₃]²⁺ and GCE/Nafion/[Ru(bpy)₃]²⁺/G/PhNO₂ were 1.71x10⁻¹² and 1.22 x 10⁻¹¹ mol cm⁻² respectively. While the diffusion coefficients were 6.89x 10⁻²⁰ and 8.4 x 10⁻¹⁹ cm²/s respectively. These values are less compared to that of GCE/Nafion/[Ru(bpy)₃]²⁺/AuNp/G/PhNO₂.

Again, the enhanced electrochemical response of GCE/Nafion/[Ru(bpy)₃]²⁺/AuNp/G/PhNO₂ is attributed to the high conductivity and large specific surface area of gold nanoparticle dotted 4 nitrophenylazo functionalised graphene (AuNp/G/PhNO₂) which increased the loaded amount of [Ru(bpy)₃]³⁺. In addition, the slight negative charge conferred on the nanocomposite by PhNO₂ units further enhanced the quantity and stability of the cation electrostatically as observed in CV characterization.

4.2.8 EIS studies of GCE/Nafion/([Ru(bpy)₃]²⁺, GCE/Nafion/[Ru(bpy)₃]²⁺/G/PhNO₂ and GCE/Nafion/[Ru(bpy)₃]²⁺/AuNp/G/PhNO₂ sensor platforms

Electrochemical impedance spectroscopy was used to study the kinetics and mechanisms of electron transfer processes of the three modified electrodes (GCE/Nafion/([Ru(bpy)₃]²⁺, GCE/Nafion/[Ru(bpy)₃]²⁺/G/PhNO₂ and GCE/Nafion/[Ru(bpy)₃]²⁺/AuNp/G/PhNO₂) comparably with that of bare GC electrode in PBS (pH 7.2). In order to get better potential, the EIS studies of the three modified electrodes were first ran over a range of bias potentials

0, 100, 200, 400, 600, 800 and 1000 mV. A similar trend of Nyquist plot as shown in Figure 4.23 was observed for all three platforms.

Based on different equivalent circuits used in modelling the results, the optimal AC potential was found to be 0 mV. This conforms to the reports that zero potential is ideal for EIS studies, reason being that it leads to low induced diffusion current and simplified electronic circuit [198-200].

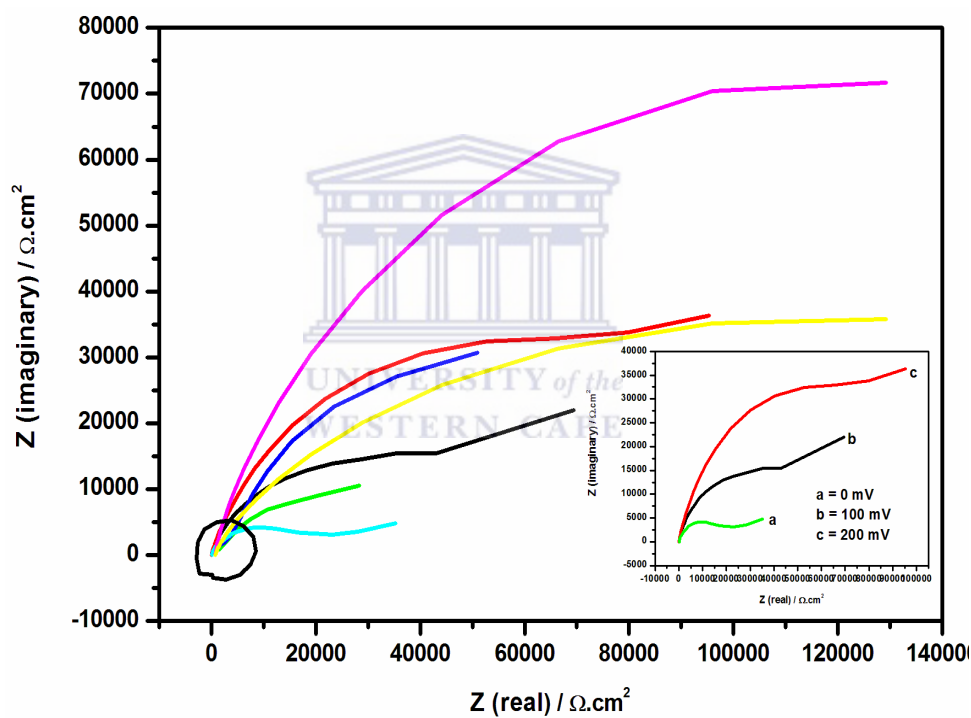


Figure 4.23: Nyquist plot of GCE/Nafion/[Ru(bpy)₃]²⁺/AuNp/G/PhNO₂ performed at different bias potentials: 0, 100, 200, 400, 600, 800 and 1000 mV respectively.

The electrocatalytic behaviour of the four electrodes GCE, GCE/Nafion/ $[\text{Ru}(\text{bpy})_3]^{2+}$, GCE/Nafion/ $[\text{Ru}(\text{bpy})_3]^{2+}$ /G/PhNO₂ and GCE/Nafion/ $[\text{Ru}(\text{bpy})_3]^{2+}$ /AuNp/G/PhNO₂ was investigated using Nyquist plot as shown in Figure 4.24.

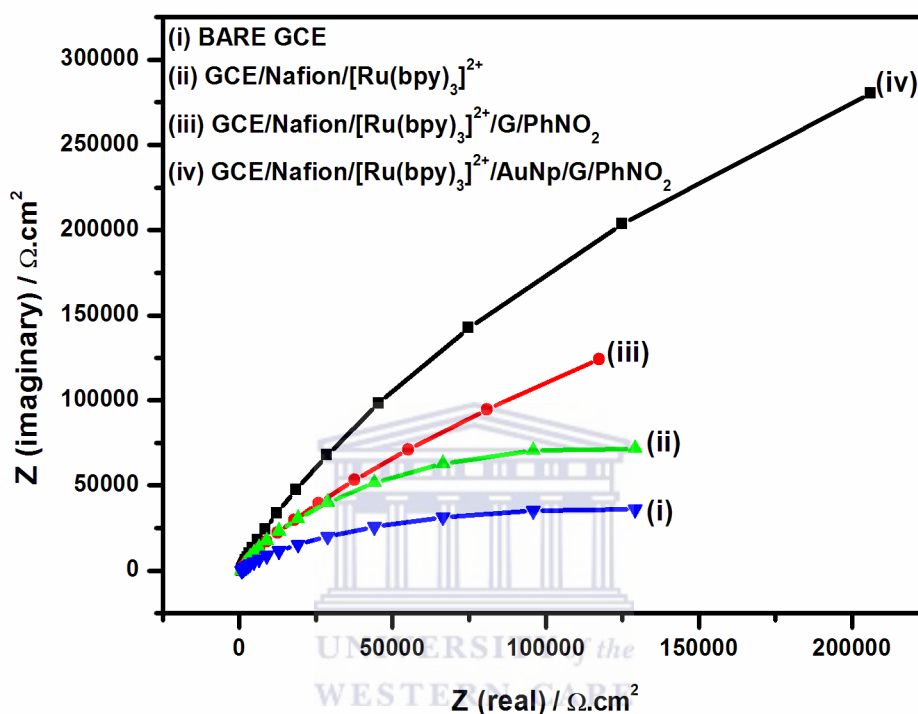


Figure 4.24: Nyquist plots for GCE, GCE/Nafion/ $[\text{Ru}(\text{bpy})_3]^{2+}$, GCE/Nafion/ $[\text{Ru}(\text{bpy})_3]^{2+}$ /G/PhNO₂ and GCE/Nafion/ $[\text{Ru}(\text{bpy})_3]^{2+}$ /AuNp/G/PhNO₂, measured in 0.1 M PBS solution at 0 mV

The analysis of the Nyquist plot was based on an equivalent circuit shown in Figure 4.25, where the solution resistance, R_s , precedes a constant phase element, CPE, which is in parallel with charge transfer resistance, R_{ct} and Warburg element short, (W_s). R_{ct} represents the resistance to charge transfer kinetics between the electrolyte and the electrode.

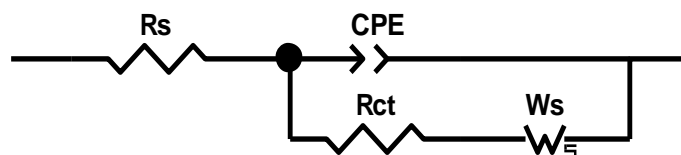


Figure 4.25: Equivalent circuit used for the analysis of the electrochemical impedance data

The R_{ct} , R_s , CPE and W_s values obtained from the circuit fitting for GCE, GCE/Nafion/ $[Ru(bpy)_3]^{2+}$, GCE/Nafion/ $[Ru(bpy)_3]^{2+}$ /G/PhNO₂ and GCE/Nafion/ $[Ru(bpy)_3]^{2+}$ /AuNp/G/PhNO₂ are shown in Table 4.1. Bare GCE curve showed characteristic diffusion limiting step in electrochemical process with a high charge transfer resistance. Upon modification of the electrodes with Nafion/ $[Ru(bpy)_3]^{2+}$, Nafion/ $[Ru(bpy)_3]^{2+}$ /G/PhNO₂, and Nafion/ $[Ru(bpy)_3]^{2+}$ /AuNp/G/PhNO₂ accordingly, a significant decrease in the respective R_{cts} was observed. The lowest R_{ct} and the highest R_s value compared to others was observed for GCE/Nafion/ $[Ru(bpy)_3]^{2+}$ /AuNp/G/PhNO₂, indicating a highest electron-transfer rate at the electrode electrolyte interface

The drop in R_{ct} values of the modified electrodes is attributed to increasingly large amount of the cationic reactant, $[Ru(bpy)_3]^{2+}$, that was loaded on GCE/Nafion/ $[Ru(bpy)_3]^{2+}$, GCE/Nafion/ $[Ru(bpy)_3]^{2+}$ /G/PhNO₂ and GCE/Nafion/ $[Ru(bpy)_3]^{2+}$ /AuNp/G/PhNO₂ accordingly, this in turn benefits closer contact between the signal probe and the transducer, and consequently faster electron transfer rate as was corroborated by CV, chronoamperometric and chronocoulometric studies above.

It also implies that the presence of AuNp/G/PhNO₂ exhibits an excellent electrocatalytic effect on oxidation of tris (bipyridine) ruthenium (II) $[Ru(bpy)_3]^{2+}$ mediated in Nafion in

which charge transport in the nanocomposite occurs through hopping within the bipyridine and graphene conjugated system enhanced by the presence of gold nanoparticles which act as donor and acceptor in the graphene matrix [198]. This makes the Nafion/[Ru(bpy)₃]²⁺/AuNp/G/PhNO₂ modified electrode very suitable for charge transfer applications and for immobilisation of charged biomolecules.

Table 4.1: EIS parameters of GCE, GCE/Nafion/[Ru(bpy)₃]²⁺, GCE/Nafion/[Ru(bpy)₃]²⁺/G/PhNO₂ and GCE/Nafion/[Ru(bpy)₃]²⁺/AuNp/G/PhNO₂

Sensor platforms	R _s (Ω)	R _{ct} (Ω)	CPE (nF)	W _s (Ωs ^{1/2})
Bare GCE	70.56	3176	0.6113	0.43119
GCE/Nafion/[Ru(bpy) ₃] ²⁺	131.93	2183	0.61498	0.44851
GCE/ Nafion/[Ru(bpy) ₃] ²⁺ /G/PhNO ₂	213.8	1827	0.50245	0.47386
GCE/Nafion/[Ru(bpy) ₃] ²⁺ /AuNp/G/PhNO ₂	269.8	950.4	0.75183	0.46073

The frequency dependence of both the phase angle and the impedance is shown in the Bode plots of Figure 4.26 (a) and (b). The impedance versus frequency plot, Figure 4.26 (b), shows that at high frequency the total impedance of the electrodes decreased due to Ohmic resistance which is solution resistance in this case and at low frequency an increase in total impedance was observed due to additional resistance in the system which is charge transfer resistance. It could be observed that the total impedance for GCE/Nafion/[Ru(bpy)₃]²⁺/AuNp/G/PhNO₂ is the lowest at low frequencies compared to others in the order GCE/Nafion/[Ru(bpy)₃]²⁺/AuNp/G/PhNO₂ <

GCE/Nafion/[Ru(bpy)₃]²⁺/G/PhNO₂ < GCE/Nafion/[Ru(bpy)₃]²⁺ < GCE, which is an indication of improved conductivity of the modified electrodes.

The electrode with the lowest impedance is the most conducting and it follows that order to GCE. The phase shift of the modified electrodes (GCE, GCE/Nafion/[Ru(bpy)₃]²⁺, GCE/Nafion/[Ru(bpy)₃]²⁺/G/PhNO₂ and GCE/Nafion/[Ru(bpy)₃]²⁺/AuNp/G/PhNO₂) at the lowest frequency were 79.92°, 64.47° and 52.52° respectively. The phase shift increased with frequency for curves (i), (ii) and (iii) until a characteristic frequency, $f_c = 1.14, 1.0$ and 0.85 Hz respectively, then they all decreased to lowest value of 3.98° which is expected for simple equivalent circuit [150].

On the contrary, the phase shift of GCE/Nafion/[Ru(bpy)₃]²⁺/AuNp/G/PhNO₂ (45.52°) at frequency, $f_c = -0.05$ Hz decreased constantly with higher frequencies to lowest value of 3.98°. This implies that the modification of the GC electrode with the newly synthesised AuNp/G/PhNO₂ greatly enhanced the electro-activity of the GC electrode surface.

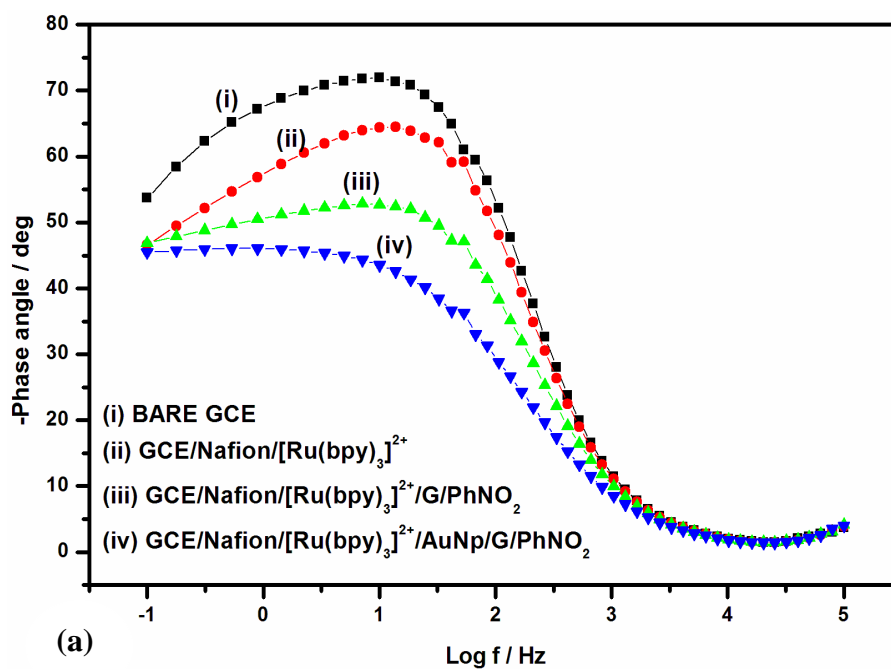


Figure 4.26(a): The phase angle versus frequency plot for EIS data.

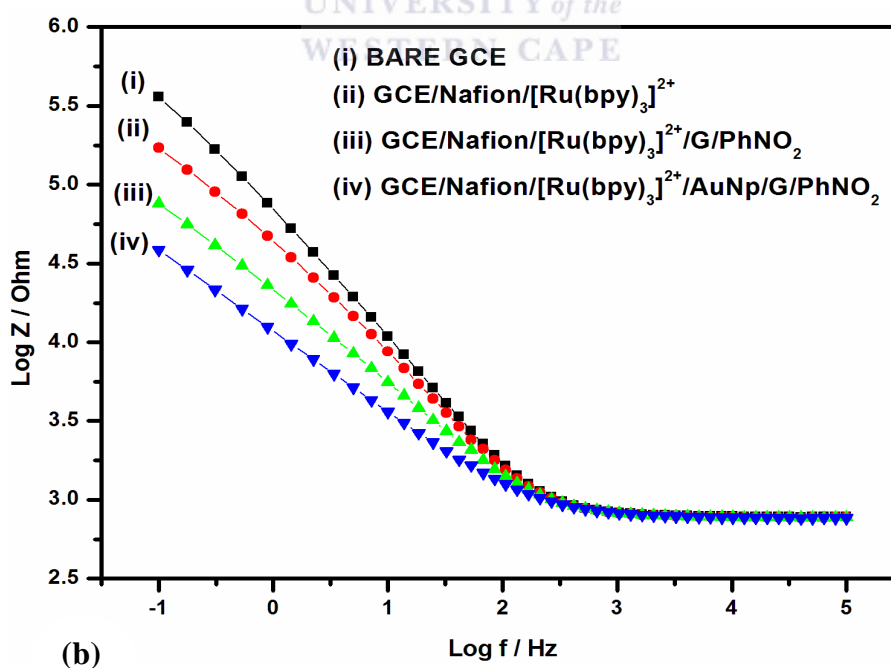


Figure 4.26(b): The impedance versus frequency plot for EIS data.

The R_s value represents the property of the bulk solution that reflects uncompensated Ohmic resistance via non-Faradaic process [201]. The great drop in R_{ct} value of GCE/Nafion/[Ru(bpy)₃]²⁺/AuNp/G/PhNO₂ led to faster reduction of ions in proximity of the electrode causing higher concentration gradient in the bulk electrolyte solution. Therefore oxidised ions in solution diffuse faster towards the electrode surface, creating a flux of oxidised species towards the electrode as the concentration gradient is increased. A comparative study of the interfacial heterogeneous electron transfer rate of all the electrodes was done using equation (55) and (56) [99].

$$R_{ct} = RT/nFI_0 \quad (58)$$

$$I_0 = nFAk^0C^* \quad (59)$$



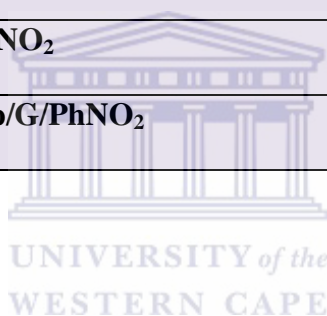
Where n (number of electrons transferred) = 1 e, F (Faraday constant) = 95484.56 C/mol, R (Gas constant) = 8.314 J/mol/K, T (Reaction temperature) = 298 K, A (Geometric area of electrode) = 0.071cm², C^* (concentration of PBS electrolyte) = 0.1 M, I_0 (Standard exchange current, A) and k^0 (Heterogeneous rate transfer const. cm/s).

The calculated values of I_0 and the corresponding k^0 values from the R_{ct} values of the electrodes are shown in Table 4.2. The larger I_0 and k^0 values for GCE/Nafion/[Ru(bpy)₃]²⁺/AuNp/G/PhNO₂ confirms that AuNp/G/PhNO₂ exhibits an excellent electrocatalytic effect on oxidation of tris (bipyridine) ruthenium (II) [Ru(bpy)₃]²⁺ mediated in Nafion. It signifies also that this newly synthesised nanocatalyst can act as a suitable electron transfer mediator for enzyme electrodes and can couple electrons from the enzyme active centre to the electrode surface. The sensitivity of this platform is ultimately

dictated by the rate at which the Ru³⁺ sites are regenerated within the film, which has reflected in the higher interfacial heterogeneous electron transfer rate, exchange current, diffusion coefficient and peak currents.

Table 4.2: Heterogeneous rate transfer constant and standard exchange current values for the three sensor platforms

Sensor platforms	I ₀ (A)	k ⁰ (cm/s)
Bare GCE	8.17x10 ⁻⁶	1.2x10 ⁻⁸
GCE/Nafion/[Ru(bpy) ₃] ²⁺	1.19x10 ⁻⁵	1.7x10 ⁻⁸
GCE/Nafion/[Ru(bpy) ₃] ²⁺ /G/PhNO ₂	1.37x10 ⁻⁵	2x10 ⁻⁸
GCE/Nafion/[Ru(bpy) ₃] ²⁺ /AuNp/G/PhNO ₂	2.6x10 ⁻⁵	3.8x10 ⁻⁸



4.3 Detection of tri-n-propylamine via electrochemiluminescent system

As mentioned earlier, electrochemiluminescence (ECL) is the emission of light observed when the excited product of an electrochemical reaction relaxes radiatively to its ground state. Luminescent signal can be obtained from the excited state of an ECL luminophore generated at electrode surface during the electrochemical reaction [161, 202-203]. As the combination of electrochemistry and chemiluminescence (CL), ECL presents several inherent advantages of two methods, such as versatility, sensitivity, simplified optical setup, and wide linear range for clinical and environmental analysis [204-205].

ECL behaviours of our sensor platforms were investigated in details using tripropylamine (TPA) as the model. The ECL emission of [Ru(bpy)₃]²⁺ - TPA system resulted from the

reaction between the de-protonated TPA radical (TPA[•]) and electro generated [Ru(bpy)₃]³⁺ to form [Ru(bpy)₃]^{2+*}, which then decays to produce emission [195-196]. See expression in Chapter three, Section 3.11.2. Two carbon screen printed electrodes (CSPE) were modified into CSPE/Nafion/[Ru(bpy)₃]²⁺/G/PhNO₂ and CSPE/Nafion/[Ru(bpy)₃]²⁺/AuNp/G/PhNO₂ as previously described.

The modified electrodes were tested in a series of TPA solutions with different concentrations prepared with 0.1 M PBS solution. And the ECL responses under continuous scanning to obtain a relative steady ECL intensity were recorded in a special 10 mL fused quartz cuvette. The results showed that the response ECL intensity increased with the concentration increment of TPA and that the ECL intensity was directly proportional to the concentration of TPA (as shown in Figure 4.28). The experimental results also show that CSPE/Nafion/[Ru(bpy)₃]²⁺/AuNp/G/PhNO₂ sensor had excellent ECL efficiency and long-term stability than CSPE/Nafion/[Ru(bpy)₃]²⁺/G/PhNO₂.

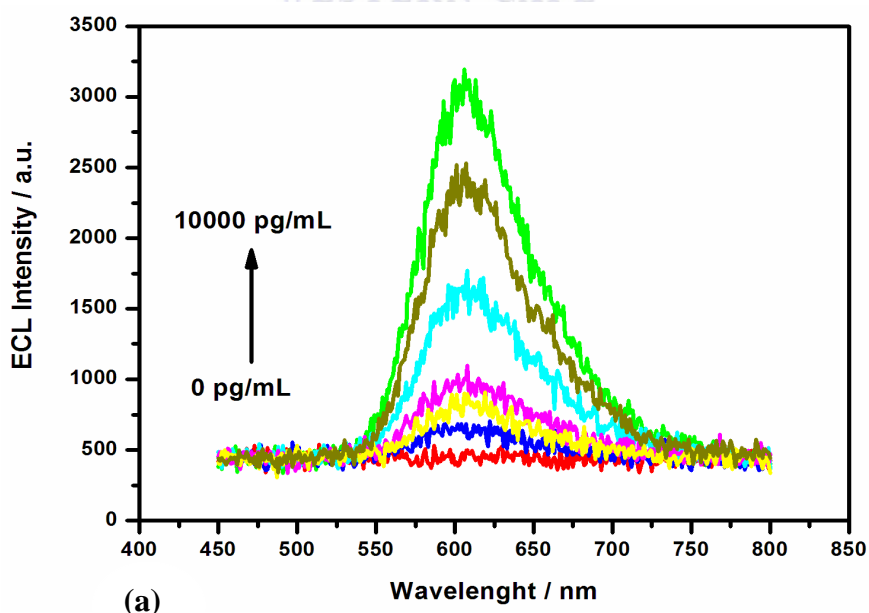


Figure 4.27(a): ECL signals of CSPE/ Nafion/[Ru(bpy)₃]²⁺/AuNp/G/PhNO₂ sensor with different concentrations of TPA (0, 5, 50, 500, 1000 and 10000 pg/mL).

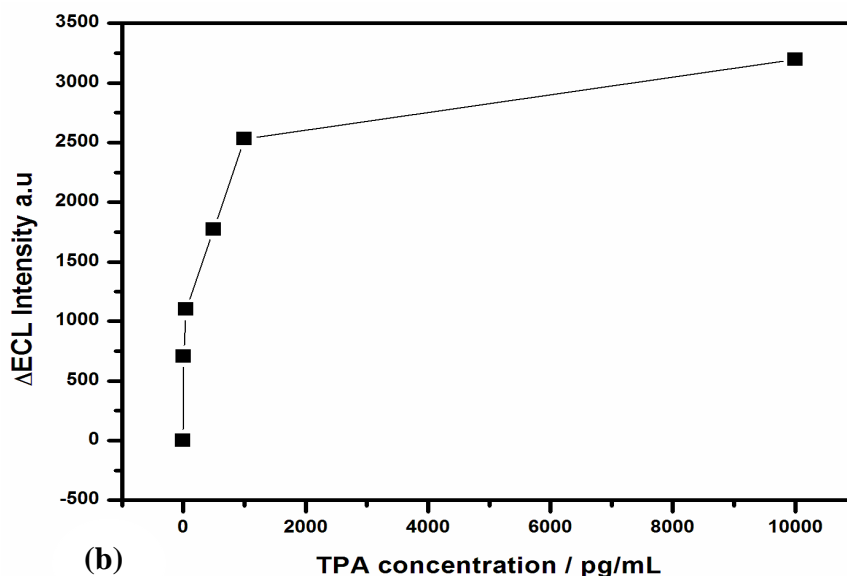
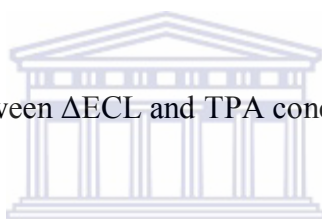


Figure 4.27(b): Relationship between ΔECL and TPA concentration



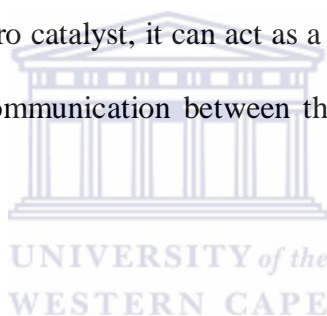
4.4 Electrochemical synthesis and characterisation of PDMA/AuNp/G/PhNO₂

The direct electron transfer rate at a bare GC electrode surface is usually very slow [32]. Therefore the modification of the electrode surface using suitable matrices as already reported is known to provide a conducive electro-environment for high interfacial heterogeneous electron transfer rate directly with the underlying electrode [32, 206]. A mediator is required to achieve this, which has been a major concern in developing electrochemical sensors. In this regard, conducting polymers have been of interest because of their electrical conductivity [206].

Among conducting polymers, polyaniline (PANI) has been one of the most studied owing to its high conductivity, environmental stability and low cost of production. PANI exists in three forms e.g., fully reduced leucoemeraldine; half oxidized emeraldine and fully oxidized

pernigraniline [207]. It can be synthesized chemically or electrochemically and it has many potential applications in various fields [208]. However, one major drawback of PANI which continues to be a problem is its poor processability. PANI in itself is not soluble in common solvents and it decomposes before it melts [209-210]. In order to improve on its processability, disubstituted form of PANI such as poly 2, 5 dimethoxyaniline was preferred in this research [32-33].

Poly 2, 5 dimethoxyaniline possesses interesting features which are superior and these includes higher electrical conductivity, environmental stability, improved processability, solubility in a variety of solvents and retention of its redox activity at pH above 4 [30, 33]. When doped with a suitable electro catalyst, it can act as a suitable electron transfer mediator for biosensors enabling direct communication between the immobilized bio-molecules and the electrode surface [30-34].



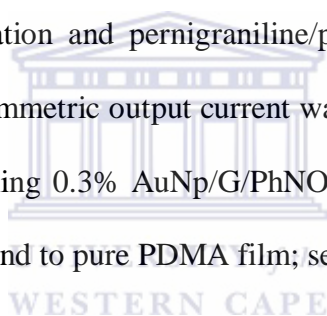
These systems could also have applications as donor-acceptor type conjugated systems [206], or electro and photochemical manipulation of the metal centres on the polymer and could represent switchable molecular wires responding to external stimuli. [31, 33, 206]. In this contribution, the interesting features of our nanostructured PDMA/AuNp/G/PhNO₂ material which was synthesized by incorporating our newly developed AuNp/G/PhNO₂ into the polymer matrix via electro-polymerisation method are explored.

4.4.1 Optimization for electrosynthesis of PDMA/AuNp/G/PhNO₂ on GCE

PDMA/AuNp/G/PhNO₂ composite films were formed on pre-cleaned glassy carbon electrode by electro polymerization of 0.05 M 2, 5 dimethoxyaniline (DMA) in 1 M HCl solution

containing 0, 0.3, 0.6, 0.8 and 1.0% AuNp/G/PhNO₂ as already described in chapter 3, section 3.7.

To evaluate the effect of AuNp/G/PhNO₂ on the properties of PDMA films, electrochemical performance of the composite films prepared from the various growth solutions were investigated by carrying out CV measurements at scan rate 50 mV/s in 1.0 M HCl and at scan rate 5 mV/s in 0.1 M PBS (pH 7.2) solutions. The results are shown in Figure 4.28 (a) and (b) respectively. A distinct redox couple could be observed from the CV measurement in PBS (Figure 4.28 b) while in the CV measurement in HCl showed three redox couples centred at 180 mV and 550 mV corresponding to leucoemeraldine radical cation/leucoemeraldine, emeraldine/emeraldine radical cation and pernigraniline/pernigraniline radical cation were observed [30, 211]. Largest voltammetric output current was observed with the film prepared from the growth solution containing 0.3% AuNp/G/PhNO₂ in HCl characterisation solution compared to other compositions and to pure PDMA film; see Figure 4.28 (a).



And a slight shift in peak potential between the 0.3% PDMA/AuNp/G/PhNO₂ and pristine PDMA could be observed too. Similar observations were recorded in PBS characterisation solution ran at scan rate 5 mV/s; see Figure 4.28 (b). The electrochemical behaviour of pure PDMA and PDMA/AuNp/G/PhNO₂ prepared from various composition solutions was clearly expressed in Figure 4.28. Therefore, PDMA/AuNp/G/PhNO₂ composite film prepared from the growth solution containing 0.3% AuNp/G/PhNO₂ was found to be the optimum ratio and used all through for the electrochemical synthesis of PDMA/AuNp/G/PhNO₂ composite since it exhibited highest peak current in both acid and PBS solutions compared to others.

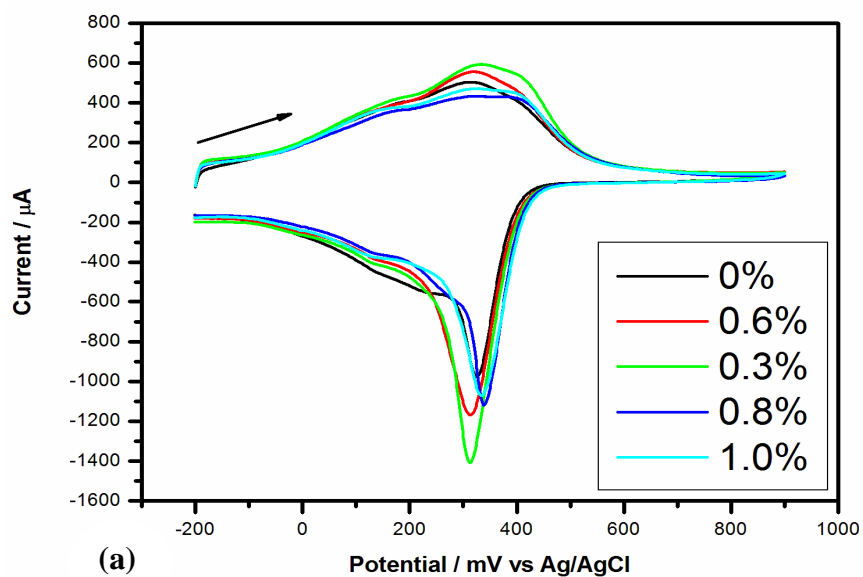


Figure 4.28(a): CV behaviour of PDMA/AuNp/G/PhNO₂ films prepared from the growth solutions containing 0, 0.3, 0.6, 0.8 and 1.0% AuNp/PhNO₂ in 1 M HCl.

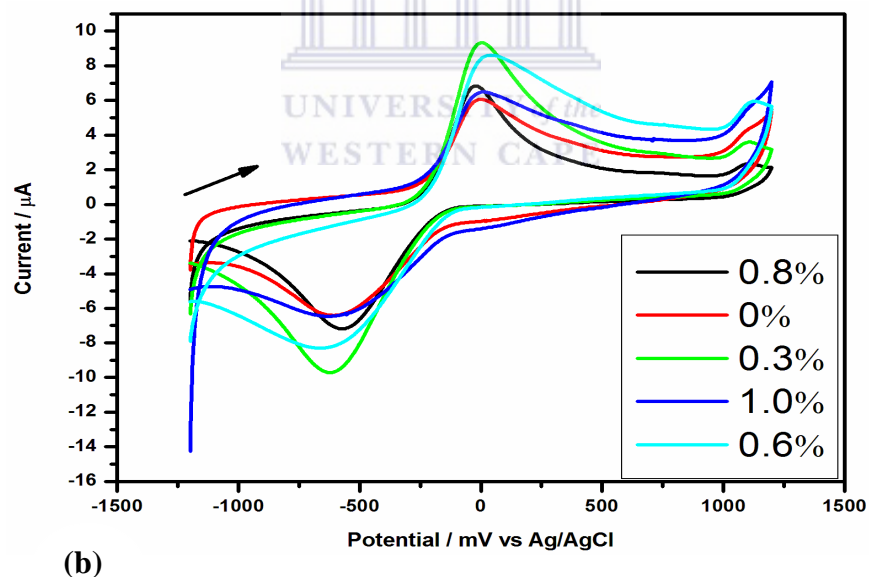


Figure 4.28(b): CV behaviour of PDMA/AuNp/G/PhNO₂ films prepared from the growth solutions containing 0, 0.3, 0.6, 0.8 and 1.0% AuNp/G/PhNO₂ in 0.1 M PBS solution.

The enhancement in electrochemical activity PANI and substituted PANI depends on the type of dopant and degree of doping/protonation [212-213], therefore a promotion in the protonation with the doping effect of AuNp/G/PhNO₂ electro catalyst was expected. This is due to the fact that our newly synthesised gold nanoparticles-dotted 4-nitrophenylazo functionalised graphene (AuNp/G/PhNO₂) have large π -bonded surface which might interact strongly with the conjugated structure of PDMA via π -stacking.

And that the resulting highly conjugated π -system would promote the degree of electro delocalization and lead to a preferential protonation of amine nitrogen atoms. It could be observed from Figures 4.29 (a) and (b) that the 0.3% PDMA/AuNp/G/PhNO₂ composite film showed a great enhancement in the CV peak currents compared to that of pristine PDMA.



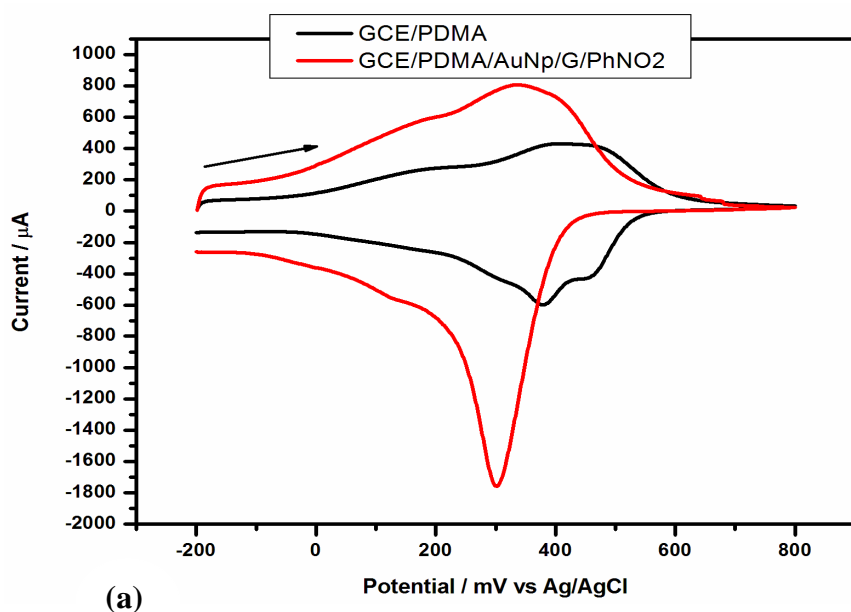


Figure 4.29(a): CV of GCE/PDMA and GCE/PDMA/AuNp/G/PhNO₂ (0.3%) in 1 M HCl solution.

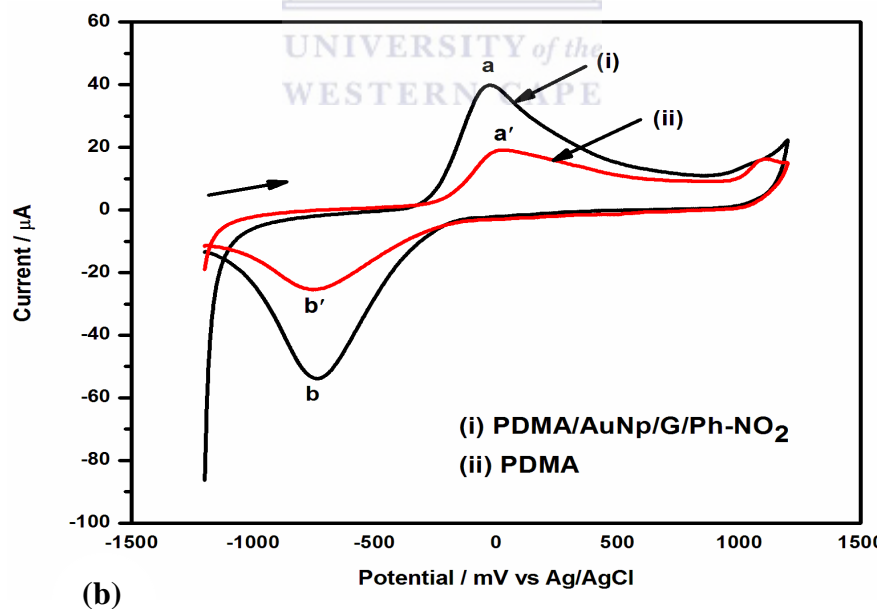


Figure 4.29(b): CV of GCE/PDMA and GCE/PDMA/AuNp/G/PhNO₂ (0.3%) in 0.1 M PBS solution.

4.4.2 Electrochemical synthesis of PDMA/AuNp/G/PhNO₂ composite

Electrochemical polymerization of 2, 5-dimethoxyaniline monomer on GCE in the absence and presence of AuNp/G/PhNO₂ was achieved by cyclic voltammetry in 1 M HCl. The electrode potential was scanned between -200 and +900 mV for 10 cycles at a scan rate 50 mV/s, following the experimental procedure described in chapter two, section 3.7.2. The polymerization reaction was initiated by the formation of resonance stabilized aniline radical cations from the protonated 2, 5-dimethoxyaniline monomer [214-215].

Throughout the electro polymerisation, it was observed that the peak current increased as the number of cyclic voltammograms increased. Also the polymer thickness increased with successive potential cycles indicating that conductive polymeric films are being formed on the surface of the glassy carbon working electrode [214, 216]. A homogenous film was produced after the 10 cyclic voltammograms. The cyclic voltammograms for the electro deposition of PDMA and PDMA/AuNp/G/PhNO₂ films on the GCE surface are shown in the Figure 4.30 (a) and (b) respectively.

Two pairs of redox peaks centred at 180 mV (a/a') and 550 mV (c/c'), corresponding to transition from leucoemeraldine to emeraldine, and emeraldine to pernigraniline states [215-216] respectively, were observed for both the pristine PDMA and the doped PDMA/AuNp/G/PhNO₂ composite. This indicates the presence of discrete electroactive regions in the films. The origin of another pair of redox peaks observed at 430 mV (b/b') for both PDMA and PDMA/AuNp/G/PhNO₂ is complex and can be attributed to different intermediates and degradation products such as cross-linked polymer, benzoquinone, emeraldine/emeraldine radical cation etc [217]. Noticeably, the incorporation of AuNp/G/PhNO₂ into the polymer matrix evidently improved the conductivity of the

composite as could be observed from better defined redox peaks (a/a'), (b/b') and (c/c') in the polymerisation CVs of Figure 4.30.

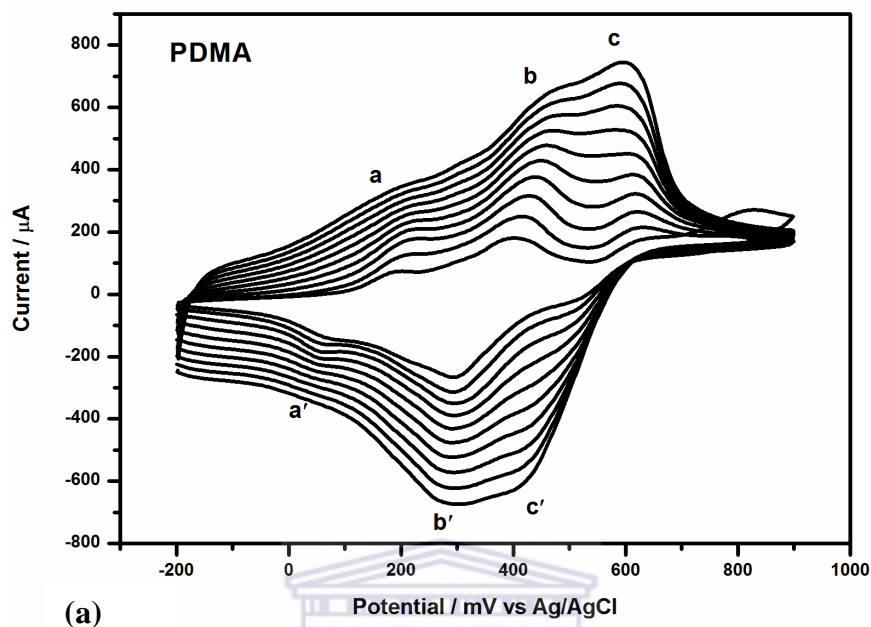


Figure 4.30(a): CV for electrochemical synthesis of PDMA in 1.0 M HCl

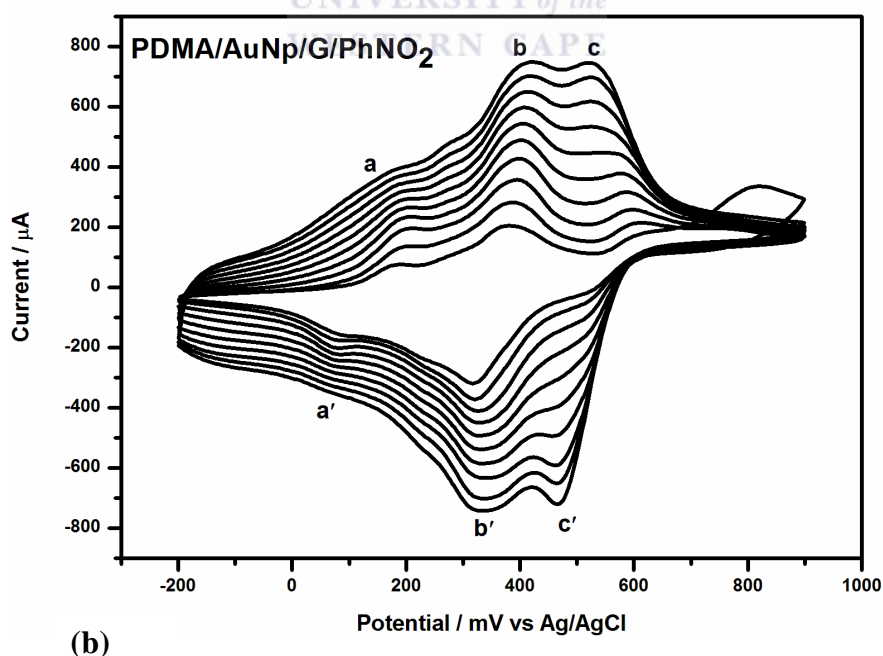


Figure 4.30(b): CV for electrochemical synthesis of PDMA/AuNp/G/PhNO₂ films in 1.0 M HCl

4.4.3 Characterisation of PDMA

The electrodeposited PDMA and PDMA/AuNp/G/PhNO₂ films were characterised by CV in 1.0 M HCl at various scan rates (10-70 mV/s) as shown in Figure 4.31 (a) and (b) respectively. The voltammograms exhibited three redox peaks; (a/a') is assigned to leucoemeraldine radical cation/leucoemeraldine, the second redox peak (b/b') is assigned to emeraldine/emeraldine radical cation and the third one (c/c') is assigned to pernigraniline/pernigraniline radical cation [30, 211]. Analysis of the voltammograms showed that the peak potentials and corresponding currents vary with increasing scan rates. The increase in peak current is greater for the composite film Figure 4.31 (b) than for pure PDMA Figure 4.30 (a) indicating that the AuNp/G/PhNO₂ nanocatalyst truly improved the conductivity of the assembled film. It was also observed that peak b' disappeared with increase of scan rate from 60 mV/s. This indicates that PDMA/AuNp/G/PhNO₂ was successfully attached onto GCE surface and it is electroactive.

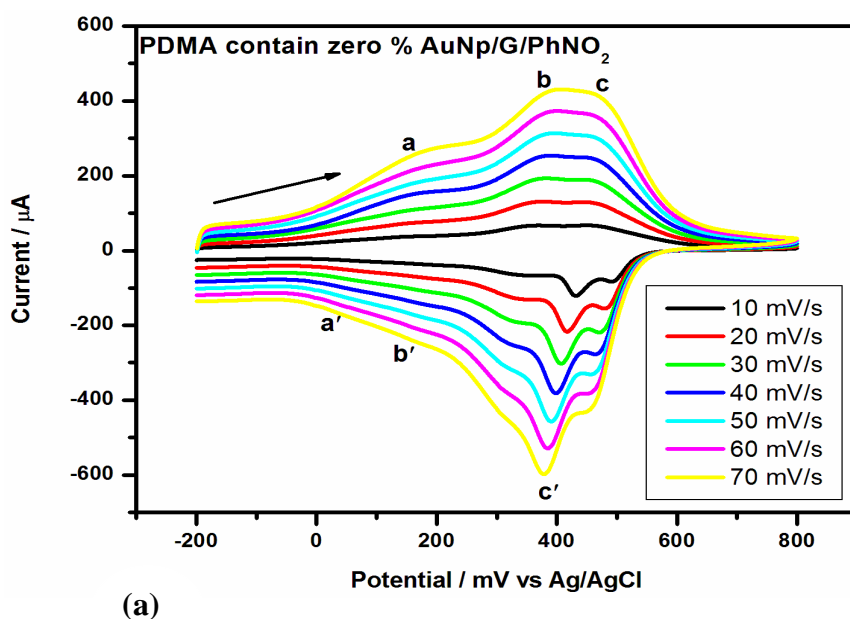


Figure 4.31(a): CV at various scan rates (10-70 mV/s) of GCE/PDMA in 1 M HCl

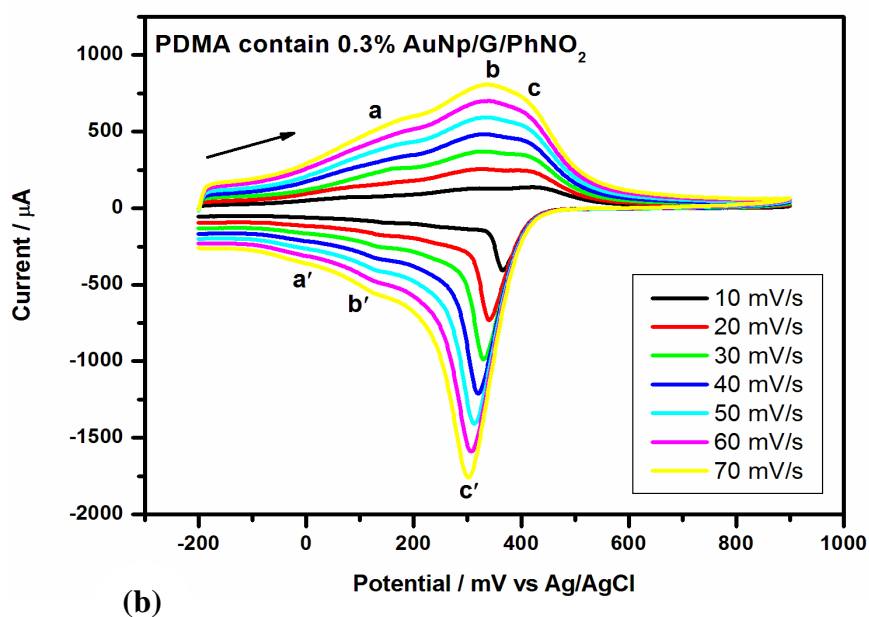
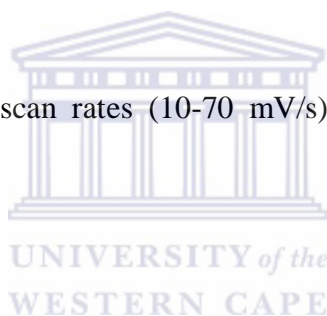


Figure 4.31(b): CV at various scan rates (10-70 mV/s) of GCE/PDMA/AuNp/G/PhNO₂ (0.3%) in 1 M HCl.



From Figure 4.31 (b), kinetic studies of PDMA/AuNp/G/PhNO₂ were performed to investigate its behaviour on GC electrode in 1.0 M HCl solution. The number of electrons transferred was estimated from peak c' at scan rate 20 mV/s and was calculated using equation:

$$|E_p - E_{p1/2}| = 2.20RT/nF = 56.5/n \quad (60)$$

Where, E_p = maximum peak potential

$E_{p1/2}$ = half maximum potential

R = gas constant, 8.314 J (mol/K)

T = absolute temperature of the system, 298 K

F = Faraday constant, 96584 C/mol

n = number of electrons transferred

It was calculated to be one (1) electro transfer system which is in agreement other reports in the literature [210, 218]. Anodic peak current versus scan rate plot, Figure 4.32(a), is linear indicating that there are conducting electroactive polymers on the electrode which undergo rapid charge transfer reactions.

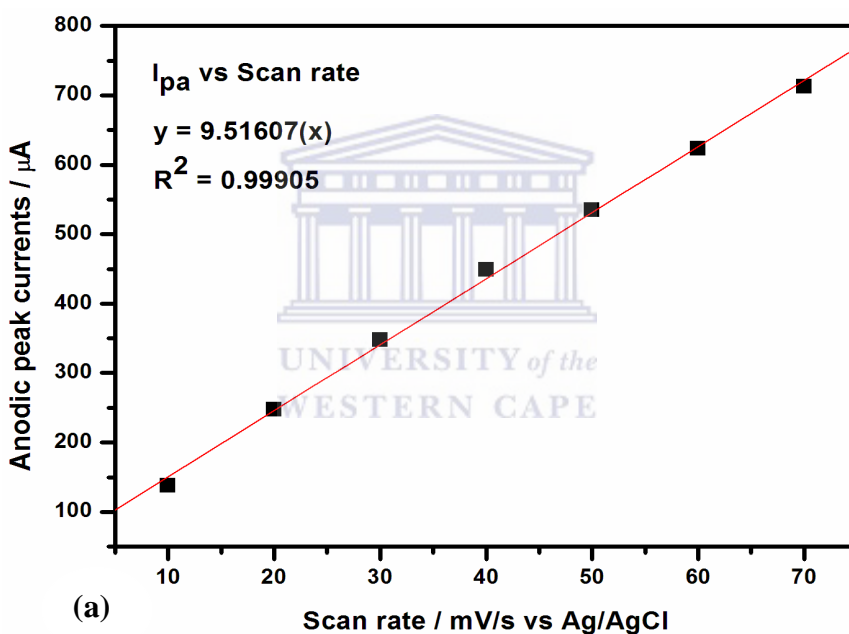


Figure 4.32(a): The Randles-Sevcik plots of I_{pa} peak (c) vs scan rate.

The surface concentration (Γ^*) of the absorbed electroactive species could be estimated from Figure 4.32 (a) using Brown Anson equation [210]:

$$I_p = \frac{n^2 F^2 \Gamma^* \nu A}{4 R T} \quad (61)$$

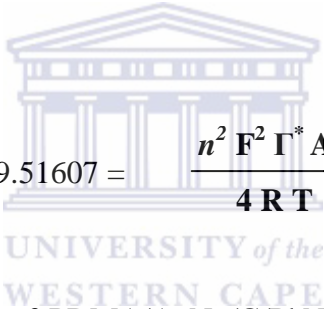
Where, I_p = peak current

A = electrode surface area

Γ^* = surface concentration of absorbed electroactive species

ν = scan rate (mV/s)

n , F , R and T are as explained in equation (60).



From Figure 4.32 (a), the slope = 9.51607 = $\frac{n^2 F^2 \Gamma^* A}{4 R T}$ (62)

Hence, the surface concentration of PDMA/AuNp/G/PhNO₂ (peak c) was estimated to be 1.269 x 10⁻⁴ mol/cm².

The linear dependence of peak current on the square root of the scan rate was done by Randles-Sevcik plot Figure 4.32 (b) for GCE/PDMA/AuNp/G/PhNO₂ peak c. The result obtained indicates a diffusion controlled system in which the peak current arises from the electro propagation through the polymer chain.

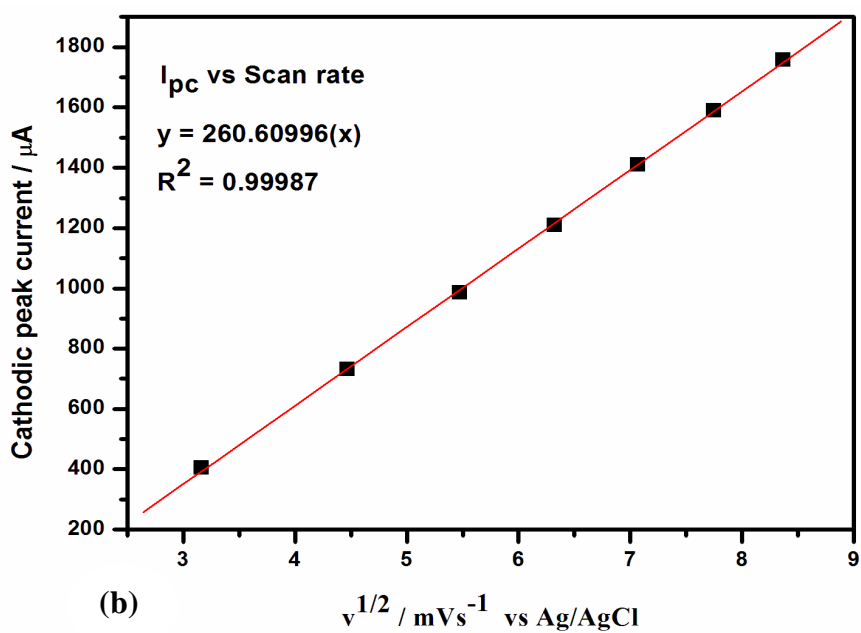


Figure 4.32(b): The Randles-Sevcik plots of I_{pc} peak (c') vs square root of scan rate.

Randles-Sevcik equation was used to estimate the rate of charge transport coefficient (D) within the polymer matrix applying the slope of the straight line plot obtained in Figure 4.32 (b) in the equation. The diffusion coefficient for GCE/PDMA/AuNp/G/PhNO₂ was estimated to be $8.853 \times 10^{-3} \text{ cm}^2/\text{s}$ for peak c.

Chapter Five

Results and discussion- Part two

This chapter presents the optimisation and characterisation of DON immunosensors fabricated with the three sensor platforms that was developed in chapter four. The results obtained from the application of these immunosensors in the detection and determination of DON in standard samples and real samples via impedimetric system are also discussed.

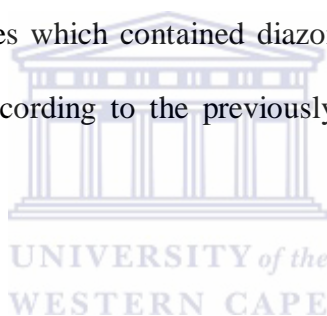
EIS is a sensitive, non-destructive and an excellent electrochemical sensing method as reviewed earlier in chapter two. It was envisaged that impedance sensing is most useful for large species that significantly perturb the sensing interface. Regardless of the method of transduction, any immunosensor relies on robust sensing interfaces with well-defined molecular interactions between an antibody and the epitope/antigenic species to which it selectively binds [179]. Hence, the efficient immobilization of biomolecules on transducers is a potentially important prerequisite for the fabrication of ultrasensitive biosensors and nanotechnology devices. The aryl diazonium salt system for modifying surfaces is one surface modification system that has the requisite stability and versatility to be applied to a wide range of different sensing interfaces [177]

5.1 Fabrication of deoxynivalenol mycotoxin immunosensors

Label free electrochemical inhibition based immunosensors for sensitive detection of deoxynivalenol (DON) mycotoxin was developed with gold nanoparticles-dotted 4-

nitrophenylazo functionalised graphene (AuNp/G/PhNO₂), as signal amplification nanocatalyst mediated in Nafion and PDMA as the sensing platforms. And I adopted diazonium chemistry as the biomolecule immobilization method. Three glassy carbon electrodes were first modified with thin film Nafion/[Ru(bpy)₃]²⁺/AuNp/G/PhNO₂, Nafion/[Ru(bpy)₃]²⁺/G/PhNO₂ and GCE/PDMA/AuNp/G/PhNO₂ as described in Chapter Three, Sections 3.6 and 3.5.

The resulting modified electrodes offered an excellent platform for high performance biosensing applications as observed from the various characterisation techniques in chapter four. The immunosensors were tailored by covalently coupling the capture antibody onto the surface of the modified electrodes which contained diazonium salt-functionalised graphene that was chemically prepared according to the previously described procedure in Chapter Three, Section 3.3.



5.1.1 Electro-reduction of nitrophenyl group to aminophenyl group.

The modified electrodes were first reduced electrochemically to obtain a modified film of 4-aminophenyl on the electrode surface in 0.1 KCl solutions by two cyclic voltammetric scans over potential range -1200 to 0 mV at scan rate of 50 mV/s. Figure 5.1 shows an irreversible long cathodic sweep of p-nitrophenyl modified electrode at around -1200 mV (Ag/AgCl). During the second scan, the long sweep drastically diminished, indicating that nearly all the electroactive -PhNO₂ groups are reduced in the first scan. However, the reduction of -PhNO₂ to -PhNH₂ is incomplete as evidenced by the reversible couple that appeared at $E_{1/2} = -260$ mV (Ag/AgCl). This couple is assigned to the aminophenyl/nitrosophenyl inter-conversion [174]

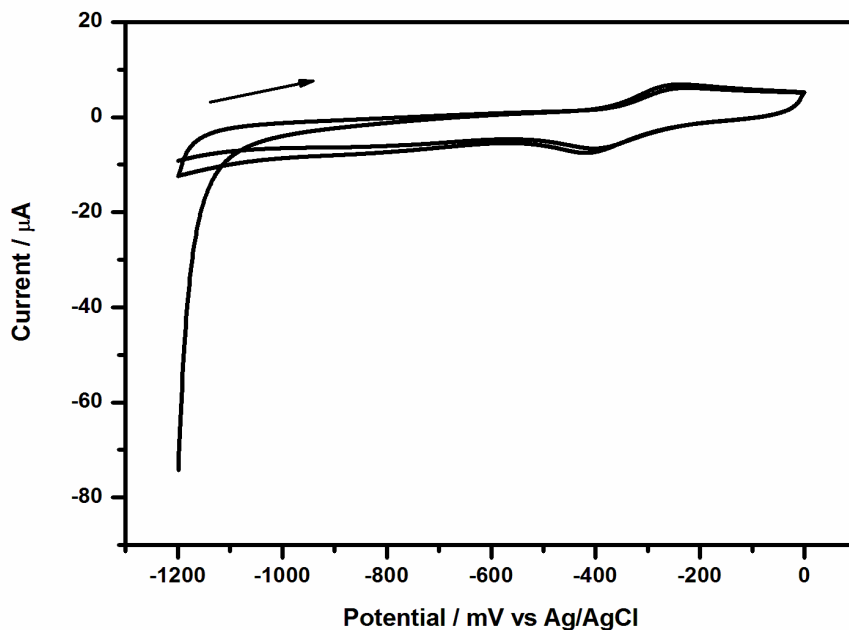
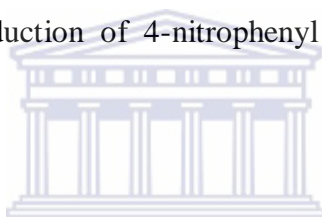


Figure 5.1: Electrochemical reduction of 4-nitrophenyl group to 4-aminophenyl on the electrode surface.



5.1.2 CV behaviour of electrochemically reduced modified electrodes

Once the p-aminophenyl surface layer was formed, the electrochemical behaviour of the modified GC/Nafion/[Ru(bpy)₃]²⁺/AuNp/G/PhNH₂ electrode surface was investigated by cyclic voltammetry in the presence of the [Ru(NH₃)₆]^{2+/3+} redox couple. Figure 5.2 shows the cyclic voltammogram for bare GC electrode, GC/Nafion/[Ru(bpy)₃]²⁺/AuNp/G/PhNO₂ electrode and for GCE/Nafion/[Ru(bpy)₃]²⁺/AuNp/G/PhNH₂ electrode, in the presence of the [Ru(NH₃)₆]^{2+/3+} redox couple. The data clearly show that the characteristic oxidation/reduction waves of the [Ru(NH₃)₆]^{2+/3+} redox couple was completely suppressed at the GCE/Nafion/[Ru(bpy)₃]²⁺/AuNp/G/PhNH₂ electrode in curve (iii). This is expected for completely blocked surfaces. The aminophenyl group is assumed to be covalently grafted to the graphene surface [176, 178]. Similar trend of CV behaviour was observed for GCE/Nafion/[Ru(bpy)₃]²⁺/G/PhNO₂ and GCE/PDMA/AuNp/G/PhNO₂.

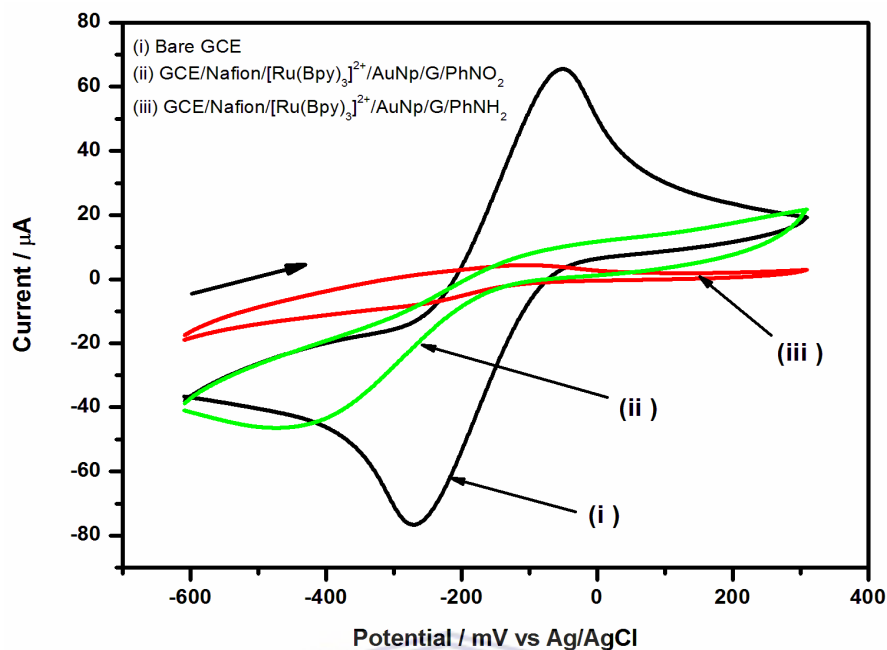


Figure 5.2: CV of (i) bare GCE, (ii) GCE/Nafion/[Ru(bpy)₃]²⁺/G/PhNO₂ and (iii) GCE/Nafion/[Ru(bpy)₃]²⁺/AuNp/G/PhNH₂ recorded in 5 mM [Ru(NH₃)₆]^{2+/3+}.

WESTERN CAPE

5.1.3 EIS study of electrochemically reduced modified electrodes

The characteristic of the modified electrode was further investigated by EIS, the results of which were completely consistent with the cyclic voltammetry results. The Nyquist plots of these impedance results are shown in Figure 5.3. The analysis of the Nyquist plots was based on an equivalent circuit shown in the inset Figure 5.3, where the solution resistance, R_s (resistance of solution and of Ohmic contacts) in series precedes a constant phase element (CPE) which is related to the capacitance of the functionalized glassy carbon sensing interface [100, 108].

CPE reflects the non-ideality of the double-layer at the functionalized glassy carbon electrode/ electrolyte interface due to the roughness and porosity of the interfacial film. The CPE is in parallel with charge transfer resistance, R_{ct} and Warburg element open, (W_o). R_{ct} represents the resistance related to the charge transfer rate of redox reactions at the functionalized electrode [98, 139, 141].

The charge-transfer resistance of the Nyquist plots is highest for the GC/Nafion/[Ru(bpy)₃]²⁺/AuNp/G/PhNH₂ electrode than for the bare GC and GCE/Nafion/[Ru(bpy)₃]²⁺/G/PhNO₂ electrodes. This is due to the formation of insulating organic layer or blocking effect of -PhNH₂ group on the modified electrode surface which leads to the lower rate of electron transfer through the film [173], evidencing high coverage of the electrode surface with p-aminophenyl group. Similar trend of result was observed for the other sensor platforms.

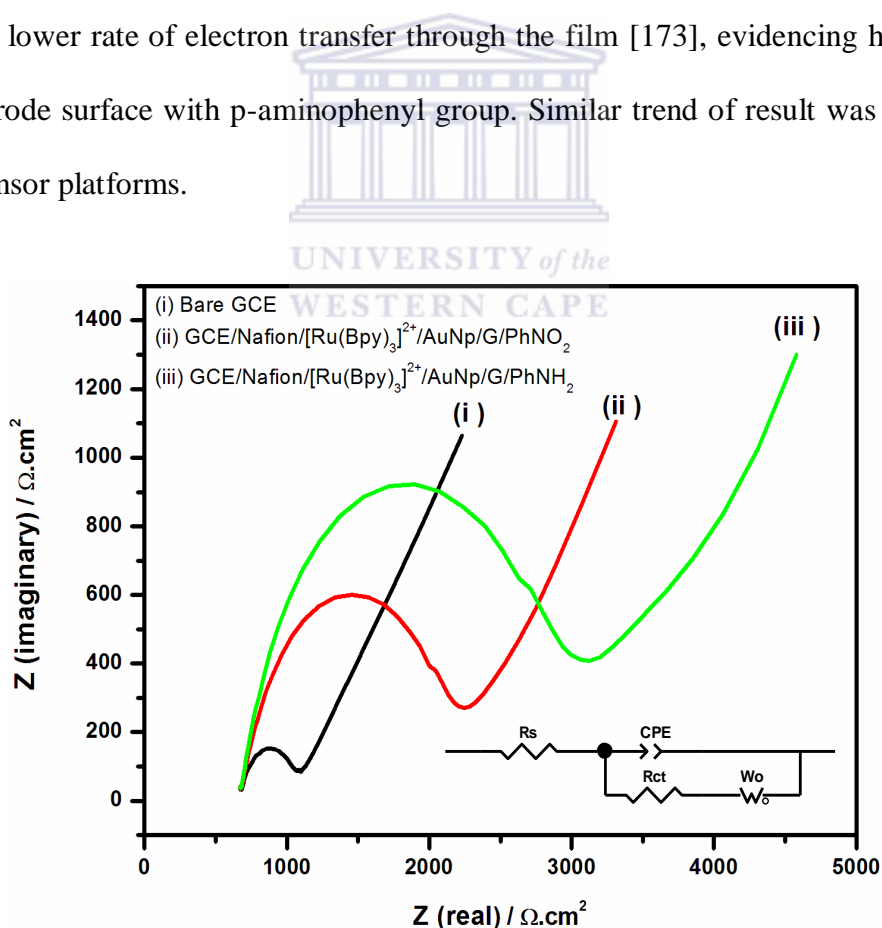


Figure 5.3: Nyquist plots in 5 mM $[\text{Fe}(\text{CN})_6]^{3-/4-}$ in frequency range of 100 mHz–10 kHz.

The R_{ct} , R_s , CPE and W_o values obtained from the circuit fitting for the Nyquist plots of impedance spectra of GCE, GCE/Nafion/[Ru(bpy)₃]²⁺/AuNp/G/PhNH₂, GCE/Nafion/[Ru(bpy)₃]²⁺/G/PhNH₂ and GCE/PDMA/AuNp/G/PhNH₂ recorded in the presence of 5 mM [Fe(CN)₆]^{3-/4-} redox system in the frequency range of 100 mHz–10 kHz are shown in Table 5.1. The R_{ct} value for GCE/PDMA/AuG/PhNH₂ is the lowest indicating that this platform is more conducting than others and it follows that sequence to the least conducting platform which is GCE/Nafion/[Ru(bpy)₃]²⁺/G/PhNH₂.

Table 5.1: EIS parameters of GCE, GCE/Nafion/[Ru(bpy)₃]²⁺/AuNp/G/PhNH₂, GCE/Nafion/[Ru(bpy)₃]²⁺/G/PhNH₂ and GCE/PDMA/AuNp/G//PhNH₂ in 5 mM [Fe(CN)₆]^{3-/4-} solution.

Sensor platforms	R_s (Ω)	R_{ct} (Ω)	CPE (nF)	W_o ($\Omega s^{1/2}$)
Bare GCE	703.7	394.3	0.79092	0.47896
GCE/PDMA/AuNp/G/PhNH ₂	641.2	1607	0.80966	0.50364
GCE/Nafion/[Ru(bpy) ₃] ²⁺ /G/PhNH ₂	517.2	2095	0.85138	0.41336
GCE/Nafion/[Ru(bpy) ₃] ²⁺ /AuNp/G/PhNH ₂	634.8	1952.3	0.82431	0.47722

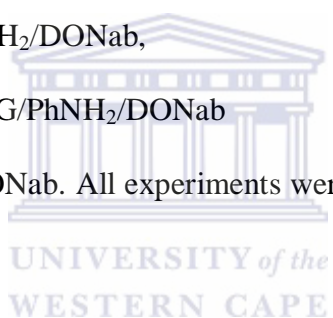
5.2 Immobilisation of DON antibody

The p-aminophenyl surface layer on the modified electrodes was activated with EDC/NHS to give a stable intermediate derivative that covalently binds with antibodies (see schematic illustration in chapter 3 scheme 9 & 10) [176]. After rinsing the electrode from the side with 0.1 M PBS (pH 7.2) solution, 30 μ L of 0.2 μ g/ μ L (in 0.1 M PBS, pH 7.2) monoclonal

deoxynivalenol antibody (DONab) was spread on the electrode surface and incubated for 30 min at room temperature.

The electrode was again rinsed from the side using 0.1 M PBS (pH 7.2) solution to remove any physically bound antibody and then 10 μ L of BSA was spread on the electrode surface to block nonspecific binding sites for 30 min at room temperature and rinsed with PBS (pH 7.2) before making impedimetric measurements [177-179]. This same immobilisation protocol was used in preparing all other electrodes.

The three immobilized electrodes were denoted as GCE/Nafion/[Ru(bpy)₃]²⁺/G/PhNH₂/DONab, GCE/Nafion/[Ru(bpy)₃]²⁺/AuNp/G/PhNH₂/DONab and GCE/PDMA/AuNp/G/PhNH₂/DONab. All experiments were carried out at room temperature (see chapter two section 3.12.4).



5.3 UV-Vis study of DON antibody-antigen reactivity

DON molecule is characterized as a tetra-cyclic sesquiterpene with seven stereo centres, six oxygen atoms consisting of an epoxide, a carbonyl-C=O, an aromatic C=C group, cyclic ether and three alcoholic -OH groups (see Chapter Two, Section 2.1 for the chemical structure of DON). As mentioned earlier, UV-visible spectroscopy is widely adopted in studying the electronic structure of chemical compounds [98, 101, 103]. Figure 5.4 (a) shows the absorbance spectrum of 5 μ g/mL deoxynivalenol (DONag) standard solution prepared in a (3:1) mixture of methanol/PBS solution, methanolic phosphate buffer saline, (MPBS).

It was recorded on a Nicolet Evolution 100 Spectrometer (Thermo Electron Corporation, UK) at a wavelength of 190 nm to 800 nm. The sample (4 mL) was measured into a pre-cleaned 5 mL fused quartz cuvette before measurements as described in Chapter Three, Section 3.8. An absorption band with a peak around 224 nm was observed. This peak corresponds to π - π^* transitions of aromatic C=C bond in the DON chemical structure [183-184].

10 μ L of various dilute concentrations of deoxynivalenol antibody (DONab) (2.5 μ g/mL, 5.0 μ g/mL, 7.5 μ g/mL and 10.0 μ g/mL) were added in separate experiments to the 5 μ g/mL DONag solution and measured. It was observed that the absorbance decreased in intensity as the concentration of the added DONab solution increased; see Figure 5.4 (b). This indicates that there is a binding interaction between the antigen and the antibody.

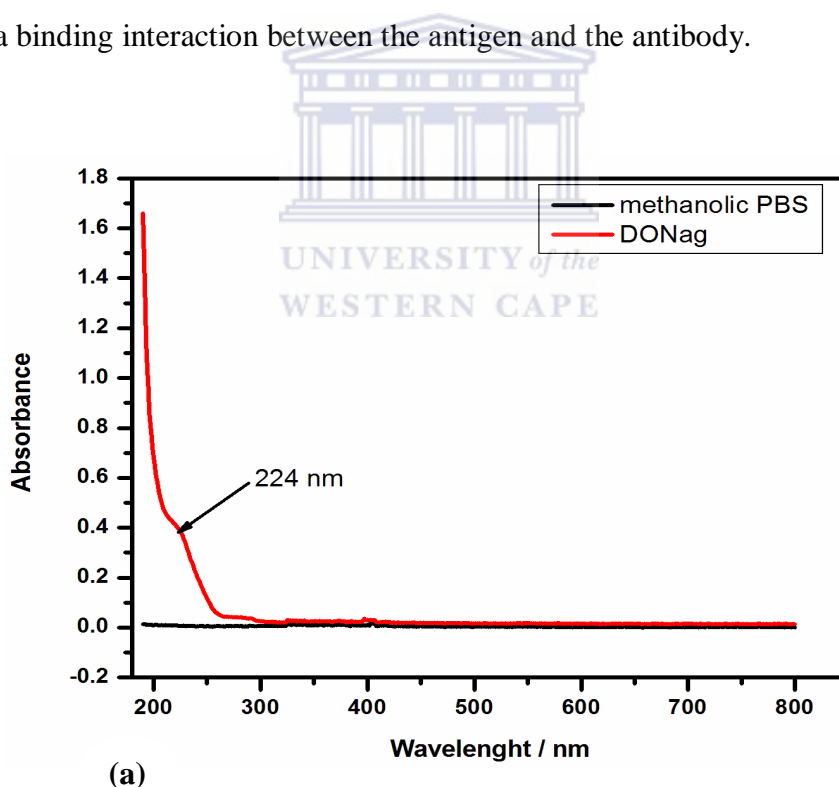


Figure 5.4(a): The absorption spectra of DON prepared in MPBS.

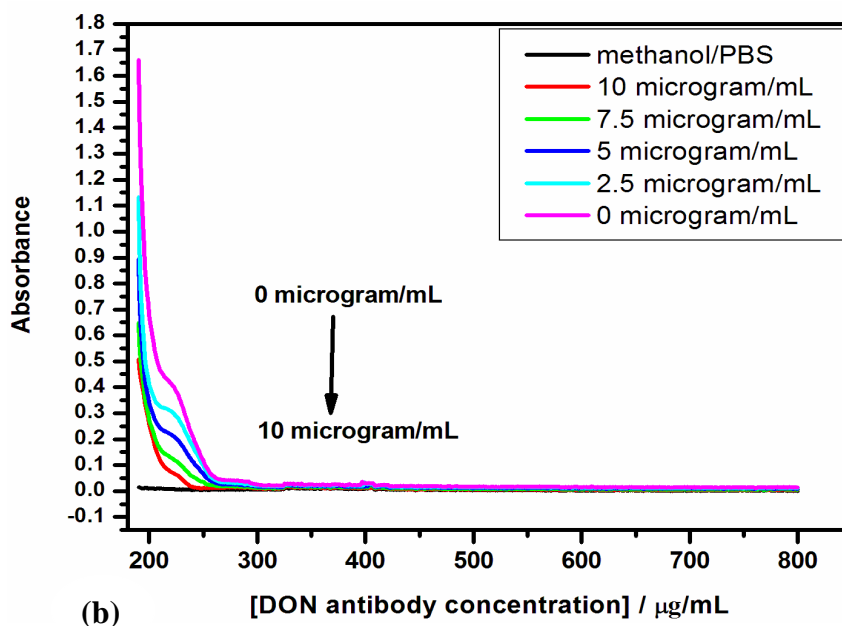
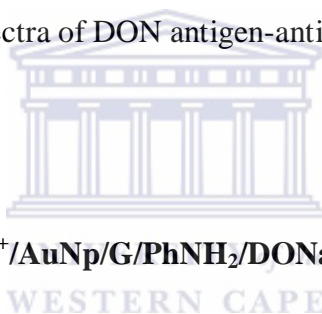


Figure 5.4(b): The absorption spectra of DON antigen-antibody reactivity.



5.4 GCE/Nafion/[Ru(bpy)₃]²⁺/AuNp/G/PhNH₂/DONab immunosensor

5.4.1 CV behaviour of the stepwise modification processes

The immunosensor was designed according to the protocol described in Chapter two, Section 3.12.4. The electrochemical behaviour of various stages in the modification of the immunosensor was studied by cyclic voltammetry. It was observed that the immobilization of deoxynivalenol antibody (DONab) on the GCE/Nafion/[Ru(bpy)₃]²⁺/AuNp/G/PhNH₂, (curve i) lead to a decrease in peak current of the [Ru(bpy)₃]²⁺ redox probe. This is due to decreased electron transfer capability of the DONab modified electrode (curve ii). This result could confirm that the immobilized DONab forms an insulating layer on the electrode and perturbs the interfacial electron transfer considerably.

After BSA was immobilized to block the remaining active sites in order to avoid any nonspecific adsorption, a further decrease of the peak currents was observed with the fact that BSA insulates the conductive support and hinders the transmission of electrons toward the electrode surface further (curve iii).

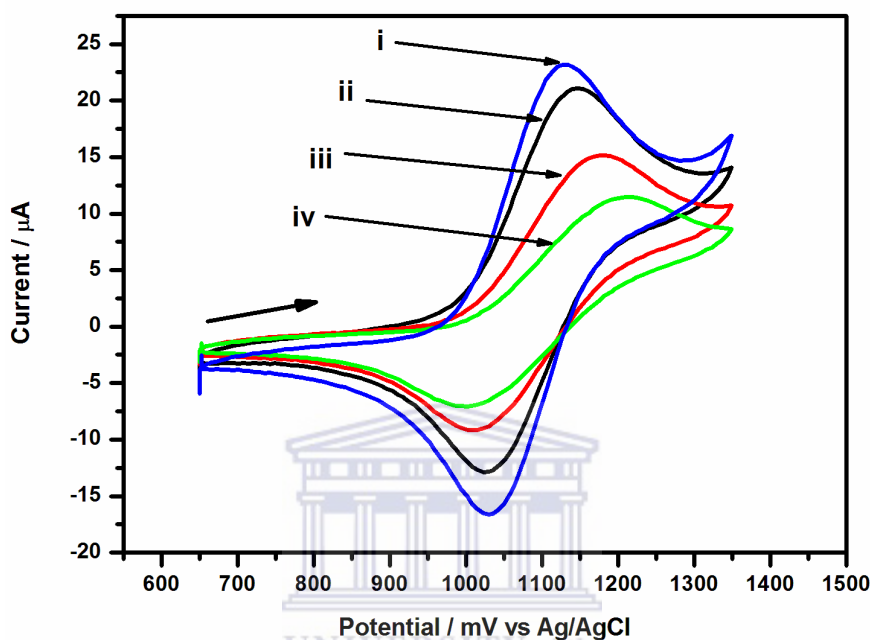


Figure 5.5: CV response of different immobilisation steps:

(i) GCE/Nafion/[Ru(bpy)₃]²⁺/AuNp/G/PhNH₂, (ii) after immobilization of DON antibody, (iii) after blocking nonspecific binding sites with BSA and (iv) after immobilization and running in standard DON solutions at scan rate of 50 mV/s, over potential range of 650 – 1350 mV.

These results indicated that the immunosensor was successfully modified as premeditation. The peak current reduced further after the immunosensor was applied in detecting DON from the standard solution (curve iv).

5.4.2 Chronoamperometric behaviour of stepwise modification processes

The electrochemical behaviour of the stepwise modification processes of GCE/Nafion/[Ru(bpy)₃]²⁺/AuNp/G/PhNH₂/DONab immunosensor was further investigated by chronoamperometry. The experiments were done in a 2 step potential mode, 2 sec quiet time, and pulse width of 500 msec in a quiescent condition. The choice of potential steps was made from the cyclic voltammogram at 50 mV/s of the immunosensor in 0.1 M PBS (pH 7.2).

The Faradaic chronoamperometric measurements were in good agreement with the CV measurements. It could be observed from the chronocoulograms in Figure 5.6 (a) and (b) that the current reduced with each modification step. This indicates that following the observed blocking effect of the PhNH₂ film in the previous sections, a further blocking effect was observed after the covalent immobilization of the antibody and blocking of nonspecific binding sites with BSA.

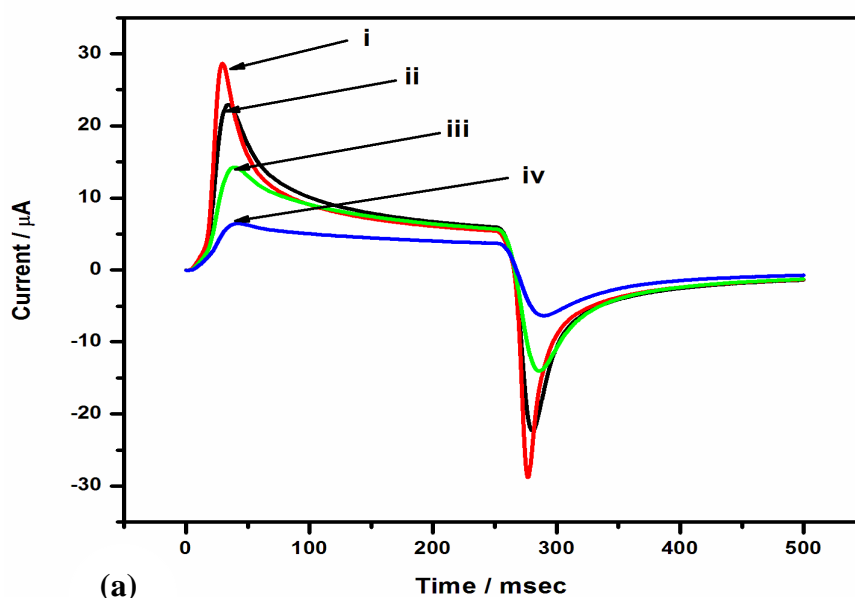


Figure 5.6 (a): Chronoamperometric response of different immobilisation steps.

Figure 5.6 (a) is represented as (i) GCE/Nafion/[Ru(bpy)₃]²⁺/AuNp/G/PhNH₂, (ii) after immobilization of DON antibody, (iii) after blocking nonspecific binding sites with BSA and (iv) after immobilization and running in standard DON solutions.

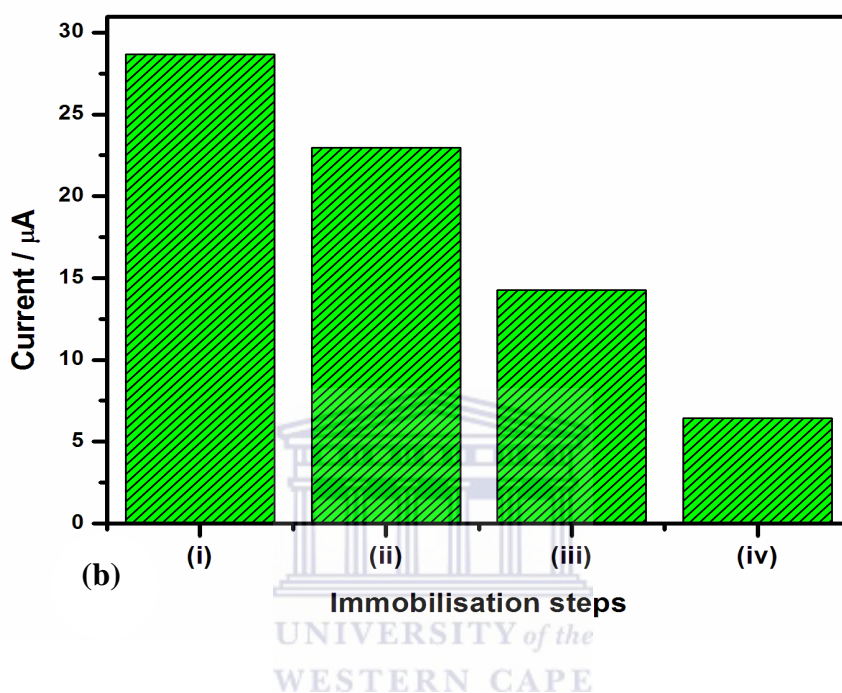


Figure 5.6 (b): Bar chart of the chronoamperogram.

5.4.3 Optimisation of assay condition

5.4.3.1 Effect of antibody concentration

The electrochemical responses of the immunosensor to various concentrations of DONab applied in the immobilisation step were determined by impedance spectroscopy. Different dilutions of DONab were prepared (1:10; 1:50; 1:100, 1:200 and 1:400 v/v, corresponding to 0.01, 0.02, 0.1, 0.2 and 0.4 μg/μL). 30 μL of each concentration was drop coated onto the modified electrode to get GCE/Nafion/[Ru(bpy)₃]²⁺/AuNp/G/PhNH₂/DONab, and then impedimetric measurements were performed in presence of 30 ng/mL DONag MPBS

solution (pH 7.2). The highest R_{ct} was obtained with 0.2 $\mu\text{g}/\mu\text{L}$ (Figure 5.7), indicating the optimal formation of immune-complexes and inhibition. Thus, concentration of 0.2 $\mu\text{g}/\mu\text{L}$ was selected for all experiments.

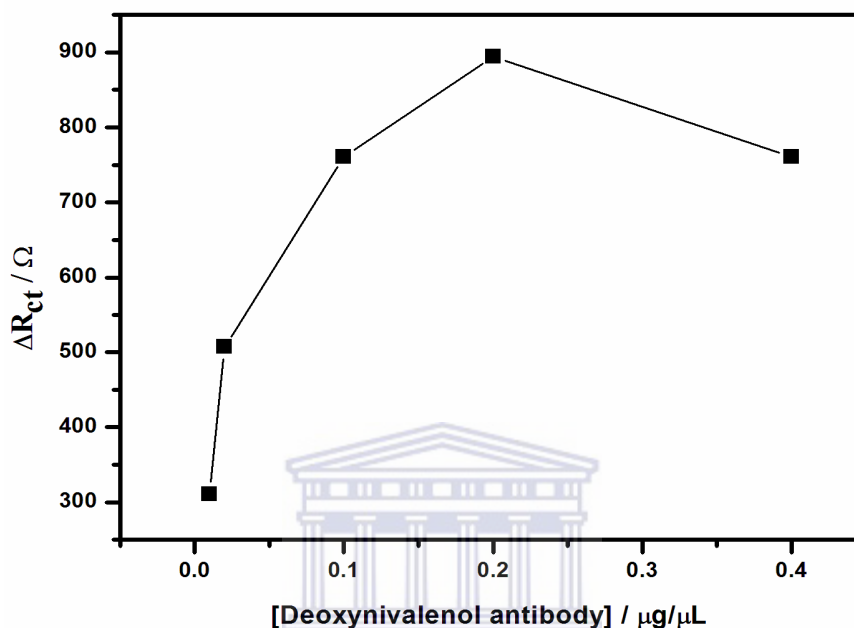


Figure 5.7: The plot of R_{ct} values versus deoxynivalenol concentration.

5.4.3.2 Effect of pH

In order to evaluate the influence of the pH on immunosensor performance, the immunosensor was tested by cyclic voltammetric technique in a series of PBS working solutions with pH ranging from 4.5 to 7.5. Figure 5.8 shows the pH effect of the detection solution on the immunosensor. The current responses in presence of 30 ng/mL DONag were monitored. There was no significant change in the peak currents between pH 4.0 – pH 6.5 indicating that the bioactivity of antigen and antibody was poor or absent in the alkaline solution. Conversely, a drastic drop in peak current was observed at pH 7.0 and the lowest current was at pH 7.2. This could be attributed to the formation of immune-complexes by the

binding of DONab and DONag which led to inhibition of electron flow. Therefore PBS of pH 7.2 was adopted as the incubation solution considering the response of the immunosensor.

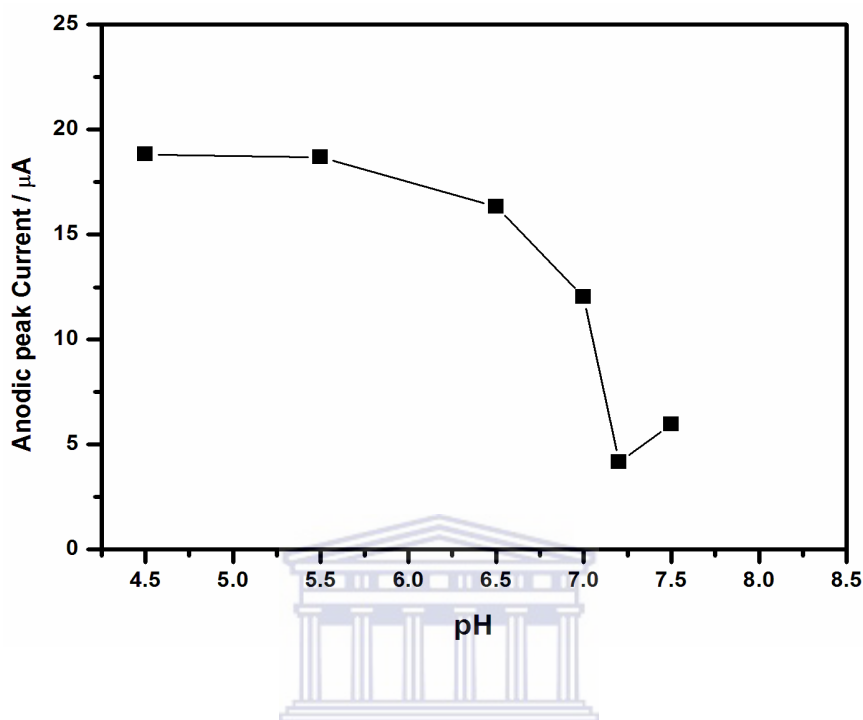


Figure 5.8: The plot of anodic peak currents from CV versus solution pH.

5.4.3.3 Effect of incubation time

Incubation time for the antigen–antibody interaction greatly influence the sensitivity of the developed immunosensor. Chronoamperometric technique was used to investigate the current responses of various immunochemical incubation time (from 5 to 40 min) of the immunosensor. The immunosensor was incubated in 30 ng/mL DONag MPBS solution (pH 7.2). It was observed that the current decreased as the incubation time increased and levelled off after 30 min, indicating the optimal formation of immune-complexes, therefore, an incubation time of 30 min was adopted for subsequent analysis (see Figure 5.8).

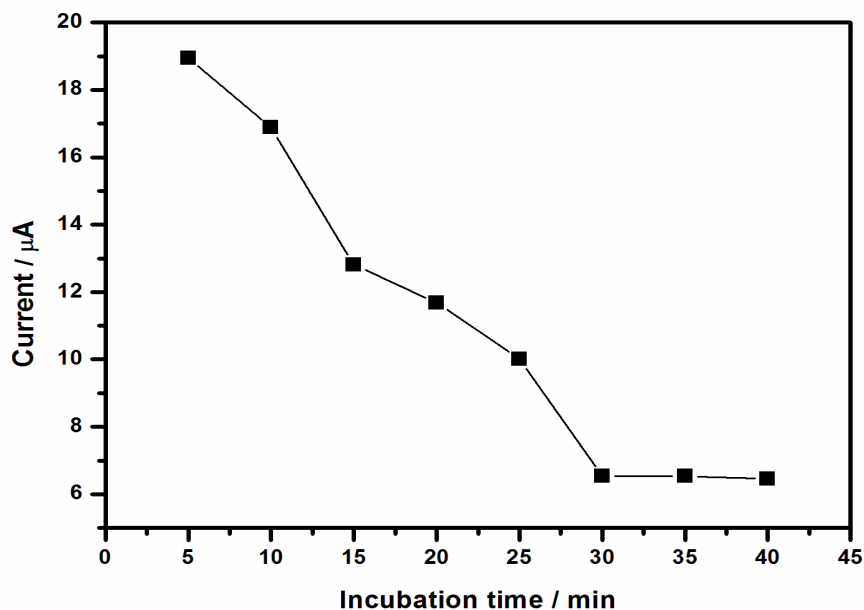


Figure 5.9: The plot of peak currents from chronocoulograms versus incubation time.

5.4.4 GCE/Nafion/ $[\text{Ru}(\text{bpy})_3]^{2+}/\text{AuNp}/\text{G}/\text{PhNH}_2/\text{DONab}/\text{BSA}$ performance

Having developed our sensor, we studied its response towards different standard concentrations of DONag. The electrode was incubated for 30 min in aliquots of a pH 7.2 MPBS solution containing various concentrations of DONag. Different concentrations of DONag were tested and similar impedance spectra with increasing R_{ct} as the concentration increased were obtained. Figure 5.10 shows the Nyquist diagrams of the immunosensor obtained after incubation in increasing concentrations (0, 6, 12, 18, 24 and 30 ng/mL) of DONag which was prepared in a methanolic PBS as described in Chapter Three, Section 3.12.2.

The observed increase in R_{ct} values with increasing DONag concentrations implies that more DONag are being bound to the interface and also indicates that the binding of DONag to the DONab immunosensor inhibits electron transfer at the sensing interface (Figure 5.11) [178,

219]. This was reflected as an increase in charge transfer resistance in both imaginary and real impedance as shown in Figure 5.10. The data, a, b, c, d, e and f in Figure 5.10 represents 0, 6, 12, 18, 24 and 30 ng/mL DON antigen respectively.

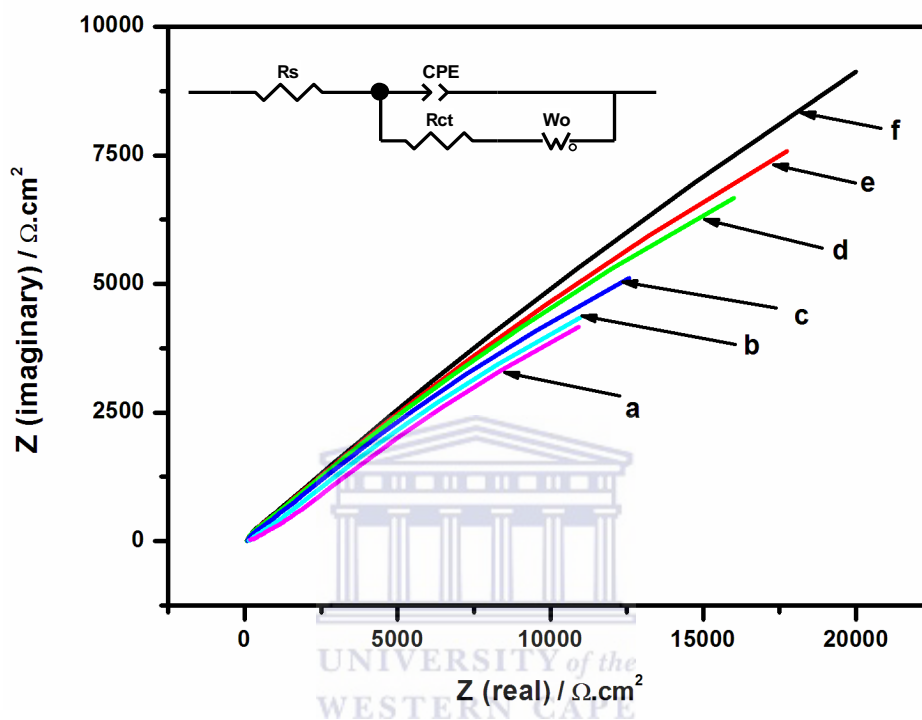


Figure 5.10: EIS responses of GCE/Nafion/[Ru(bpy)₃]²⁺/AuNp/G/PhNH₂/DONab/BSA immunosensor to standard DONAg solutions.

The equivalent electrical circuit presented in Figure 5.10 insert was used to fit the responses of the immunosensor to various standard DONAg solutions in order to obtain the value of the charge transfer resistance at each concentration. In order to compare the different electrode measurements under equivalent conditions and to obtain the normalised values that were plotted in Figure 5.11, the R_{ct} value for the blank (0 ng/mL DONAg) was subtracted from the R_{ct} values of DONAg concentrations.

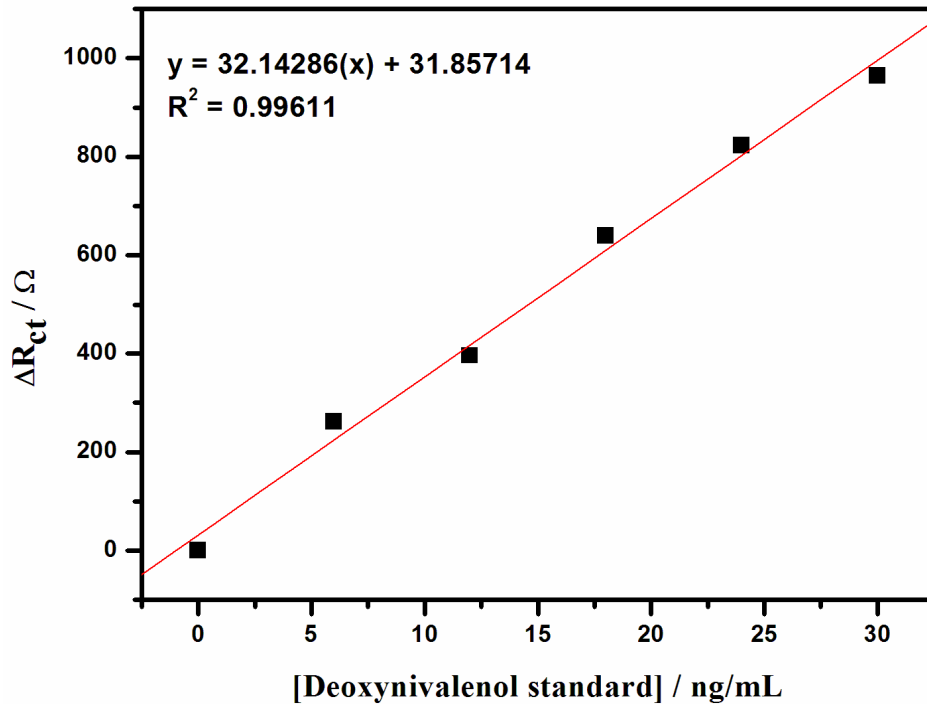


Figure 5.11: The calibration plot of EIS detection data of the immunosensor.

A linear relationship between the electron transfer resistance and DONag concentrations was found ranging from 0 to 30 ng/mL. When DONag was increased beyond 30 ng/mL, the change in impedance spectroscopy gradually levelled out indicating that all the available binding sites on sensor were occupied by the DONag. The detection limit of 0.2994 pg/L was obtained on the basis of $3 \times$ S.D. of determination of the zero standards [220] and the sensitivity is 32.14286 Ω /ng.

5.5 GCE/Nafion/[Ru(bpy)₃]²⁺/G/PhNH₂/DONab/BSA immunosensor

5.5.1 CV behaviour of the stepwise modification processes

This sensor was designed as already described in Chapter two, Section 3.12.4. The CV behaviour of various stages of modification is shown in Figure 5.12. And the inhibition characteristics observed were very similar to the first immunosensor as explained in Chapter five, Section 5.4.1 but in a lesser degree (see Figure 5.12). It could be observed that the peak currents at every step are less compared to the first sensor. Evidencing that the additional presence of gold nanoparticles acting as donor and acceptor in the first sensor platform (GCE/Nafion/[Ru(bpy)₃]²⁺/AuNp/G/PhNH₂/DONab/BSA) greatly enhanced the rate of electron transfer [221].

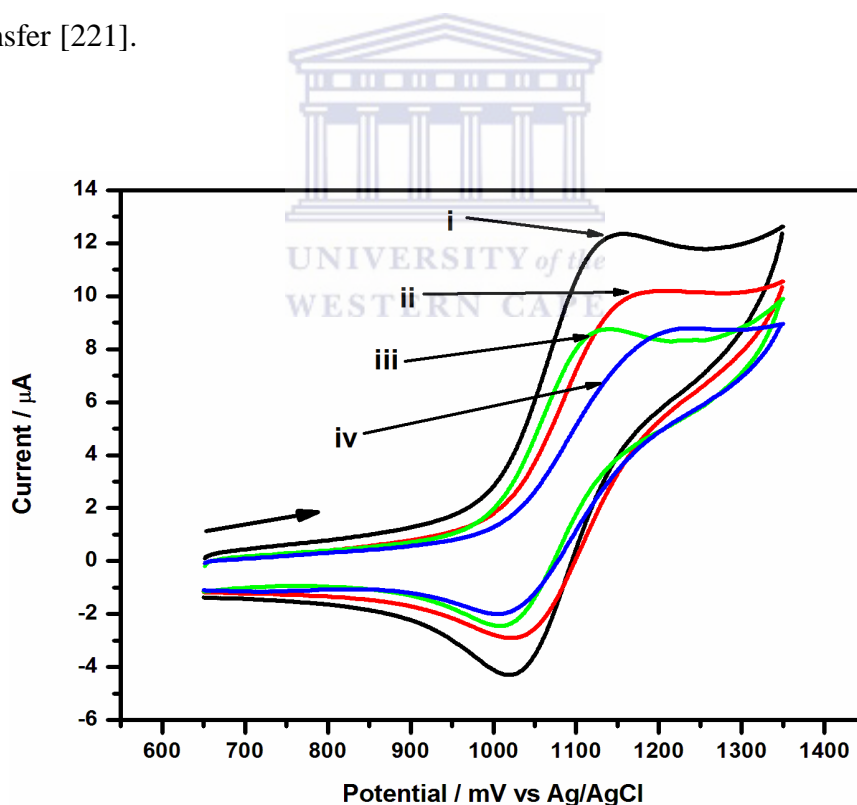


Figure 5.12: CV response of different immobilisation steps.

The data in Figure 5.12 is represented as (i) GCE/Nafion/[Ru(bpy)₃]²⁺/G/PhNH₂, (ii) after immobilization of DON antibody, (iii) after blocking nonspecific binding sites with BSA and (iv) after immobilization and running in standard DONag solutions at scan rate of 50 mV/s, over potential range of 650 – 1350 mV.

5.5.2 Chronoamperometric behaviour of stepwise modification processes

To further investigate the electroactivity at every modification stage, chronoamperometric experiments were performed at each stage as already explained in Section 5.4.2. Similar inhibition results were also observed with the peak currents at every stage being less in comparison to the first sensor. This indicates that AuNp/G/PhNO₂ exhibited an excellent electrocatalytic effect on redox activity of tris (bipyridine) ruthenium (II) [Ru(bpy)₃]²⁺, see Figure 5.13 (a) and (b).

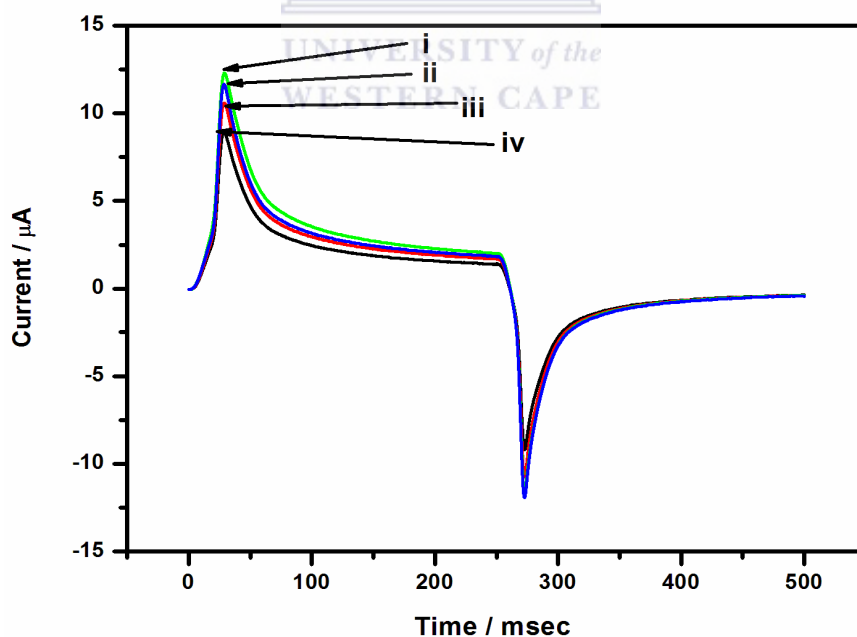


Figure 5.13(a): Chronoamperometric response of different immobilisation steps.

The data in Figure 5.13 (a) is represented as (i) GCE/Nafion/[Ru(bpy)₃]²⁺/G/PhNH₂, (ii) after immobilization of DON antibody, (iii) after blocking nonspecific binding sites with BSA and (iv) after immobilization and running in standard DONag solutions.

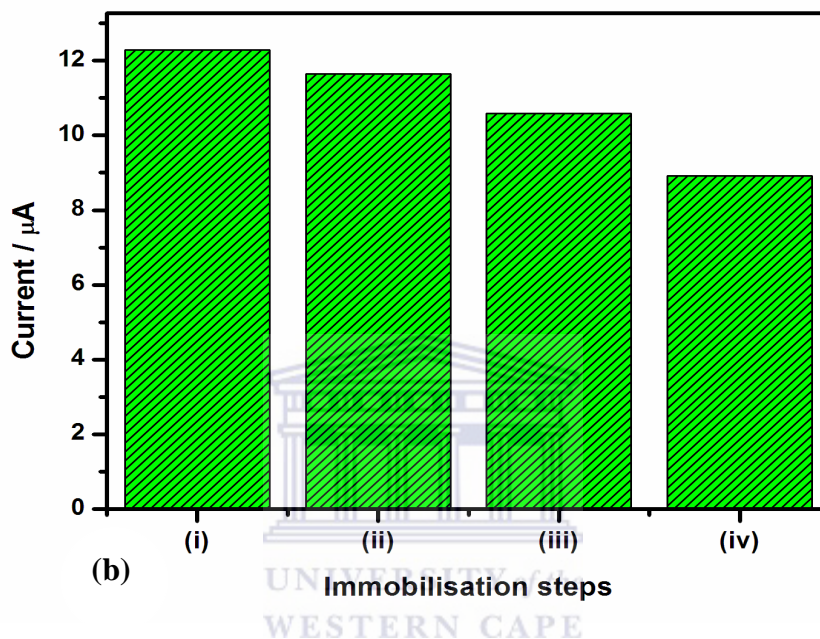


Figure 5.13(b): Bar chart of the chronoamperogram.

5.5.3 GCE/Nafion/[Ru(bpy)₃]²⁺/G/PhNH₂/DONab/BSA performance

Under the established optimal conditions, this immunosensor was designed and used as a sensing interface for the detection of DONag. The sensor was incubated for 30 min in aliquots of a pH 7.2 MPBS solution containing various concentrations of DONag as already described in section 5.4.4. Similar increase in the R_{ct} values as the DONag concentration increased was observed as shown in Figure 5.14. This implies that more DONag are being bound to the interface and also indicates that the binding of DONag to the DON immunosensor inhibits electron transfer at the sensing interface [219]

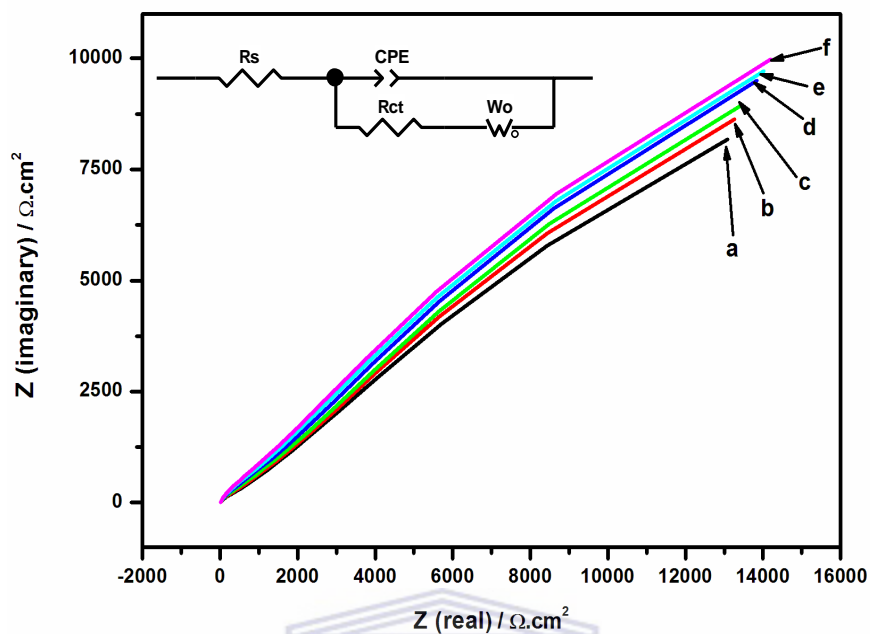


Figure 5.14: EIS responses of GCE/Nafion/[Ru(bpy)₃]²⁺/G/PhNH₂/DONab/BSA immunosensor to standard DONag solutions: a, b, c, d, e and f represents 0, 6, 12, 18, 24 and 30 ng/mL DONag respectively.

The equivalent circuit presented in the insert Figure 5.14 was used to fit the EIS responses of the immunosensor to DONag standard concentrations. The R_{ct} value for the blank (0 ng/mL DONag) was subtracted from the R_{ct} values of DONag concentrations and used to prepare the linear calibration plot, Figure 5.15.

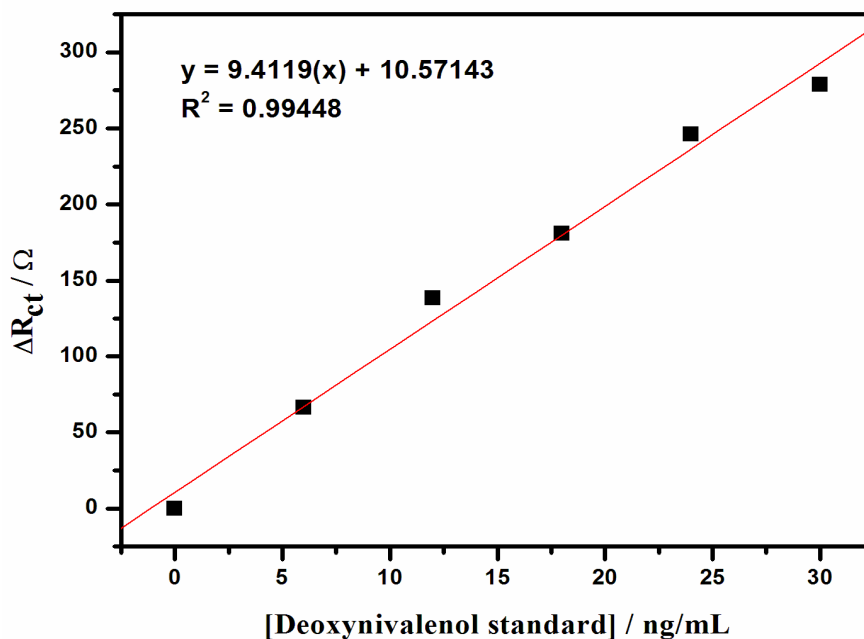


Figure 5.15: The calibration plot of EIS detection data of the immunosensor.

A linear relationship was observed in the range 0 to 30 ng/mL of DONag concentrations. From the calibration plot, the detection limit and sensitivity were obtained as 1.0621 pg/L and 9.4119 Ω /ng respectively. Relatively, GCE/Nafion/[Ru(bpy)₃]²⁺/AuNp/G/PhNH₂/DONab/BSA immunosensor has a higher sensitivity and lower detection limit owing to better electrocatalytic properties of AuNp/G/PhNH₂

5.6 GCE/PDMA/AuNp/G/Ph-NH₂/DONab/BSA immunosensor

The electrochemical synthesis of PDMA/AuNp/G/PhNH₂ film on GC was done as described in Chapter three, Section 3.7 and characterised as already explained in Chapter four, Section 4.3. The use of acidic medium is necessary to produce emeraldine salt which is the most conducting state of the polymer composite. It has been reported that the conductivity of PDMA film in its protonated emeraldine state (ES) is similar to that of a metal and that its

conductivity is due to the formation of polaron band resulting from the proton-induced spin-un-pairing mechanism [207, 210].

The acidic PDMA/AuNp/G/PhNH₂ was conditioned in 0.1 M PBS solution using cyclic voltammetry to lower the effect of hysteresis [209]. The proposed mechanism of acid-base treatment of PDMA/AuNp/G/PhNH₂ involving protonation-deprotonation process is presented in Chapter three, Scheme 8.

5.6.1 Immobilisation of DON antibody

After the conditioning in PBS, the GCE/PDMA/AuNp/G/PhNO₂ was rinsed from the side using deionised water. The polymer nanocomposite was further reduced in 0.1 KCl solution by two cyclic voltammetric scans over potential range -1200 to 0 mV at scan rate of 50 mV/s. to obtain a modified film of 4-aminophenyl on the electrode surface (GCE/PDMA/AuNp/G/PhNH₂) as described previously. The reduction spectrum, the CV behaviour of the reduced sensor and the stepwise modification processes were similar to those already reported in Sections 5.1.1, 5.1.2 and 5.4.1. See Table 5.1 for comparative EIS studies of the three sensor platforms at the reduction stage. GCE/PDMA/AuNp/G/PhNH₂ has the lowest R_{ct} value after reduction indicating that it was more conducting than others.

This is an evident that incorporation of AuNp/G/PhNO₂ into the polymer matrix greatly enhanced its conductivity as observed in Chapter four, Section 4.3. The p-aminophenyl surface layer on the modified electrodes was activated with 1:1 mixture of 0.5 mM EDC and 8 mM NHS to give a stable intermediate derivative. Then 30 μ L of diluted monoclonal deoxynivalenol antibody (0.2 μ g/mL in 0.1 M PBS, pH 7.2) was spread on the electrode surface and incubated for 30 min at room temperature.

The electrode was again rinsed from the side using 0.1 M PBS (pH 7.2) solution to remove any physically bound antibody and then 10 μ L of BSA was spread on the electrode surface to block nonspecific binding sites for 30 min at room temperature and rinsed with PBS (pH 7.2) before measurement, see Chapter three, Section 3.12.4.

5.6.2 GCE/PDMA/AuNp/G/PhNH₂/DONab/BSA performance

The modified electrode (GCE/PDMA/AuNp/G/PhNH₂/DONab/BSA) was used as a sensing interface for the detection of DONag under optimal conditions. The electrode was incubated for 30 min in aliquots of a pH 7.2 MPBS solution containing various standard concentrations of DONag. The different concentrations of DONag were tested and similar impedance spectra were observed with increasing charge transfer resistance as DONag concentration increased (see Figure 5.16). The insulating property is attributed to the formation of immune-complexes by the binding of DONab and DONag which led to inhibition of electron flow. Increase in R_{ct} indicates that more DONag were being captured.

In Figure 5.16, a, b, c, d, e and f represents 0, 6, 12, 18, 24, 30 and 36 ng/mL DON antigen, respectively. The equivalent electrical circuit presented in Figure 5.16 insert was used to fit the EIS responses of the immunosensor in order to obtain the values of R_{ct} for each measurement. Normalised R_{ct} values were obtained by subtracting the R_{ct} value for the blank (0 ng/mL DONag) from the R_{ct} values of DONag concentrations. Figure 5.17 shows the calibration plot of ΔR_{ct} versus DONag concentrations. A linear relationship was observed in the range 0 to 36 ng/mL of DONag concentrations (see Figure 4.17). The detection limit of 1.1098 pg/L was obtained on the basis of $3 \times$ S.D. of the determined zero standard [144, 220] and the sensitivity was 43.445 Ω L/ng.

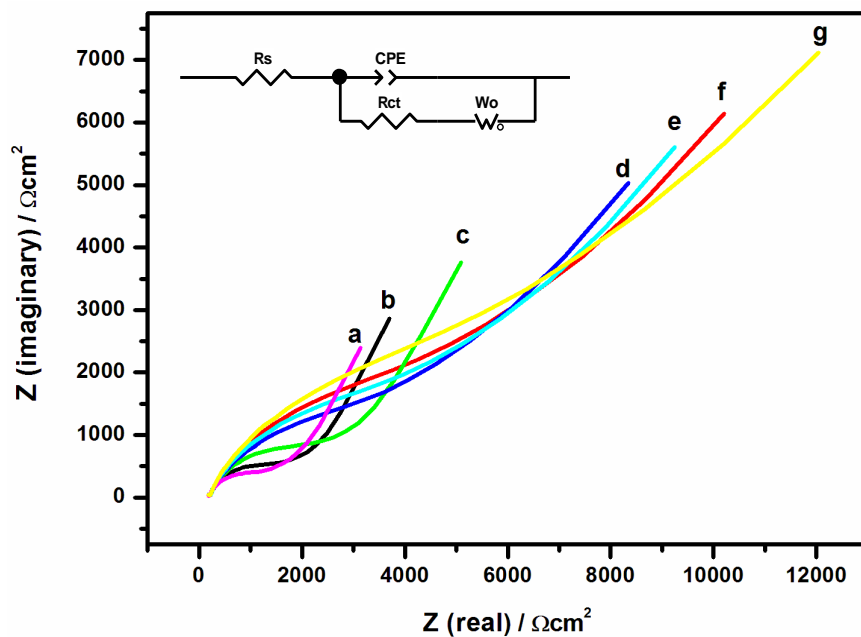


Figure 5.16: EIS responses of GCE/PDMA/AuNp/G/PhNH₂/DONab/BSA immunosensor to standard DONag solutions in PBS.

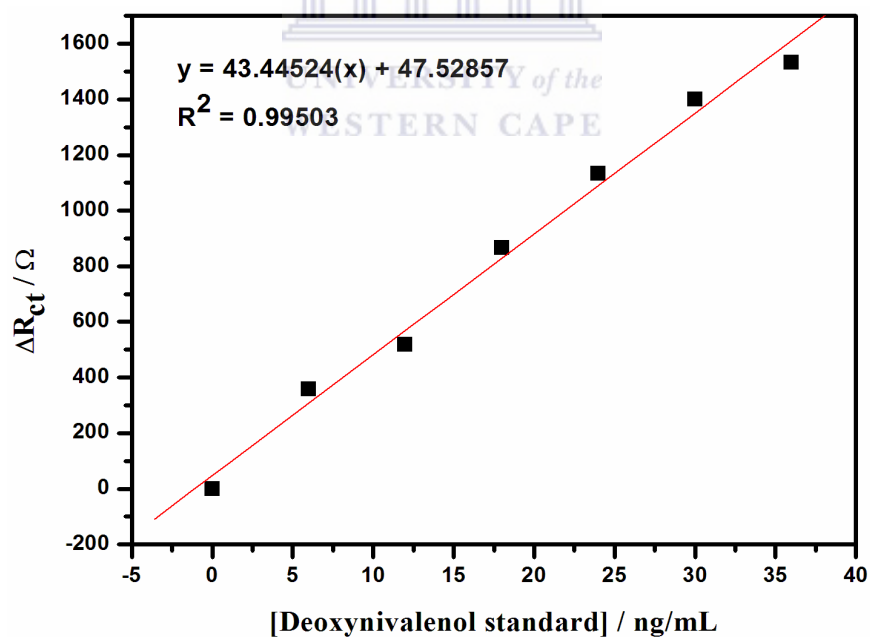


Figure 5.17: The calibration plot of EIS detection data of the immunosensor.

Table 5.2 compares the sensitivity and detection limits of the three immunosensors. The highest sensitivity was achieved with GCE/PDMA/AuNp/G/PhNH₂/DONab immunosensor followed by GCE/Nafion/[Ru(bpy)₃]²⁺/AuNp/G/PhNH₂/DONab which has an additional advantage of having the lowest detection limit over the rest sensors. From these results, it is evident that AuNp/G/PhNO₂ is a very good electro catalyst and can greatly enhance any signal of interest.

Table 5.2: Sensitivity and detection limits of the immunosensors

Immunosensors	Sensitivity (ΩL/ng)	Limit of detection (pg/L)
GCE/PDMA/AuNp/G/PhNH₂/DONab	43.45	1.1
GCE/Nafion/[Ru(bpy)₃]²⁺/G/PhNH₂/DONab	9.412	1.1
GCE/Nafion/[Ru(bpy)₃]²⁺/AuNp/G/PhNH₂/DONab	32.14	0.3

5.7 Stability of the immunosensors

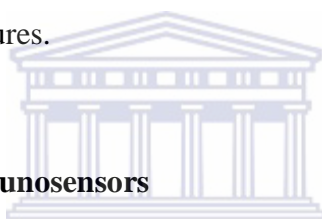
For stability study, the three immunosensors were prepared as described previously and stored at 4 °C. They were measured impedimetrically at daily intervals using 30 ng/mL of DONag MPBS solution. The electrodes were used for 5 days with minimal detectable loss of the activity as compared to the original signal of the freshly prepared electrodes. The results show that the immunosensors were 89.7%, 80.3% and 67.6% stable for,

GCE/PDMA/AuNp/G/PhNH₂/DONab, GCE/Nafion/[Ru(bpy)₃]²⁺/AuNp/G/PhNH₂/DONab and GCE/Nafion/[Ru(bpy)₃]²⁺/G/PhNH₂/DONab respectively. The sensors were not measured after this period but longer term stability may be expected due to the strong

covalent attachment of the antibody molecules to the modified electrode which could prevent the antibody from leaking out from the surface

5.8 Reproducibility of the immunosensors

The reproducibility of the response of the immunosensors was investigated by analysis of the same DONag (30 ng/mL) concentration using five equally prepared electrodes for each immunosensor. A relative standard deviation of 7.2%, 6.5%, and 4.8% was calculated for, GCE/PDMA/AuNp/G/PhNH₂/DONab, GCE/Nafion/[Ru(bpy)₃]²⁺/AuNp/G/PhNH₂/DONab and GCE/Nafion/[Ru(bpy)₃]²⁺/G/PhNH₂/DONab respectively. Such good precision reflects the reproducibility of the electrode modification as well as the immobilization, immune-binding and impedimetric procedures.



5.9 Repeatability of the immunosensors

The repeatability of each immunosensor was investigated by five successive measurements of the same DONag (30 ng/mL) concentration. The relative standard deviation (RSD) for five parallel impedimetric measurements for each immunosensor gave 8.1%, 6.9% and 5.2% for GCE/PDMA/AuNp/G/PhNH₂/DONab, GCE/Nafion/[Ru(bpy)₃]²⁺/AuNp/G/PhNH₂/DONab and GCE/Nafion/[Ru(bpy)₃]²⁺/G/PhNH₂/DONab respectively. This result indicated that the repeatability of the sensors were within experimental error.

5.10 Selectivity study of the immunosensors

To investigate the selectivity of the proposed immunosensors, each of them was incubated in 30 ng/mL DONab standard solution containing different interfering agents such as Nudularin and Fumonisin. No remarkable change of R_{ct} was observed in comparison with that which contains only DONab except for the slight increase in R_{ct} observed when Fumonisin was

added. The immunosensors were also incubated in 30 ng/mL Fumonisin and 30 ng/mL Nudularin standard solutions prepared in PBS (pH7.2) solution. Almost the same R_{ct} value was obtained when compared with the blank PBS2 (pH 7.4) solution. Figure 5.18 shows the result for GCE/PDMA/AuNp/G/PhNH₂/DONab immunosensor. Similar results were observed for GCE/Nafion/[Ru(bpy)₃]²⁺/AuNp/G/PhNH₂/DONab and GCE/Nafion/[Ru(bpy)₃]²⁺/G/PhNH₂/DONab immunosensors. These results indicated that the proposed immunosensors had a good selectivity.

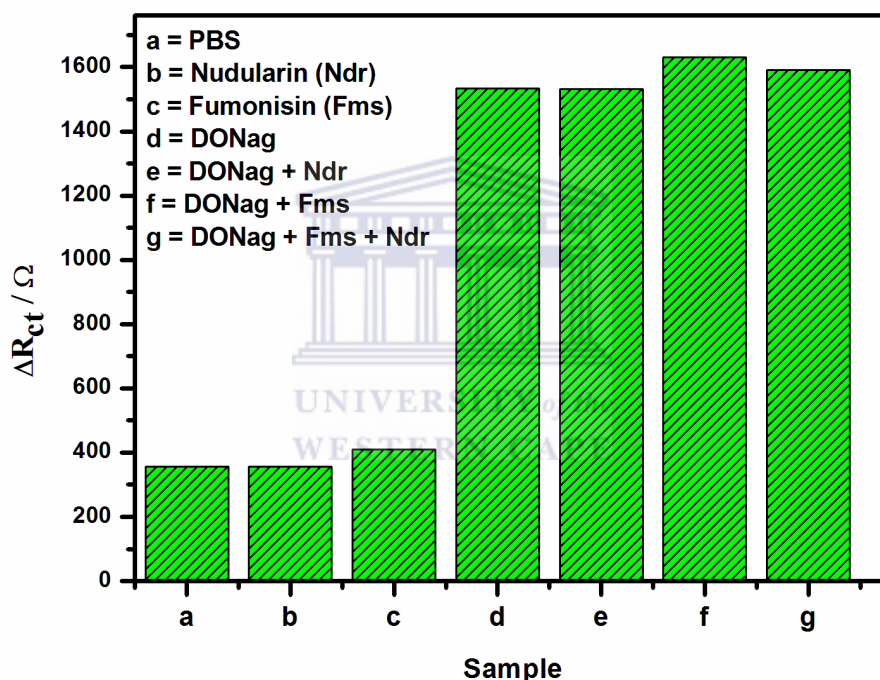


Figure 5.18: The selectivity chart of GCE/PDMA/AuNp/G/PhNH₂/DONab.

5.11 Detection of DONag and certified reference materials by Veratox ELISA test kit

Veratox for DON 5/5 is intended for the quantitative analysis of deoxynivalenol in grains and grain products. Therefore, various standard concentrations of DONag and certified reference materials of corn, wheat and roasted coffee were tested using ELISA method for validation of the fabricated immunosensors. Veratox for DON 5/5 is a competitive direct enzyme-linked

immunosorbent assay (CD-ELISA) which allows the user to obtain exact concentrations in parts per million (ppm).

The concentration range of DON_g standard for the ELISA test was between 0.25 – 1.99 ppm. A standard calibration curve of absorbance versus deoxynivalenol concentrations was plotted as shown in Figure 5.19. The sensitivity obtained from the slope of the initial linear part of the graph was calculated to be 0.041 mg/L and the limit of detection was 2.1 ppm. These values represent a better feedback in detecting DON_g, and make the use of ELISA an appropriate technique in validating the fabricated immunosensors.

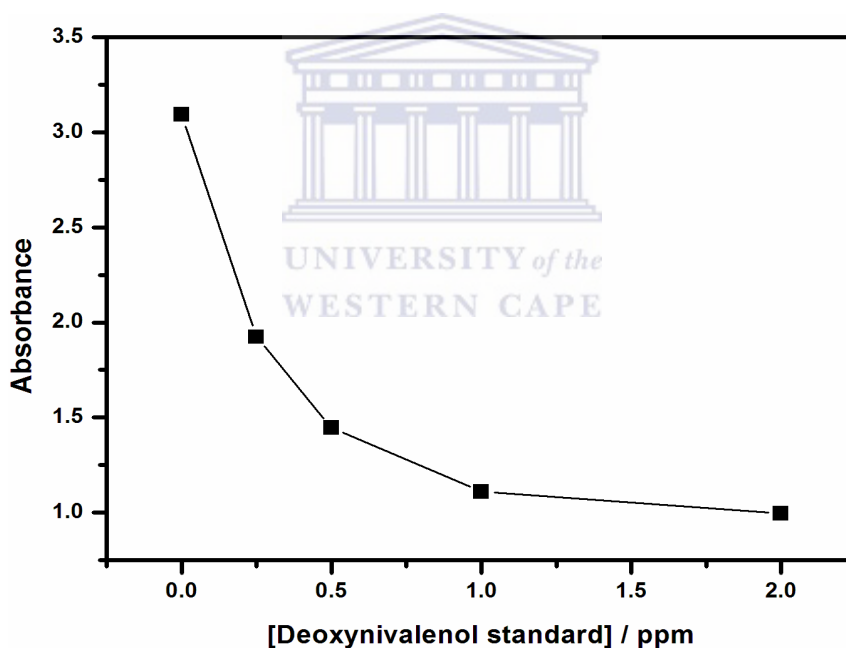


Figure 5.19: The detection plot of DON_g standards by ELISA.

The feasibility of the proposed impedimetric immunosensor for real sample analysis was investigated by detecting DON_g in extracted certified reference materials of wheat; roasted coffee and corn following the extraction procedure described by Veratox Elisa Kit manual

(see Chapter three, Section 3.12.3). The DON extract was analysed with GCE/PDMA/AuG/PhNH₂/DONab, GCE/Nafion/[Ru(bpy)₃]²⁺/AuG/PhNH₂/DONab and GCE/Nafion/[Ru(bpy)₃]²⁺/G/PhNH₂/DONab as described in Chapter, Section 3.12.6 and the results are shown in Table 5.3 .

The GCE/PDMA/AuG/PhNH₂/DONab had higher sensitivity to all the certified samples. The DON values of the immunosensors to certified reference materials were comparable to those obtained with ELISA technique as well as the quantity advertised by the vendor.

Table 5.3: DON content of corn, wheat and roasted coffee certified reference materials

Certified Reference materials	A (ppm)	B (ppm)	C (ppm)	Vendor (ppm)	ELISA (ppm)
Wheat	0.29	0.3	0.26	0.71	0.2
Corne	1.2	0.92	0.89	1.88	1.1
Roasted coffee	0.22	0.19	0.16	0.77	0.24

Where A = GCE/PDMA/AuG/PhNH₂/DONab/BSA immunosensor

B = GCE/Nafion/[Ru(bpy)₃]²⁺/AuG/PhNH₂/DONab/BSA immunosensor

C = GCE/Nafion/[Ru(bpy)₃]²⁺/G/PhNH₂/DONab/BSA immunosensor

Chapter Six

Conclusions and Recommendations

This chapter discusses and draws conclusions regarding the success of the developed DON immunosensors with recommendations.

6.1 Conclusions

A highly dispersive gold dotted 4-nitrophenylazo functionalised graphene nanocomposite (AuNp/G/PhNO₂) was successfully synthesised and applied in enhancing sensing platform signals. Electrochemical immunosensors for ultrasensitive detection and quantitation of deoxynivalenol mycotoxin in cereals was effectively fabricated with this nanocatalyst. Impedimetric detection technique was employed and its principle was based on the formation of immune-complexes by the binding of DONab and DONag which led to inhibition of electron flow, consequently increased the charge transfer resistance of the sensing interface. The inhibition effect was found to be increasing as the concentration of DONag increased under optimum conditions.

Three immunosensors were developed and their detection range for DONag in standard samples was 6–30 ng/mL. The sensitivity and detection limit of the immunosensors: GCE/PDMA/AuNp/G/PhNH₂/DONab, GCE/Nafion/[Ru(bpy)₃]²⁺/AuNp/G/PhNH₂/DONab and GCE/Nafion/[Ru(bpy)₃]²⁺/G/PhNH₂/DONab were 43.45 ΩL/ng and 1.1 pg/L; 32.14 ΩL/ng and 0.3 pg/L; 9.412 ΩL/ng and 1.1 pg/L respectively, which was better than those reported in the literature and compares favourably with the ELISA results.

The immunosensors had very good detection limits and exhibited high sensitivity for DONag except for GCE/Nafion/[Ru(bpy)₃]²⁺/G/PhNH₂/DONab immunosensor. This is due to the presence of gold nanoparticles in the sensing platforms which acted as donors and acceptors. This in effect introduced more molecular orbital states to the total possible states of the composite thereby lowering the band gap energy/energy of transitions as expected by the theory of molecular orbitals. Also the effective surface area of the nanocatalyst was enhanced by the presence of gold nanoparticles which in turn facilitated the covalent immobilization of DON antibodies to the sensor platform.

Indeed the new AuNp/G/PhNO₂ nanocomposite improved the electrocatalytic efficiency of [Ru(bpy)₃]^{2+/3+} in the Nafion film. The Nafion nanocomposite-modified electrode efficiently loaded large amount of [Ru(bpy)₃]²⁺ cationic redox probe. This is attributable to the enlarged electroactive surface area of the composite. In addition, the slight negative charge conferred on the nanocomposite by the PhNO₂ units also contributed in enhancing the quantity and stability of the cation electrostatically. The sensitivity of the functionalised Nafion electrode was determined by the rate at which the Ru²⁺ sites were regenerated within the film. In comparison to pure Nafion film, the Nafion/AuNp/G/PhNO₂ nanocomposite film exhibited 100% relative electroactivity, 30% increase in peak currents and 34.9% reduction in charge transfer resistance. Ultimately, Nafion/[Ru(Bpy)₃]²⁺/AuNp/G/PhNO₂ sensing platform could be used to develop reproducible, high-performance, ultra-sensitive electrochemiluminescence, voltammetric or amperometric sensors as briefly demonstrated in Chapter four, Section 4.3

The diazonium-based procedure offers the advantages of simplicity, efficiency and speed of the chemistry involved. Certainly, the modification protocol could be compatible with

majority of the biomolecules and appears to be very promising in the development of new biocompatible interfaces for more widespread biosensing applications.

6.2 Recommendations

The results indicated that GCE/PDMA/AuNp/G/PhNH₂/DONab and GCE/Nafion/[Ru(bpy)₃]²⁺/AuNp/G/PhNH₂/DONab immunosensors are sensitive enough to detect deoxynivalenol mycotoxin at very low concentrations. The selectivity study in Chapter 5, Section 5.10 showed a little increase in R_{ct} in the presence of Fumonisin, indicating that the sensor was slightly sensitive to it. Therefore, for the immunosensors to be fully applied in the detection of deoxynivalenol in samples containing complex matrices, further optimization and selectivity studies is required. A follow up procedure should include the studies of interfering species in the analyte solutions.

However, once optimized further, it is clear that this inhibition based immunosensor would provide ultrasensitive, rapid and reproducible monitoring of deoxynivalenol in cereal and cereal products effectively. Integration of these immunosensors into an automated system would be more attractive to provide the detection of DONag in many samples and as such reduce the time of analysis. Miniaturization is further required for the immunosensors to be applied for on-site monitoring of DONag.

References

- [1] J.R. Barrett, Mycotoxins: Of Molds and Maladies, *Environmental Health Perspectives* 108 (2000) 1.
- [2] P. Sobrova, V. Adam, A. Vasatkova, M. Beklova, L. Zeman, R. Kizek, Review article, deoxynivalenol and its toxicity, *Interdisc Toxicol* 3 (2010) 94.
- [3] H.P. vanEgmond, W.H. Paulsch, Determination of mycotoxins, *Pure and Applied Chemistry* 58 (1986) 315.
- [4] S. Bony, L. Olivier-Loiseau, M. Carcelen, A. Devaux, Genotoxic potential associated with low levels of the *Fusarium* mycotoxins nivalenol and fusarenon X in a human intestinal cell line, *Toxicology in Vitro* 21 (2007) 457.
- [5] E.O.M. Hajjaji A, Bouya D, A. Bouseta, F. Mathieu, S. Collin, A. Lebrihi, Occurrence of mycotoxins: Ochratoxin A, Vomitoxin (deoxynivalenol) and toxigenic fungi in Moroccan wheat grains: impact of ecological factors on the growth and ochratoxin A production, *Molecular Nutrition & Food Research* 10 (2006) 1.
- [6] A.M. Tritscher, S.W. Page, The risk assessment paradigm and its application for trichothecenes, *Toxicology Letters* 153 (2004) 155.
- [7] IARC, monographs on the evaluation of the carcinogenic risk of chemicals to man, World Health Organization, International Agency for Research on Cancer 431 (1993) 56.
- [8] C.J. Amuzie, *Biomarkers and risk assessment for Deoxynivalenol*, in *Department of Pathobiology and Diagnostic Investigation Michigan State University*. 2009.
- [9] F.R. Julie, P. Meneely, H.P.V Egmond, C.T. Elliott, Current methods of analysis for the determination of trichothecene mycotoxins in food, *Trends in Analytical Chemistry* 30 (2011) 41.

- [10] S.R.B. Mahendra, K. Rai, P.I. Avinash, K.G. Aniket, Mycotoxin: rapid detection, differentiation and safety, *Journal of Pharmaceutical Education and Research* 3 (2012) 12.
- [11] L.H.S. Biselli, H. Wegner, C. Hummert, Analysis of Fusarium Toxins Using LC-MS-MS: Application to Various Food and Feed Matrices, *Spectroscopy* 31 (2005) 36.
- [12] H.L.F. Ji, Jianhong Xu, J. Shi, Enzyme-Linked Immunosorbent-Assay for Deoxynivalenol (DON), *Toxins* 5 (2011) 968.
- [13] J.J. Matić, M. Igor M, Š.M. Bojana, M.C. Aleksandra, K.Z. Saša, M.I. Anamarija, ELISA and HPLC analyses of deoxynivalenol in maize and wheat, *Academic Journal* 121 (2011) 25.
- [14] W.T. Shen, D. Cui, H. Yang, D.Z. Bian, Nanoparticle-based electrochemiluminescence immunosensor with enhanced sensitivity for cardiac troponin I using N-(aminobutyl)-N-(ethylisoluminol)-functionalized gold nanoparticles as labels, *Biosensors and Bioelectronics* 27 (2011) 18.
- [15] G. Jie, P. Liu, L. Wang, S. Zhang, Electrochemiluminescence immunosensor based on nanocomposite film of CdS quantum dots-carbon nanotubes combined with gold nanoparticles-chitosan, *Electrochemistry Communications* 12 (2010) 22.
- [16] J. Hjelm, W.H. Robyn, A. Hagfeldt, E.C. Constable, C.E. Housecroft, R.J. Forster, Conducting polymers containing in-chain metal centers: electropolymerization of oligothieryl-substituted complexes and in situ conductivity studies, Os(II), Ru(II), *Inorganic Chemistry* 44 (2005) 1073.
- [17] T.F. Otero, I. Boyano, Comparative study of conducting polymers by the ESCR model, *Journal of Photochemistry and Photobiology B* 107 (2003) 6730.
- [18] J. Qian, C. Zhang, X. Cao, S. Liu, Versatile immunosensor using a quantum dot coated silica nanosphere as a label for signal amplification, *Analytical Chemistry* 82 (2010) 6422.

- [19] B.C. Hsieh, Y. Choua, W. Chena, Fabrication and electrochemical activity of carbon nanotubes decorated with PtRu nanoparticles in acid solution, *Journal of Alloys and Compounds* 466 (2008) 233.
- [20] Y. Zhao, Y. Cai, J. Tian, H. Lan, Facile preparation and excellent catalytic performance of PtRuPd hollow spheres nanoelectrocatalysts, *Materials Chemistry and Physics* 115 (2009) 831.
- [21] H.M. Nabika, M. Kajinami, A. Deki, S. Akamatsu, Kensuke, Preparation and characterization of Au/Co nano-alloys, *Journal of Electroanalytical Chemistry* 559 (2003) 99.
- [22] J.L. Yang, J.T. Yang, Heng-Phon, Core-Shell Ag-Au nanoparticles from replacement reaction in organic medium, *Journal of Physical Chemistry B* 109 (2005) 19208.
- [23] B.S. Zhanga, Y. Shaob, G. Yina, Y. Linb, Facile synthesis of PtAu alloy nanoparticles with high activity for formic acid oxidation, *Journal of Power Sources* 195 (2010) 1103.
- [24] S.A.Z. Dong, Shi-Ping, Photochemical synthesis of colloidal gold nanoparticles, *Materials Science and Engineering B* 140 (2007) 153.
- [25] B.M.K. Muñoz-Flores, B.I. Jiménez-Pérez, V.M.E. Martínez, P. Lopez, T. Susana, Recent advances in the synthesis and main applications of metallic nanoalloys, *Industrial & Engineering Chemistry Fundamentals* 30 (2011) 11.
- [26] A.S. Devadoss, A.M. Tanner, D.A. Bertoncello, P. Marthi, R. Keyes, T.E. Forster, J. Robert, Enhanced electrochemiluminescence and charge transport through films of metallopolymer-gold nanoparticle composites, *Langmuir* 26 (2009) 2130.
- [27] M. Pattabi, S.A. B, Effect of precursor concentration on the particle size of mercaptopropionic acid-capped CdS nanoparticles, *Journal of New Materials for Electrochemical Systems* 10 (2005) 43.
- [28] D.B.M. Lambrick, N. Hoon, S.R.M. Kilner, Preparation and properties of Ni-Fe magnetic fluids, *Journal of Magnetism and Magnetic Materials* 65 (1987) 257.

- [29] M.K. Mandal, S. Ghosh, S.K. Sau, T.K. Yusuf, S.M. Pal, Tarasankar, Wet chemical method for synthesis of superparamagnetic alloyed Ni-Pd and Ni-Pt nanomagnets in micelles, *Journal of Colloid and Interface Science* 265 (2003) 23.
- [30] S.E. Mavundla, G.F. Malgas, P. Baker, E.I. Iwuoha, Synthesis and characterization of novel nanophase hexagonal poly (2,5-dimethoxyaniline), *Electroanalysis* 20 (2008) 2347
- [31] J. Hjelm, *Conducting Polymers Containing In-Chain Metal Centres: Electropolymerization and Charge Transport*. 2003, Department of Physical Chemistry, Uppsala University.
- [32] P. Yin, P.A. Kilmartin, Formation of poly 2, 5-dimethoxyaniline on steels, *Current Applied Physics* 4 (2004) 141.
- [33] G.D. Storrier, S.B. Colbran, D.B. Hibbert, Chemical and electrochemical syntheses, and characterization of poly (2,5-dimethoxyaniline) (PDMA): a novel, soluble, conducting polymer, *Synthetic Metals* 62 (1994) 179.
- [34] M.D.G. Bidhan, L. Bhowmik, J.K. Ray, Synthesis and characterization of poly (2,5-dimethoxyaniline) and poly (aniline-Co-2,5-dimethoxyaniline): The processable conducting polymers, *Bulletin of Materials Science* 24 (2001) 389.
- [35] S.M. Yanwu Zhu , W. Cai , L. Xuesong, J.W. Suk , J.R. Potts , R.S. Ruoff, Graphene and graphene oxide: synthesis, properties, and applications, *Advanced Materials* 12 (2010) 1.
- [36] S. Zhang, Y. Shao, H.G. Liao, J. Liu, I.A. Aksay, G. Yin, Y. Lin, Graphene decorated with PtAu alloy nanoparticles: facile synthesis and promising application for formic acid oxidation, *Chemistry of Materials* 23 (2011) 1079.
- [37] O.C.N. Compton, T. SonBinh, Graphene oxide, highly reduced graphene oxide, and graphene: versatile building blocks for carbon-based materials, *Small* 6 (2010) 711.
- [38] S.R. García-Rodríguez, S. Vellosillo, M. Peña, M.A. Fierro, J.L.G. Ocón, Role of perfluorosulfonic ionomer as protective agent against strong adsorption of (bi)sulfate anions.

Relevance in the determination of the area of Pt/C electrocatalysts, *International Journal of Hydrogen Energy* 35 (2010) 11576.

[39] J.W. Li, G.M. Kyle, A. Louis, Anisotropic diffusion and morphology in perfluorosulfonate ionomers investigated by NMR, *Macromolecular Symposia* 42 (2008) 255.

[40] N.R. Hendricks, T.T.Waryo, O. Arotiba, N. Jahed, P.G.L. Baker, E.I. Iwuoha, Microsomal cytochrome P450-3A4 (CYP3A4) nanobiosensor for the determination of 2,4-dichlorophenol-An endocrine disruptor compound, *Electrochim. Acta* 54 (2009) 1925.

[41] Y. Si, E.T. Samulski, Synthesis of water soluble graphene, *Nano Letters* 8 (2008) 1679.

[42] R.R. King, R. Greenhalgh, Structural elucidation of a novel deoxynivalenol analog, *The Journal of Organic Chemistry* 52 (1987) 1605.

[43] C.M. Nagy, S.N. Fejer, L. Berek, J. Molnar, B. Viskolcz, Hydrogen bondings in deoxynivalenol (DON) conformations-a density functional study, *Journal of Molecular Structure: THEOCHEM* 726 (2005) 55.

[44] L.J. Gouze ME, G. Dedieu, A. Galinier, J.P. Thouvenot, I.P Oswald, P. Galtier, Individual and combined effects of low oral doses of Vomitoxin (deoxynivalenol) (DON) and nivalenol in mice, *Fermentek* 22 (2005) 1.

[45] B.L.Y Cetin, Confirmation of reduced toxicity of Vomitoxin (deoxynivalenol) (DON) in extrusion-processed corn grits by the MTT bioassay., *Journal of Agricultural and Food Chemistry* 54 (5) (2006) 1949.

[46] P.L. Stiles, J.A. Dieringer, N.C. Shah, R.P.V. Duyne, *Surface-Enhanced Raman Spectroscopy*. 2008: Illinois, USA.

[47] B.C. Curley, G. Rossi, R. Ferrando, R.L. Johnston, Theoretical study of structure and segregation in 38-atom Ag-Au nanoalloys, *The European Physical Journal D* 43 (2007) 53.

[48] R. Overney, Nanothermodynamics and Nanoparticle Synthesis, *NME* 498A (2010) 1.

- [49] C.Y. Shan, H. Huafeng, D. Zhang, Q. Ivaska, A.L Niu, Water-soluble graphene covalently functionalized by biocompatible polylysine, *Langmuir* 25 (2009) 12030.
- [50] J.X. Min-Song, ChangziWu, The effect of surface functionalisation on the immobilization of gold nanoparticles on graphene sheets, *Journal of Nanotechnology* 2012 (2012) 5.
- [51] J. Liu, Y. Chen, Y. Guo, F. Yang, F. Cheng, Electrochemical Sensor for o-nitrophenol based on cyclodextrin functionalized graphene nanosheets, *Journal of Nanomaterials* 2013 (2013) 6.
- [52] P.C. Painter, M.M. Coleman, *Fundamentals of polymer science*, (1997).
- [53] S. Baeurle, A. Hotta, A.A. Gusev, On the glassy state of multiphase and pure polymer materials, *Polymer* 47 (2006) 6243.
- [54] C.D. Roberto, A.S. Diego, M.G. Jesús, Crosslinking and thermal stability of thermosets based on novolak and melamine, *Journal of Applied Polymer Science* 114 (2009) 4059.
- [55] S. Nishimura, A. Takagaki, K. Ebitani, Characterization, synthesis and catalysis of hydrotalcite-related materials for highly efficient materials transformations, *Green Chemistry* 15 (2013) 2026.
- [56] J. Alemán, A.V. Chadwick, J. He, M. Hess, K. Horie, R. G. Jones, P. Kratochvíl, I. Meisel, I. Mita, G. Moad, S. Penczek, R.F.T. Stepto, Definitions of terms relating to the structure and processing of sols, gels, networks, and inorganic-organic hybrid materials, *Pure and Applied Chemistry* 79 (2007) 1801.
- [57] J. Kim, M.M. Mok, R.W. Sandoval, D.J. Woo, J.M. Torkelson, Uniquely broad glass transition temperatures of gradient copolymers relative to random and block copolymers containing repulsive comonomers, *Macromolecules* 39 (2006) 6152.
- [58] J. Kim, H.Y. Zhou, S.T. Nguyen, J.M. Torkelson, Synthesis and application of styrene/4-hydroxystyrene gradient copolymers made by controlled radical polymerization:

compatibilization of immiscible polymer blends via hydrogen bonding effects, *Polymer* 47 (2006) 5799.

[59] C.L.H. Wong, J. Kim, C.B. Roth, J.M. Torkelson, Comparison of critical micelle concentrations of gradient copolymer and block copolymer in homopolymer: novel characterization by intrinsic fluorescence, *Macromolecules* 40 (2007) 5631

[60] S. Schick, ed. *Ionomers: Characterization, Theory, and Applications*. Vol. 1. 1996, CRC Press LLC: United States of America. 320.

[61] Q. Zhao, *Structures and properties of sulfonated ionomers probed by transport and mechanical measurements: the role of solute activity*, in *Chemical and Biological Engineering*. 2012, PRINCETON UNIVERSITY.

[62] C. Heitner-Wirguin, Recent advances in perfluorinated ionomer membranes: structure, properties and applications, *Journal of Membrane Science* 120 (1996) 1.

[63] M.R. Tant, K.A. Mauritz, G.L. Wilkes, eds. *Ionomers: Synthesis, structure, properties and applications*. Second ed, Blackie Academic and Professional, an imprint of Chapman & Hall: Mississippi United States of America 2 (1997) 514.

[64] A.K. Jochen, Development of ionomer membranes for fuel cells, *Journal of Membrane Science* 185 (2001) 3.

[65] M.A. Hickner, Hossein Ghassemi, Yu Seung Kim, Brian R. Einsla, J.E. McGrath, Alternative polymer systems for proton exchange membranes (PEMs), *Chemical Reviews* 104 (2004) 4587.

[66] J. Rabani, M. Kaneko, A. Kira, Hydrophobic and ionic exchange of tris (2,2'-bipyridine) ruthenium (II) and methyl viologen in Nafion solutions, *Langmuir* 7 (1991) 941.

[67] H.N. Choi, L. Ja-Young, L. Young-Ku, W.Y. Lee, Tris (2,2'-bipyridyl) ruthenium(II) electrogenerated chemiluminescence sensor based on carbon nanotube dispersed in sol-gel-derived titania-Nafion composite films, *Analytica Chimica Acta* 565 (2006) 48.

- [68] U. Paolo, B. Paolo, V. Francesca, Langmuir-Blodgett films of different ionomeric polymers deposited on electrode surfaces, *Electrochimica Acta* 49 (2004) 3785.
- [69] F. Nguyen, F.C. Anson, Electrochemical examination of electrostatic attraction of cations and the ejection of anions by polyanionic electrode coatings stable in non-aqueous solvents, *Electrochimica Acta* 44 (1998) 239.
- [70] R. Huang, N. Hu, Direct electrochemistry and electrocatalysis with horseradish peroxidase in Eastman AQ films, *Bioelectrochemistry* 54 (2001) 75.
- [71] J.O.M. Bockris, B. E. Conway, R.E. White, eds. *Modern aspects of electrochemistry No.14* 1982 Plenum Press New York and London
- [72] K.A. Mauritz, C.J. Hora , A.J. Hopfinger, *Ions in Polymers*, in *ACS Advances in Chemistry Ser. No. 187*, A. Eisenberg, Editor. 1980, American Chemical Society: Washington, DC. p. 124.
- [73] K.A. Mauritz, R.B. Moore, State of Understanding of Nafion, *Chemical Reviews* 2004 (2004) 4585.
- [74] H.J. Yeager, A. Eisenberg, *Perfluorinated Ionomer Membranes*, in *ACS Symp. Ser. No.180*, A. Eisenberg and H.L. Yeager, Editors. 1982, American Chemical Society: Washington, DC. p. 1.
- [75] M.K.A. Eisenberg, Ion-containing polymers: physical properties and structure, Academic Press: New York 2 (1977) 163.
- [76] T.D. Gierke, W.Y. Hsu, *The cluster network model of ion clustering in perfluorosulfonated membranes*, in *perfluorinated ionomer membranes*, *ACS Symposium Series 180*, A. Eisenberg and H.L. Yeager, Editors. 1982, America Chemical Society: Washington, DC. p. 283.
- [77] P.J. Brookman, J.W. Nicholson, *Developments in ionic polymers*, A.D. Wilson and H.J. Prosser, Editors. 1986, Elsevier Applied Science Publishers: London. p. 269.

- [78] J.R. Stetter, William R. Penrose, S. Yao, Sensors, chemical sensors, electrochemical sensors and ECS, Journal of The Electrochemical Society 150 (2003) 11.
- [79] A. Hulanicki, S. Geab, F. Ingman, Chemical sensors definitions and classification, Pure and Applied Chemistry 63 (1991) 1247.
- [80] D.R. Thévenot, K. Toth, R.A. Durst, G.S. Wilson, Electrochemical biosensors: recommended definitions and classification, Biosensors and Bioelectronics 16 (2001) 121.
- [81] S. Mobley, S. Yalamanchili, H. Zhang, R. Marullo, Z.G. Chen, C.S. Moreno, D.M. Shin, P.W. Doetsch, W.D. Hunt, Procedure for developing linear and Bayesian classification models based on immunosensor measurements, Sensors and Actuators B: Chemical 190 (2014) 165.
- [82] R. Monošíka, M. Stred'anskýb, E. Šturdíka, Biosensors-classification, characterization and new trends, Acta Chimica Slovaca 5 (2012) 109-120.
- [83] F. Schubert, U. Wollenberger, F.W. Scheller, H.G. Müller, *Artificially coupled reactions with immobilized enzymes: biological analogs and technical consequences*, in *Bioinstrumentation and Biosensors*, D.L. Wise, Editor. 1991, Marcel Dekker, Inc.: New York. p. 19.
- [84] A.S. Yuan, M.L. Morris, K.C. Yin, J.Y.K. Hsieh, B.K. Matuszewski, Development and implementation of an electrochemiluminescence immunoassay for the determination of an angiogenic polypeptide in dog and rat plasma, Journal of Pharmaceutical and Biomedical Analysis 33 (2003) 719.
- [85] S. Moises, M. Schäferling, Toxin immunosensors and sensor arrays for food quality control, Bioanalytical Reviews 1 (2009) 73.
- [86] L. Hu, Z. Bian, H. Li, S. Han, Y. Yuan, L. Gao, G. Xu, $[\text{Ru}(\text{bpy})_2\text{dppz}]^{2+}$ electrochemiluminescence switch and its applications for DNA interaction study and label-free ATP aptasensor, Analytical Chemistry 81 (2009) 9807.

- [87] W. Zhan, A.J. Bard, Electrogenerated chemiluminescence. 83. Immunoassay of human C-reactive protein by using $[\text{Ru}(\text{bpy})_3]^{2+}$ encapsulated liposomes as labels, *Analytical Chemistry* 79 (2006) 459.
- [88] W.R.G. Baeyens, S.G. Schulman, A.C. Calokerinos, Y. Zhao, A.M.G. Campaña, K. Nakashima, D.D. Keukeleire, Chemiluminescence-based detection: principles and analytical applications in flowing streams and in immunoassays, *Journal of Pharmaceutical and Biomedical Analysis* 17 (1998) 941.
- [89] X. Li, R. Wang, X. Zhang, Electrochemiluminescence immunoassay at a nanoporous gold leaf electrode and using CdTe quantum dots as labels, *Microchimica Acta* 172 (2011) 285.
- [90] Y. Liu, R. Yuan, Y. Chai, C. Hong, K. Liu, S. Guan, Ultrasensitive amperometric immunosensor for the determination of carcinoembryonic antigen based on a porous chitosan and gold nanoparticles functionalized interface, *Microchimica Acta* 167 (2009) 217.
- [91] M.M. Richter, Electrochemiluminescence (ECL), *Chemical Reviews* 104 (2004) 3003.
- [92] S. Cosnier, Biosensors based on electropolymerized films: new trends, *Analytical and Bioanalytical Chemistry* 377 (2003) 507.
- [93] T. Ahuja, I.A. Mir, D. Kumar, Rajesh, Biomolecular immobilization on conducting polymers for biosensing applications, *Biomaterials* 28 (2007) 791.
- [94] S. Xu, Y. Liu, T. Wang, J. Li, Positive potential operation of a cathodic electrogenerated chemiluminescence immunosensor based on luminol and graphene for cancer biomarker detection, *Analytical Chemistry* 83 (2011) 3817.
- [95] F. Arduini, I. Errico, A. Amine, L. Micheli, G. Palleschi, D. Moscone, Enzymatic spectrophotometric method for aflatoxin b detection based on acetylcholinesterase inhibition, *Analytical Chemistry* 79 (2007) 3409.

- [96] Y. Cao, R. Yuan, Y. Chai, L. Mao, X. Yang, S. Yuan, Y. Yuan, Y. Liao, A solid-state electrochemiluminescence immunosensor based on MWCNTs-Nafion and Ru(bpy)₃²⁺/Nano-Pt nanocomposites for detection of α -fetoprotein, *Electroanalysis* 23 (2011) 1418.
- [97] J.C. Vidal, E. Garcia-Ruiz, J.R. Castillo, Recent advances in electropolymerized conducting polymers in amperometric biosensors, *Microchimica Acta* 143 (2003) 93.
- [98] D.A. Skoog, F.J. Holler, S.R. Crouch, eds. *Principles of Instrumental Analysis*. 6 ed., ed. T. Brooks/Cole. 2007: Belmont, CA. 169.
- [99] L.R.F., A.J. Bard, *Electrochemical methods fundamentals and applications*. 2001, John Wiley & sons, inc.: New York Chichester • Weinheim Brisbane Singapore Toronto.
- [100] D.A. Skoog, D.M. West, F.J. Holler, S.R. Crouch, *Fundamentals of Analytical Chemistry*. 2002, Thomson Brooks/Cole.
- [101] J.J. Vollmer, K.L. Servis, Woodward-Hoffmann rules: Cycloaddition reactions, *Journal of Chemical Education* 47 (1970) 491.
- [102] J.J. Vollmer, K.L. Servis, Woodward-Hoffmann rules: Electrocyclic reactions, *Journal of Chemical Education* 45 (1968) 214.
- [103] J.C. Kotz, P.M. Treichel, G.C. Weaver, *Bonding and Molecular Structure:Orbital Hybridization and Molecular Orbitals*. *Chemistry & Chemical Reactivity*, 457 (2006) 32
- [104] Y. Nakaoka, Y. Nosaka, Electron spin resonance study of radicals produced by photoirradiation on quantized and bulk zns particles, *Langmuir* 13 (1997) 708.
- [105] M.H. Ullah, I. Kim, C.S. Ha, pH selective synthesis of ZnS nanocrystals and their growth and photoluminescence, *Materials Letters* 61 (2007) 4267.
- [106] M. Zhang, R. Wang, X. Wu, J. Wang, Principle, system, and applications of tip-enhanced Raman spectroscopy, *Science China Physics, Mechanics and Astronomy* 55 (2012) 1335.

- [107] R. Brunner, F.E. Talke, Tribological and mechanical characterization of carbon-coated sliders and disks, *Tribology Letters* 40 (2010) 213.
- [108] J. Wang, *Analytical Electrochemistry*. 2000, A John Wiley & Sons, Inc., Publication: New York.
- [109] G. Binnig, C.F. Quate, C. Gerber, Atomic force microscope, *Physical Review Letters* 56 (1986) 930.
- [110] J. Goldstein, *Scanning electron microscopy and x-ray microanalysis*, Springer (2003) 689.
- [111] R.F. Egerton, *Physical principles of electron microscopy : an introduction to TEM, SEM, and AEM*, Springer (2005) 202.
- [112] L. Reimer, *Scanning electron microscopy : physics of image formation and microanalysis*, Springer (1998) 527.
- [113] A.C. Curtis, D.G. Duff, P.P. Edwards, D.A. Jefferson, B.F. Johnson, A.I. Kirkland, A.S. Wallace, Preparation and structural characterization of an unprotected copper sol., *Journal of Physics Chemistry* 92 (1988) 2270.
- [114] D.G. Duff, A.C. Curtis, P.P. Edwards, D.A. Jefferson, Johnson B.F., D.E. Logan, The microstructure of colloidal silver-evidence for a polytetrahedral growth sequence, *Journal of the Chemistry Society, Chemical Communications* 16 (1987) 1.
- [115] J.C. Russ, *Fundamentals of Energy Dispersive X-ray Analysis*. 1984, Butterworths: London.
- [116] V.D. Scott, G. Love, *Quantitative Electron Probe Microanalysis*,. 1994, Ellis Horwood,: Chichester.
- [117] J.I. Goldstein, et al, *Scanning Electron Microscopy and X-ray Microanalysis*. 2003, Plenum Press: New York.

- [118] K.F.J. Heinrich, D.E. Newbury, *Electron Probe Quantitation* 1991, Plenum Press: New York.
- [119] N.H. Turner, R.J. Colton, Surface analysis: x-ray photoelectron spectroscopy, auger electron spectroscopy, and secondary ion mass spectrometry, *Analytical Chemistry* 54 (1982) 5.
- [120] J.J.V. Benschoten, J.Y. Lewis, W.R. Heineman, D.A. Roston', P.T. Kissinger, Cyclic Voltammetry Experiment, *Journal of Chemical Education*.
- [121] P.M.S. Monk, *Analytical Techniques in the Sciences (AnTS)*, in *Fundamentals of Electroanalytical Chemistry*, C. Series Editor: David J. Ando, Dartford, Kent, UK, Editor. 2005, JOHN WILEY & SONS LTD: Chichester New York Weinheim Brisbane Toronto Singapore.
- [122] F.C. Anson, Cyclic and differential pulse voltammetric behavior of reactants confined to the electrode surface, *Analytical Chemistry* 49 (1977).
- [123] P.T. Kissinger, W.R. Heineman, Cyclic Voltammetry, *Journal of Chemical Education*.
- [124] F. Harnisch, S. Freguia, A basic tutorial on cyclic voltammetry for the investigation of electroactive microbial biofilms, *Chemistry-an Asian Journal* 00 (2012) 0.
- [125] D.K. Gosser, *Cyclic Voltammetry: Simulation and Analysis of Reaction Mechanisms*. 1993, VCH Publishers, Inc. : New York.
- [126] E. Gileadi, *Electrode kinetics for chemists, chemical engineers and material scientists*. 1993, VCH Publishers, Inc.: 220 East 23rd Street New York, New York 10010.
- [127] M.O. Brett, *Electrochemistry principles, methods, and applications*. 1993, Oxford New York Tokyo oxford university press.
- [128] C.G. Zoski, *Handbook of Electrochemistry*. 2007, Elsevier: New Mexico, USA.

- [129] P. Zanello, *Inorganic Electrochemistry Theory, Practice and Application*. 2003, The Royal Society of Chemistry: Thomas Graham House, Science Park, Milton Road, Cambridge CB4 0WF, UK.
- [130] P. Atkins, J.D. Paula, *Physical Chemistry*, Oxford University Press.
- [131] P. Monk, *Fundamentals of Electroanalytical Chemistry*. 2001, John Wiley & Sons Ltd: Chichester New York.
- [132] H.H. Girault, *Analytical and Physical Electrochemistry*, M. Parsons, Editor. 2004, EPFL Press: New York, NY 10016, U.S.A.
- [133] M. Kendig, J. Scully, Basic aspects of electrochemical impedance application for the life prediction of organic coatings on metals, *Corrosion* 46 (1990) 22.
- [134] W.G.W., A review of impedance plot methods used for corrosion performance analysis of painted metals, *Corrosion Science* 26 (1986) 681.
- [135] E. Barsoukov, J.R. Macdonald, *Impedance spectroscopy; theory, experiment, and applications*. 2005, Wiley Interscience Publications.
- [136] F. Mansfeld, Electrochemical impedance spectroscopy (EIS) as a new tool for investigation methods of corrosion protection, *Electrochimica Acta* 35 (1990) 1533.
- [137] M.E. Orazem, B. Tribollet, *Electrochemical impedance spectroscopy*. 2008, John Wiley & Sons, Inc.: Hoboken, New Jersey.
- [138] S. Fletcher, Basic aspects of electrochemical impedance application for the life prediction of organic coatings on metals, *Corrosion* 46 (1990) 22.
- [139] D. Loveday, P. Peterson, B. Rodgers, eds. *Fundamentals of Electrochemical Impedance Spectroscopy*. Evaluation of organic coatings with electrochemical impedance spectroscopy. Part 1, *Journal of Coatings Technology and Research* (2004) 46.

- [140] P. Agarwal, M.E. Orazem, L.H. Garcia-Rubio, Measurement models for electrochemical impedance spectroscopy I. Demonstration of applicability, *Journal of the Electrochemical Society* 139 (1992) 1917.
- [141] P.W. Atkins, *Physical Chemistry*. 1990, Oxford University Press.
- [142] D. Loveday, P. Peterson, B. Rodgers, eds. *Protocols for Testing Coatings with EIS*. Evaluation of organic coatings with electrochemical impedance spectroscopy. Part 3, *Journal of Coatings Technology and Research* 22 (2005) 12
- [143] B.A. Boukamp, A linear kronig kramers transform test for immittance data validation, *Journal of the Electrochemical Society* 142 (1995) 1885.
- [144] A. Lasia, *Electrochemical impedance spectroscopy and its applications*, in *electrochemical impedance spectroscopy and its applications, modern aspects of Electrochemistry*. 1999, Département de chimie, Université de Sherbrooke, Sherbrooke Québec, J1K 2R1. p. 143.
- [145] D.D. Macdonald, Review of mechanistic analysis by electrochemical impedance spectroscopy, *Electrochimica Acta* 35 (1990) 1525.
- [146] D. Loveday, P. Peterson, B. Rodgers, eds. *Application of EIS to Coatings*. Evaluation of organic coatings with electrochemical impedance spectroscopy Part 2, *Journal of Coatings Technology and Research* 88 (2004) 51.
- [147] P. Ferloni, M. Mastragostino, L. Meneghello, Impedance analysis of electronically conducting polymers, *Electrochimica Acta* 41 (1996) 27.
- [148] M.N. Peter, N.J. Abongile, R.A. Olowu, S.N. Mailu, F.R. Ngece, A. Williams, T.T. Waryo, P.G.L. Baker, E.I. Iwuoha, Impedimetric response of a label-free genosensor prepared on a 3-mercaptopropionic acid capped gallium selenide nanocrystal modified gold electrode, *International Journal of Electrochemical Science* 6 (2011) 1438

- [149] F.S., Tables of degenerate electrical networks for use in the equivalent-circuit analysis of electrochemical systems, *Journal of The Electrochemical Society* 141 (1994) 1823.
- [150] R.A.D. Hui, M. Chipara, Morjan, Gh. Aldicac, M. D. Chipara, K. T. Lau D, Impedance spectroscopy studies on doped polyanilines, *Journal of Optoelectronics and Advanced Materials* (2004) 13.
- [151] M.K.A. Kadir, I.E. Tothill, Development of an electrochemical immunosensor for fumonisins detection in foods, *Toxins* 2 (2010) 382.
- [152] W.R.H. Adrian, W. Bott, Chronocoulometry, *Current Separations* 20 (2004) 2.
- [153] F.C. Anson, R.A. Osteryoung, Chronocoulometry: A convenient, rapid and reliable technique for detection and determination of adsorbed reactants, *Journal of Chemical Education* 60 (1983) 293.
- [154] R. Pyati, M.M. Richter, ECL-Electrochemical luminescence, *Annual Reports Section "C" (Physical Chemistry)* 103 (2007) 12.
- [155] Q. Jiang, Electrochemiluminescent and chemiluminescent labels for bioaffinity assays, Doctoral Dissertation, Helsinki University of Technology, Department of Chemical Technology TKK Dissertations 29 (2006).
- [156] S. Kulmala, M. Helin, T. Ala-Kleme, L. Väre, D. Papkovsky, T. Korpela, A. Kulmala, Electrochemiluminescent labels for applications in fully aqueous solutions at oxide-covered aluminium electrodes, *Analytica Chimica Acta* 386 (1999) 1.
- [157] A.H. Wu, J.J. Sun, Y.M. Fang, R.J. Zheng, G.N. Chen, Hot electron induced cathodic electrochemiluminescence at disposable screen printed carbon electrodes, *Electroanalysis* 22 (2010) 2702.
- [158] P. Laakso, H. Anttila, V. Kairisto, J. Eskola, S. Kulmala, T. Ala-Kleme, Hot electron-induced electrogenerated chemiluminescence of SYBR® Green I, *Analytica Chimica Acta* 541 (2005) 83.

- [159] R.J. Forster, P. Bertoncello, T.E. Keyes, *Electrogenerated Chemiluminescence*, *Annual Review of Analytical Chemistry* 2 (2009) 359.
- [160] M. Latva, S. Kulmala, K. Haapakka, Solution structures of luminescent chelates of europium (III) with 2,6-bis[N,N-bis(carboxymethyl) aminomethyl]-4-benzoylphenol, *Inorganica Chimica Acta* 247 (1996) 209.
- [161] M.M. Collinson, J. Taussig, S.A. Martin, Solid-State Electrogenerated chemiluminescence from gel-entrapped Ruthenium(II) Tris(bipyridine) and tripropylamine, *Chemistry of Materials* 11 (1999) 2594.
- [162] D.G. Nocera, H.B. Gray, Electrochemical reduction of molybdenum(II) and tungsten(II) halide cluster ions. Electrogenerated chemiluminescence of tetradecachlorohexamolybdate(2⁻) ion, *Journal of the American Chemical Society* 106 (1984) 824.
- [163] L. Dennany, R.J. Forster, B. White, M. Smyth, J.F. Rusling, Direct electrochemiluminescence detection of oxidized DNA in ultrathin films containing [Os(bpy)₂(PVP)₁₀]²⁺, *Journal of the American Chemical Society* 126 (2004) 8835.
- [164] K. Aslan, M. Wu, J.R. Lakowicz, C.D. Geddes, Fluorescent Core-Shell Ag@SiO₂ nanocomposites for metal-enhanced fluorescence and single nanoparticle sensing platforms, *Journal of the American Chemical Society* 129 (2007) 1524.
- [165] A.M. Spehar-Deleze, Y. Pellegrin, T.E. Keyes, R.J. Forster, Electrochemiluminescent metallopolymers: Tuning the emission wavelength by energy transfer between two bound centres, *Electrochemistry Communications* 10 (2008) 984.
- [166] A. Devadoss, C. Dickinson, T.E. Keyes, R.J. Forster, Electrochemiluminescent metallopolymer-nanoparticle composites: nanoparticle size effects, *Analytical Chemistry* 83 (2011) 2383.

- [167] P.L. Stiles, J.A. Dieringer, N.C. Shah, R.P. Van Duyne, Surface-enhanced Raman spectroscopy, *Annual Review Of Analytical Chemistry (Palo Alto, Calif.)* 1 (2008) 601.
- [168] D.V.K., D.C. Marcano, J.M. Berlin, A. Sinitskii, Z. Sun, A. Slesarev, B.L. Alemany, L. Wei, J.M. Tour, Improved synthesis of graphene oxide, *ACS Nano*. 4 (2010) 36.
- [169] M.B.M. Terrones, R.C.D. Andrés, J.U. López, V.C. Florentino, I.R.M. Yadira, J.E. Fernando, A.L.M. Sandoval, E.C. Márquez, A.G. Charlier, J.T. Christophe, Humberto, Graphene and graphite nanoribbons: morphology, properties, synthesis, defects and applications, *Nano Today* 5 (2010) 351.
- [170] L.J.C. Jaemyung, K. Franklin, W. Yuan, K.R. Shull, J. Huang, Graphene oxide sheets at interfaces, *Journal of the American Chemical Society* 132 (2010) 8180.
- [171] W.S.O. Hummers, E. Richard, Preparation of graphitic oxide, *Journal of the American Chemical Society* 80 (1958) 1339.
- [172] N.I. Kovtyukhova, P.J. Ollivier, B.R. Martin, T.E. Mallouk, S.A. Chizhik, E.V. Buzaneva, A.D. Gorchinskiy, Layer-by-layer assembly of ultrathin composite films from micron-sized graphite oxide sheets and polycations, *Chemistry of Materials* 11 (1999) 771.
- [173] C.O. Saby, B. Champagne, G.Y. Bélanger, Daniel, Electrochemical modification of glassy carbon electrode using aromatic diazonium salts. 1. Blocking effect of 4-nitrophenyl and 4-carboxyphenyl groups, *Langmuir* 13 (1997) 6805.
- [174] A. Chrouda, M. Braiek, K.B. Rokbani, A. Bakhrouf, A. Maaref, N. Jaffrezic-Renault, An immunosensor for pathogenic staphylococcus aureus based on antibody modified aminophenyl-Au electrode, *ISRN Electrochemistry* 2013 (2013) 9.
- [175] P.A. Brooksby, A.J. Downard, Electrochemical and atomic force microscopy study of carbon surface modification via diazonium reduction in aqueous and acetonitrile solutions, *Langmuir* 20 (2004) 5038.

- [176] P. Allongue, M. Delamar, B. Desbat, O. Fagebaume, R. Hitmi, J. Pinson, J.M. Save´ant, Covalent modification of carbon surfaces by aryl radicals generated from the electrochemical reduction of diazonium salts, *Journal of the American Chemical Society* 119 (1997) 201.
- [177] A.E. Radi, X. Muñoz-Berbel, M. Cortina-Puig, J.L. Marty, An electrochemical immunosensor for ochratoxin A based on immobilization of antibodies on diazonium-functionalized gold electrode, *Electrochimica Acta* 54 (2009) 2180.
- [178] R. Wang, C. Xue, A sensitive electrochemical immunosensor for alpha-fetoprotein based on covalently incorporating a bio-recognition element onto a graphene modified electrode via diazonium chemistry, *Analytical Methods* 5 (2013) 5195.
- [179] G. Liu, J. Liu, T.P. Davis, J.J. Gooding, Electrochemical impedance immunosensor based on gold nanoparticles and aryl diazonium salt functionalized gold electrodes for the detection of antibody, *Biosensors and Bioelectronics* 26 (2011) 3660.
- [180] L. Zhisong, C.X. Guo, H.B. Yang, Y. Qiao, J. Guo, L.C. Ming, One-step aqueous synthesis of graphene-CdTe quantum dot-composed nanosheet and its enhanced photoresponses, *Journal of Colloid and Interface Science* 353 (2010) 588.
- [181] Q.L. Xu Zhu, X. Zhu, L. Chunlan, X. Maotian, Y. Liang, Reduction of graphene oxide via ascorbic acid and its application for simultaneous detection of dopamine and ascorbic acid, *International Journal of Electrochemical Science* 7 (2012) 5172.
- [182] K.T.V. Loryuenyong, P. Eimburanaprat, A.B.W. Boonchompoo, Preparation and characterization of reduced graphene oxide sheets via water-based exfoliation and reduction methods, *Advances in Materials Science and Engineering* 2013 (2013) 5.
- [183] D. Philip, Synthesis and spectroscopic characterization of gold nanoparticles, *Spectrochimica Acta Part A: Molecular and Biomolecular Spectroscopy* 71 (2008) 80.
- [184] S.R. M. Behera, Synthesis and characterization of core-shell gold nanoparticles

with poly(vinyl pyrrolidone) from a new precursor salt, *Applied Nanoscience* 3 (2013) 83.

[185] M.D.S. Bhandari, A.G Joshi, A.P Saxena, A.K Srivastava, Revelation of graphene-Au for direct write deposition and characterization, *Nanoscale Research Letters* 424 (2011).

[186] L. Jing, L. Chun-yan, Ag/Graphene heterostructures: synthesis, characterization and optical properties, *European Journal of Inorganic Chemistry* 2010 (2010) 1244.

[187] Q.R. Zhang, M. Qiaoqiao, Y. Yuan, J. Wang, L. Kaikai, H. Fenghua, N. Dongxue, One-step synthesis of graphene/polyallylamine-Au nanocomposites and their electrocatalysis toward oxygen reduction, *Talanta* 89 (2012) 391.

[188] L.J.A.N Jing, C. Wen-xia, Y. Chun-xia, H. Fang-di, W. Chun-ming, Electrochemical study and application on shikonin at poly(diallyldimethylammonium chloride) functionalized graphene sheets modified glass carbon electrode, *Chemical Journal of Chinese Universities* (2012) 12.

[189] Z.G. Le, L. Zhirong, Q.Y. Wang, Chunyan, A facile and efficient approach to decoration of graphene nanosheets with gold nanoparticles, *Applied Surface Science* 258 (2012) 5348.

[190] M.M. Chehimi, A. Lamouri, M. Picot, J. Pinson, Surface modification of polymers by reduction of diazonium salts: polymethylmethacrylate as an example, *Journal of Materials Chemistry C* 48 (2013) 87.

[191] P. Allongue, M. Delamar, B. Desbat, O. Fagebaume, R. Hitmi, J. Pinson, J.M. Save'ant, Covalent modification of carbon surfaces by aryl radicals generated from the electrochemical reduction of diazonium salts, *Journal of the American Chemical Society* 119 (1997) 207

[192] A. Chausse', M.M. Chehimi, N. Karsi, J. Pinson, F. Podvorica, C. Vautrin-UI, The electrochemical reduction of diazonium salts on iron electrodes. The formation of covalently bonded organic layers and their effect on corrosion, *Chemistry of Materials* 14 (2002) 400.

- [193] R.N. McDonald, Generation, thermochemistry, and chemistry of carbene anion radicals and related species, *Tetrahedron* 45 (1989) 4015
- [194] G. Zhihui, D. Shaojun, Electrogenerated chemiluminescence from $\text{Ru}(\text{bpy})_3^{2+}$ ion-exchanged in carbon nanotube/perfluorosulfonated ionomer composite films, *Analytical Chemistry* 76 (2004) 2683.
- [195] J. Choi, *ECL Mechanism of $\text{Ru}(\text{bpy})_3^{2+}/\text{TPrA}$ System*, The University of Texas at Austin.
- [196] P. Bertoncello, L. Dennany, R.J. Forster, P.R. Unwin, Nafion-Tris (2-2 ϕ -bipyridyl)ruthenium(II) Ultrathin Langmuir-Schaefer Films: Redox Catalysis and Electrochemiluminescent Properties, *Analytical Chemistry* 79 (2007) 7549.
- [197] E.I. Iwuoha, Z. Shiba, Z. Smyth, R.F. Malcolm, O. Uwe, R. Paul, Drug metabolism biosensors: electrochemical reactivities of cytochrome P450cam immobilised in synthetic vesicular systems, *Journal of Pharmaceutical and Biomedical Analysis* 17 (1998) 1101.
- [198] J.C. Dyre, The random free-energy barrier model for ac conduction in disordered solids, *Journal of Applied Physics* 64 (1998) 2456.
- [199] J. Owino, A. Ignaszak, A. Al-Ahmed, P. Baker, H. Alemu, J. Ngila, I. E., Modelling of the impedimetric responses of aflatoxin B1; immunosensor prepared on an electrosynthetic polyaniline platform, *Analytical and Bioanalytical Chemistry* 388 (2007) 1069.
- [200] M. Munkombwe, E.I. Iwuoha, P. Edmund, W. Natasha, J. Nazeem, B. Priscilla, W. Tesfaye, W. Avril, Electrochemical Ochratoxin-A immunosensor system developed on sulfonated polyaniline, *Electroanalysis* 23 (2011) 122.
- [201] A. Sargent, O.A.Sadik, Monitoring antibody-antigen reactions at conducting polymer-based immunosensors using impedance spectroscopy, *Electrochimica Acta* 44 (1999) 4667.
- [202] L. Dennany, G.G. Wallace, R.J. Forster, Luminescent metal complexes within polyelectrolyte layers: tuning electron and energy transfer, *Langmuir* 25 (2009) 14053.

- [203] E. O'Reilly, *Conjugated Metallopolymer Systems for Electrochemiluminescence Enhancement; New Approaches and Materials.*, in *School of Chemical Sciences*. 2008, Dublin City University: Dublin Ireland.
- [204] P. Bertoncello, R.J. Forster, Nanostructured materials for electrochemiluminescence (ECL)-based detection methods: Recent advances and future perspectives, *Biosensors and Bioelectronics* 24 (2009) 3191.
- [205] W. Gao, Y. Chen, J. Xi, A. Zhang, Y. Chen, F. Lu, Z. Chen, A novel electrochemiluminescence sensor based on $[\text{Ru}(\text{bpy})_3]^{2+}$ immobilized by graphene on glassy carbon electrode surface via in situ wet-chemical reaction, *Sensors and Actuators B: Chemical* 171 (2012) 1159.
- [206] S.C. Rasmussen, D.W. Thompson, V. Singh, J.D. Petersen, Controlled Synthesis of a New, Soluble, Conjugated Metallopolymer Containing Ruthenium Chromophoric Units, *Inorganic Chemistry* 35 (1996) 3449.
- [207] M. Munkombwe, T. Waryo, O. Arotiba, E. Kazmierska, A. Morrin, A.J. Killard, M.R. Smyth, N. Jahed, B. Kgarebe, P.G.L. Baker, E.I. Iwuoha, Electrochemical nitrite nanosensor developed with amine and sulphate functionalised polystyrene latex beads self-assembled on polyaniline, *Electrochimica Acta* 33 (2010) 4280.
- [208] I.A. Jessop, P.P. Zamora, F.R. Diaz, M.A. del Valle, A. Leiva, L. Cattin, M. Makha, J. C. Bernède, New polymers based on 2,6-di (thiophen-2-yl)aniline and 2,2'- (thiophen-2,5-diyl)dianiline monomers. Preparation, characterization and thermal, optical, electronic and photovoltaic properties, *International Journal of Electrochemical Science* 7 (2012) 9502.
- [209] I.L. Kogan, G.V. Gedrovich, L.S. Fokeeva, S.I. G., Electrochemical and conducting properties of polyaniline in the neutral aqueous solutions of potassium acetate and zinc salts, *Electrochimica Acta* 41 (1996) 1833.

- [210] N.G.R. Mathebe, A. Morrin, E.I. Iwuoha, Electrochemistry and scanning electron microscopy of polyaniline/peroxidase-based biosensor, *Talanta* 64 (2004) 115.
- [211] E.I. Iwuoha, S.E. Mavundla, V.S. Sormerset, L.F. Petrik, M.J. Klink, M. Sekota, Electrochemical and spectroscopic properties of fly ash-polyaniline matrix nanorod composites, *Microchimica Acta* 155 (2006) 453.
- [212] A.F. Diaz, J.A. Logan, Electroactive polyaniline films, *Journal of Electroanalytical Chemistry and interfacial Electrochemistry* 111 (1980) 111.
- [213] T. Kobayashi, H. Yoneyama, T. H., Electrochemical reactions concerned with electrochromism of polyaniline film-coated electrodes, *Journal of Electroanalytical Chemistry and interfacial Electrochemistry* 177 (1984) 281.
- [214] E.I. Iwuoha, D.S. de Villaverde, N.P. Garcia, M.R. Smyth, J.M. Pingarron, Reactivities of organic phase biosensors. 2. The amperometric behaviour of horseradish peroxidase immobilised on a platinum electrode modified with an electrosynthetic polyaniline film, *Biosensors and Bioelectronics* 12 (1997) 749.
- [215] A. Benyoucef, S. Boussalem, M.I. Ferrahi, M. Belbachir, Electrochemical polymerization and in situ FTIRS study of conducting polymers obtained from oaminobenzoic with aniline at platinum electrodes, *Synthetic Metals* 160 (2010) 1591.
- [216] K. Grennan, A.J. Killard, C.J. Hanson, A.A. Cafolla, S.M. R., Optimisation and characterisation of biosensors based on polyaniline, *Talanta* 68 (2006) 1591.
- [217] S.Y. Hong, Y.M. Jung, S.B. Kim, P. S.M, *Electrochemistry of Conductive Polymers*. 34. Two-dimensional correlation analysis of real-time 320 spectroelectrochemical data for aniline polymerization, *The Journal of Physical Chemistry B* 109 (2005) 3844.
- [218] M.J. Klink, E.I. Iwuoha, E.E. Ebenso, The electrocatalytic and redox-mediator effects of nanostructured pdma psa modified-electrodes as phenol derivative sensors, *International Journal of Electrochemical Science* 6 (2011) 2429

- [219] J.T. La Belle, K. Bhavsar, A. Fairchild, A. Das, J. Sweeney, T.L. Alford, J. Wang, V.P. Bhavanandan, L. Joshi, A cytokine immunosensor for multiple sclerosis detection based upon label-free electrochemical impedance spectroscopy, *Biosensors and Bioelectronics* 23 (2007) 428.
- [220] G. Robinson, H. Hill, R. Philo, J.M. Gear, S.J. Rattle, F. GC, Bioelectrochemical enzyme immunoassay of human choriogonadotropin with magnetic electrodes, *Clinical Chemistry* 31 (1985) 1449.
- [221] J.J. Gooding, Advances in interfacial design for electrochemical biosensors and sensors: aryl diazonium salts for modifying carbon and metal electrodes, *Electroanalysis* 20 (2008) 573.

